



Polymeric membranes functionalized by poly(ionic liquid)s and palladium nanoparticles : application for CO² capture and catalytic membranes

Yingying Gu

► To cite this version:

Yingying Gu. Polymeric membranes functionalized by poly(ionic liquid)s and palladium nanoparticles : application for CO² capture and catalytic membranes. Chemical and Process Engineering. Université Paul Sabatier - Toulouse III, 2015. English. NNT : 2015TOU30157 . tel-01356666

HAL Id: tel-01356666

<https://theses.hal.science/tel-01356666>

Submitted on 26 Aug 2016

HAL is a multi-disciplinary open access archive for the deposit and dissemination of scientific research documents, whether they are published or not. The documents may come from teaching and research institutions in France or abroad, or from public or private research centers.

L'archive ouverte pluridisciplinaire **HAL**, est destinée au dépôt et à la diffusion de documents scientifiques de niveau recherche, publiés ou non, émanant des établissements d'enseignement et de recherche français ou étrangers, des laboratoires publics ou privés.



THÈSE

En vue de l'obtention du

DOCTORAT DE L'UNIVERSITÉ DE TOULOUSE

Délivré par : *l'Université Toulouse 3 Paul Sabatier (UT3 Paul Sabatier)*

Présentée et soutenue le 21/07/2015 par :

Yingying GU

Membranes polymères fonctionnalisées par des poly(liquide ionique)s et des nanoparticules de palladium: applications au captage de CO₂ et aux membranes catalytiques

JURY

ERIC FAVRE	Professeur des Universités (LRGP, ENSIC, Nancy)	Rapporteur
LAURENT DJAKOVITCH	Directeur de recherche CNRS (IRCELYON)	Rapporteur
THÉODORE TZEDAKIS	Professeur des Universités (LGC, U. Toulouse III)	Président du Jury
JEAN-CHRISTOPHE REMIGY	Maitre de conférences, HDR (LGC, U. Toulouse III)	Membre du Jury
MONTSERRAT GÓMEZ	Professeur des Universités (LHFA, U. Toulouse III)	Invitée
RICHARD D. NOBLE	Professeur de University of Colorado, Boulder, USA	Invité

École doctorale et spécialité :

MEGEP : Génie des procédés et de l'Environnement

Unité de Recherche :

Laboratoire de Génie Chimique - CNRS (UMR 5503)

Directeur(s) de Thèse :

Jean-Christophe Remigy

Rapporteurs :

Eric Favre et Laurent Djakovitch

Acknowledgements

In the very first place of this thesis, I would like to give my sincere acknowledgements to all those who have made contributions or support for this work. There are just too many people to thank to.

I express my deep gratitude to my supervisor Jean-Christophe Remigy for his enlightening guidance and great support throughout the whole thesis project and for the enough freedom that he accorded to me to explore the subject. I would also like to deliver my most sincere thankfulness to all the co-supervisors : Jean-François Lahitte, Montserrat Gómez, Richard D. Noble and Douglas L. Gin for their valuable instructions, availability, huge support and personal help. Without them, this project could not be a success.

I deeply appreciate Professor Eric Favre and Laurent Djakovitch, research director at IRCELYON for having accepted to evaluate this thesis and for their valuable advices. I'm also grateful to the Ministère de l'Enseignement Supérieur et de la Recherche for providing financial support for the thesis.

My warm thanks also go to Pierre Aimar, Jean-Christophe Rouch, Sandrine Desclaux, Laure Latapie, Isabelle Favier, Emmanuelle Teuma, Christian Pradel, Patrice Bacchin and Hans H Funke for their useful help on the research work and their willingness to do so. I would like to thank Patrice Bacchin again, Hélène Roux-de Balman, Régine Legoff and Naïma Khoujane as well for giving supports and helps on all the administrative work. Besides, I owe my thanks to Christel Causserand for her constructive comments on the 2nd year report and to Catherine Stasiulis for her great help on the application of carte de séjour.

In addition, I would like to address my gratefulness to Clélia Emin, Elsa Lasseuguette, Faouzi Chahdoura, Thibaut Savart, Marta Rodriguez Rodriguez, Antonio Reina Tapia, Marcelo, Lee Miller, Nathaniel Urban, Matthew Cowan, William McDanel, Blain Carter, Phuc Tien Nguyen, Lilly Robertson, Sarah Dischinger and my friends for their friendliness, their help in the research and for having created the warm and joyful ambience around.

At last, I would like to dedicate this thesis in memory of my parents. Their love and support are beyond expression.

Contents

General introduction	5
1 Bibliographic study	9
1.1 General introduction on synthetic membranes	12
1.1.1 Membrane classification and corresponding separation processes concerned	12
1.1.2 Membrane performance evaluation	13
1.1.3 Transport mechanism through membranes	17
1.1.4 Filtration mode and module configurations	20
1.2 Preparation of composite polymer membranes	22
1.3 Membrane for CO ₂ capture	25
1.3.1 Basic types of CO ₂ capture	25
1.3.2 Polymer membranes for CO ₂ capture	25
1.3.3 CO ₂ plasticization and competitive sorption in polymer membranes	31
1.4 Process intensification	34
1.4.1 Microreactors	36
1.4.2 Catalytic membrane reactors	36
1.5 Metallic nanoparticles (MNPs) in catalysis	39
1.5.1 Synthesis of MNPs	40
1.5.2 Mechanisms of nanoparticle formation	41
1.5.3 Stabilization of MNPs	42
1.5.4 Polymer swelling by solvent and mass transfer inside polymer ma- trices	44
1.6 Ionic liquids for CO ₂ capture and MNP stabilization	47
1.6.1 RTILs for MNP stabilization	47
1.6.2 RTILs for CO ₂ capture	49
1.7 Conclusions	50
2 Materials and methods	53
2.1 General	56
2.1.1 Materials	56
2.1.2 Analyses	56

2.2	Modification of hollow fibers by room temperature ionic liquids for CO ₂ capture	57
2.2.1	Composite hollow fiber preparation	57
2.2.2	Gas permeance test for composite hollow fibers	59
2.2.3	Experimental conditions for tensile test	60
2.3	Preparation of colloidal palladium systems and their catalytic performance	60
2.3.1	Synthesis of colloidal palladium nanoparticles in ionic liquid	60
2.3.2	Synthesis of colloidal palladium nanoparticles in glycerol	60
2.3.3	Catalytic tests on the colloidal systems	61
2.4	Preparation, characterization and performance of the catalytic membrane	62
2.4.1	Synthesis of ionic liquids a and b	62
2.4.2	ICP-OES analyses	64
2.4.3	Preparation of the catalytic membrane	65
2.4.4	Permeability test	65
2.4.5	Reactions performed on the catalytic membrane	66
2.4.6	Colloidal palladium stabilized in glycerol served as reference for more challenging reactions	68
3	Preparation of composite hollow fiber with a thin polyRTIL-RTIL gel layer for CO₂ capture	69
3.1	Introduction	72
3.2	General Information	73
3.2.1	Ionic liquids concerned and their gas permeability	73
3.2.2	Support membranes	74
3.2.3	UV Lamp and optical filter type	75
3.3	Influential factors in photo-grafting and composite membrane performance	75
3.3.1	Compatibility between the support membrane and the grafting solution — General considerations on solvent choice	76
3.3.2	Diffusion of the monomers into the support membrane pores — Oxyphan [®] as support membrane	80
3.3.3	Wetting of the support membrane surface — Teflon AF covered Oxyphan as support membrane	85
3.3.4	Gas separation performance and influence of monomer concentration and fiber velocity — Oxyplus [®] as support membrane	89
3.3.5	IL monomer type	99
3.4	Conclusions	101
4	Study of the catalytic behavior of palladium nanoparticles dispersed in liquid phase	105
4.1	Introduction	108
4.2	Synthesis of colloidal PdNPs	108
4.3	Catalytic study in [MMPIM][NTf ₂] under batch conditions	112
4.3.1	Pd-catalyzed hydrogenation reactions	112
4.3.2	Pd-catalyzed C-C bond formation	115

4.3.3	Pd-catalyzed cross-coupling/hydrogenation sequential process . . .	121
4.4	Catalytic study in glycerol — Exploration of other solvents with physico-chemical properties close to RTILs	122
4.5	Conclusions	123
5	Catalytic polymeric membrane containing palladium nanoparticles	125
5.1	Introduction	128
5.2	Preparation and characterization of the catalytic membrane	129
5.2.1	Choice and synthesis of imidazolium-based ionic liquids	129
5.2.2	Preparation of the catalytic membrane	129
5.2.3	Characterization of the catalytic membrane	130
5.3	Comparison of catalytic activity between the catalytic membrane and the colloidal PdNPs in batch reactor on Suzuki-Miyaura cross-coupling reaction	137
5.3.1	Catalytic performance of the colloidal PdNPs in the batch reactor	137
5.3.2	Performance of the catalytic membrane	140
5.4	Catalytic performance of the catalytic membrane on other reactions . . .	150
5.4.1	Hydrogenation	150
5.4.2	More challenging reactions	152
5.5	Conclusions	154
6	Extrapolation of the catalytic membrane for exothermic reactions and industrial-scale applications	157
6.1	Introduction	162
6.2	Fluid dynamics and concentration profile inside membrane pores	162
6.3	The catalytic membrane for exothermic reactions	164
6.3.1	Reactor model	165
6.3.2	Heat transfer coefficient and Nusselt number	169
6.3.3	Flow rate and heat transfer Péclet number	170
6.3.4	Temperature profile and Stanton number	170
6.3.5	Reactor temperature and external Stanton number	172
6.3.6	Case study	173
6.4	Potential for industrial-scale production	175
6.4.1	Reactor configurations and corresponding working points	176
6.4.2	Considerations on boundary layer and filtration mode	179
6.4.3	Production capacity of the membrane reactor and estimation on the cost of palladium	181
6.5	Conclusions	184
	Conclusions and perspectives	187
	References	192

General introduction

Background and research interest

Systematic studies of membrane phenomena can be traced to the eighteenth century philosopher scientists. For example, Abbé Nolet coined the word ‘osmosis’ to describe permeation of water through a diaphragm in 1748 [1]. By 1960, the elements of modern membrane science had been developed, but membranes were used in only a few laboratory and small, specialized industrial applications (e.g. desalination, dairy industry) [2,3]. While nowadays, membranes and membrane processes have gained important place in chemical technology and are used in a broad range of applications. The fast development of membrane based processes in the last few decades are undoubtedly related to their attractive properties such as low energy cost and environment impact, low weight and space requirements and good modularity, etc. Those unique characteristics permit membrane processes to achieve extraordinary levels of process intensification, a possible solution to the crucial challenges currently facing the world: sustainable industrial growth [4].

Our research lies within the concept of process intensification and sustainable development, with major interest in the advanced functionalization of polymer membranes. The work presented in the thesis concerns the development of two membrane processes: one for CO₂ capture (contributing to global climate change mitigation), one for catalytic membrane (in the pursuit of high productivity/reactor volume ratio and energy efficiency).

Motivations and objectives

Membrane based CO₂ separation processes have advantages mainly in terms of high energy efficiency over other gas separation processes. And the use of room temperature ionic liquids (RTILs) in/as membranes are receiving growing attention. Two major approaches are involved: Supported ionic liquid membranes (SILMs) and dense membranes made from polyRTILs. Recently, a new approach combining the two above – polyRTIL containing RTILs, has witnessed substantial research interest [4–9]. However, most of the studies concerning polyRTIL-RTIL composite membranes are based on lab-scaled flat sheet membranes of small surface area. One of the objectives of this work is to fabricate continuously hollow fibers functionalized by a thin top layer of polyRTIL-RTIL. This modification can further increase the gas permeance and membrane area/surface ratio and thus improve the overall gas separation performance of the membrane. But this modification is generally not feasible using coating or extrusion processes. Herein, we seek to prepare such a composite hollow fiber using photo-grafting process. Success in doing so will be a step further for the innovative lab made membrane materials towards industrial-scale applications.

Concerning catalytic membranes, the most studied up to now are based on inorganic materials (metals or ceramics). Much less attention has been paid to polymeric membranes. Although largely cheaper than inorganic counterparts, polymeric membranes suffer from limited thermal stability (They can only be used at temperatures inferior to 200 °C). It's true that inorganic catalytic membranes are more adapted for high temperature applications, but what about reactions for which such a temperature

is unnecessary? What advantages can polymeric catalytic membranes bring out? How efficient can they be? We try to find answers to those questions in this work. In this pursuit, we prepared a polymeric catalytic membrane (containing palladium nanoparticles (PdNPs) as catalyst) and studied its catalytic performance in order to figure out its mechanism (mass transfer, reactivity) and to compare its performance with that of batch reactors.

Organization of the thesis

Chapter 1 provides a bibliography background of the study. Basic notions and state-of-art of CO₂ capture and of catalytic membrane reactors are introduced. Chapter 2 assembles all the experimental analysis and protocols involved. Chapter 3 deals with the results on polyRTIL based composite hollow fibers for CO₂/N₂ separation. Study on the obtained fiber permeation performance and on the influence of various experimental parameters are presented. Criteria on the choice of materials (i.e. support membrane, solvent). Chapter 4 describes the preparation of an active palladium nanoparticle colloidal system (NPs dispersed in ionic liquid) and their catalytic activity under batch conditions. This colloidal system was used later on to compare with the catalytic membrane, particularly in terms of activity. Chapter 5 comprises a comprehensive study on the catalytic membrane: from preparation methods, study of the NPs dispersion inside the membrane to its catalytic performance. Theoretical calculations were effectuated to understand the origin of the efficiency of the catalytic membrane. Chapter 6 explores through calculations the potential of the catalytic membrane for exothermic reactions and industrial applications.

Chapter 1

Bibliographic study

Résumé du Chapitre

Ce chapitre donne le contexte de l'étude et l'état de l'art qui servent à faciliter la compréhension de cette thèse. Les notions sur les membranes et leurs préparations sont présentées en premier, suivi par les procédés membranaires appliqués au captage de CO_2 . Les membranes catalytiques et les principes d'intensification correspondantes sont ensuite discutées. La synthèse et la stabilisation des nanoparticules métalliques sont également élaborées. Pour terminer, une brève revue sur des applications des liquides ioniques à température ambiante pour le captage de CO_2 et leur utilisation pour stabiliser les nanoparticules métalliques est présentée.

Ces travaux combinent les avantages des procédés membranaires (compacité élevée), des liquides ioniques à température ambiante (avec nombreuses applications et un grand potentiel) et des nanoparticules métalliques qui sont très actives, afin d'obtenir une intensification remarquable des procédés. Notre étude bibliographique est basée non seulement sur des connaissances existantes mais aussi sur leur évolution récente pour le captage de CO_2 par des membranes fibres creuses (décrit dans Chapitre 3) et pour les membranes polymères catalytiques (Chapitre 5 et 6).

This chapter provides a background and state-of-art study that serves as a fundamental basis for the understanding of the thesis. Notions on membranes and their preparation are introduced in the first place, followed by membrane-based applications on CO₂ capture. Then the classification of catalytic membranes and the corresponding intensification principles are discussed, succeeded by elaborations on the synthesis and stabilization of metallic nanoparticles (MNPs). Brief reviews on applications room temperature ionic liquids in CO₂ capture and MNP stabilization are given in the last part.

This thesis combines the ‘membrane processes’ (featuring a high compactness), room-temperature ionic liquids (with wide applications and enormous potential) together with the highly active MNPs in the pursuit of outstanding process intensification. This research is based on the existing knowledge and recent developments as illustrated in this chapter for the realization of the innovative CO₂ capture hollow fiber membrane (elaborated in Chapter 3) and a polymeric catalytic membrane (Chapter 5 and 6).

1.1 General introduction on synthetic membranes

1.1.1 Membrane classification and corresponding separation processes concerned

A membrane can essentially be defined as a barrier that separates two phases and selectively restricts the transport of various chemicals [2]. Membrane based processes have found their wide applications in various domains such as chemical, food, and pharmaceutical industries, biotechnology, and the treatment of toxic industrial effluents, etc [2, 10], thanks to the following advantages [11]:

- Appreciable energy savings
- Environmentally benign
- Clean technology with scale-up and operational ease
- Substitution of conventional processes such as filtration, distillation, ion-exchange and chemical treatment systems
- High quality products
- Greater flexibility in system design.

Membranes can be classified by the type of material (organic, polymeric, inorganic, metallic, etc.) the membrane is made from and also according to the pore size. According to the IUPAC classification, porous membranes with average pore diameters larger than 50 nm are classified as macroporous, and those with average pore diameters in the intermediate range between 2 and 50 nm as mesoporous; microporous membranes have average pore diameters which are smaller than 2 nm. Current membrane processes (classified by pore size) include: [12]

1. Microfiltration (MF, pore sizes ranging from 0.03 to 10 μm) : mainly used for the removal of large particulates, colloids, and bacteria from feed streams; especially popular in the food and beverage industry for treating wastewater before discharging it

to a municipal sewer.

2. Ultrafiltration (UF, pore sizes ranging from 0.002 to 0.1 μm): used in rejecting viruses and polypeptides, and are widely used in protein concentration and wastewater treatment.

3. Nanofiltration (NF, pore size on the order of 1 nm): Nanofiltration membranes are similar to reverse osmosis membranes in that they contain a thin-film composite layer ($<1\ \mu\text{m}$) on top of a porous layer (50 to 150 μm) for small ion selectivity. NF membranes are able to reject multivalent salts and uncharged solutes, while allowing some monovalent salts to pass through. It is often used to soften hard water.

4. Reverse osmosis (RO, pore size around 0.1 nm or dense membranes): Reverse osmosis membranes are even tighter than nanofiltration membranes, and are able to reject all monovalent ions while allowing water molecules to pass through in aqueous solutions. They can also remove viruses and bacteria found in feed solutions. Common applications for reverse osmosis filtration include seawater desalination and industrial water treatment. It is important to note that since the operating pressure for RO and NF is much higher than the pressure applied by MF and UF, the overall yield is relatively lower than that of MF and UF membranes.

5. Pervaporation (PV, dense membranes in general): Pervaporation is recognized as a separation process in which a binary or multicomponent liquid mixture is separated by partial vaporization through a dense membrane. During pervaporation, the feed mixture is in direct contact with one side of the membrane whereas the permeate is removed in a vapor state from the opposite side into a vacuum or sweeping gas and then condense. Pervaporation is unique among membrane separations, involving the liquid-vapor phase change to achieve the separation [13].

6. Gas and vapor separation (GS, dense membranes in general): Gas membranes are now widely used in variety of applications, as shown in Table 1.1.

In addition to the above membrane separation processes, a number of specialty membrane applications also exist, namely electrodialysis, dialysis and membrane distillation, etc. Fig.1.1 illustrates the type and molecular size of species typically separated by these different processes. For porous membranes, the molecular size of the species to be separated plays an important role in determining the pore size of the membrane to be utilized, and the related membrane process. The choice of a porous vs. a dense film, and of the type of material used for manufacturing depends on the desired separation process, operating temperature, driving force used for the separation and thermal and mechanical stability requirements.

1.1.2 Membrane performance evaluation

The ability of a membrane to effectuate separation of mixtures is evaluated by two parameters, its permeability and permselectivity.

For liquid phase separation, the liquid permeability is defined as the ratio of flux density (molar or volumetric flow rate per unit membrane area) to the driving force. In

Table 1.1: Gas separation membrane applications and suppliers [14].

Common gas separation	Application	Supplier
O ₂ /N ₂	Oxygen enrichment nitrogen generation	Permea(Air Products) Generon (IGS), IMS(Praxair) Medal (Air Liquide) Parker Gas Separation, Ube
H ₂ /Hydrocarbons	Refinery hydrogen recovery	Air Products, Air Liquide Praxair, Ube
H ₂ /N ₂	Ammonia Purge gas	as above
H ₂ /CO	Syngas ratio adjustment	as above
CO ₂ /CH ₄	Acid gas treatment enhanced oil recovery landfill gas upgrading	Cynara (NATCO) Kvaerner, Air Products Ube
CO ₂ /N ₂	CO ₂ capture from flue gas	GKSS, MTR, Air liquide
H ₂ S/Hydrocarbons	Sour gas treating	as above
H ₂ O/Hydrocarbons	Natural gas dehydration	Kvaerner, Air Products
Hydrocarbons/air	Pollution control hydrocarbon recovery	Borsig, MTR, GMT NKK
Hydrocarbons from process streams	monomer recovery	SIHI
H ₂ O/Air	Air dehumidification	Air Products, Parker Balston Ultratroc, Praxair

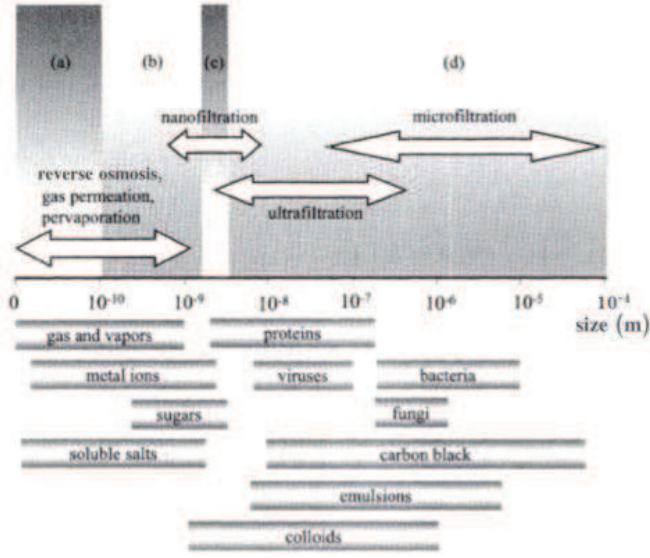


Figure 1.1: Membrane processes differing in pore size and corresponding molecules involved in the separation. (a) dense and ultramicroporous, (b) microporous, (c) mesoporous, (d) macroporous [15]

the case where transport is due, for example, to a partial pressure gradient, the unit of the liquid permeability is $\text{mol (or } m^3) \cdot m^{-2} \cdot Pa^{-1} \cdot h^{-1}$. (Eq. 1.1)

$$L_p = \frac{J}{\Delta P} \quad (1.1)$$

where L_p is the liquid permeability, J is the flux density and ΔP is the transmembrane pressure.

The analogy of the liquid permeability however, is referred to as permeance (Pe) in gas separation, frequently expressed in GPU (gas permeation unit, Eq.1.2, the gas flux is given at standard temperature and pressure (STP)):

$$1 \text{ GPU} = 10^{-6} \text{ cm}^3(\text{STP}) \cdot \text{cm}^{-2} \cdot \text{s}^{-1} \cdot \text{cmHg}^{-1} \quad (1.2)$$

The gas permeability (P) is defined as the amount of gas permeating per second through a material with a surface area of 1 cm^2 and a thickness of 1 cm normalized for the driving force (pressure) in 1 cmHg . It is therefore the product of the gas permeance (Pe) and the membrane thickness (L) (Eq.1.3), generally given in the unit of *barrer* (Eq.1.5). Gas permeability is an intrinsic property of the membrane material and gas permeance is an apparent, directly measurable value that depends on the membrane thickness. The conversion between *barrer* and GPU can be made via Equation 1.5.

$$P = Pe \cdot L \quad (1.3)$$

$$1 \text{ barrer} = 10^{-10} \text{ cm}^3(\text{STP}) \cdot \text{cm} \cdot \text{cm}^{-2} \cdot \text{s}^{-1} \cdot \text{cmHg}^{-1} \quad (1.4)$$

$$10 \text{ barrer}/0.1 \mu\text{m} = 100 \text{ GPU} \quad (1.5)$$

Another important parameter to evaluate the membrane performance is the permselectivity (α_{ij}), which characterizes the ability of the membrane to separate two given species (i and j). In the case of gas separation, the ideal permselectivity is defined as the ratio of the individual permeability for the two species (Eq. 1.6).

$$\alpha_{ij} = \frac{P_i}{P_j} \quad (1.6)$$

Both high permeability and permselectivity are desirable for membrane performance. However there is a trade-off between the two parameters. In 1991, the now well-known Robeson plot for polymeric membranes was published (Fig. 1.2) [16], widely used later for gauging the progress of polymer gas separation membranes. These log-log charts plot ideal permselectivity for a gas pair against the ideal permeability of the more permeable gas. The “upper bound” can be viewed as a target for researchers to exceed in the development of new membranes. The further to the upper right a material lies, the more potential it has for industrial implementation [17].

The Robeson plot is used to evaluate the performance of the polymer material

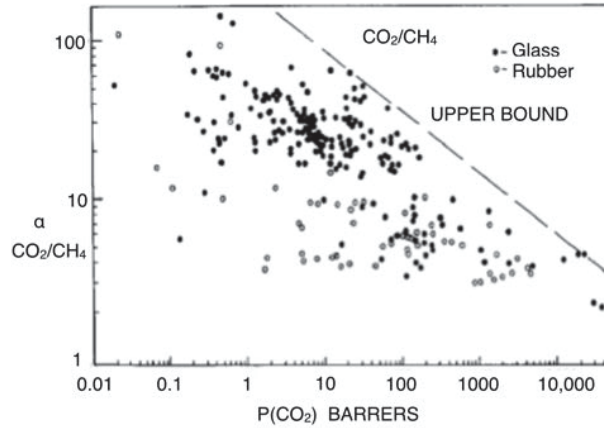


Figure 1.2: Robeson plot for CO_2/CH_4 selectivity versus CO_2 permeability [16].

from which the membrane is made of. For multilayer composite membranes, at least two materials are involved. Change in the thickness of sub-layers can lead to a change of the overall permeance, even when the total membrane thickness is kept the same. It is therefore impossible to deduce the intrinsic permeability value, the permeation property of the membrane can thus only be interpreted in terms of permeance. As a result, those membranes, (including the polyRTIL based composite membrane) can not be positioned in the Robeson plot. The gas separation composite membranes studied in the thesis are evaluated based on permeance.

1.1.3 Transport mechanism through membranes

Driving forces

In order to obtain mass transfer across a membrane, a driving force (i.e. a potential difference) must be applied. Hence the components are transported from the high potential side to the low potential side. The driving force can be a pressure difference (ΔP) or a partial pressure difference (ΔP_i), a concentration difference (Δc), a temperature difference (ΔT) or an electrical potential difference (ΔE). In a steady-state membrane process, energy is dissipated continuously and this energy is required for the transport to occur (Fig.1.3) [18]. In Table 1.2, membrane processes are classified according to their driving forces.

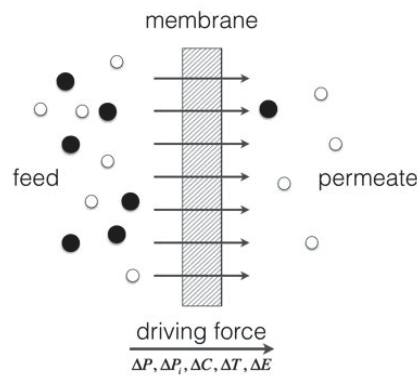


Figure 1.3: Schematic representation of a membrane process under driving force [18].

Table 1.2: Classification of membrane processes according to driving forces.

ΔP	ΔP_i	ΔT	ΔC	ΔE
MF, UF, NF, RO	GS	Thermo-osmosis, Membrane distillation	Dialysis	Electrodialysis, Membrane electrolysis

* MF=Microfiltration; UF=Ultrafiltration; NF=Nanofiltration;
RO=Reverse Osmosis; GS=Gas Separation.

Transport of liquid through membranes

A simple model to describe liquid flow through porous membranes is to consider the membrane as a series of parallel cylindrical capillary pores of diameter d (m) (Fig.1.4). The liquid flux density through the membrane (J , $m^3 \cdot m^{-2} \cdot s^{-1}$) is given by Hagen-



Figure 1.4: Schematic of symmetrical cylinder pore geometry assumed for Hagen-Poiseuille law

Poiseuille equation as:

$$J = \frac{\epsilon \cdot d^2}{32 \cdot \mu \cdot \tau_o} \cdot \frac{\Delta P}{L} \quad (1.7)$$

where ϵ is the membrane surface porosity; μ is the liquid dynamic viscosity ($Pa \cdot s$); τ_o is the membrane tortuosity; ΔP is the transmembrane pressure difference (Pa); L is the membrane thickness (m).

Mechanisms for gas separation

Various mechanisms for gas transport across membranes have been proposed depending on the properties of both the permeant and the membrane.

When it comes to transport of gas molecules through porous membranes, different mechanisms (or a combination of them) are involved as listed below [19, 20]. Those transport mechanisms in the membrane pores are visualized in Fig.1.5.

1. Poiseuille flow (pore size larger than the gas molecule mean free path, no separation occurs)
2. Knudsen diffusion (pore size smaller than the gas molecule mean free path)
3. Selective adsorption followed by surface diffusion across the pore
4. Capillary condensation
5. Molecular sieving (pore size smaller than molecules)

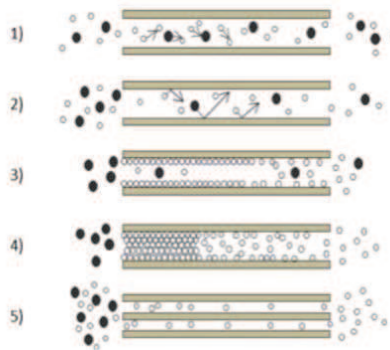


Figure 1.5: Schematic presentation of transport of gas through porous membranes (black and white dots represent two different gases)

Gas transport in dense membranes (membranes with no visible pores, also called nonporous membranes) is best described by the solution-diffusion model, proposed by Lonsdale et al. in 1965 [21], with flux based on Fick's law. Gas permeability (P) is directly proportional to the product of solubility (S) and the diffusion rate (D) of the gas (Eq.1.8).

$$P = S \cdot D \quad (1.8)$$

The transport mechanism of gases through nonporous membranes involves the following steps (Fig.1.6): [11]

- adsorption of the gas at one surface of the membrane
- solution of the gas into the membrane
- diffusion of the gas through the membrane
- release of the gas from solution at the opposite surface
- desorption of the gas from the surface (permeate).

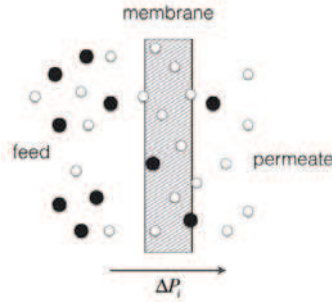


Figure 1.6: Schematic presentation of gas transport through dense membranes: solution-diffusion mechanism

For polymer dense membranes, the spaces between the polymer chains (free volume) in these membranes are less than 5 Å in diameter and so are within the normal range of thermal motion of the polymer chains that make up the membrane matrix [1]. Molecules permeate the membrane through free volume elements between the polymer chains that are transient on the timescale of the diffusion processes. The non-porous structure of the polymer is hence related to the non-continuous passages present in the polymer chain matrix. These passages are created and destroyed due to thermally induced motion of the chains. Therefore, the transport of a penetrant is based on its movement through these passages. The effects of penetrant activity (driving force) and operating conditions then play an important role in governing the gas transport rate and separation property of the membrane. In fact, the major physicochemical factors influencing the gas permeability and permselectivity of polymers are (1) the mobility of polymer chains (as reflected in many cases by glass or sub-glass transition temperature of the polymer); (2) the intersegmental spacing, which is taken as a measure of the mean free volume of the polymer, and (3) the penetrant-polymer interactions (as reflected by the solubility of the

penetrant gases in polymers) [22]. Various free volume models [23–26] and molecular models [27–29] have been proposed to describe the gas diffusion processes in polymers.

1.1.4 Filtration mode and module configurations

Filtration mode

There are mainly two basic modes for liquid phase filtration: dead-end filtration and crossflow filtration [1], as shown in Fig.1.7:

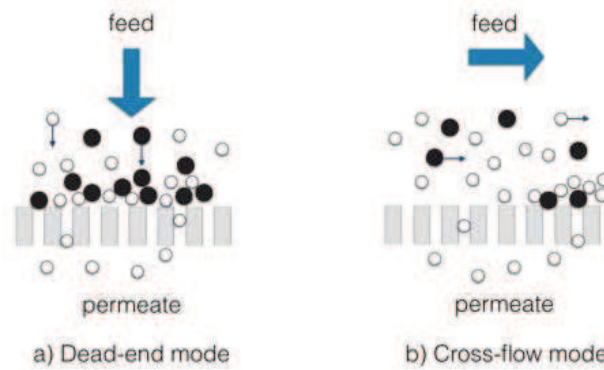


Figure 1.7: Schematic representation of (a) dead-end and (b) cross-flow filtration with porous membranes.

In dead-end filtration, the entire fluid flow is forced through the membrane under pressure (Fig. 1.7-a). As particles accumulate on the membrane surface or in its interior (membrane fouling), the pressure required to maintain the required flow increases. Hence backwashing needs to be performed periodically and/or filter medium has to be replaced at some point. The energy loss is less than when a cross-flow filtration is applied. This filtration mode is particularly effective when feed water carries low level of foulants.

It was in the 1970s that cross-flow filtration began to be used. In cross-flow systems, feed moves parallel to the filter medium to generate shear stress to scour the surface (Fig. 1.7-b). Extra energy is required to generate crossflow, but cake layer thickness can be controlled. Pseudo steady-state may exist, where scouring effect and particle deposition find a balance and cake layer hardly grows. This filtration mode is particularly effective when feed water carries high level of foulants such as suspended solids and macromolecules. The equipment required for cross-flow filtration is more complex, but the membrane lifetime is longer than with dead-end filtration. The fluid speed of the feed fluid flow parallel to the membrane is relatively high. The cleaning of cross-flow installations still needs to be applied from time to time.

Module configurations

Membranes are manufactured as flat sheets, capillaries, or in tubular shapes and are applied in various module configurations. The following membrane modules are commonly used for industrial applications [1, 2]:

(a) Plate and frame module

The plate-and-frame modules (Fig. 1.8-a) were one of the earliest types of membrane system, but because of their relatively high cost and low specific surface area they have been largely replaced in most applications by spiral-wound modules and hollow-fiber modules. Plate-and-frame modules are now used only in electrodialysis and pervaporation systems and in a limited number of reverse osmosis and ultrafiltration applications with highly fouling conditions.

(b) Spiral wound module

Industrial-scale modules contain several membrane envelopes, each with an area of 1 to 2 m², wrapped around the central collection pipe. Multi-envelope designs minimize the pressure drop encountered by the permeate travelling toward the central pipe. The standard industrial spiral-wound module is 20 cm in diameter and 1 m long. The module is placed inside a tubular pressure vessel. The feed solution passes across the membrane surface, and a portion of the feed permeates into the membrane envelope, where it spirals towards the centre and exits through the collection tube as shown in Fig. 1.8-b. Four to six spiral-wound membrane modules are normally connected in series inside a single pressure vessel. A typical 20 cm diameter tube containing 6 modules has 100 to 200 m² of membrane area.

(c) Tubular membrane module

Tubular modules are now generally limited to ultrafiltration applications, for which the benefit of resistance to membrane fouling due to good fluid hydrodynamics outweighs their high cost. Typically, the tubes consist of a porous paper or fiberglass support with the membrane formed on the inside of the tubes, as shown in Fig. 1.8-c.

(d) Hollow fiber membrane module

Hollow-fiber modules are characteristically 10-20 cm in diameter and 1.0-1.6 m long. Hollow-fiber units are almost always run with the feed stream on the outside of the fibre. Fluid passes through the membrane into the inside or “lumen” of the fiber. A number of hollow-fibers are collected together and “potted” in an epoxy resin at both ends and installed into an outer shell. An example is shown in Fig.1.8-d. These so-called capillary fibers are used in ultrafiltration, pervaporation, and some low to medium pressure gas applications. The single greatest advantage of hollow-fibre modules is their high compactness (ability to pack a very large membrane area into a single module). Hollow fiber modules also benefit from a long life span: degraded or broken fibers can be easily isolated and the module can thus continue functioning. Low cost is another major advantage of hollow-fiber modules. Production costs are sensitive to volume, but

in a hollow-fiber spinning plant operating on an around-the-clock basis, they are in the range \$2-5/m². This is much less than the production costs of equivalent spiral-wound modules, which are in the \$10-100/m² range [17].

The hollow fibers must be homogeneous distributed in the housing so that preferential paths, which generate detrimental effects on mass transfer, can be avoided. The techniques to obtain this uniform display of the bundle differs among manufacturers. Two common techniques used are: the adaptation of the fiber geometry by “wings” on the outer diameter or by “structuring” the fiber bundle, either by knitting (knitting and rolling the fibers) or by simply cross-winding the fibers (cross-winding + rolling) [30].

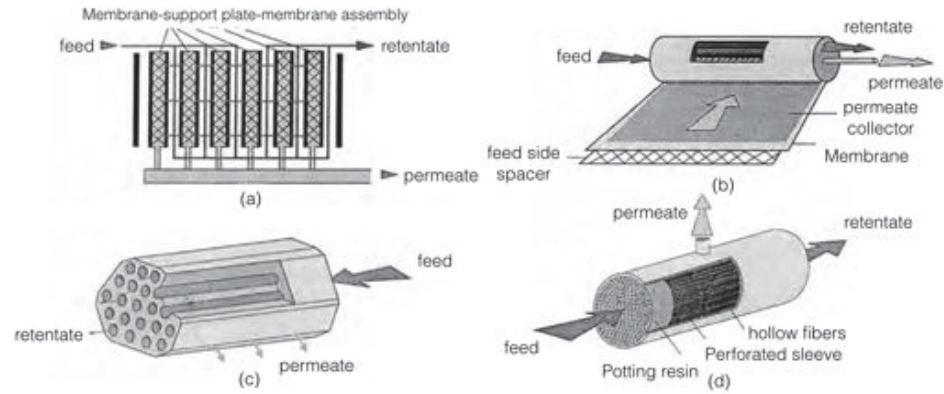


Figure 1.8: Schematic representation of the four principle membrane modules: (a) plate-and-frame; (b) spiral-wound; (c) tubular; (d) hollow-fiber. [31].

1.2 Preparation of composite polymer membranes

Composite membranes emerged right after the discovery of asymmetric RO membranes [32]. This development opened the door for tailor-made membranes to a much wider range of applications. The membrane surface properties play an important role on their performance in many branches of industrial applications (e.g., separation of gas, liquid mixtures, bonding, coating, adhesion, etc.). The most frequently practiced methods used to prepare composite polymer membranes and to realize membrane surface modifications include [33–35]:

Dip coating: The membrane surface can be modified by dipping the polymeric membrane (A) into a bath containing a dilute solution of another polymer (B). A thin layer of polymer (B) is left on top of the support membrane (A) after solvent evaporation. This technique has been applied in anti-fouling of ultrafiltration membranes [36]. Preparation of CO₂ capture membranes using dip-coating has also been reported [37,38]. The dip coating is limited to non-crosslinked modifying polymers since cross-linked polymers can not be dissolved to prepare a dipping solution.

Interfacial polymerization: This method was developed by Cadotte and the cowor-

kers of Film Tech in the 1970s [39,40] and is currently most widely used to prepare high performance reverse osmosis and nanofiltration membranes. When reactive monomers are dissolved in two different solvent phases and these two phases are brought into contact, polymerization occurs only at the interface between the two phases, creating a thin polymer film.

Co-extrusion: Co-extrusion is a straight forward fabrication method to make a multi-layer configuration in the form of film, sheet, or fiber by simultaneous extrusion of two or more polymers through a single die [41]. Co-extrusion avoids many of the manufacturing steps required by conventional lamination and coating processes, such as making and handling of individual films, application of coating primers, and solvent drying. However, there are also limits of the co-extrusion process. For example, lower durometer materials tend to be ‘sticky’ or have a tackiness that requires the application of coatings to reduce surface friction. A solution to this problem is the use of PTFE liners; however, this is a more expensive process and also limits the sterilization options, durability and resistance to abrasion. It also can be too stiff for some applications that require high flexibility [42]. In co-extrusion, polymers are often dissolved in a solvent to form a polymer solution. Hence another limit imposed on this method is that the polymers used should be soluble in organic solvents. Co-extruded dense membranes include dialysers [43] and gas separation membranes [44–47].

Graft polymerization: Grafting is a method wherein monomers are covalently bonded onto the membrane. The techniques to initiate grafting comprise: (i) chemical, (ii) photochemical and/or via high-energy radiation, (iii) plasma, and (iv) enzymatic initiation (relative new technique) [48]. The choice for a specific grafting technique depends on the chemical structure of the membrane and the desired characteristics after surface modification. This method has advantages over other methods in several points, including easy and controllable introduction of graft chains with a high density and exact localization of graft chains to the surface with the bulk properties unchanged. Furthermore, covalent attachment of graft chains onto a polymer surface avoids their delamination, and assures the long-term chemical stability of introduced chains, in contrast to physically coated polymer chains.

Chemical grafting:

In general, chemical grafting is a simple and cheap technique, leading to membranes that are claimed to be less sensitive to fouling due to the presence of the hydrophilic grafted monomers, but it is a harsh treatment.

Photo grafting:

When a chromophore on a macromolecule absorbs light, the molecule is brought in an excited state, and one or more chemical bonds may dissociate into radicals that can act as initiators for the radical polymerization. Radicals that are generated in this manner on the membrane surface can react with the monomer to form the grafted copolymer. UV irradiation and UV-assisted graft polymerization are techniques that can selectively alter membrane surface properties without affecting the bulk polymer.

Plasma grafting:

Plasma surface treatment usually refers to a plasma reaction that either results in mo-

dification of the molecular structure of the surface, or atomic substitution. Plasma polymerization process is a technique that allows us to obtain highly crosslinked polymers from nonfunctional monomers that are not used in conventional polymer synthesis. The disadvantages of plasma grafting include high investment and operation costs, bulk structure change when treating thin surface layers, etc. [49]. The applications of plasma grafting have penetrated other domains as well, e.g. gas separation, pervaporation, etc [50, 51].

In our research work, the photo graft polymerization is employed for membrane modification. Coating a poly(ionic liquid) - ionic liquid gel (polyIL-IL) onto a hollow fiber support (for CO₂ capture) would be difficult or more complicated using other modifying methods (Chapter II). The polyIL-IL gel was coated onto the hollow fiber via in-situ photo polymerization. For photo-inertia support membrane materials, there may not be covalent bonds formed between the top layer and the support membrane. Hence, it's in reality a coating process (realized by photo polymerization using a monomer solution), differing from the dip coating technique where the modifying solution is a polymer solution. While for photo sensitive support membranes such as polysulfone, which generates radicals under UV irradiation, the monomers were covalently grafted onto the support membrane. This is the case for the catalytic membrane elaborated in Chapter V. The polysulfone membrane follows a photo polymerization mechanism as shown in Fig.1.9 [52]. Polyethersulfone (PES) membrane, whose structure is given in Fig. 1.10 contains the same functional groups. It follows therefore the same photo initiation mechanism [53, 54].

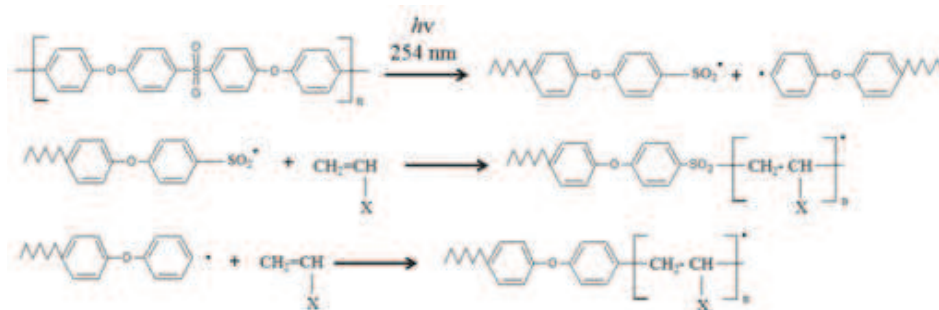


Figure 1.9: Photo polymerization mechanism of polyarylsulfone (PS) [52].

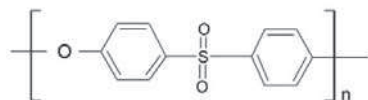


Figure 1.10: Structure of polyethersulfone (PES).

1.3 Membrane for CO₂ capture

1.3.1 Basic types of CO₂ capture

Carbon capture and storage (CCS) is a potential means of mitigating the contribution of fossil fuel emissions (from power generation) to global warming [55,56] and ocean acidification [57]. Depending on the process or power plant application in question, there are three main approaches to capture the CO₂ generated from a primary fossil fuel (coal, natural gas or oil), biomass, or mixtures of these fuels:

Post-combustion systems separate CO₂ from the flue gases produced by the combustion of the primary fuel in air. It concerns mainly the separation of the small fraction of CO₂ (typically 3-15% by volume) from the main constituent N₂ (from air).

Pre-combustion systems process the primary fuel in a reactor with steam and air or oxygen to produce a mixture consisting mainly of carbon monoxide and hydrogen (“synthesis gas”). Additional hydrogen, together with CO₂, is produced by reacting the carbon monoxide with steam in a second reactor (a “shift reactor”). The resulting mixture of hydrogen and CO₂ can then be separated into a CO₂ gas stream, and a stream of hydrogen. Although the initial fuel conversion steps are more elaborate and costly than in post-combustion systems, the high concentrations of CO₂ produced by the shift reactor (typically 15 to 60% by volume on a dry basis) and the high pressures often encountered in these applications are more favourable for CO₂ separation.

Oxyfuel combustion systems use oxygen instead of air for combustion of the primary fuel to produce a flue gas that is mainly water vapour and CO₂. This results in a flue gas with high CO₂ concentrations (greater than 80% by volume). Oxyfuel combustion requires the upstream separation of oxygen from air, with a purity of 95-99% oxygen assumed in most current designs. Further treatment of the flue gas may be needed to remove air pollutants and noncondensed gases (such as nitrogen) from the flue gas before the CO₂ is sent to storage. The oxyfuel combustion systems are still in the demonstration phase [58].

The schematic presentation of the above CO₂ capture processes are demonstrated in Fig.1.11. Besides the above systems, CO₂ capture is also used in large-scale production of hydrogen (ammonia and fertilizer manufacture, petroleum refinery operations) and in natural gas sweetening (separation mainly from CH₄). Generally speaking, the separation of CO₂ from N₂, CO₂ from CH₄, and CO₂ from H₂ are three distinct separation challenges faced by the electrical energy, natural gas, and syngas production sectors, respectively.

1.3.2 Polymer membranes for CO₂ capture

Membrane-based technology is under development aiming at advancing towards sustainable systems that minimize CO₂ emissions. Three main approaches are mainly under study (Fig. 1.12): (i) non-dispersive contact via a microporous membrane (mostly focused on postcombustion capture); (ii) gas permeation, mainly by using dense mem-

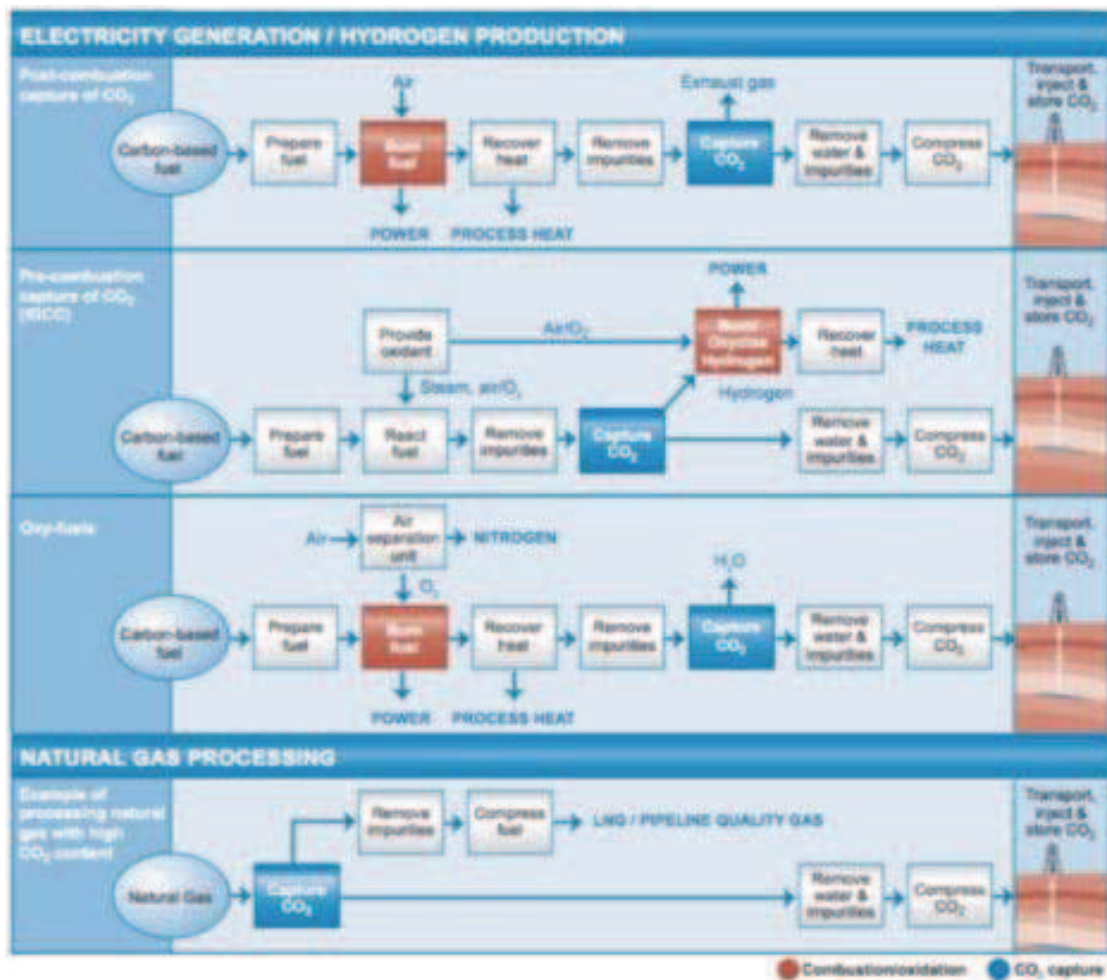


Figure 1.11: Schematic presentation of CO₂ capture in post-combustion, pre-combustion, oxyfuel and natural gas processing [59].

branes (mostly for pre-combustion capture); and (iii) supported liquid membranes (pre-combustion and post-combustion capture are both targets).

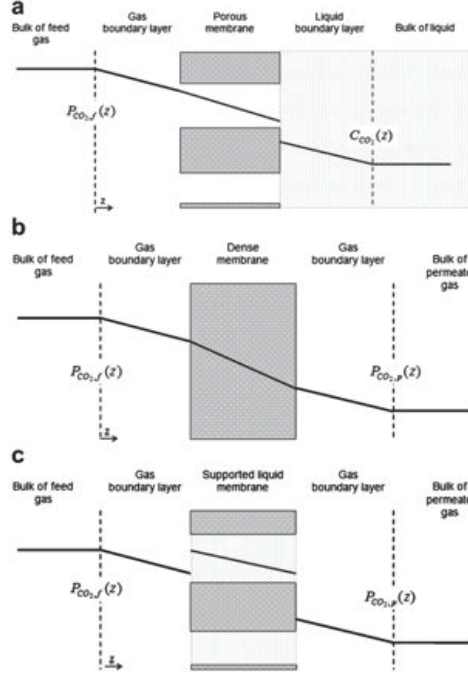


Figure 1.12: Schema of mass transfer in the systems: (a) non-dispersive contact via a microporous membrane (membrane contractor); (b) gas permeation through a dense membrane; (c) support liquid membrane [60]

Non-dispersive Contact via a Microporous Membrane

Non-dispersive absorption using a gas-liquid contactor presents interesting advantages compared to the conventional absorption towers and also, they may be strong competitors to the use of dense membranes and supported liquid membranes. It is mainly applied in post-combustion capture. Regarding the traditional absorption performed in scrubbers, the use of membrane-based absorption has more operational flexibility due to the independent control of gas and liquid flow rates, a controlled and known interfacial area, a linear scale-up thanks to the modularity of membrane contactors; it is compact and less energy consuming and does not suffer from dragging of drops of solvent since the gas and liquid phases are kept separated in the two compartments of the contactor (the shell and tube sides) and the mass transfer takes place through the membrane pores. The mass transfer of CO_2 from the gas to the liquid phase does not have a significant impact on the gas flow because of the low concentration of CO_2 in the gas stream [61]. In addition, compared to other membrane systems, the membrane pores are filled (in theory) with gas and the mass transfer through the membrane should be favoured in

comparison to using dense membranes or membranes with pores filled by liquid (supported liquid membranes). The membrane does not provide selectivity to the separation since its role is to act as a barrier and to increase the surface for mass transfer exchange between both phases but the morphology of the membrane has a non-negligible influence on the process performance [62]. The pore size and porosity of the membrane are key factors to consider since the contact between the gas and liquid phase occurs in the pores of the membrane and higher membrane porosity leads to a better performance [63–66]. However, the selection of the absorption liquid determines the selectivity of the separation; also, it is critical to have good chemical compatibility between the solvent and the membrane contactor (i.e., membrane, potting material and housing) and the prevention of membrane wettability is essential to ensure a long-term application.

Faced to current challenges to develop this technology in an industrial scale, it can be stated that there are four main aspects to consider and solve [67,68]: (i) wetting of the membrane, which increases the resistance to mass transfer and decreases the process efficiency dramatically (Favre et al. have prepared a membrane contractor with a dense layer to effectively prevent wetting [69]); (ii) limited long-term stability, mainly related to the chemical resistance of the membrane material (many solvents may react chemically with the polymer) and to the effect of temperature on the membrane structure; (iii) volatility of the solvent, which is an issue of concern from an economic and environmental point of view and promotes the use of non-volatile solvents such as ionic liquids; and (iv) presence of other compounds in the gas stream, acting as competitors and limiting the mass transfer of the target compound. All these considerations are strongly linked with the selection of the membrane-solvent system.

Gas Permeation

In gas permeation, the membrane is responsible for the separation since it determines the permeability and selectivity of the process. Thus, no liquid is involved. This approach is mainly focused on pre-combustion capture (H_2/CO_2 mixture) but also many studies try to develop membranes for post-combustion separations (CO_2/N_2 mixture).

Although the upper bound of the Robeson plot has been revisited over the last years [70–72], contributing to the experimental and theoretical upper bounds for polymeric membranes, the trade-off between the selectivity and the permeability is still the challenge to face in synthesis of membranes for gas permeation. The Robeson plot revisited in 2008 is shown in Fig. 1.13 [71].

The driving force of gas separation membranes for CO_2 permeation is the partial pressure difference between the feed and the permeate side. Consequently, the major challenge that has to be faced for their implementation in the industry is the scale of the process due to the high volume of gas stream to be treated and the low concentration (i.e. low driving force) of CO_2 (e.g. 3-15 vol.% CO_2 in post-combustion processes), leading to the requirement of large membrane areas to perform the separation. The use of hollow fibers is hence particularly interesting.

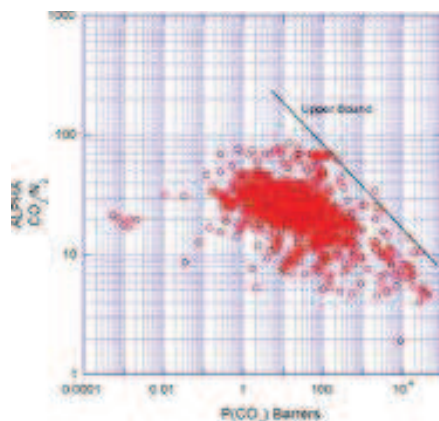


Figure 1.13: Robeson plot 2008 for CO_2/N_2 [71].

The plasticization effect has to be also considered in the development of polymeric membranes. High solubility of CO_2 (and other compounds that can be present in the gas stream such as H_2S , SO_2 , NH_3 , water, etc) in the polymer may induce plasticization, causing the polymer to swell with disruption of the polymer matrix, with an increase in the mobility of the polymer chains, thereby adversely changing the membrane permeation characteristics [73, 74]. (see Section 1.3.3)

The effect of water in the gas stream has significant influence in the process performance. For example, Liu et al. studied the gas permeation through water-swollen hydrogel membranes. They found that the permeability of CO_2 and N_2 increased with an increase in the water content in the membrane and tended to level off when the water content was sufficiently high (with gas permeability lower than the gas permeability in pure water). The corresponding CO_2/N_2 selectivity did not vary substantially with water content. Reijerkerk et al. [73] observed that the presence of water vapour had a stronger influence on the N_2 permeability in polyethylene oxide-based membranes and the CO_2/N_2 selectivity increased with increasing water vapour activity. Since flue gas contains water (usually in saturation levels), those systems can be used for the simultaneous removal of CO_2 and water.

Facilitated transport membranes (also in ionic liquid-based structures) have received a lot of attention in gas separation because they can improve significantly the permselectivity, making the membrane go far beyond the upper bound shown in Robeson's plot. There are different approaches but the basis is the incorporation of a carrier agent into the membrane (linked structurally, immobilized into the pores or supported on the membrane), which reacts reversibly with the penetrating species [75]. The permeating species (e.g. CO_2) diffuses across the membrane until released to the permeate side and the presence of the carrier enhances significantly the selectivity towards the target compound and also, the permeability.

Supported Liquid Membranes

The development of supported liquid membranes (SLMs) has taken a great impulse in the last years thanks to the use of ionic liquids as solvent. The basis of this approach consists of a liquid supported on the surface of the membrane or introduced inside the pores of the membrane (in this last case, a more appropriate denomination would be immobilized liquid membranes).

The main technical challenge of SLMs is the stability of the membrane since the solvent in the pores can evaporate or be ‘washed out’ after long time of operation.

In addition, the driving force needed to perform the separation is the pressure difference between the feed and the permeate side, which means that the permeation of CO₂ through the membrane will be enhanced when the feed gas is compressed [76] (since flue gases are normally at low pressures, such as 1 atm) or the permeate side works under vacuum conditions. However, the first situation increases the cost of the overall process and the second option promotes the instability of the membrane over time due to solvent volatilization.

In contrast, there is an important effect of the concentration of CO₂ in the feed stream. But it is important to distinguish the increase of CO₂ partial pressure due to an increase of the total pressure and due to an increase of the CO₂ concentration since their effects on the membrane performance are not the same. Gorji et al. observed that the CO₂ capture performance through amine solution membranes decreases with increasing CO₂ partial pressure of the feed at constant total pressure [77]. This means that high concentration of CO₂ penalizes the overall performance, although better separation may be obtained for low concentration of CO₂ in the gas stream in contrast with the use of porous membranes and liquid flowing inside the contactor [78].

Membrane stability and solvent viscosity can be considered as the bottlenecks of this technology. An increase of the concentration of the reagent should involve a better CO₂ removal since the selectivity and permeability are given by the interaction with the solvent. However, when the viscosity of the solvent becomes high, CO₂ diffusivity through the SLM decreases. Using ionic liquids eliminates the problem of solvent evaporation that may occur in conventional SLMs, aiming at high stability. Their high CO₂ solubility, selectivity of ionic liquids are also appreciable. However, viscosity and pressure stability are pending issues [79,80].

The addition of carriers to the SILMs to promote the facilitated transport is being studied by several authors [81,82]. Nevertheless, it was observed that there was not a large potential for an overall improvement of performances.

Also, as same as non-dispersive absorption and gas permeation, the effect of operating conditions on the process efficiency is large enough to promote the study under real conditions.

1.3.3 CO₂ plasticization and competitive sorption in polymer membranes

Plasticization phenomenon

Gas separation through dense membranes is generally more effective using glassy polymers, which can differentiate gases based on their different diffusivities. Theoretical models for the permeability coefficients of gases through glassy polymers distinguish between the behavior below and above the glass transition temperature [83]. Above the glass transition temperature, the permeability coefficient of a (rubbery) polymer is constant for low pressures and increases eventually at elevated feed pressures. Below the glass transition temperature, the plasticization effect is often observed when highly sorbing gas such as CO₂ is fed at a large partial pressure. A typical effect of plasticization is that the permeability versus pressure curves go through a minimum, as illustrated in Figure 1.14. Initially, there is a decrease in permeability as the pressure is increased, due to a faster decrease in solubility than an increase in diffusivity with increasing pressure [84]. At a certain point, the high sorbing gas concentration disrupts the chain packing, leading to an increase in free volume and an enhanced segmental mobility. At this point, the increase in diffusivity is stronger than the decrease in solubility, and thereby the permeability increases with pressure. The pressure corresponding to the minimum permeability is called the plasticization pressure (Fig. 1.14).

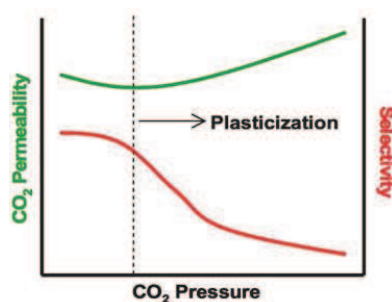


Figure 1.14: Schematic presentation showing plasticization effects on membrane separation performance: plasticization causes an increase in permeability and decrease in selectivity as pressure of sorbed penetrant increases [85].

In membrane science and in particular in gas separation, the phenomenon of penetrant-induced plasticization is generally considered as an undesired, ‘negative’ feature since it represents losses in membrane performance [86–89]. The increase in local segmental motion of the polymer chains results in enhanced transport rates of all penetrants to be separated. Since the transport rate of a ‘slow’ penetrant is more affected than that of a ‘fast’ component, plasticization typically results in a loss of membrane selectivity when gas mixtures are fed to the membrane (Fig.1.14). Plasticization can be suppressed by various chemical means to mitigate or to prevent membrane selectivity loss. The most widely used methods include annealing, cross-linking and polymer blending. Thermal

annealing induces a densification of the polymer. Cross-linking increases chain packing and inhibits the intrasegmental and intersegmental mobilities. Polymer blends involves the blending of a polymer affected by the sorbed molecules with one that is hardly affected.

Competitive sorption in gas mixtures

Another factor that influences the mixed gas separation membrane performance is the competitive sorption: the presence of one gas species can affect the solubility of another gas species. Competitive sorption can affect both rubbery and glassy polymers to varying extents. For rubbery polymers, the effects can be described by Flory-Huggins theory. The competitive sorption of one gas can lead to an increase or to a decrease in the solubility of another. For glassy polymers, the permeabilities of penetrants are always decreased due to the competition effects between penetrants on Langmuir sorption sites (which are associated with the non-equilibrium free volume in glassy polymers), according to the dual mode sorption model [90]. Different from plasticization, competitive sorption is related to intrinsic material properties and cannot be tailored.

Researches on plasticization behavior and competitive sorption of room temperature ionic liquids (RTILs) and poly(RTILs)

Concerning the plasticization and mixture gas competitive sorption in ionic liquids, several papers were published. F. Karadas et al. studied CO₂ absorption on 1-butyl-3-methylimidazolium hexafluorophosphate, 1-ethyl-3-methylimidazolium bis(trifluoromethylsulfonyl) imide, and 1-butyl-3-methylimidazolium bis(trifluoromethylsulfonyl) imide ionic liquids and observed a remarkable swelling effect upon CO₂ from pressures higher than 10 MPa, which led to an apparent decrease of the CO₂ absorbed amount [91]. M. Wessling and R. D. Noble reported the plasticization behavior of poly(ionic liquid) (synthesized from styrene-based imidazolium bis(trifluoromethane)sulfonamide RTIL monomers) at pressures above 10 bar (the gas mixture used was CO₂/CH₄) [92]. They discovered that although poly(RTILs) are glassy in nature, poly(RTILs) do not show a minimum in permeation rates for CO₂: the permeability increases continuously with increasing feed pressure. Another distinctly different phenomenon of poly(RTILs) opposed to regular glassy polymers such as polyimides, polysulfones or polycarbonates is the full reversibility of the diffusional processes on the time scale. Those unique properties were attributed to the strong ionic interactions counter-balancing the volume dilation induced by the sorbed CO₂ as poly(RTILs) with short side chains are less vulnerable than those with longer side chains. Hert et al. discovered experimentally the competition sorption between CO₂ and O₂ (50/50 mol%) in 1-hexyl-3-methylimidazolium bis(trifluoromethylsulfonyl) imide. The CO₂ solubility in the mixed gas system was less than the CO₂ solubility in the pure gas system [93]. This is coherent with the CO₂ permeability decrease observed by Li et al. at 10 atm in 50/50 mol% CO₂/N₂ gas mixture on a poly(RTIL)-RTIL membrane

(which was attributed to the competitive sorption). According to them, CO₂-induced plasticization dominated the competitive sorption at 20 atm and the CO₂ permeability in the mixed gas became higher than pure CO₂ permeability.

Concerning thin polymer films

Another interesting point to mention is that the behavior of integrally thin-skinned ($\delta < 0.5 \mu\text{m}$) or thin dense ($\delta < 3 \mu\text{m}$) polymer films may be different from thick dense polymer films, as the physicochemical properties are different from polymer bulk properties. One example is the thickness dependence of the glass transition temperature in thin polymer films. Forrest and Dalnoki-Veress [94] observed a T_g -reduction with decreasing polymer film thickness ($\delta < 0.3 \mu\text{m}$), which was explained by polymer chain confinement [95]. In membrane gas separation experiments also evidence was found for difference in polymer properties between thick and thin polymer films. Jordan et al. [96] used CO₂ as a conditioning agent to enhance the transport of O₂ and N₂ in thick dense films and asymmetric hollow fibers and recognized that lower CO₂ pressures were needed to induce swelling effects for asymmetric hollow fibers than for thick dense films. They hypothesized that the dense skin of an asymmetric hollow fiber consists of layers of nodules that are interconnected by polymer chains. These loosely packed chains are susceptible to movement and structural change by the highly sorbing CO₂. However, Shishatskii et al. [97], who investigated the effect of film thickness on material density, showed that a decreasing thickness resulted in an increase of cohesive energy density (CED) and consequently a higher gas solubility and lower gas diffusivity for the thin material. This was verified by Dorkenoo and Pfromm [98], who characterized physical aging by gas permeation experiments in poly[1-(trimethylsilyl)-1-propyne] films. The activation energies for permeation were often significantly higher for thin-skinned membranes, implying higher cohesive energy densities (CED), due to a lower free volume in comparison to the bulk polymer. Besides that, Pfromm et al. [99] observed an increased permselectivity for O₂ and N₂ in asymmetric PSF films compared to the isotropic properties due to increased activation energies for permeation. Besides physical ageing and other physicochemical properties, also plasticization behavior is thickness dependent, as observed by Wessling et al. [100]. They showed that the CO₂ permeability in composite membranes, consisting of PI top layers (thickness between 1.5 and 4 μm) and a PDMS (polydimethylsiloxane) support film continuously increased with feed pressure, and became more pronounced with decreasing polyimide (PI) layer thickness. It was hypothesized by Pfromm and Koros [98] that, due to elimination of Langmuir sorption sites as a consequence of accelerated aging (the polymer may be locally more ordered due to aging), there is less CO₂ needed to induce plasticization. On the other hand, Shishatskii et al. [97] reported an increasing solubility with increasing density (as a consequence of decreasing film thickness). They suggested that this was due to increases in the CED. The inverted pressure dependence on CO₂ permeability was also found by Pfromm et al. [99] in an asymmetric poly(ester carbonate) film. A combination of factors would explain the unusual shape of this curve, such as a different distribution of free volume,

a different orientation of the polymer molecules in the skin layer, a lower free volume in the skin layer and a smaller number/size of hypothetical Langmuir sites.

Researchers also found that plasticization may also be suppressed in skin layered polymers by using a gas mixture (besides the conventional chemical methods). Kapan-taidakis [101] and Barsema [102] found that plasticization of integrally skinned asymmetric hollow fibers of polyethersulfone/polyimide (Matrimid 5218) and P84 (co-PI, Lenzing) seems to be suppressed when CO₂/N₂ mixtures of 55/45 and 80/20 wt.% are used. The CO₂ and N₂ permeability decreased slightly as a function of the CO₂ partial pressure over the whole pressure range 1-20 bar studied, both in the same order, leading to a constant separation factor. This observed phenomenon was hypothesized to be based on competitive sorption. The same explanation was given by Vu et al. [103] for the observed depression of the CO₂ permeance as a function of pressure 7-55 bar using Matrimid polyimide hollow fibers in a 10% CO₂/90% CH₄ gas mixture. Their CO₂/CH₄ separation factor kept nearly constant up to 40 bar. Yoshino et al. [104] performed gas separation experiments in integrally skinned asymmetric hollow fibers with 50/50 mol% binary mixtures of C₃H₆/C₃H₈ and C₄H₆/C₄H₁₀ and observed no plasticization effects for the first mixture, but strong plasticization effects for the second (pressure range, 1-5 bar). Wessling et al. found that when an inert gas (N₂ or CH₄) was introduced to a binary gas mixture of CO₂ plasticization was suppressed. Based on the mixed gas permeation model they consider that there exists a subtle balance between competitive sorption and plasticization, which means that plasticization effects such as polymer network dilation are masked during mixed gas experiments [105]. On the other hand, Wang et al. [106] investigated the true separation performance of 6FDA-based polyimide hollow fiber membranes in a binary (40/60 mol%) gas mixture of CO₂ and CH₄ and did observe plasticization effects. They hypothesized that plasticization, which increased the permeability, offsets the combined effects of competitive sorption and non-ideal gas behavior (especially in a gas mixture), which normally both decrease the permeability. However, their gas permeation results were reported at one partial CO₂ pressure, 13.9 bar and were compared to pure gas permeation results at the accompanying partial pressure, 5.5 bar.

1.4 Process intensification

The birth of process intensification as a chemical engineering discipline was marked by the paper published in 1983 by Colin Ramshaw, describing process intensification as “devising an exceedingly compact plant which reduces both the ‘main plant item’ and the installation’s costs” [107]. While according to Heggs, process intensification is concerned with order-of-magnitude reductions in process plant and equipment [108]. In one of his subsequent papers, Ramshaw writes about typical equipment volume reduction by two or three orders of magnitude [109].

The philosophy of process intensification has been traditionally characterized by four words: smaller, cheaper, safer, slicker [110]. And indeed, equipment size, land use

costs, and process safety are among the most important process intensification incentives. But the motivation for developing and applying process intensifying equipment and methods is finally not only given by the prospect of dramatic cost reductions, but also by increasing the sustainability of chemical production [111]. Today, process intensification represent one of the most promising strategies believed to bring drastic improvements in manufacturing and processing, substantially decreasing equipment-size/production-capacity ratio, reducing raw materials, saving energy input, replacing and reducing hazardous waste, recycling waste materials (Fig. 1.15).

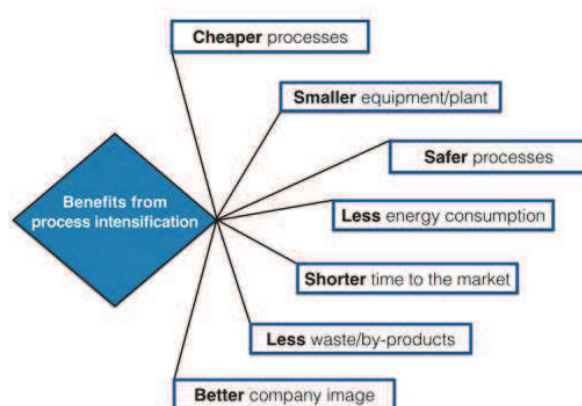


Figure 1.15: Main benefits from process intensification [110].

In general, the process intensification can be classified as following:

- Novel reactors as well as intensive mixing, heat-transfer and mass- transfer devices (static mixers, monolithic catalysts, microreactors, rotating devices);
- Integration of reaction and one or more unit operations (separation, heat exchange, or phase transition) into so-called multifunctional reactors (reverse-flow reactor, reactive distillation, membrane reactors, reactive extrusion, fuel cells);
- Development of new or hybrid separations (membrane absorption and stripping, membrane distillation, adsorptive distillation);
- Use of alternative forms and sources of energy for processing (centrifugal fields, ultrasound, solar energy, microwaves, electric fields, gliding arc);
- New process-control methods (like intentional unsteady-state operation).

The reactor concept investigated in the work at hand is a flow-through catalytic membrane reactor. It can be regarded a part of the process intensification family, closely related to microreactors due its small characteristic dimensions. Hereinafter, concepts on both microreactors and catalytic membranes are briefly introduced as the similarities and differences between them help to better understand the concept and potential benefits of the flow-through membrane reactor.

1.4.1 Microreactors

Microreactors are usually defined as miniaturized reaction systems fabricated by applying, at least partially, methods of microtechnology and precision engineering. The characteristic dimensions of the internal structures of microreactors, like fluid channels, typically range from the sub-micrometer to the sub-millimeter scale [112]. The increase of specific properties, such as the surface to volume ratio, is a direct consequence of reducing the characteristic dimensions. The second potential benefit is given by the reduced total size of the system. Resulting characteristics of microreactors are:

- Virtually always laminar flow pattern;
- High heat transfer rates, allowing for isothermal or periodic operation;
- Improved mass transport due to fast diffusive mixing;
- Inherently safe operation of potentially dangerous reactions;
- Exact reaction control due to narrow residence time distributions;
- High pressure stability;
- Reduced time-to-market by numbering up instead of scale up.

The given characteristics are responsible for observed higher conversions and selectivities in micro-structured reactors in comparison to conventional ones. Advantages can especially be expected for fast, highly exothermic or endothermic reactions [113]. The reaction time is shorter as compared to conventional reactors, allowing for less degradation and side products [114]. The small hold-up in the microstructures significantly reduces the hazard of highly exothermic and explosive reactions.

Microreactor types can be distinguished by their main function, which can be improved heat exchange, mixing or catalyst support. Potential benefits are pure products, increased yields, reduced resource consumption and innovative process management. Several materials and microstructuring methods are applied to produce microreactors. Materials range from metals to ceramics, glasses and silicon. Production processes include machining, spark erosion, laser processes, lithography and etching methods. Surface treatment methods such as coating, surface increase or catalyst insertion are often applied. Standardized modular concepts with compact overall dimensions are available. Due to their potential mobile application and the reduction of development time, they are especially attractive for lab research.

Frequently quoted disadvantages of microreactors are the high fabrication cost, low throughput, incompatibility with solids and the omission of cost reduction by scale up effects which lead to still poor industrial acceptance. Instead it seems that multi-scale approaches [115] are increasingly successful regarding application on pilot or plant scale. This means that the appropriate scale is selected for the respective purpose, and size reduction is often limited according to the policy “as small as necessary” [116].

1.4.2 Catalytic membrane reactors

Process integration by combining reaction and membrane separation in a single unit promises numerous benefits compared to conventional processes. In the recent years a

multitude of concepts have been proposed about how membranes can be applied in combination with a chemical or biochemical reaction in order to intensify the process as a whole. The International Union of Pure and Applied Chemistry (IUPAC) defines a membrane reactor as a device for simultaneously carrying out a reaction and membrane-based separation in the same physical enclosure [117]. According to a wider definition any reactor in which a chemical reaction is performed in presence of a membrane is called membrane reactor [118]. In a membrane reactor the membrane can fulfill different functions and be categorized accordingly into three main concepts [119]:

- Selectively remove the products from the reaction mixture (Extractor);
- Control the addition of reactants to the reaction mixture (Distributor);
- Intensify the contact between reactants and catalyst (Contactor).

Extractor membrane reactors

The most common type of membrane reactor works according to the extractor principle. The extractor requires a selective membrane that continuously remove one of the reaction products from the reaction mixture (Fig. 1.16). Consequently, for reactions limited by the thermodynamic equilibrium, the hypothetical equilibrium conversion (that can be reached in a closed system) can be outperformed due to the shift effect [120]. Membrane extractors are used in etherification and dehydrogenation reactions where selective removal of water or hydrogen is respectively required [119].

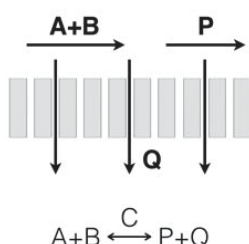


Figure 1.16: Principles of extractor membrane reactors: selective product removal (C=catalyst).

Distributor membrane reactors

The distributor principle is the second field of application for permselective membranes in chemical reactors. The distributor membrane doses one of the reagents in a controlled manner to the reaction zone. Even distribution of the limiting reactant along the reactor can prevent hot spots and side reactions. Figure 1.17 shows a sequential reaction with the desired product P and the undesired product Q performed in a distributor membrane reactor. Selective addition of component B leads to a continuously low concentration of B. If the reaction follows power law kinetics, the membrane reactor can

reach a higher selectivity to product P than a conventional reactor. This configuration can be used in gas phase reaction e.g. to maintain the mixture below the explosion limits. Other applications of the distributor membrane reactors include selective oxidation and hydrogenation reactions [121–124].

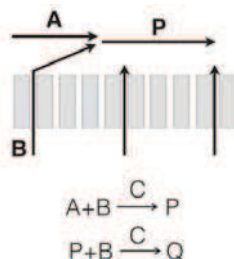


Figure 1.17: Principles of distributor membrane reactors: controlled reactant addition (C=catalyst).

Contactor membrane reactors

The membrane contactors are used to facilitate the contact between the reagents and catalyst. In membrane contactors, the membrane can be intrinsically active as a catalyst or the catalyst can be supported onto the membrane matrix. No permselectivity is required for the membrane. But the membrane provides a region where the reactions take place. There are two possible ways to bring the reagents to the catalytic sites.

The first option is the interfacial membrane contactors mode, where the reactants are separately dosed from each side of the membrane, and they react over the catalytic site (Fig. 1.18-a). This configuration is mainly used in reactions with non-miscible reagents. Exemplary applications include selective oxidation of light alkanes under mild conditions (by means of super acidic catalytic membranes) [125], controlled catalytic combustion for energy recovery, complete conversion of pollutants [126], etc.

The second operation mode is the flow through catalytic membrane reactor (FTCMR). A mixture of reactants is forced to flow through the non permselective catalytic porous membrane. Different from interfacial membrane contactors, premixed reactants are fed from the same side of the membrane, resulting in completely different reactor behavior. This configuration provides a reaction place with short residence time with a high catalytic activity. A scheme of a flow through membrane contactor is depicted in Figure 1.18-b. In classical fixed bed reactors the conversion is limited by pore diffusion. When the reactant mixture is forced to flow through the pores of a membrane, which have been impregnated with catalyst, the intensive contact allows for high catalytic activity with negligible mass transport resistances [126], leading to high catalytic activity.

In the early 1990s, this setup was still regarded as a less investigated concept (Saracco and Specchia, 1994). Dixon (1999) identified the control of contact time as a promising area for membrane reactor research. In 2003, the same author observed increased use of membranes to control the contact time of reactants and catalysts, par-

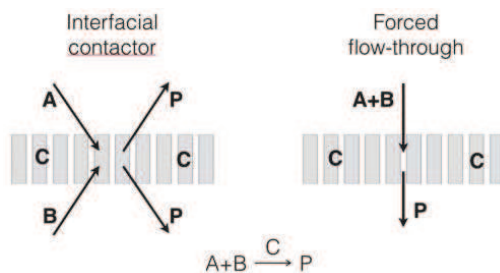


Figure 1.18: Principles of contactor membrane reactors. (a) interfacial contactor; (b) forced flow-through (C=catalyst).

ticularly in the flow-through configuration and forecasted it to become a strong third area of catalytic membrane reactor research amongst the permselective extractor and distributor membrane reactors [120].

The motivation for applying a FTCMR is either to reach complete conversion in minimum time or space, taking advantage of the high catalytic efficiency, or to reach maximum selectivity for a given reaction due to the narrow contact time distribution. Up to now, most reactions carried out on the FTCMRs are in gas phase based on inorganic membranes (e.g. decomposition of volatile organic compounds (VOC) [127–129], partial oxidation [130, 131], partial hydrogenation [132–135]). Liquid phase reactions carried out in FTCMRs have also been reported, hydrogenation of nitrate in water is an example [136–139].

1.5 Metallic nanoparticles (MNPs) in catalysis

A metallic nanoparticle is a metallic particle whose size is in the range of 1 to 100 nm (10^2 to 10^7 atoms) from zero (0D) to three dimensions (3D), exhibiting the unique physicochemical properties due to the quantum size effect that cannot be anticipated from bulk counterparts [140]. The massive increase of surface area observed upon reduction of scale results in unrecognisable properties when a nanomaterial is compared to its bulk counterpart. A simple calculation shows that decreasing the radius of a sphere from 1 mm to 1 nm will result in a 10^{12} fold increase of surface area if the overall mass of the sample is kept constant. The following are some examples of MNPs of noble metals: Au_{13} , Au_{20} , Pt_{38} , M_{55} (M=Au, Pt, and Rh), Pt_{309} , Pd_{561} , Pd_{1415} , and Pd_{2057} [141–146]. With the exceptions of Au_{20} and Pt_{38} , these NPs can be referred to as “full-shell nanoparticles” in which their constituent atoms assume a closed geometry with the densest sphere packing possible (Fig. 1.19). For example, starting with a central atom, 12 and 42 atoms can be placed around it to form a second and third shell, respectively, and thus M_{13} and M_{55} particles. In general, $10n^2 + 2$ atoms need to be incorporated into the n th shell to form a particle with the densest packing of atoms [147]. As shown in Figure 1.19, the fraction of surface atoms, at edges or corners, which are

under coordinated, becomes significant in the case of small particles. Those facts are of particular interest for catalytic applications in terms of reactivity [148].

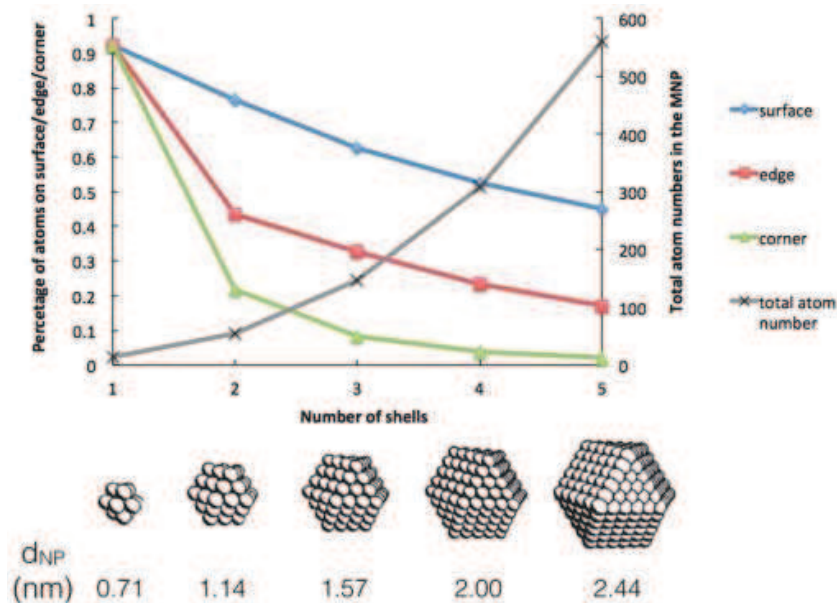


Figure 1.19: Representation of total atom numbers in the MNP and the percentage of atoms on surfaces, edges and corners for MNPs as a function of number of shells (diameters of the MNPs (d_{NP}) are also given in the figure in nm).

1.5.1 Synthesis of MNPs

Generally, the synthetic methodologies for MNPs can be divided into two major categories: “top-down” and “bottom-up” methods according to the processes involved (Fig.1.21). A top-down approach corresponds to using nanofabrication tools that are controlled by external experimental parameters to create nanoscaled structures with the desired shapes and characteristics starting from larger dimensions and reducing them to the required values [149–155]; e.g. by mechanical grinding of bulk metals and subsequent stabilization of the resulting nanosized metal particles by the addition of colloidal protecting agents [156]. The application of “physical means” such as metal vapour techniques for the production of a wide range of nanostructured metal colloids on a preparative laboratory scale has extensively been reviewed in a handbook article [157]. On the other hand, bottom-up approaches seek to have molecular or atomic components built up into more complex nanoscale assemblies or directed self-assemblies based on complex mechanisms and technologies [158–160]. In general, this approach of nanofabrication starts from atoms or small molecules as building blocks of multi-level structures to perform various operations. It is an extremely promising methodology since it could lead to no waste or unused materials. The “bottom up methods” can be classified into

the following strategies [161–164]:

- chemical reduction of metal salts [165–171] including electrochemical pathways
- thermolysis [172–181], also including photolytic [172–178, 182–197], radiolytic [184], and sonochemical [198–201] pathways
- controlled decomposition of pre-formed organometallic complexes [202].

In this work, the synthesis of PdNPs in the batch reactor and inside the membrane are both based on the ‘bottom-up’ strategy [203–205].

1.5.2 Mechanisms of nanoparticle formation

The “top-down” strategy generally involves physical methods, i.e. mechanic subdivision of the bulk metal. As for the “bottom-up” strategy, Turkevich who established the first reproducible standard procedure for the preparation of metal colloids [206] also proposed a mechanism for the stepwise formation of nanoparticles based on nucleation and growth [207, 208].

The metal salt is first reduced to give zerovalent metal atoms. These collide in solution with further metal(0) atoms or with “sub-clusters” that have already been formed to give irreversibly a stable “seed” nucleus. To initiate nucleation, the concentration of metal atoms in solution must be high enough to reach “supersaturation” [209, 210]. LaMer and coworkers, studying sulphur sols rather than metal nanoparticles [211], were the first to propose that nucleation from supersaturated solutions occurs as a sudden burst; and they also revealed that a short nucleation burst followed by slow controlled growth, without further nucleation, is essential to produce colloids with a narrow size distribution [211, 212]. According to LaMer plot for the nucleation process, in which the concentration of atoms steadily increases with time as the precursor is decomposed by heating, colloidal nanoparticle formation comprises the following three steps: (i) The atoms start to aggregate into nuclei via self-nucleation when the atom concentration in the solution achieves supersaturation levels; (ii) Then atoms continuously aggregate on the pre-existing nuclei or seed, leading to gradual decrease in the atom concentration. As long as the atom concentration is kept below the critical level, further nucleation is discouraged; (iii) With a continuous supply of atoms via ongoing precursor decomposition, the nuclei will grow into nanoparticles of increasingly larger size until an equilibrium state is reached between the atoms on the surface of the nanoparticles and the atoms in the solution [213].

Subsequent to nucleation, the particle formation depends solely on the specific surface energy of a given metal. If this is significantly higher than the entropy loss, the growing particles tend to undergo “Ostwald ripening” or coalescence - an undesired mechanism that will inevitably broaden the size distribution and cause polydispersity [215].

The thesis of R. Vernal concluded that for a closed system (that is, having a fixed amount of precursor), in the absence of aggregation between particles, the integrated area under the nucleation function determines the number of growing particles, and therefore, along with the quantity of metal present determines the final average particle size [216].

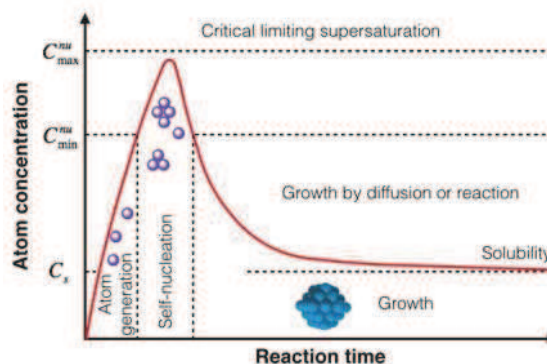


Figure 1.20: La Mer plot describing the generation of atoms, nucleation, and subsequent growth of colloidal synthesis [211, 214].

1.5.3 Stabilization of MNPs

The high ratio of surface atoms to bulk atoms in small NPs leads to an extremely high driving force for these particles to minimize the surface energy, which thus results in uncontrolled growth, particle agglomeration and accordingly, loss in catalytic activities (Fig.1.21). The most common methodologies to prevent these unwanted features include stabilization modes as follows:

- electrostatic stabilization [142];
- steric stabilization (often using polymers) [142];
- stabilization by ligands [204, 217–221]
- electrosteric stabilization [222–224]

The role of stabilizers and the “top-down” and “bottom-up” strategies for MNP preparation is presented in Fig.1.21

Electrostatic stabilization

Electrostatic stabilization results from the electrical double layer formed by the anions and cations interacting with the metallic particle surface. This results in coulombic repulsion between particles. If the electric potential associated with the double layer is sufficiently high, electrostatic repulsion will prevent the NP agglomeration (Fig. 1.22). A dispersion of MNPs that are only stabilized electrostatically can, however, coagulate easily if the ionic strength of the dispersing medium is increased sufficiently for the double layer to become compressed. The level of stabilization can be influenced by altering the total charge on the metal cluster surface. The polarity of the solvent affects the degree of particle dispersion [206]. Efficient electrostatic stabilization can be achieved using ionic liquids, where the ionic liquids act as solvent, stabilizer, ligand and support for MNPs [225, 226].

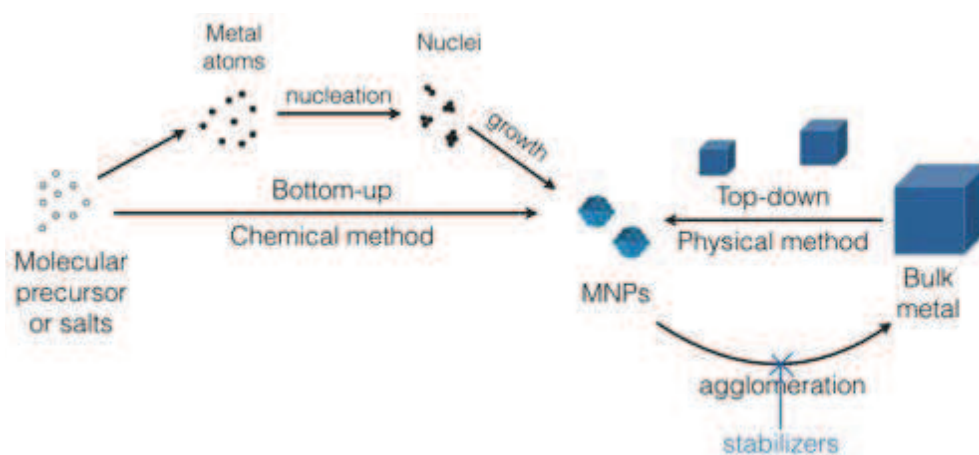


Figure 1.21: Schematic illustration of preparative methods of MNPs and the role of stabilizers.

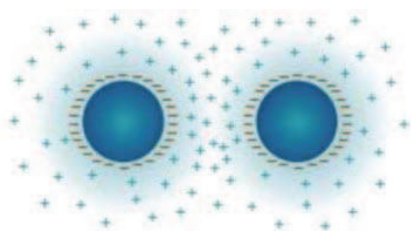


Figure 1.22: Schematic representation of electrostatic stabilization of MNPs.

Steric stabilization

Steric stabilization is the process by which adsorbed nonionic surfactants or polymers produce strong repulsion between nanoparticles (Fig. 1.23). When two particles with adsorbed polymer layers approach each other at a distance of less than twice the thickness of the adsorbed layer, there is a local increase of polymer concentration and hence an excess of osmotic pressure and a repulsive force [227]. This mode of stabilization has been shown to be very versatile [161].

Stabilization by ligands

The introduction of “organometallic ligands” as stabilizers by Schmid et al. in 1981 [228] and Vargaftik et al. in 1985 [229] paved the way for the precise molecular definition of metallic “full shell” particles, which are well defined in size and shape [230,231]. Ligand stabilization refers to the methods of stabilizing MNPs by the addition

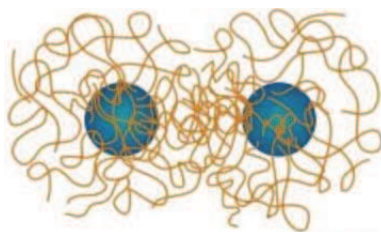


Figure 1.23: Schematic representation of steric stabilization of MNPs.

of an organic ligand that typically contains a heteroelement bearing an accessible lone pair. The organic chain of the ligand prevents agglomeration, whilst the heteroatom binds strongly to the surface of the metal. P, N, S donor ligands have been exploited extensively over the years [140,232] (Fig. 1.24). π -interaction of ligands to the metallic surface has also been proved to be efficient for MNPs stabilization [220,233].

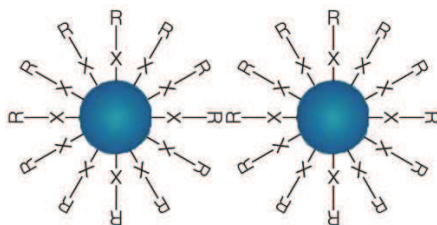


Figure 1.24: Schematic representation of ligand stabilization of MNPs.

Electrosteric stabilization

Electrosteric (i.e. combination of electrostatic and steric effects) stabilization has proved to be a very reliable means to prevent particle agglomeration (Fig. 1.25). The key feature is to adsorb bulky molecules such as charged polymers or surfactants at the surface of the particles. In general, electrostatic stabilization is insensitive to impurities and additives that could affect the charge on the stabilizers. This makes this method suitable for multigram syntheses [63]. For our catalytic membranes, the electrosteric stabilization is involved with polyRTIL used as stabilizer.

1.5.4 Polymer swelling by solvent and mass transfer inside polymer matrices

Cross-linked functional polymers (CFPs) are (disappointingly underscored) ideal supports for the preparation of supported MNP catalysts under liquid phase conditions. The introduction of the metal precursor into the CFP can occur upon metal coordination or ion exchange (Scheme 1.1) [161]. It is essential to stress that CFPs can accomplish their chemical task only when they are in the swollen state [161]. Swelling occurs when

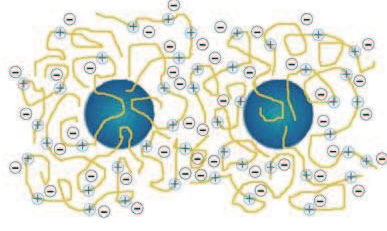
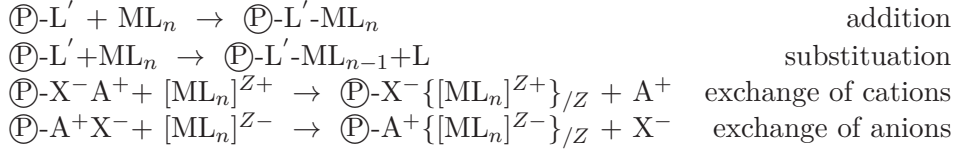


Figure 1.25: Schematic representation of electrosteric stabilization of MNPs.

the molecules of a liquid put in touch with a cross-linked polymer penetrate inside the polymer framework. For gel-type CFPs, this process implies an appreciable increase of the total volume of the materials. The ability of a liquid to swell a CFP depends on its ability to solvate the polymer chains. A fully swollen polymer framework can be considered to some extent as a viscous pseudosolution or suspension.



Scheme 1.1: Possible reaction to metalate CFPs (\textcircled{P} = CFP, L' or L = ligand, X^- = anion, A^+ = cation).

Figure 1.26 shows the process of metal immobilization in the CFP: (a) The solution containing the metal precursor starts to solvate the polymer chain after getting into contact with the CFP; (b) The polymer chain begins to stretch out and the apparent volume of the polymer increases under full swelling is achieved (when increasing elastic forces set up by unfolding of the polymer chains counterbalance the forces which drive the molecules of the swelling agent into the polymer framework); nanopores are formed, inside which metal precursor is homogeneously dispersed; (c) Metal atoms are formed (e.g. via chemical reduction); (d) Nucleation of the metal atoms and growth process; (e) MNPs are formed inside the nanopores of the swollen CFP. B. Corain and co-workers observed in the case of gel type CFPs that the nanoporosity of the swollen support is able to limit the size of the formed metal nanoparticles effectively [234, 235].

The ease to incorporate MNPs into the CFP depends on, in the first place, the swelling behavior of the CFP. If the liquid employed for dissolving the metal precursor swells the support to a relatively high extent, the interior of the swollen polymer will be readily accessible [236]. In addition, the partition coefficient between the liquid phase and the swollen-gel phase also plays an important role for the integration of reagents into the polymer framework.

Rubinstein et al. used scaling theory to derive the time dependence of the mean-

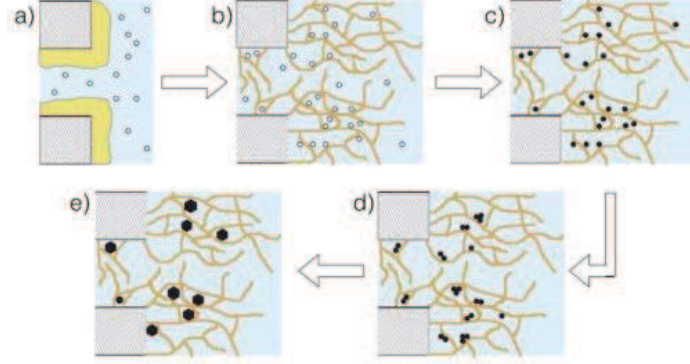


Figure 1.26: Schematic description of the CFP swelling and the MNP formation inside the CFP matrix (\circ = metal precursor, \bullet = metal atom, \bullet = MNP).

square displacement of a probe nanoparticle of a determined size experiencing thermal motion in polymer solutions and melts [237]. They concluded that there are three different cases for particle diffusion in polymer liquids depending on the relation of particle size (d) with respect to the correlation length ξ (defined as the average distance from a monomer on one chain to the nearest monomer on another chain [238]) and the tube diameter a (typically a factor of 5 larger than the correlation length ξ and is proportional to ξ in athermal solvent):

(i) Small particles. Mobility of small particles ($b < d < \xi$) is not strongly affected by polymers, and their diffusion coefficient is mainly determined by the solvent viscosity. (b is the length of the Kuhn segment)

(ii) Intermediate size particles. Motion of intermediate size particles ($\xi < d < a$) is not affected by entanglements. At time scales shorter than the relaxation time τ_ξ of a correlation blob the motion of intermediate size particles is not much affected by polymers and is diffusive with diffusion coefficient mainly determined by solvent viscosity. The intermediate size particles probe modes of surrounding polymers at intermediate time scales $\tau_\xi < t < \tau_d$, where τ_d is the relaxation time of a polymer section with size comparable to particle size d , and therefore, the particle motion is subdiffusive with mean-square displacement proportional to $t^{1/2}$. At longer time scales ($t > \tau_d$) the motion of intermediate size particles is diffusive but with diffusion coefficient determined by the viscosity of a polymer liquid with polymer size on the order of particle size.

(iii) Large particles. Motion of particles with size larger than the entanglement length ($d > a$) at time scales shorter than the relaxation time τ_e of an entanglement strand is similar to that of intermediate size particles. At time scales longer than τ_e , the large particles are trapped by entanglements, and in order to move further they have to wait for the polymer liquid to relax during relaxation time. Terminal diffusion coefficient of very large particles ($d \gg a$) is determined by bulk viscosity of polymer liquids. Particles slightly larger than the tube diameter ($d \gtrsim a$) do not have to wait for the whole polymer liquid to relax and can diffuse by hopping between neighboring entanglement cages.

1.6 Ionic liquids for CO₂ capture and MNP stabilization

Room temperature ionic liquids (RTILs) are organic salts that are molten at room temperature (Fig. 1.27) [239, 240]. They have generated more and more attention in recent years due to their attractive properties, including a negligible vapor pressure, nonflammability, thermal stability and tunable structures [241, 242]. Because of their ultralow vapor pressure, RTILs are considered as a possible “green” solvent replacements for many volatile organic solvents [243–245].

Research in room temperature ionic liquids (RTILs) has currently its main focus on exploring the unique and specific solvent and catalytic properties in homogeneous and heterogeneous catalysis aiming for greater selectivity, specificity and yield at reduced environmental liabilities. Many ionic liquids also exhibit unique gas solubility, transport and separation properties, providing opportunities for developing new gas separation/gas enrichment technologies [246, 247].

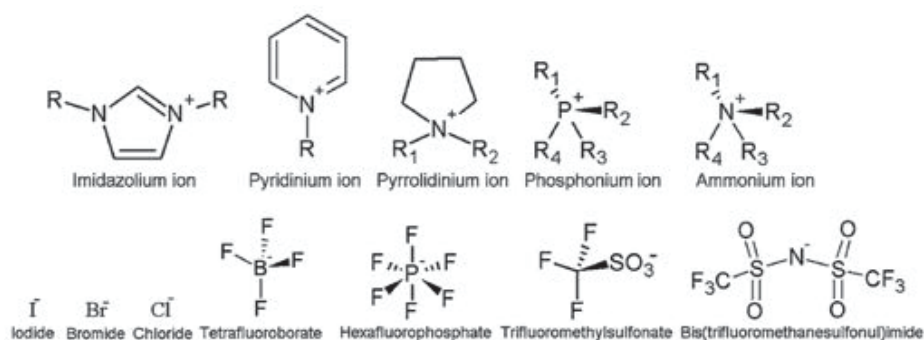


Figure 1.27: Some cations and anions constituting room temperature ionic liquids (RTILs) [248]

1.6.1 RTILs for MNP stabilization

RTILs have emerged as one of the most important and investigated classes of stabilizing agents for the synthesis of MNPs [249]. The use of ILs provides several advantages over reactions in organic solvents in terms of activity and enantioselectivity. Even more important, the catalyst immobilization in ILs can avoid its leaching and consequently favor its recycling [250].

It is well known that ILs, in particular imidazolium-derived salts, can be used to generate in situ and stabilize metallic NPs [251]. ILs differ from the classical ammonium salts, at least in one very important aspect: they possess pre-organised structures, mainly through hydrogen bonds that induce structural directionality (IL effect) [251–253]. By

contrast, aggregates of classical salts display charge-ordered structures. ILs act as stabilizing media, but most importantly, they display high self-organization on the nanomolecular scale. The ILs form extended hydrogen-bond networks at the liquid state and therefore are by definition “supramolecular” fluids. This structural organisation of ILs can be used as “entropic drivers” (the so-called “IL effect”) for the spontaneous, well-defined and extended ordering of nanoscale structures. It is now clear that the properties of ILs, especially the imidazolium-based salts, are based on their formation of aggregates rather than on their isolated cations and anions [254–256]. Indeed, the structures of 1,3-dialkylimidazolium salts follow a typical trend, forming an extended network of cations and anions connected together by hydrogen bonds in the condensed phase, which is maintained to a great extent in the gas phase [254]. The monomeric unit is always composed of one imidazolium cation surrounded by at least three anions, and in turn, each anion is surrounded by at least three imidazolium cations. The 3D arrangement of the imidazolium ILs is generally formed through chains of the imidazolium rings. This molecular arrangement generates channels in which the anions are generally accommodated as chains [252] (Fig. 1.28). These IL structures can adapt to or are adaptable by many species, as they provide hydrophobic or hydrophilic regions and a high directional polarisability, which can be oriented parallel or perpendicular to the included species [252].

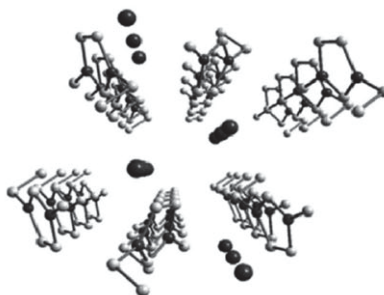


Figure 1.28: Supramolecular arrangement of 1,3-dialkylimidazolium-based ILs showing the channels where the anions (spheres) are accommodated [252]

Researches show that the stabilization of very small metal NPs (1-10 nm) is essentially due to the positive charge on the metal surface, which is ultimately induced by the adsorption of the anionic IL species onto the coordinatively unsaturated, electron-deficient, and initially neutral metal surface (Fig. 1.29). However, recent surface-enhanced Raman spectroscopy (SERS) studies using gold NPs dispersed in an ether-functionalized IL suggest that the surface-type interaction of the relatively large metal nanoparticles occurs with the imidazolium cation of the IL [257, 258].

The interaction between imidazolium ILs and MNPs has been assessed. It is revealed that the 2-position of the imidazolium cation mainly forms N-heterocyclic carbenes (NHCs) from ILs in the presence of NPs [260]. The non-innocent behavior of ILs may not always be beneficial to catalysis [261]. For example, in the telomerisa-

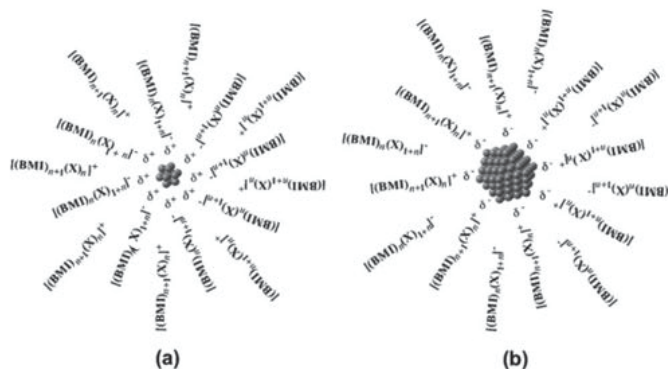


Figure 1.29: Interaction of metal NPs with IL supramolecular aggregates: (a) small particles tend to interact preferentially with anionic aggregates of the ILs, whereas (b) large ones probably interact preferentially with the cationic aggregates [259].

tion of 1,3-butadiene with methanol, using Pd-phosphine catalyst systems, in $[bmim]^+$ and $[emin]^+$ ($bmim$ =1-butyl-3-methylimidazolium; $emin$ =1-ethyl-3-methylimidazolium) salts of non-coordinating anions as solvents [262, 263], very low activities were observed and it was separately found the addition of even small amounts of 1,3-dialkyl imidazolium salts was sufficient to poison the Pd-phosphine catalyst; probably forming catalytically inactive L_2Pd -($bmiy/emiy$) complexes ($emiy$ =1-ethyl-3-methylimidazolin-2-ylidene), in which coordination sites required for catalysis were blocked. [262] Running the reactions in 1-n-butyl-2,3-dimethylimidazolium ILs, where the imidazolium C2 position was blocked with a methyl group, resulted in activity comparable to the Pd-phosphine reference systems run in MeOH, with improved chemoselectivity and regioselectivity [262].

1.6.2 RTILs for CO₂ capture

Considerable research work is being done showing high carbon dioxide solubility in certain RTILs, especially in those having imidazolium-based cations [264]. A number of factors like free volume, size of the counter ions, and strength of cation-anion interactions within the ionic liquid structure seem to govern CO₂ solubility in RTILs. Baltus et al. reported that imidazolium based RTILs with alkyl groups had higher CO₂ solubility than those with phenyl groups [265]. Increase in alkyl-side chain usually results in higher gas solubility, owing to the increased free volume available for CO₂ with corresponding decrease in cation-anion interactions [266, 267]. However, the influence of alkyl chain length is not as prominent as anions. The anion moiety enhances interactions by favoring particular distributions of CO₂ molecules around the cation [268]. As a matter of fact, the nature of anion also has stronger influence on gas solubility than that of the cation [268, 269]. Ionic liquids possessing $[Tf_2N]$ anion show higher CO₂ solubility among imidazolium-based RTILs [265]. The thermal stability and negligible volatility make RTILs quite imposing. Hou and Baltus found that even after regenerating the

ionic-liquid six times, by purging N_2 followed by evacuation at 70 °C, there was practically no change in the gas capture capacities [267].

Functionalization of ionic liquids with a suitable moiety (like amine) can further enhance the CO_2 capture ability of RTILs. But these functionalized species exhibit much higher viscosities as compared to the corresponding RTILs or other commercially available CO_2 scrubbing solutions, posing too serious complications to be applicable on industrial scale. This downside can be overcome by making use of supported ionic-liquid membranes (SILMs). One of the negative aspects of SILMs is the leaching of the liquid through membrane pores as the pressure drop surpasses the liquid stabilizing forces within the matrix.

Membranes made up of polymerizable ionic liquids may be a better option for CO_2 separation [247]. Poly(RTIL)s are typically synthesized by free radical polymerization of their corresponding ionic liquid monomers using a photo initiator [270]. The ionic liquids in polymeric forms are solid at room temperature. However, these polymerized structures can capture larger amount of CO_2 with faster absorption and desorption rates than compared to the classical RTILs [271]. For example, the polymers of tetraalkylammonium-based ionic liquids have CO_2 sorption capacities 6.0-7.6 times higher than room temperature ionic liquids [271]. In most cases, gas permeability and diffusivity increase considerably in poly(RTIL)s when the length of the alkyl chain increases. The efficiency of these polymeric structures can be enhanced further by modifying monomers with appropriate entities like oligo(ethylene glycol) or nitrile-containing alkyl groups [6]. By incorporating an appropriate amount of RTIL and consequently introducing free ion pairs into the poly(RTIL) membranes, CO_2 permeability and CO_2/N_2 selectivity may be increased up to about 300%-600% and 25% respectively [6, 272]. In this thesis (Chapter 3), oligo(ethylene glycol) functionalized imidazolium-based RTILs with $[Tf_2N]$ anions were chosen for the CO_2 capture application for their high CO_2 permeability.

Due to negligible loss of ionic liquids during recycling, these technologies will also decrease the CO_2 capture cost to a reasonable extent when applied on industrial scale. From a sustainable point of view, it is also important to look deeply into the noxious behavior of these unique species. Nevertheless, the flexibility in synthetic structure of ionic liquids may make them opportunistic in CO_2 capture scenarios [248].

1.7 Conclusions

In this chapter, general background related to the thesis and the state-of-art have been studied. Membrane materials can be classified according to their pore size, which determines their separation capability.

Modification of the membrane can confer them with more advanced functions. In this work, polymerizable room temperature ionic liquids have been used to modify the membrane. Although a lot of work has been done on ionic liquids to exploit their capability on CO_2 capture as mentioned above, no results, to the best of our knowledge,

have been reported on the continuous preparation of polyRTIL as hollow fibers. What we want to realize in the thesis is to prepare hollow fibers using a gel polyRTIL that retains free RTIL inside its polymer matrix. The extrapolation from lab-made membranes to the continuous production of polyRTIL-RTIL based hollow fibers will help the polyRTIL-based CO₂ capture to go further towards industrial applications.

Talking about membranes, in most of the cases, we talk about separations. However, membranes, even polymer based, can be used as reactors. The main classification of catalytic membrane reactors are given in this chapter. In our research, a polymeric catalytic membrane was developed by combining a polymer support (pore size = 0.2 μm) with poly(ionic liquid) and metallic nanoparticles. What unique properties will generate through this combination? Is the generally accepted understanding on catalytic membrane reactors able to explain those properties? Well, answers will be revealed in the following chapters.

Chapter 2

Materials and methods

Résumé du Chapitre

Ce chapitre décrit des méthodes et des protocoles expérimentaux utilisés dans ce travail, organisés dans l'ordre des chapitres qui suivent (Chapitre 3, 4 et 5). Les informations générales sur les matériaux et méthodes d'analyse sont données en premier lieu. Les protocoles expérimentaux de préparation des membranes et d'évaluation de leurs performances sont ensuite décrits l'un après l'autre.

This chapter provides experimental methods and protocols applied in this work. Contents are organized in the order of the chapters following (Chapter 3, 4 and 5). Chapter 6 is based on theoretical calculations, hence no experiments are involved. General information on materials and analysis methods are given in the first place, followed by experimental protocols of how membranes and catalytic systems were prepared and how their performances were evaluated.

2.1 General

2.1.1 Materials

[MMPIM][NTf₂] (1,2-dimethyl-3-propylimidazolium bis(trifluoromethylsulfonyl)azide) was purchased from Solvionic, France. MicroPES[®], Oxyphan[®], Oxyplus[®] and MicroPES[®] (2F) flat-sheet membrane was purchased from Membrana GmbH (Germany) and directly used without pre-treatment. Cylinders of CO₂ and N₂ gas were purchased from AlphagazTM or Linde (at least of 99.99% purity). Amicon stirred ultra-filtration cell was purchased from EMD Millipore. The Ismatec SA-Reglo Analog peristaltic pump was purchased from IDEX Health & Science.

2.1.2 Analyses

ATR-FTIR spectra were obtained with Thermo-Nicolet Nexus 670, with samples supported on diamond crystal substrates. The mechanical property of the hollow fibers were determined by tensile test using Instron[®] series 3342. Viscosity measurements were carried out on Physica MCR 301, surface tension was measured on GBX-3S tensiometer. SEM images were obtained with Hitachi Tabletop Microscope TM-1000. Samples of the membrane cross-section are prepared by cryofracture: Membranes were first immersed in ethanol, fractured in liquid nitrogen. Membrane samples were sputtered with a thin layer of gold before SEM analysis for better contrast. Contact angles were measured using GBX Digidrop contact angle meter (model DGD/Fast 60). ¹H and ¹³C NMR spectra were acquired using a Bruker Avance-III 300 (300 MHz). GC analyses were carried out on an Agilent GC6890 with a flame ionisation detector, using a SGE BPX5 column composed by 5% of phenylmethylsiloxane. Electrospray analyses were recorded on a UPLC Xevo G2 QTof. TEM images were obtained with HT 7700 Hitachi or JOEL JEM 1400 transmission electron microscope. The membrane samples for TEM and X-ray tomography were prepared by ultramicrotome after embedding the membrane in epoxy resin. The same membrane samples were treated with gold nanoparticles before analyzed by electronic tomography. The TEM sample preparation of colloidal palladium was as follows: A drop of solution was deposited on a copper holey carbon grid and the excess of [MMPIM][NTf₂] was removed with Kimwipe tissue in order to obtain a film as thin as possible. EDX-TEM analysis was carried out with JOEL JEM 2100F transmission electron microscope. EDX-SEM analysis was carried out with JOEL JEM 7100F scanning electron microscope. ICP-OES analyses were carried out with Horoba Jobin Yvon Ultima 2. The size distribution of the palladium nanoparticles in the membrane

and in the colloidal system were obtained by analyzing the TEM images with Image-J software associated to a Microsoft Excel macro.

2.2 Modification of hollow fibers by room temperature ionic liquids for CO₂ capture

2.2.1 Composite hollow fiber preparation

The hollow fiber outer-surface modification was realized using a continuous photografting polymerization set-up shown in Fig.2.1, as described in previous papers [69,273]. The velocity of the fiber can be adjusted by a tri-cylinder device according to need. The hollow fiber bobbin is installed on a motor-driven rotary axle whose rotational speed is adjustable. All wheels between the hollow fiber bobbin and the tri-cylinder line rate controlling system are under passive rotation. The virgin fiber passes through a solution bath, thus the fiber carries a liquid film (of thickness e) on its surface when it leaves the bath (Fig.2.2).

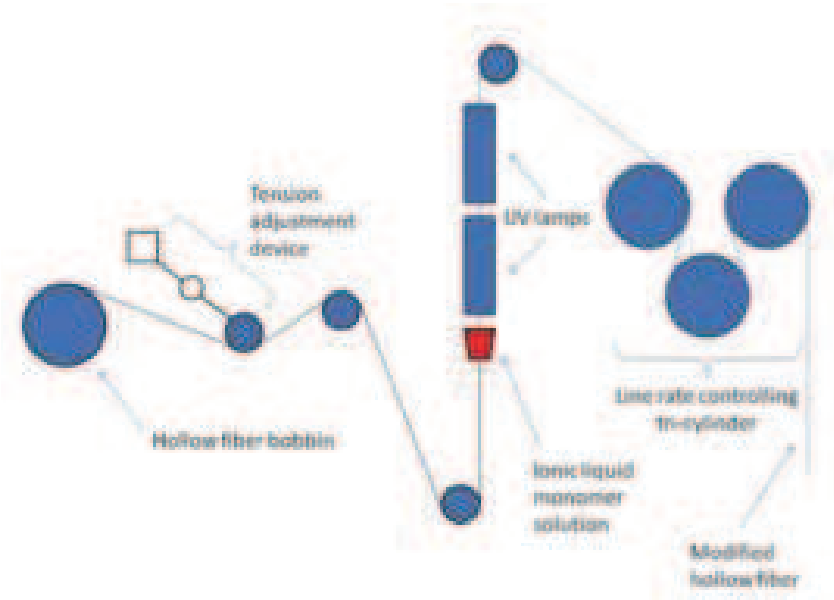


Figure 2.1: Schematic diagram of continuous photografting set-up for hollow fiber modification.

A 600 μm -diameter hole was pierced at the bottom of the bath container to let the Oxyphan[®] or Oxyplus[®] fiber pass through (a 700 μm -diameter hole for MicroPES[®] fiber). After a short moment of relaxation, the liquid film moves upwards with the fiber at the same velocity (see Fig.2.2). So the liquid is motionless with respect to the axes that move with the fiber. Then, fiber passes through the UV lamps (high power Mercury lamps, UVA-PRINT LE, Hoenle UV France, $I = 4188\text{--}7109 \text{ mW cm}^{-2}$), where

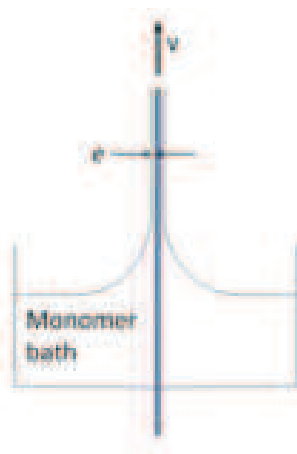


Figure 2.2: Entrainment of the liquid film by the hollow fiber [274].

the radical polymerization reaction takes place. The infra-red part (IR) of the irradiation heats the fiber and causes a progressive evaporation of the solvent. The UV reactors are equipped with elliptical mirrors to ensure that UV rays are centralized on the hollow fiber (Fig.2.3).

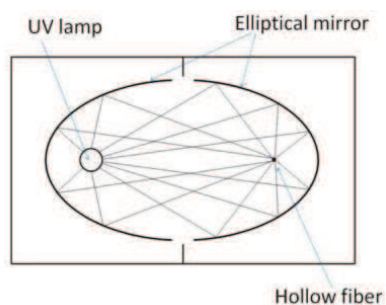


Figure 2.3: Schematic presentation of UV reactors equipped with UV lamps and elliptical mirror.

The distance between the center of the UV lamp and the hollow fiber is 12 cm. An air cooling system is also installed on the UV reactors in order to dissipate heat while the lamps are turned on. An optical filter is placed within the lamps so that different wavelengths can be selectively transmitted according to needs. The velocity of the grafting process can vary from 0 to 40 m/min. However, too low velocities lead to the destruction of the fiber due to overheating. The minimum experimental speed tried was around 8 m/min. The exact type of filter, solution concentrations and compositions chosen in different cases are given in Chapter III.

The UV intensity of the two types of lamps (high power Iron (F) and Mercury (H) lamp) at varied powers were previously measured by our group (Fig.2.4). Light intensities are given respectively in UVA (400-315 nm), UVB (315-280 nm) and UVC

(280-100 nm) wavelength ranges.

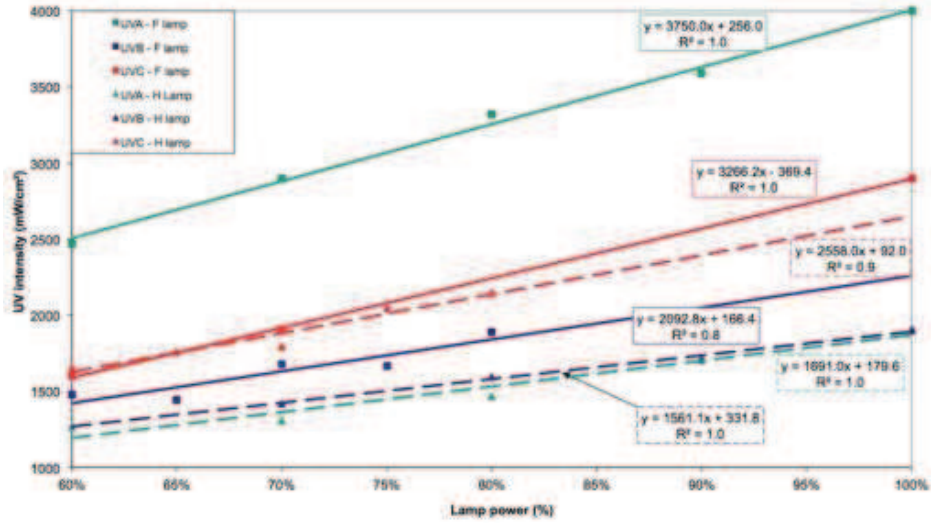


Figure 2.4: UV intensity at as a function of nominal lamp power for .

2.2.2 Gas permeance test for composite hollow fibers

Ideal gas permeance was measured at room temperature using laboratory made stainless steel modules. One to ten fibers with a length around 30 cm were assembled in the module. Pure gases were fed to the shell side of the module at regulated pressures. The permeance flow rate was measured in the lumen side, which is open to atmosphere. The permeance of gas species i , Pe_i ($\text{mL(STP)} \cdot \text{min}^{-1} \cdot \text{cm}^{-2} \cdot \text{bar}^{-1}$; or $\text{L(STP)} \cdot \text{h}^{-1} \cdot \text{m}^{-2} \cdot \text{bar}^{-1}$) was determined by plotting its flux density ($\text{mL(STP)} \cdot \text{min}^{-1} \cdot \text{cm}^{-2}$, or $\text{L(STP)} \cdot \text{h}^{-1} \cdot \text{m}^{-2}$) as a function of its partial transmembrane pressure ΔP_i (bar) (Eq.2.1). The permeance is usually also given in GPU ($10^{-6} \text{cm}^3(\text{STP}) \cdot \text{cm}^{-2} \cdot \text{s}^{-1} \cdot \text{cmHg}^{-1}$).

$$Pe_i = \frac{J_i}{\Delta P_i} \quad (2.1)$$

The permeability test was carried out first by increasing the pressure to a maximum value (from 3 to 7 bar depending on the type of fiber). The pressure was then decreased back to atmospheric pressure to re-measure the pure gas permeability. Tests started randomly with either gas and then switched to another (the permeabilities were measured after values had stabilized). The same fibers were re-tested several times at varied time intervals.

The selectivity was determined as the ratio of the permeance of the more permeable species to the permeance of the less permeable species. Measurements were randomly started with CO_2 or N_2 , then switched to the other gas before going back to the first gas for recheck. For each gas, the permeability was first tested under 3 bar of transmembrane pressure before being tested for higher pressures.

2.2.3 Experimental conditions for tensile test

At least 5 samples were tested for each membrane. For MicorPES[®] membrane or polyRTIL composite membrane with MicroPES[®] as support, the grip distance was 50 mm and tensile velocity was set at 100 mm/min. For Oxyplus[®] membrane or polyRTIL composite membrane with Oxyplus[®] as support, the grip distance was 50mm and tensile velocity was 300 mm/min.

2.3 Preparation of colloidal palladium systems and their catalytic performance

Syntheses and reactions with presence of H₂ were carried out in a Fischer-Porter bottle. All other manipulations were performed using standard Schlenk techniques under argon atmosphere. [MMPIM][NTf₂] was heated at 60 °C under vacuum overnight prior to use in order to eliminate water traces.

2.3.1 Synthesis of colloidal palladium nanoparticles in ionic liquid

Synthesis under thermal conditions

11.5 mg (0.05 mmol) of palladium acetate together with (or without) the corresponding quantity of PVP (1-ethenylpyrrolidin-2-one) were added in 5 mL of [MMPIM][NTf₂] or glycerol and stirred at room temperature under argon in a schlenk tube until complete dissolution. The mixture was then heated and stirred at 100 °C overnight to give complete decomposition of the metallic precursor.

Synthesis under H₂ pressure

11.5 mg (0.05 mmol) of palladium acetate together with or without corresponding quantity of PVP were added in 5 mL of [MMPIM][NTf₂] and stirred at room temperature under argon in a Fischer-Porter bottle until complete dissolution. The system was then pressurized under dihydrogen and stirred at regulated temperature overnight, leading to a black colloid. The reaction mixture was then cooled down and residual gas was released.

2.3.2 Synthesis of colloidal palladium nanoparticles in glycerol

11.2 mg of palladium acetate (0.05 mmol) and 111 or 222 mg of PVP (for 1 or 2 mmol of monomer) were placed with 5 mL of glycerol (previously dried overnight at 60 °C under vacuum) in a Fisher-Porter vessel and then pressurized under 3 bar hydrogen atmosphere during 3 hours. The solution was then depressurized and transferred in a Schlenk vessel without any further treatment.

2.3.3 Catalytic tests on the colloidal systems

Procedure for hydrogenation reaction

1 mmol of *trans*-4-phenyl-3-buten-2-one (147.7 mg) or 1-iodo-4-nitrobenzene (254.1 mg) was added to 1 mL of preformed palladium nanoparticles in [MMPIM][NTf₂]. The system was then pressurized with dihydrogen and stirred at regulated temperature. The mixture was then cooled to room temperature. Products were extracted with cyclohexane (5×2 mL) from the catalytic phase. In the case of the formation of anilines, a short-column chromatography on silica gel was used to separate the product. The organic phases were dried over anhydrous MgSO₄, filtered and the solvent evaporated under reduced pressure. Conversions were determined by ¹H NMR spectroscopy and GC-MS chromatography, using respectively 1,3,5-trimethylbenzene and decane as internal standards.

Palladium colloidal systems in glycerol were tested for the hydrogenation reaction following the same protocol, except that dichloromethane was used for product extraction instead of cyclohexane. Both a Pd/substrate molar ratio of 1/100 and 1/1000 were used for the catalytic test.

Procedure for C-C cross-couplings

Heck-Mizoroki cross-coupling

Iodobenzene (1 mmol, 204 mg), butenone (1.2 mmol, 0.1 mL) and Na₂CO₃ (2.5 mmol, 265 mg) dissolved in water (1 mL, previously degassed) were consecutively added to 1 mL of preformed palladium nanoparticles in [MMPIM][NTf₂]. The resulting mixture was heated at 100 °C. The reaction mixture was then cooled to room temperature and 0.2 mL of the reaction mixture was taken from the Schlenk and extracted with diethylether (10×2 mL). The extracted phases were then dried over anhydrous MgSO₄ and filtered on celite. Solvent was removed under reduced pressure. Conversions were determined by GC-MS chromatography with decane as internal standard.

Suzuki-Miyaura cross-coupling

Phenyl halide (1 mmol), phenyl boronic acid (1.2 mmol, 151 mg) and disodium carbonate (2.5 mmol, 265 mg) or potassium 2-methylpropan-2-olate (2.5 mmol, 286 mg) were consecutively added to 1 mL of preformed palladium nanoparticles in [MMPIM][NTf₂]. The resulting mixture was heated at regulated temperature and then cooled to room temperature. 0.2 mL of the reaction mixture was taken from the Schlenk and extracted with diethylether (10×2 mL). The extracted phase was then dried over anhydrous MgSO₄, filtered on celite. Solvent was removed under reduced pressure. Conversions were determined by ¹H NMR spectroscopy and GC-MS chromatography, with respectively 1,3,5-trimethylbenzene and decane as internal standard.

Procedure for one-pot sequential reactions

Heck-Mizoroki coupling followed by hydrogenation

The Heck-Mizoroki reaction mixture (see above) was stirred in the autoclave for 85 h at 100 °C before cooled to room temperature and put under vacuum for 30 min. The catalytic mixture was then pressurized under hydrogen (3 bar) for 17 h at 80 °C. 0.2 mL of the reaction mixture was taken from the autoclave and was extracted with cyclohexane (5x2 mL). The extracted organic phases were dried over anhydrous MgSO₄, filtered and the solvent evaporated under reduced pressure. The solutions were then analyzed by ¹H NMR spectroscopy and GC-MS chromatography.

Suzuki-Miyaura coupling followed by hydrogenation

1-Iodo-4-nitrobenzene (0.254 g, 1 mol), phenyl boronic acid (0.151 g, 1.2 mol) and potassium tert-butoxide (0.286 g, 2.5 mol) were consecutively added to 1 mL of preformed palladium nanoparticles in [MMPIM][NTf₂]. The resulting mixture was heated at 100 °C during 20 h and then cooled to room temperature and introduced into the autoclave and pressurized under hydrogen (3 bar) for 14 h at 80 °C. 0.2 mL of the reaction mixture was taken from the autoclave and was extracted with cyclohexane (5x2 mL). The organic phases were dried over anhydrous MgSO₄, filtered and the solvent evaporated under reduced pressure. The solutions were then analyzed by ¹H NMR spectroscopy and GC-MS chromatography.

Procedure for catalyst recycling test on hydrogenation reaction

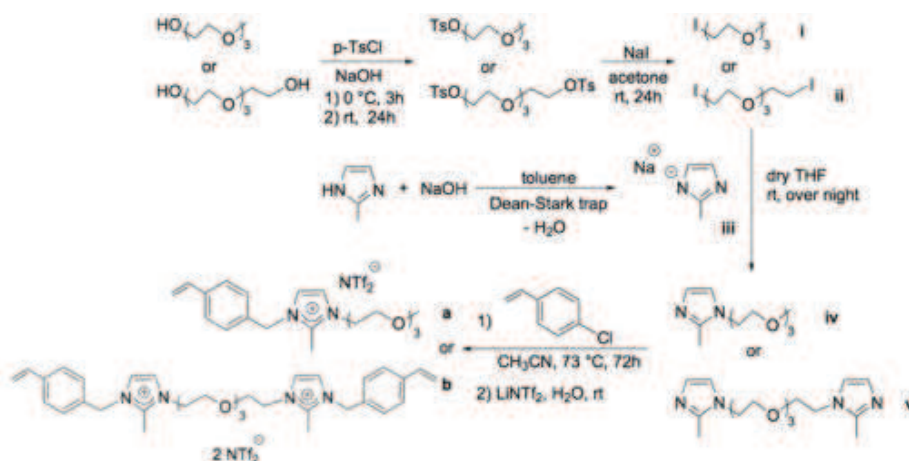
The hydrogenation product of *trans*-4-phenyl-3-buten-2-one was extracted from the reaction mixture with cyclohexane (7x1 mL). The RTIL catalytic phase from the previous run was maintained for 30 min under reduced pressure. Then, reagents were re-added for the next run. The catalytic mixture was then treated under the corresponding conditions applied for the first run.

2.4 Preparation, characterization and performance of the catalytic membrane

2.4.1 Synthesis of ionic liquids **a** and **b**

The methodology described below concerns the synthesis of cross-linker **b** and is directly applicable to the synthesis of monomer **a** (scheme 2.1). Detailed syntheses of compound **i** and **ii** were previously published by Richard D. Noble's group [9].

Imidazole (8.210 g, 100 mmol) was suspended in 50 mL toluene and added to a 100 mL round bottom flask equipped with a magnetic stir bar. Sodium hydroxide (4.000 g, 100 mmol) was added to the flask. A Dean-Stark trap was then attached to the round bottom flask. The reaction was heated at 120 °C under reflux for 30 h. After the reaction was cooled down, toluene was decanted and diethyl ether (50 mL) was added to the flask. The mixture was stirred for a while. Diethyl ether was then decanted. The



Scheme 2.1: Synthesis of imidazolium-based RTIL **a** and **b**.

solids were filtered off, washed with diethyl ether and then left in a vacuum oven at 65 °C for 24 h to afford compound **iii** as a yellow powder (10.3464 g, 99% yield).

From here on, all the reactions were shielded from light. Compound **iii** (1.561 g, 15 mmol) was dissolved in dry THF (35 mL) and added to a pre-dried 100-mL Schlenk flask equipped with a magnetic stir bar. Compound **ii** (2.957 g, 7.1 mmol) was added dropwise with a syringe while stirring the mixture. The reaction was left stirred overnight. The solution was then dissolved in dichloromethane (15 mL) and extracted three times into 50 mL diluted sodium bicarbonate solution (4 mL saturated NaHCO₃ solution dissolved in 45 mL of deionized water). Brine was added to the water phase, which was then extracted with dichloromethane (3 x 150 mL). The organic phase was dried over anhydrous MgSO₄ and filtered. Dichloromethane was removed via rotary evaporation followed by vacuum overnight at room temperature to give **v** (Scheme 2.1) as yellow oil (1.477 g, 64% yield).

Compound **v** (1.477g, 4.6 mmol) was dissolved in CH₃CN (45 mL) and added to a 100 mL Schlenk flask equipped with a magnetic stir bar and a reflux condenser. The flask and the condenser were purged with argon and wrapped with aluminum foil to protect the system from light. 4-Vinylbenzyl chloride (1.58 mL, 10.1 mmol) was added to the flask and the reaction was heated to reflux (at 73 °C) and stirred for 72h. The reaction was then cooled and the product was dissolved in methanol (40 mL) and washed with cyclohexane (3 x 20 mL) to get rid of the 4-vinylbenzyl chloride in excess. Methanol was removed via rotary evaporation. The product was then dissolved in water (5 mL) and transferred to a 10-mL round bottom flask equipped with a magnetic stir bar. The flask was wrapped with aluminum foil. LiNTf₂ (2.928 g, 10.2 mmol) was then added. The reaction was allowed to stir at room temperature overnight. An oil precipitate was observed. The aqueous phase was then decanted and the product was extracted with CH₂Cl₂ (15 mL) and washed with deionized water (11 x 8 mL) until the addition of AgNO₃ to an aliquot of the aqueous phase did not result in precipitate formation (i.e.

presence of halides). The organic phase was then dried over anhydrous MgSO_4 and filtered. Dichloromethane was then removed via rotary evaporation followed by vacuum overnight at room temperature to afford monomer **b** as lightly yellow viscous oil (4.772 g; yield: 92%).

*Characterization of monomer **a***

Global yield: 41%, 5.623 g. ^1H NMR (300 MHz, DMSO-d_6): δ 2.62 (s, 3H), 3.22 (s, 3H), 3.35-3.52 (m, 8H), 3.76 (t, 2H), 4.32 (t, 2H), 5.31 (dd, 1H), 5.42 (s, 2H), 5.83 (dd, 1H), 6.73 (dd, 1H), 7.30 (d, 2H), 7.50 (d, 2H), 7.70 (d, 1H), 7.74 (d, 1H). $^{13}\text{C}\{^1\text{H}\}$ NMR (75.5 MHz, DMSO-d_6): δ 9.67, 47.84, 50.50, 57.96, 68.41, 69.54, 71.25, 117.44 (q, CF_3), 114.98, 121.56, 121.93, 126.67, 128.01, 133.93, 135.89, 137.42, 144.92. ESI (m/z): calculated as $[\text{A}]^+$, 345.46; found, 345.20.

*Characterization of crosslinker **b***

Global yield: 59%, 4.772 g. ^1H NMR (300 MHz, DMSO-d_6): δ 2.62 (s, 6H), 3.38 (m, 4H), 3.45 (m, 4H), 3.74 (t, 4H), 4.32 (t, 4H), 5.32 (dd, 2H), 5.43 (s, 4H), 5.89 (dd, 2H), 6.75 (dd, 2H), 7.31 (d, 4H), 7.50 (d, 4H), 7.68 (d, 2H), 7.75 (d, 2H). $^{13}\text{C}\{^1\text{H}\}$ (75.5 MHz, DMSO-d_6): δ 9.68, 47.77, 50.45, 68.37, 69.53, 113.13, 117.40 (q, CF_3), 121.60, 121.91, 126.68, 128.03, 133.98, 135.89, 137.39, 144.87. ESI (m/z): calculated as $[\text{A}]^{2+}[\text{B}]^-$, 836.88; found 836.26.

2.4.2 ICP-OES analyses

To quantify the palladium loading of the membrane, a membrane piece of known surface area was left in aqua regia for two days to ensure total oxidation of palladium. The acid solution was then filtered on a filter paper and diluted 10 times in deionized water.

ICP test is a destructive measurement. In order to pre-evaluate the palladium loading of a catalytic membrane, a larger membrane was prepared and then chopped into smaller parts so that the palladium loading of the smaller membrane to be used can be calculated based on the surface area and the ICP results of other parts cut off from the same membrane. After use, the membrane was analyzed by ICP as well to compare to the estimated value and to verify the homogeneity of palladium over different parts of the membrane.

In the case of leaching test for the product (obtained from the permeate), the product was dissolved in the aqua regia instead of the membrane. To verify the leaching during filtration, 96% ethanol was filtered through the membrane. Then two methods were used to prepare the ICP samples. (1) 750 mL permeate was collected in a round bottom flask. Ethanol was removed via rotary evaporator before aqua regia was added to the flask. (2) 1 mL of the ethanol permeate was dissolved in aqua regia and left for two days before ethanol was removed via rotary evaporator. The following steps (filtration, dilution) were the same as above-described.

The atomic spectra of palladium have 4 representative emission lines at 248.9, 340.3, 342.1 and 361.0 nm. We chose the two most intensive bands (340.3 and 361.0 nm) for

analysis. The detection limits were estimated to be 3 and 15 ppb respectively. Aqua regia solution prepared with the same dilution ratio served as a blank sample.

2.4.3 Preparation of the catalytic membrane

Grafting of poly(ionic liquid)s on the PES (polyethersulfone) support membrane

A round-shaped membrane was cut from a MicroPES® 2F flat sheet (purchased from Membrana GmbH, 0.2 μm nominal pore size). A 25%wt. IL monomer solution was prepared in methanol with a cross-linker/non-crosslinker molar ratio of 1/20. 2-Hydroxy-2-methylpropiophenone (1% wt. of total monomer weight) was added to the solution as photo-initiator. The membrane was dipped in the solution for a few seconds and taken out before being exposed to UV light (Heraeus TQ 150 lamp with quartz filter, cooled by a water circuit) for 1 h in air. The distance between the membrane and the quartz filter was 4 cm. After removal from the UV light, the membrane was rinsed thoroughly with ethanol to eliminate surplus IL monomers prior to the metal loading step.

Metal loading

The membrane was first soaked in 10 mL solution of $\text{K}_2[\text{PdCl}_4]$ (0.05 mol/L) in H_2O /Methanol (1/1 volume ratio) for 90 min while shaking on a IKA KS 260 basic shaker at 100 rpm. The membrane was then rinsed with ionized water before installation in an Amicon filtration cell with IL-grafted side of the membrane facing up. 10 mL of 0.5 mol/L NaBH_4 solution in H_2O /methanol (1:1 volume ratio, freshly prepared) was then filtered through the membrane (transmembrane pressure ≈ 0.2 bar). The membrane was then soaked in NaBH_4 for one hour before it was rinsed with and kept in deionized water. The membrane was then directly used or cut into appropriate size before use.

2.4.4 Permeability test

Since ethanol is the solvent used for the catalytic reaction, ethanol permeability of the catalytic membrane was measured. The flux measurements were carried out in an Amicon cell at room temperature. The permeability was determined by the slope of the plot of volumetric flux density J ($\text{mL} \cdot \text{min}^{-1} \cdot \text{cm}^{-2}$) as a function of transmembrane pressure ΔP (bar) (Eq.2.2). The permeability was corrected to 25°C by Eq.2.3 [275] to take into account the variation of viscosity with temperature. Measurements were repeated twice on each membrane.

$$L_p = \frac{J}{\Delta P} \quad (2.2)$$

$$L_p^{25} = L_p^T \frac{\mu_T}{\mu_{25}} = L_p^T \cdot e^{1708.1(1/T - 1/298.15)} \quad (2.3)$$

with L_p^{25} as permeability corrected to 25 °C, L_p^T as permeability measured at the temperature when the measurement was done, μ_{25} and μ_T respectively as ethanol dynamic viscosity at 25 °C and at the temperature when the measurement was done.

2.4.5 Reactions performed on the catalytic membrane

Flow-through configuration

The Amicon cell, equipped with a magnetic stir bar, was placed in a water bath at 60 °C. The reagents were dissolved in 96%vol ethanol, stirred and heated in an oil bath at 60 °C for 20 min before it was poured into the Amicon cell 8050 and filtered through the membrane while stirring. The permeate flow was controlled by a peristaltic pump (Fig.2.5). The membrane was then washed by filtering ethanol at the reaction temperature 5 times using the same volume of the reactive solution after each test. The permeate was collected and analyzed by GC-MS and ^1H NMR spectroscopy in order to identify the products obtained. Conversion (related with the consumption of the substrate) and yield (related to the desired product) at the outlet of the catalytic membrane were calculated by two analytical approaches (GC-FID and ^1H NMR), using decane and 1,3,5-trimethylbenzene, respectively, as internal standards; both methodologies gave similar results. Isolated yields were also determined. The stirring speed was 210 rpm. The pump permitted to vary the permeate flow rate. The transmembrane pressure was not measured but was in the range of 1 to 150 mbar as deduced from the solvent permeability.

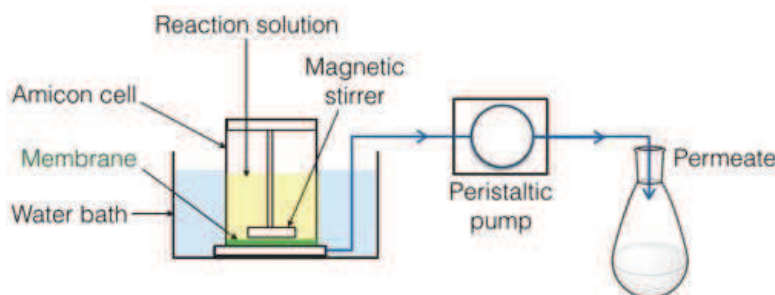


Figure 2.5: Experimental set-up for catalytic test of the membrane in a flow-through configuration.

Protocol for Suzuki-Miyaura cross-coupling reaction

The molar ratio $\text{KtBuO}/\text{Ph-B(OH)}_2/4\text{-iodonitrobenzene}$ was 2.5/1.2/1. Product isolation: The ethanol present in the permeate was removed via rotary evaporation. The product was then re-dissolved in dichloromethane and washed with water to remove the remaining KtBuO . The water phase was discarded and the organic phase was dried over anhydrous MgSO_4 and filtered. Dichloromethane was then removed under reduced pressure and the cross-coupling product was obtained and analyzed by ^1H NMR and GC-MS.

The same product isolation method was applied in the Sonogashira coupling/cyclization tandem process and Heck cross-coupling.

Protocol for Sonogashira cyclization tandem reaction

One membrane: 0.4 mmol of 2-iodophenol (89.8 mg), 0.4 of mmol phenylacetylene (41.7 mg) and 1 mmol of t-BuOK (114.5 mg) were dissolved in 31 mL ethanol. The resulting solution was heated for 20 min at 60 °C before filtered on the catalytic membrane.

Two membranes in series: 0.4 of mmol 2-iodophenol (89.8mg) and 0.4 of mmol phenylacetylene (41.7 mg) and 1 mmol of t-BuOK (114.5 mg) were dissolved in 12.5 mL ethanol and heated for 20 min at 60°C. The solution was then filtered through two membranes in series.

Protocol for Heck cross-coupling reaction

1 mmol of 4-bromoanisole (190.9 mg), 1.5 mmol of styrene (157.8 mg) and 2 mmol tBuOK (229.0 mg) were dissolved in 31 mL ethanol. The resulting solution was heated for 20 min at 60 °C before filtered on the catalytic membrane.

Protocol for hydrogenation reaction

0.2 mmol of *trans*-4-phenyl-buten-2-one (29.53 mg) was dissolved in 50 mL of ethanol in a round bottom flask. The solution was bubbled with dihydrogen for 30 min. Then the solution was filtered through the membrane under H₂ pressure (\approx 0.1 bar). The permeate was collected and re-added to the round bottom flask for a second filtration. The procedure was repeated eight times with a total residence time of 2.6 s. The final permeate was collected and ethanol was evaporated under reduced pressure. The isolated product was then analyzed by ¹H NMR spectroscopy and GC-MS chromatography.

Submerging configuration (for hydrogenation reaction)

Bubbling mode: 0.4 mmol of *trans*-4-phenyl-3-buten-2-one (59.7mg) was dissolved in 20 mL ethanol. The solution was added to the Amicon cell equipped with magnetic stirrer and bubbled under H₂ (10 nL/h) for 30min. The Amicon cell was placed in a water bath regulated at 35 °C. Ethanol was removed under reduced pressure and the obtained sample was analyzed by ¹H NMR spectroscopy and GC-MS chromatography.

Autoclave mode: A membrane with a surface area of 11.9 cm² was dried under reduced pressure at 60°C for 6h and then put into the autoclave. A glass support (to prevent the magnetic stirrer from touching the membrane) was placed above the membrane. The reaction solution (0.71 mmol (104.8 mg) of *trans*-4-phenyl-3-buten-2-one dissolved in 5 mL ethanol) was added to the autoclave. The autoclave was then pressurized with H₂ (1 bar) and heated at 65°C for 1h.

2.4.6 Colloidal palladium stabilized in glycerol served as reference for more challenging reactions

0.05 mmol of palladium precursor (11.2 mg for $\text{Pd}(\text{OAc})_2$) and 0.05 mmol of ligand TPPTS (Tris(3-sulfophenyl)phosphine trisodium salt, 28.4 mg) were dissolved in 5 mL of glycerol and stirred at room temperature under argon in a Fischer-Porter bottle until complete dissolution. The system was then pressurised with 3 bar of dihydrogen and stirred at 80 °C overnight, leading to a black colloidal. After releasing the residual gas, the solution was washed with pentane (2×5 mL) and dried under reduced pressure for 1h [276].

Chapter 3

Preparation of composite hollow fiber with a thin polyRTIL-RTIL gel layer for CO₂ capture

Résumé du Chapitre

L'élimination du CO_2 du gaz de combustion (séparation du CO_2/N_2) joue un rôle important dans l'atténuation du changement climatique mondial. Les méthodes les plus souvent utilisées telles que l'adsorption modulée en pression, l'absorption du CO_2 dans des solutions aqueuses d'amines, la condensation cryogénique génèrent de grosses consommations énergétiques. Alors que l'utilisation de procédés membranaires peut baisser ce coût énergétique à un niveau économiquement acceptable.

Nous avons préparé des membranes composites de forme fibres creuses. Les modules fibres creuses ont des très hautes compacités permettant de réduire la taille des installations en intensifiant le transfert. Une couche fine de poly(liquide ionique) (polyLI) gonflée par du liquide ionique a été déposée par photo-greffage à la surface externe des fibres creuses. Cette configuration permet de résoudre à la fois le problème de l'instabilité sous pression des membranes à liquide ionique supportées et celui de la basse perméabilité des membranes denses en poly(liquide ionique).

Dans ce chapitre, les choix des paramètres tel que les solvants, les membranes de supports, les vitesses de filage et la concentration en monomère de la solution de greffage ont été étudiés. Deux fibres creuses composites de polyLI à base d'Oxyplus[®] obtenues montrent respectivement une perméabilité à CO_2 de 613 GPU avec une sélectivité de CO_2/N_2 de 17 et une perméabilité à CO_2 de 724 GPU avec une sélectivité de CO_2/N_2 de 13. Ces valeurs correspondent bien aux calculs basés sur le modèle de résistance en série. Les fibres obtenues sont beaucoup plus perméables que les membranes polymères commerciaux. Le phénomène de plastification n'a pas été observé sur les fibres polyLI-Oxyplus jusqu'à une pression de 7 bar. Une pression transmembranaire moindre est donc nécessaire, permettant une économie sur le coût de compression.

3.1 Introduction

CO₂ removal from post-combustion flue gas streams (CO₂/N₂ separation) plays an important role in mitigating global climate change [58]. And it is becoming more and more important as global energy demand keeps growing and electricity production by fossil fuels (coal, oil, natural gas) combustion remains indispensable for its low price [277]. Pressure swing adsorption, aqueous amine scrubbing and cryogenic condensation are the three primary industrial approaches for gas separation. However, all those methods suffer from high energy and operating cost for refrigeration or regeneration (by heating) of the absorption/adsorption medium [278]. Existing CO₂ capture costs are in the range of 50-60 €/ton. The use of membranes can reduce the energy costs associated with CO₂ separation to 20-30 €/ton [279].

Membranes-based gas separation offers another competitive possibility which may be much more energy saving compared to above-mentioned traditional techniques since the operation of membrane modules only requires a trans-membrane pressure. The large size reduction of the gas separation unit could also decrease the capital cost of the process. Therefore, the application of membranes, with such advantages as small footprint, easy operation and scalability, offers promising perspectives.

There are two main configurations for membrane-based CO₂ capture that do not use a scrubbing liquid: supported liquid membranes (SLMs) and dense selective membrane [60]. Despite very attractive CO₂ permeabilities, SLMs are limited to low differential pressures to avoid blowing the liquid out of the membrane pores. The evaporation of the liquid to the gas phase is another disadvantage of SLMs. Room-temperature ionic liquids (RTILs), organic salts that are liquid at ambient conditions, have been largely studied in many domains, such as electrochemistry, catalysis, analytical chemistry, etc, for their unique properties [280]. Imidazolium-based ionic liquids in general have inherently high solubility and solubility selectivity for CO₂ over N₂. Using RTILs to replace volatile solvents for SLM can solve the evaporation problem thanks to the negligible vapor pressure of RTILs. Whereas, the limit on low pressure differential still remains (burst pressure typically around 1 atm) [281]. Preparation of a dense solid membrane from polymerizable ionic liquids is one approach to overcome this pressure issue. Despite good pressure stability and excellent selectivity, the main drawback of the dense poly(room-temperature ionic liquid) (polyRTIL) membrane consists in the low permeability since the active separation material is no more a fluid, but a solid. Efforts have been made by researchers to combine the advantages of supported ionic liquid membranes and dense polyRTIL membranes and to minimize their shortcomings. Recent solution involves the incorporation of “free IL” into a polyRTIL matrix to form a cross-linked poly(RTIL) gel membrane, whose structure is illustrated in Fig.3.1 [247, 264, 272]. Those polyRTIL-RTIL composite gel membranes demonstrated promising properties as a configuration that both “stabilizes” the liquid RTIL and possesses “liquid-like” CO₂ separation performance.

As permeability is an intrinsic property of the material while the value of permeance is inversely proportional to the membrane thickness, researchers look for an

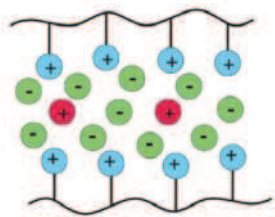


Figure 3.1: Representation of poly(RTIL)-RTIL composite. Red circles are free IL cations, green circles are anions, and blue circles are polymer bound cations.

ultra-thin membrane material in the pursuit of high permeances. However, the decrease of membrane thickness often results in mechanical strength degradation of the membrane. Coating a selective thin layer of the functionalized material on top of a highly permeable support can break this trade-off, maintaining good gas-separation properties without loss in mechanical resistance. The material cost reduction is another advantage of the composite membrane.

With higher surface area to volume ratio, hollow fibers are more interesting than flat sheet membranes in terms of high packing densities (surface/volume ratios). Co-extrusion and dip coating are the most commonly used preparation methods for thin-film composite hollow fibers. Both processes employ a coating solution, with polymer dissolved in a solvent. They are hence not adapted for coating the polyRTIL-RTIL composite gel layer since the polyRTIL-RTIL gel matrix is formed in-situ during the polymerization. The ideal selective layer thickness can be determined as a function of the mass transfer resistance of the selective layer and the support membrane [69].

Our objective is to try for the first time coating a polyRTIL-RTIL gel layer onto a highly permeable hollow fiber support for effective CO_2 capture via a continuous photopolymerization process and to understand the principle of the process, the influence of choice of materials and experimental parameters. The CO_2/N_2 selective polyRTIL-RTIL thin layer studied herein was based on the previous work of T.K. Carlisle *et al.*, while once succeed, the same process can also be applied to other polyRTILs-RTIL gel polymers, useful not only for gas separation but also for other potential applications such as antistatic agents [282] and electrolytes for lithium ion batteries [283, 284].

3.2 General Information

3.2.1 Ionic liquids concerned and their gas permeability

The ionic liquids used for membrane modification are as shown below (Fig.3.2). The cross-linker **b** was added to better retain liquid RTIL **c** in cross-linked polyRTIL network. The monomer solution used during photo-grafting was prepared by dissolving **a**, **b** and **c** at different compositions in solvents (ethanol, acetone, acetonitrile, ethyl acetate, etc.) at varied concentrations. The photo-initiator 2-hydroxy-2-methylpropiophenone

was added to the solution at 1%wt of total ionic liquid mass. Pure gas permeabilities and ideal selectivities at different compositions were tested on a flat-sheet membrane made from RTIL **a**, **b** and **c**, (see Table. 3.1, previously reported by T.K. Carlisle [9]). Membrane compositions given in the table (and throughout this chapter) are identified as X-Y, where X is the mol% of **b** out of total monomer (**a** and **b**), and Y is the wt.% of **c** out of the total mass of **a**, **b** and **c**. Besides the compositions listed in Table 3.1, other compositions were also tested for photo-grafting on hollow fibers, specified in the Results part using the same naming rule.

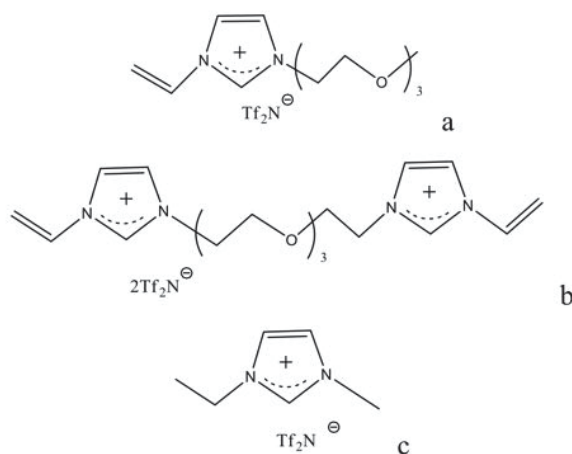


Figure 3.2: Ionic liquids used for photo-grafting.

Table 3.1: Gas permeability properties measured on a flat sheet membranes prepared from RTIL **a**, **b** and **c** at different compositions

Membrane [*]	$\text{Pe}(\text{CO}_2)$ / barrer	$\alpha(\text{CO}_2/\text{N}_2)$
40-65	470 ± 20	37
60-65	430 ± 20	37

^{*} Membrane compositions expressed as mol% of **b** out of total monomer–wt.% of **c** out of the total mass of **a**, **b** and **c**.

3.2.2 Support membranes

Four support membranes were tested. Their specifications are given in Table 3.2. In all gas permeation tests, gases were fed to the shell side of the module.

Table 3.2: Specifications of the four hollow fibers tested

Membrane type	Material	Pore size
MicroPES [®]	Polyethersulfone	0.2 μm (nominal)
Oxyphan [®]	Polypropylene	0.2 μm (maximum)
Oxyplus [®]	Polymethylpentene	dense surface
Teflon AF covered	Polytetrafluoroethylene	dense surface
Oxyphan [®]	Polypropylene compo- site membrane	

3.2.3 UV Lamp and optical filter type

The two UV lamps can both be adjusted from 60% to 110% of the nominal power. The regulation of lamp power depends on fiber velocity, which determines the residence time of hollow fibers inside the UV reactors. The UV lamps should be appropriately adjusted to provide sufficient energy within the residence time, but not in large excess. Lamps set at high powers also emit more heat, which can cause mechanical property deterioration or even breaking of the fiber. UV energy intensity of the lamps set at different powers was previously measured, permitting us to evaluate quantitatively the total UV energy received by the fiber moving at a certain velocity (see Chapter II. section 2.1).

Lamp and filter type were chosen according to the UV absorption spectra of the photo-initiator — 2-hydroxy-2-methylpropiophenone (Fig.3.3). Mercury (H) lamp (used in this work) has advantages over Iron (F) lamp for its higher emission around 250 nm (ca. 22 W/nm for H lamp and 8 W/nm for F lamp, Fig.3.4). In fact, the radical polymerization rate R is proportional to the square root of the molar source of photons I_a :

$$R = k_p C \sqrt{\frac{\phi I_a}{k_t}} \quad (3.1)$$

with ϕ as quantum yield, k_p as propagation coefficient and k_t as termination coefficient. Hence, the polymerization rate can be 1.7 times faster using H lamp instead of F lamp. The quartz filter was chosen over pyrex and glass filter for the same reason. Among the three filters available, only quartz filter lets through radiation in the UVC range (200-280 nm).

3.3 Influential factors in photo-grafting and composite membrane performance

With the objective to coat an ultra-thin polyRTIL-RTIL gel layer on a hollow fiber support by photo-grafting method, we found in the course of experiments that the a lot

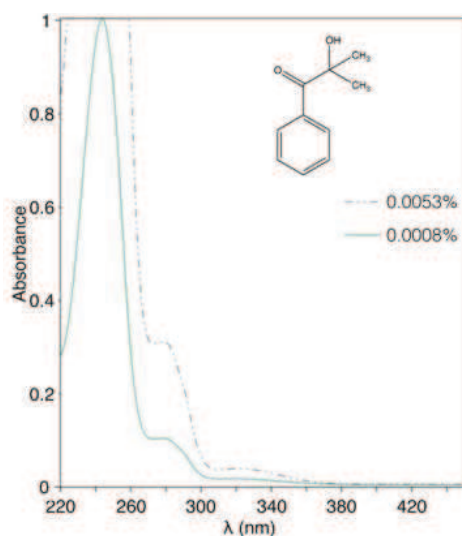
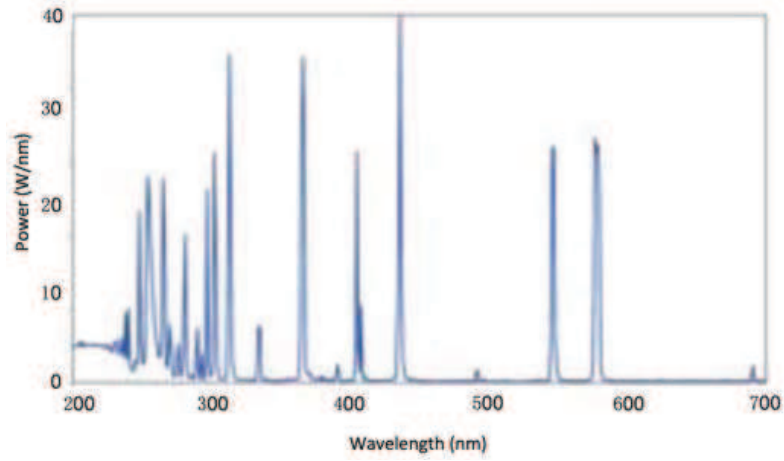


Figure 3.3: UV absorption spectrum of 2-hydroxy-2-methylpropiophenone [285].

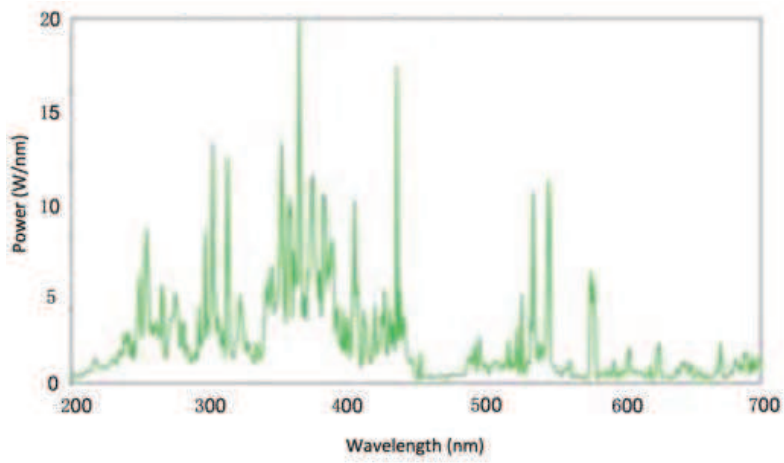
of parameters (e.g. support membrane material, fiber velocity, grafting solution concentration and composition) have influences on the properties of the final composite membranes obtained by photo-grafting. Effect of those parameters are analyzed case-by-case in the following parts.

3.3.1 Compatibility between the support membrane and the grafting solution — General considerations on solvent choice

PES is a heat-resistant polymer that remains in satisfactory condition without causing decline in flexural modulus at temperatures of up to nearly 200°C [286]. It is also photo-sensible, generating free radicals under UV irradiation. This allows the polyRTIL layer to attach to PES support by covalent bonds (see Chapter I). Our group has successfully grafted poly(acrylic acid) on PES for catalytic membrane applications [139]. However, attempts to graft polyRTIL onto PES did not succeed. The photo-grafting was carried out on water soaked MicroPES[®] using a 40%wt ionic liquid solution (composition 40-65) with ethanol as solvent. The hollow fiber became physically fragile after the photo-grafting. Numerous cracks were observed on the grafted membrane surface (Fig. 3.5), leading to the mechanical degradation of the fiber and non-selectivity for gases. The Young modulus of the fiber after modification (measured through tensile test) decreased to around 10% of that of the virgin fiber. The breaking energy change in the hollow fiber is shown in Figure 3.6. Virgin MicroPES[®] fibers were soaked in ethanol and the ionic liquid monomer solution for 1 h and tested wet for tensile analysis. The mechanical properties were basically not influenced by ethanol whereas the ionic liquid solution brought out an obvious mechanical deterioration of the membrane, due to partial dissolution of MicroPES[®] in IL-ethanol solution. The dissolution should have been



(a) H lamp



(b) F lamp

Figure 3.4: UV spectra of (a) H (Mercury) and (b) F (Iron) lamp.

largely accelerated under heat and UV irradiation during the photo-grafting process, which explains the abrupt decrease in the breaking energy for grafted PES. Actually, PES is affected by polar solvents. Ionic liquids, as moderately polar molecules that have to be dissolved in polar solvents [287]. The ionic liquid solution, therefore, behaves as a polar liquid that can swell or dissolve the PES membrane. For this reason, MicroPES[®] by its nature gives few possibilities to be applied in the photo-grafting based on the ionic liquids herein.

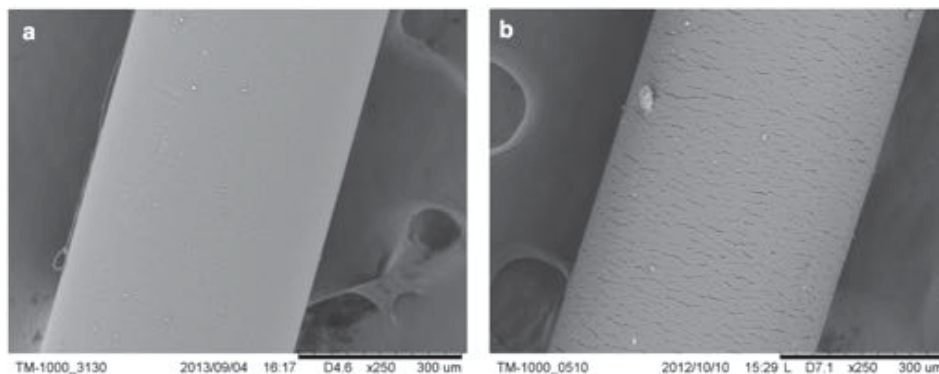


Figure 3.5: SEM images of a) virgin PES surface; b) grafted PES surface.

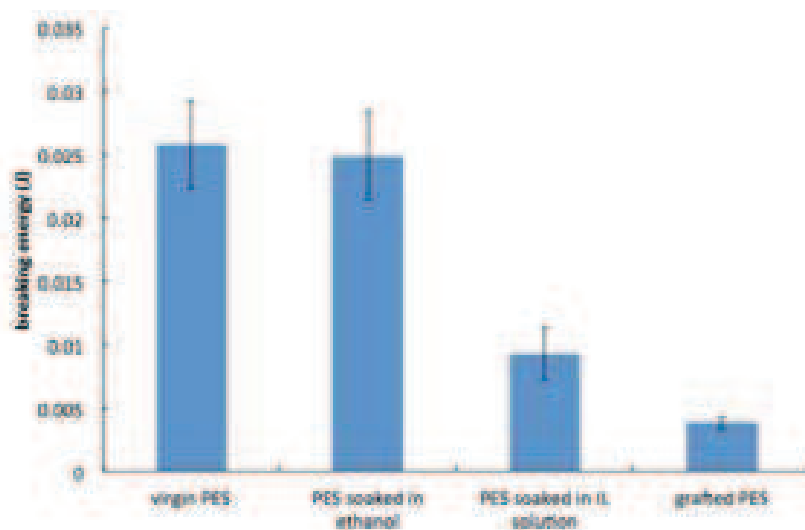


Figure 3.6: Breaking energy of differently treated PES fibers.

The fact that both the ionic liquids and the solvent chosen are compatible with the support membrane does not necessarily ensure that the membrane will remain intact when treated by the ionic liquid solution. As an example, when running photo-grafting on Oxyphan[®] fiber, three modifying solutions were tried. Results listed in Table 3.3 show that changing either the solute (entry 1 and 2) or the solvent (entry 2 and 3) can

bring about a dramatic change in the final aspect of the hollow fiber. When Oxyphan[®] fiber began to be solubilized by the modifying solution, the fiber melted and broke under the heat emitted by UV lamps (entry 2, Table 3.3). Therefore, to choose the right solvent, ILs and the support membrane should be considered as a whole.

Table 3.3: Fiber status after photo-grafting using different modifying solutions

	Solute	Solvent	Fiber status after the photo-grafting
1	Ionic liquid a , b and c	Ethyl acetate	Intact
2	Polymerized ionic liquid a	Ethyl acetate	Broken immediately under UV irradiation
3	Polymerized ionic liquid a	Ethanol/Acetone (77/23 wt.)	Intact

Hansen solubility parameters (HSPs) predict if one material dissolves in another [288]. Each material is attributed four Hansen parameters: δ_d (energy from dispersion forces between molecules), δ_p (energy from dipolar intermolecular force between molecules), δ_h (energy from hydrogen bonds between molecules), and an interaction radius R_0 . When the distance of interaction between two substances R_a is inferior to the interaction radius of the substance being dissolved R_0 , then it is soluble in the other substance. R_a is calculated by Equation 3.2.

$$R_a = \sqrt{4(\delta_{d2} - \delta_{d1})^2 + (\delta_{p2} - \delta_{p1})^2 + (\delta_{h2} - \delta_{h1})^2} \quad (3.2)$$

Hansen solubility parameters for mixtures can be calculated as the weighted average of the volume percent of the components.

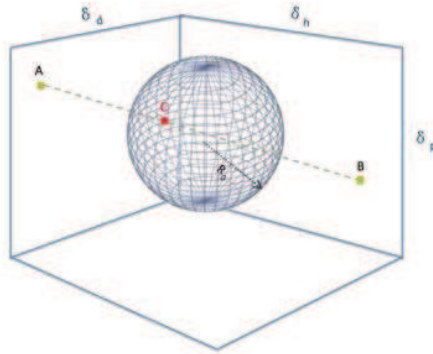


Figure 3.7: Hansen parameters presented in Hansen space.

HSPs can be presented in a 3D chart as Fig.3.7. It is noteworthy that two components both with a large HSP distance, in other words, poor solubilizing capability, like point

A and B in Figure 3.7, may be effectively dissolving if mixed together (assuming they are miscible) (point C, Fig.3.7).

The solubility issue is only one aspect of consideration. General criteria concerning the choice of solvent are summarized as follows:

1. The solvent dissolves well the ionic liquids.
2. The monomer solution (solvent+IL) does not dissolve or swell the support membrane so that the modification by monomer solution would not cause membrane degradation.
3. The solvent has an appropriate boiling point—A high boiling point helps to protect the hollow fiber from heat emitted by the UV lamps (heat taken up by solvent evaporation). The temperature of evaporation has also an influence on polymerization kinetics [274]. The boiling point should not be too high either ($<200\text{ }^{\circ}\text{C}$). Otherwise the fiber may remain wet at the exit of the lamps.
4. The solvent should have a good wettability on the support membrane surface (see section 3.3.3).
5. The solvent should preferably have a low toxicity preferably.

3.3.2 Diffusion of the monomers into the support membrane pores — Oxyphan[®] as support membrane

Compared to PES fiber, Oxyphan[®] fiber possesses better resistance towards polar solvents, making it more suitable for IL-based photo-grafting. Tests were carried out on Oxyphan[®] using 30%wt of ionic liquid dissolved in 77.5%wt acetone water solution (IL composition of 53-25) and 35%wt IL—ethyl acetate (IL composition of 40-65) as monomer solution. Oxyphan[®] fiber was soaked in deionized water (in the case of IL-acetone solution) and in ethyl acetate (in the case of IL-ethyl acetate solution) respectively prior to photo-grafting. The Oxyphan[®] fiber suffered a substantial drop in permeability (see Table 3.4) after photo-grafting while the CO_2/N_2 permeability selectivity remained almost unchanged (≈ 1 , same as the virgin Oxyphan[®] fiber). The permeance values in Table 3.4 were measured below a transmembrane pressure of 3 bar. Above 3 bar (pressure exerted on shell side), the permeability increased irreversibly with pressure augmentation, might be due to the displacement of polyRTIL inside the membrane pores under higher pressures. SEM analysis showed that membrane pores were not completely covered by polyRTIL, leading to the non-selectivity of the modified hollow fiber towards CO_2 (see Figure 3.8).

Table 3.4: CO_2 permeability of virgin and modified Oxyphan[®] fiber

	Virgin Oxyphan [®]	polyRTIL-modified Oxyphan [®]
Pe(CO_2) (gpu)	8250	10-58

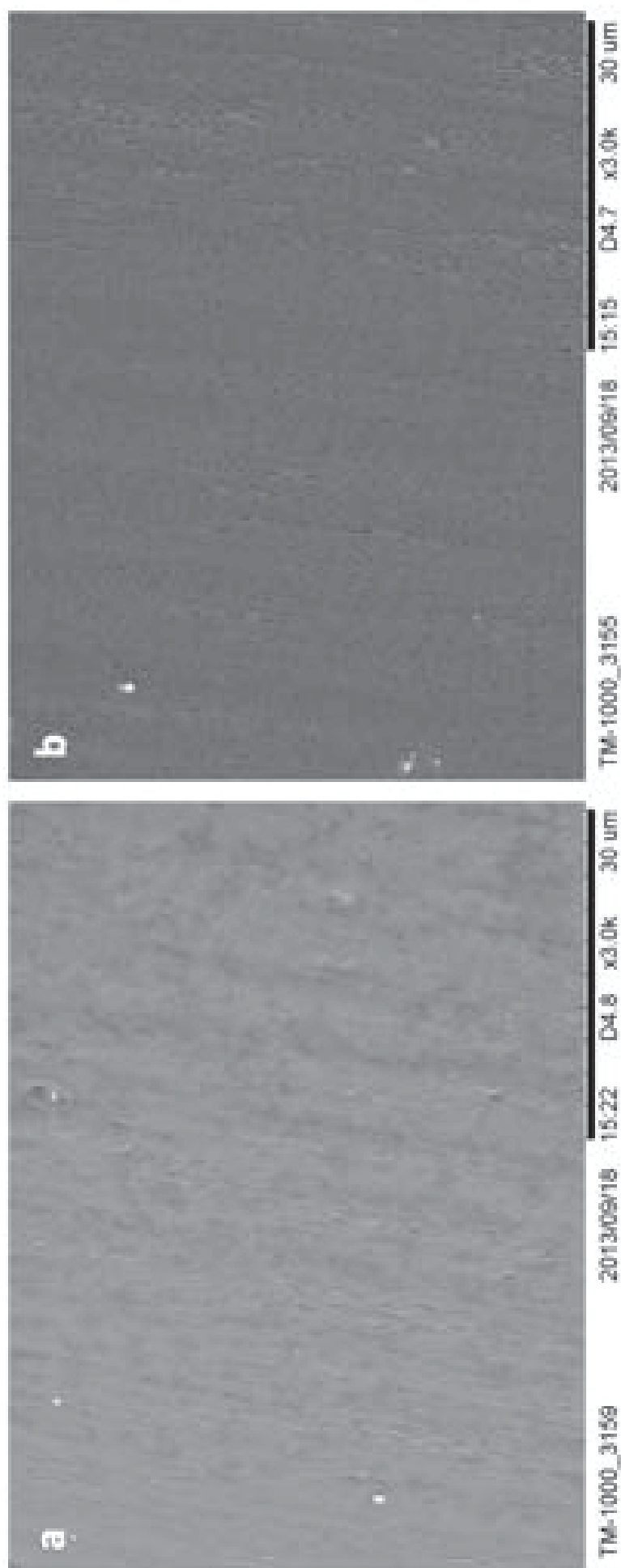


Figure 3.8: SEM images of a) polyRTIL-modified Oxyphan® surface (obtained using 35%wt IL-ethyl acetate solution at fiber velocity of 15 m/min, with one UV lamp at turned on at 60% of its nominal power) and b) virgin Oxyphan® surface.

Assuming that a quasi-uniform polyRTIL layer was formed on the surface of the Oxyphan[®] support, as illustrated in Figure 3.9. Then theoretically, a dense top layer



Figure 3.9: Schematic representation of pore size reduction after the photografting: polyRTIL layer in blue and support membrane in gray, e representing the graft layer thickness.

with a thickness at least of half the initial pore size should be able to cover the support membrane pores and lead to a dense-surface composite membrane. As Oxyphan[®] has a maximum pore size of $0.2 \mu m$, a polyRTIL layer thicker than $0.1 \mu m$ should be able to cover the support membrane pores. The theoretical permeance of the two-layer composite membrane can be calculated using a resistance-in-series model (Equation 3.3). The ideal selectivity $Pe_{AB}(CO_2)/Pe_{AB}(N_2)$ can be deduced through calculations of CO_2 and N_2 permeance.

$$\frac{1}{Pe_{AB}} = \frac{1}{Pe_A} + \frac{1}{Pe_B} = \frac{e}{P_A} + \frac{1}{Pe_B} \quad (3.3)$$

with Pe_{AB} , Pe_A , Pe_B as respectively the permeance of the composite membrane, the polyRTIL layer and the support Oxyphan[®] membrane (in gpu), P_A as permeability of the polyRTIL layer (in barrer) and its thickness (in μm).

According to the calculation, a thickness of $0.1 \mu m$ of the polyRTIL leads to a permeance of 2994 gpu for the composite membrane, 50 - 300 times higher than the experimental values. Vice versa, the calculated thickness of the polyRTIL layer deduced from the experimentally measured permeance is approximately $20 \mu m$. But in reality, no obvious polyRTIL top layer was observed on SEM images of the membrane cross-section. The large deviations of experimental results from theoretical calculations are caused by severe diffusion of the monomer solution into Oxyphan[®] membrane pores during the grafting under capillary effect. As a result, the ionic liquid monomers polymerized not only on the surface of the support membrane but also inside the pores, causing a very large drop in permeance. The obtained composite membrane was more like a polymer blend rather than a two-layered membrane. Generally speaking, for a porous membrane, the largest pores have much more impact on the permeability than other smaller pores. Therefore, for the obtained polyRTIL-Oxyphan composite membrane, the size reduction of larger pores should be more responsible for the permeance drop than the blockage of smaller pores. In this study, solute molecules smaller than the pore size, low viscosity of the monomer solution ($\approx 1.5 \times 10^{-3} \text{ Pa}\cdot\text{s}$ at 20°C) and high sorptivity of the membrane towards the IL monomer solution should all be responsible for the significant capillary phenomenon and severe penetration of the IL inside the support membrane pores. In fact, pre-soaking of the support membrane in water or in solvent prior to photo-grafting

was to mitigate the capillary action. Despite the pre-soaking, the obtained composite membrane still suffered a low permeance. In contrast, monomer solution diffusion into the support membrane was much less remarkable when using acrylic acid (AA) as monomer and MicroPES[®] as support [139]. There should be a competition between the polymerization and diffusion kinetics during the photografting process. Once the support membrane enters the monomer bath and gets into contact with the solution, the diffusion starts. When the fiber is pulled out the bath, a liquid film is entrained on the membrane surface and the diffusion continues. As the membrane passes through the UV lamps, the polymerization and the diffusion occurs simultaneously. A fast polymerization can therefore effectively stop further diffusion by ‘solidifying’ the liquid. And vice versa, a slow polymerization means that polymers are more likely to be really in the support membrane than on the outer surface. The ionic liquid monomers that we used polymerize much slower than AA does, leading to more severe solution diffusion into the membrane than in the case of AA. As mentioned above, the polymerization rate is proportional to the square root of photon source intensity, determined by lamp power. And the grafting quantity increases with the total UV energy (product of lamp power intensity and fiber residence time in the UV reactors) received by the fiber. Table 3.5 shows that at a fixed velocity, higher power of the bottom lamp led to higher permeances (entry 3 and 4 compared to entry 1, 2 and 5.), with either total power of the two lamps (entry 4 and 5) or the upper lamp power (entry 1 and 3, 2 and 4) being the same. This is reasonable since it is the lower lamp that plays the role of diffusion inhibition.

Table 3.5: Permeance of polyRTIL-Oxyphan composite fiber obtained under varied UV energy at fiber velocity of 15 m/min (30%wt IL solution with composition 53-25) .

Entry	Lamp power		Permeance gpu
	lower lamp (percentage of the nominal power, %)	upper lamp	
1	85	60	11
2	85	85	32
3	110	60	42
4	110	85	36
5	85	110	29

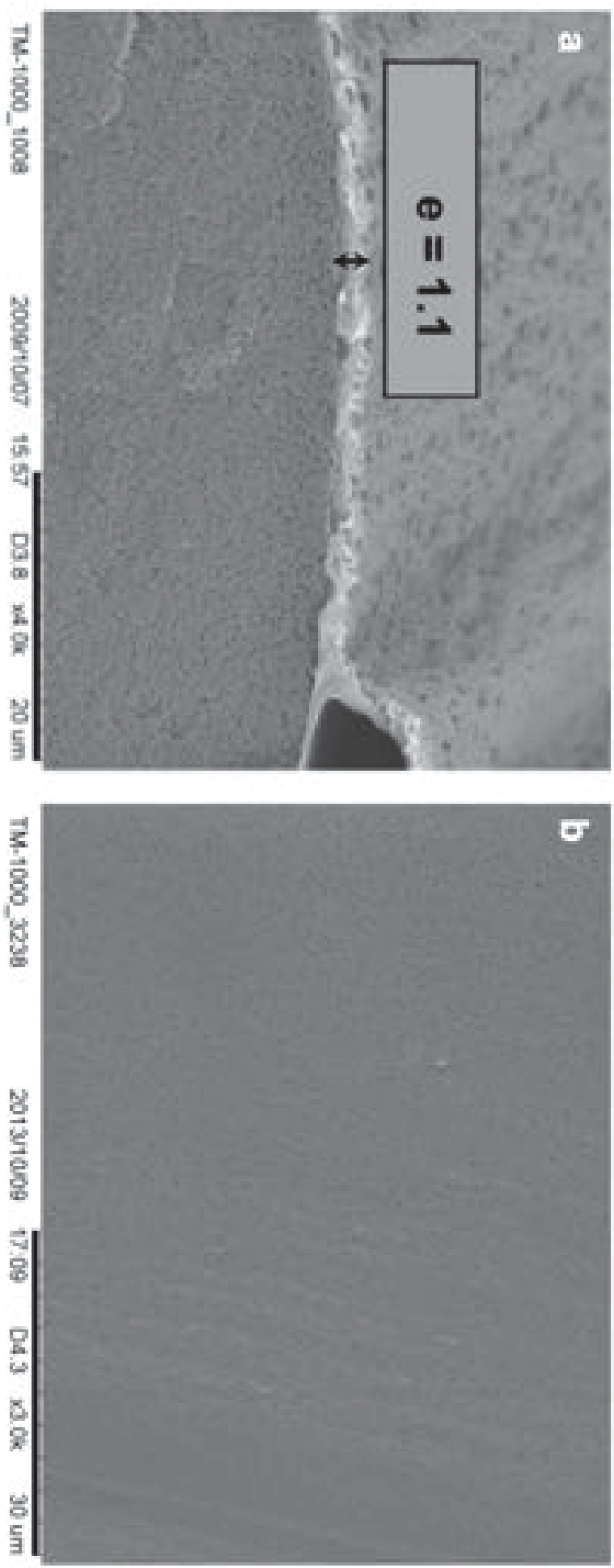


Figure 3.10: SEM images of Teflon covered Oxyphane: (a) cross-section [69]; (b) outer surface.

3.3.3 Wetting of the support membrane surface — Teflon AF covered Oxyphan as support membrane

A Teflon AF covered Oxyphan fiber was previously reported for the application of membrane contactor [69]. A dense Teflon top layer with a thickness of 1.1 μm was obtained via the same photo-grafting process using a Teflon/Fluorinert polymer solution. The UV irradiation only serves to evaporate the solvent. No polymerization was involved. Its cross-section and surface were as shown in Figure 3.10.

The Teflon AF covered Oxyphan was highly permeable ($\text{Pe} \approx 2400$ gpu). Thus it will constitute little mass transfer resistance for the composite membrane when using as the support layer, giving rise to the good performance of the composite membrane both in terms of high permeance and high selectivity. Besides, its dense surface also avoids the penetration of monomer solution inside the support membrane pores.

The ionic liquid monomer solution was prepared in ethyl acetate at a concentration of 35%wt with composition 60-65. Various conditions were tested, as listed in Table 3.6. A slight increase in CO_2/N_2 selectivity was achieved only at the velocity of 8

Table 3.6: Experimental conditions (fiber velocities and lamp powers) and corresponding fiber properties for IL photo-grafting on Teflon covered Oxyphan

entry	Fiber velocity (m/min)	Lamp power ^a (%)	Pe (CO_2) gpu	α (CO_2/N_2)
1	8	65	2324	4.5
2	10	65	2328	3.5
3	13	60+60	1441	3.9
4	17	100	1311	3.6
5	17	65+65	1570	3.8

^a total power of the two lamps, expressed in percentage of the nominal power.

m/min (from 3.5 for non-modified Teflon covered Oxyphan to 4.5 for IL modified fiber), accompanied by very little decrease in permeance (entry 1). For other fiber velocities, CO_2/N_2 selectivity remained the same as the support fiber. The SEM image of the surface of the fiber modified at 8 m/min (Fig.3.11-a) shows that the support membrane surface was almost totally covered by polyRTIL except some defects. It should be those defects that lowered the CO_2/N_2 selectivity to the same level as support membrane. Besides, formation of some ‘mini-droplets’ was observed on the surface (Fig.3.11-a), implying a partial wetting of the Teflon fiber by ionic liquid monomer solution and thus a non-homogeneous dispersion of polyRTIL on the surface. Fig.3.11 also indicates that the coverage of the support fiber by polyRTIL became worse when fiber velocity increased due to the poor-wettability of the support membrane surface by the monomer solution. In addition, high surface roughness was observed for some zones of the Teflon AF covered Oxyphan. Those zones are prone to defects owing to non-homogeneous entrainment of the liquid film (Fig.3.12).

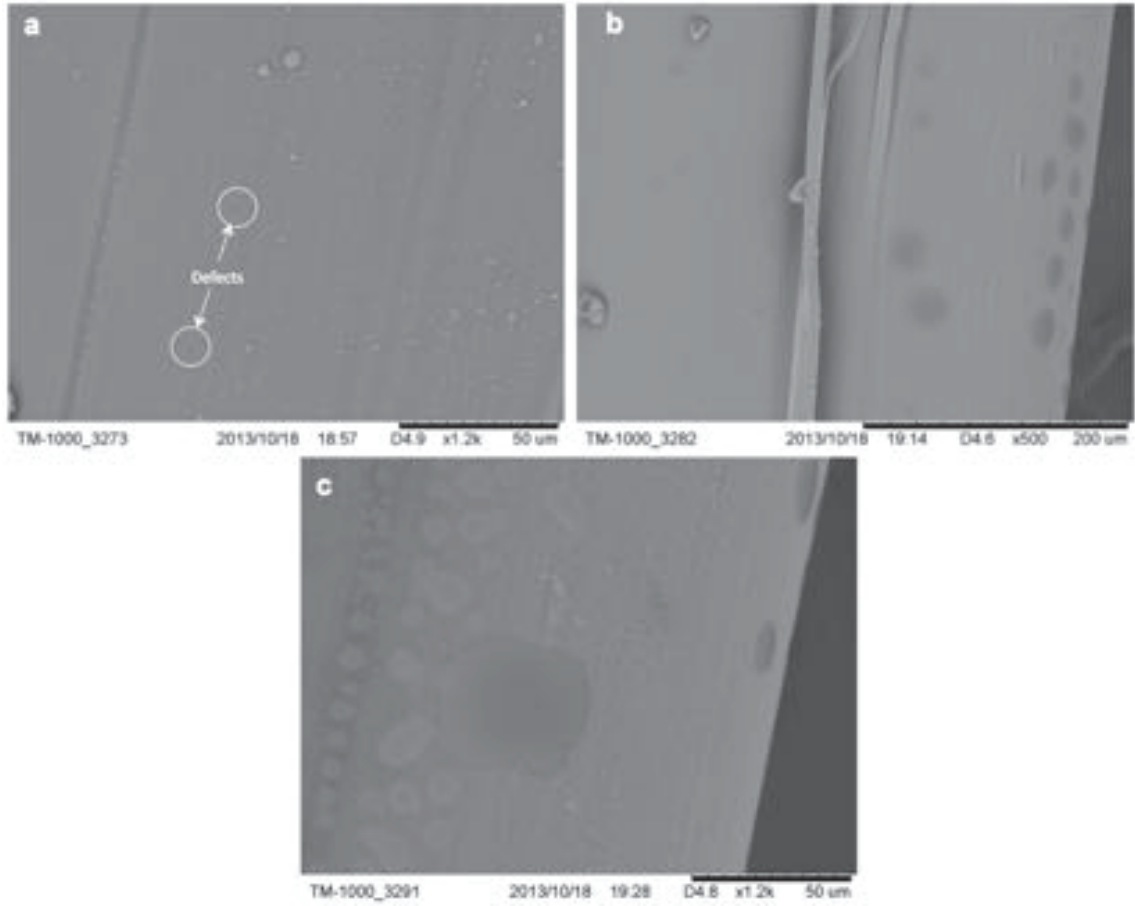


Figure 3.11: SEM images of the surface of Teflon covered Oxyphan after polyRTIL based photo-grafting obtained at varied fiber velocities: a) $v=8$ m/min, $P_{UV}=65\%$; b) $v=13$ m/min, $P_{UV}=60\%+60\%$; c) $v=17$ m/min, $P_{UV}=65\%+65\%$

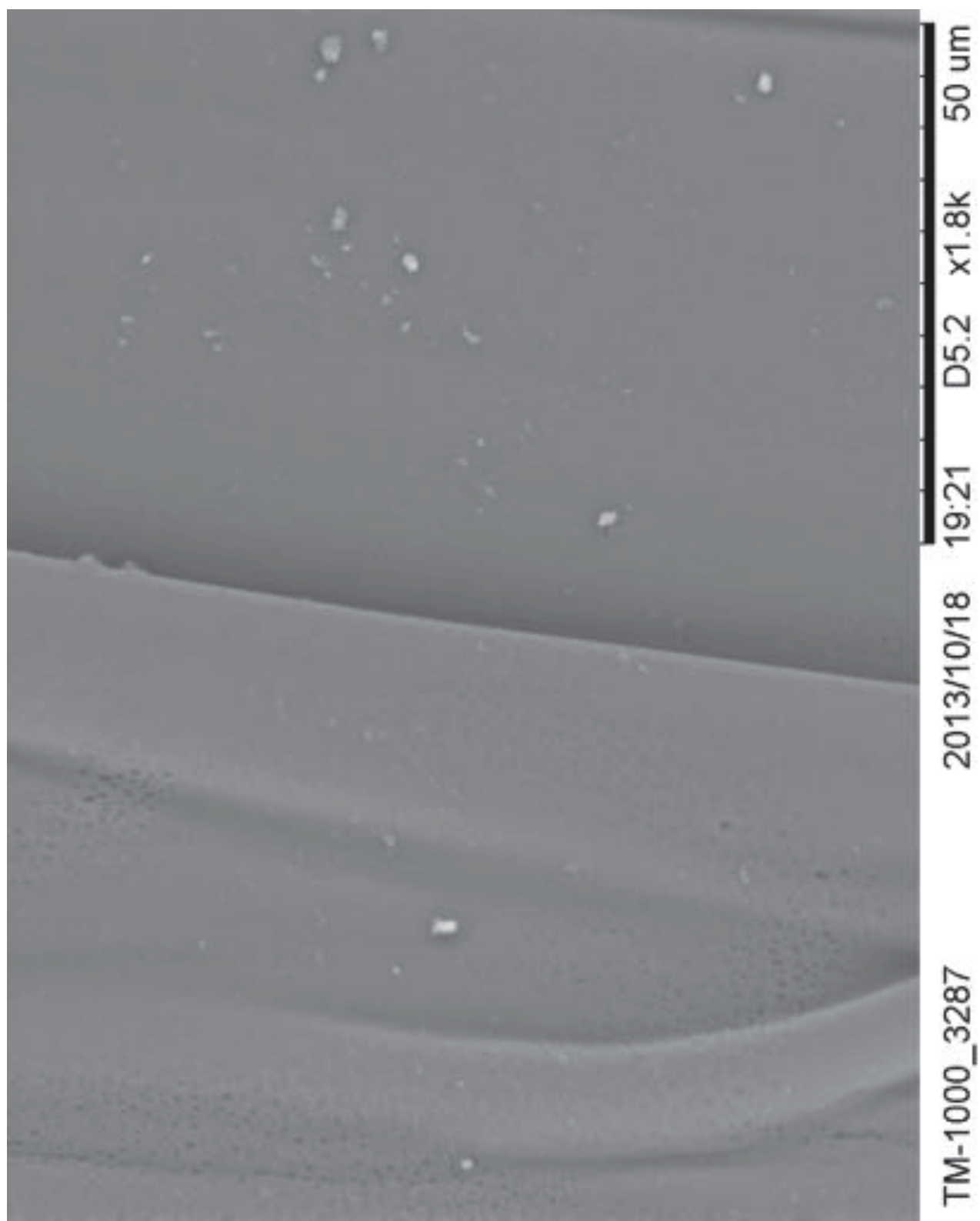


Figure 3.12: SEM image showing defects in the zones with high roughness (Teflon covered Oxyphane modified by polyIL)

Qu  r   shows that the mode of entrainment of the liquid film can be predicted, depending on the Capillary number (Ca) and Weber number (We) [289]:

$$Ca = \frac{\mu v}{\gamma} \quad (3.4)$$

$$We = \frac{\rho v^2 r_f}{\gamma} \quad (3.5)$$

where r_f is the fiber radius (in m), μ is the dynamic viscosity of the monomer solution (in Pa  s), v is the fiber velocity (in m/s), γ is the surface tension of the monomer solution (in N/m) and ρ is the liquid density (in kg/m³).

The above parameters of the ionic liquid solution were measured and given in Table 3.7. Thus, with fiber velocity $v \leq 17 \text{ m/min}$, $Ca \leq 0.016$, $We \leq 0.64$.

Table 3.7: Properties of the IL monomer solution and Teflon AF covered Oxyphan fiber radius

γ^a mN/m	ρ^b g/cm ³	μ^c mPa��s	r_f μm
25.69	1.08	1.47	190.5

^a measured at 24.5  C.

^b measured at RT.

^c measured at 20  C.

When both Ca and We are inferior to 1, it concerns the visco-inertial regime. And the liquid film thickness entrained (e) can be calculated by Equation 3.6 [289].

$$e = \frac{r_f Ca^{2/3}}{1 - We} \quad (3.6)$$

The entrained liquid thickness increase as a function of fiber velocity is plotted in Figure 3.13. Meanwhile, increase of fiber velocity also resulted in a shorter residence time of the fiber inside the UV lamps and less UV energy absorbed. In consequence, there exists the risk at higher velocities that the thick liquid film entrained out of the monomer bath does not fully polymerize under limited UV energy. And the non-wettability can make the situation even worse. Lamp power intensity divided by the liquid film thickness (in $\mu\text{W}/\mu\text{m}^3$) was used to quantify the UV energy received by the liquid film during the photo-grafting, which decreases with fiber velocity (Fig.3.13). Fig.3.11-c evidenced the presence of many non-polymerized liquid drops on the fiber surface obtained at $v=17 \text{ m/min}$ due to non-sufficient UV irradiation.

Failure to obtain a fiber with high selectivity towards CO₂ with Teflon covered Oxyphan and formation of defects are probably due to low wettability of Teflon by the ionic liquid monomer solution and the surface roughness of the fiber surface (Fig.3.10,

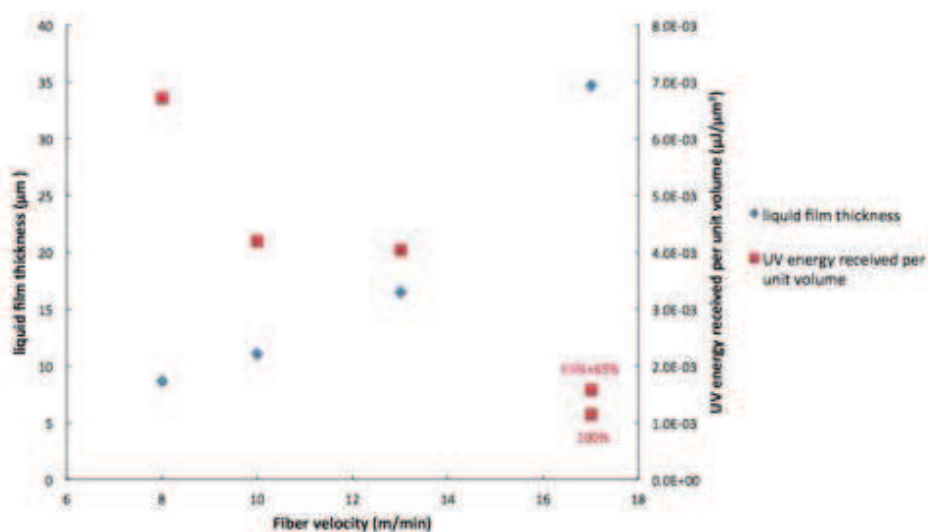


Figure 3.13: Liquid film thickness and UV energy received by per unit volume as a function of fiber velocity. (At $v=17$ m/min, two data points are presented, corresponding to UV lamp power at 100% and 65%+65% (Table 3.6). Only UVB and UVC were taken into account for the UV energy calculation here because the absorption band of the photo-initiator is below 300 nm.)

3.12). The poor wettability can lead to the high tendency of droplet formation (once the fiber was entrained through the monomer solution). The liquid film thickness would become locally thicker. The membrane is hence more likely to suffer from incomplete polymerization. Changing the solvent (from ethyl acetate to a better wetting one, e.g. fluorinated solvents) and other parameters may improve the situation. Teflon-Covers Oxyphan is consequently still a possible candidate.

3.3.4 Gas separation performance and influence of monomer concentration and fiber velocity — Oxyplus® as support membrane

Gas separation performance

Oxyplus® is an integral asymmetric hollow fiber made of the thermoplastic polymer polymethylpentene which has a glass transition point around 30 °C and a high melting point (>200 °C). Polymethylpentene has excellent chemical resistance and low moisture absorption. The external dense surface of Oxyplus support makes it easier to get a dense defect-free poly(ionic liquid) coating. In fact, much better results were obtained compared to the three hollow fibers above.

First photo-grafting on Oxyplus® was carried out using a 38%wt IL solution (composition 40-65), with ethyl acetate as solvent. When two lamps were turned on together, fiber became very thin. Since Oxyplus® is a thermoplastic polymer, the elongation should be due to stretching under the heat of lamps in the presence of a swelling solu-

tion. Fibers that remained at roughly the initial diameter were obtained using the lower lamp alone at velocities of 8 m/min (lamp power of 65%) and 17 m/min (lamp power of 85%).

To tackle the stretching problem, a better adapted solvent should be used. Hansen solubility parameters and interaction radius of Oxyplus[®] fiber and IL mixtures (at the composition used for photo-grafting (40-65) were deduced using HSPiP software based on their solubility in various solvents tested at room temperature. Results are presented in Table 3.8. It needs to be mentioned that at the temperature inside the UV reactors (equaling to the solvent evaporation temperature [274]), the HSPs will deviate from the values obtained at RT, especially the interaction distance R_0 , which increases with temperature [290]. This means that monomer solutions showing a R_a slightly larger than the interaction distance R_0 of the support membrane at RT may induce swelling phenomenon during the photo-grafting as well. Solvents listed in Table 3.8 are some of the possible candidates that can dissolve IL without degrading the Oxyplus[®] (ethyl acetate is also included in the table). The boiling points of those solvents are in the range of 60 - 100 °C. The relatively short distance between Oxyplus[®] and ethyl acetate reasonably explains the severe stretching of the fiber observed. Apparently, distances between IL monomer solution and the Oxyplus[®] fiber were greatest while using methanol and acetonitrile as solvents. Acetonitrile was eventually chosen for its higher boiling point, which can protect the fiber better from heat during the photo-grafting.

Table 3.8: Hansen parameters for Oxyplus[®], IL mixture (composition 40-65) and solvents and interaction distance (R_a) between the IL solution and the fiber determined at room temperature

	δ_d	δ_p	δ_h	R_0^a	R_a (IL+solvent)/Oxyplus [®]	Bp (°C)
	MPa ^{0.5}					
Oxyplus [®]	17.7	1.4	2.6	7.1	-	-
IL monomer mixture (40-65)	15.0	18.8	7.6	16.1	-	-
Acetonitrile	15.3	18.0	6.1	-	17.9	82
Ethyl acetate	15.8	5.3	7.2	-	9.6	77
Methanol	14.7	12.3	22.3	-	21.2	65
THF	16.8	5.7	8.0	-	9.6	66

^a Calculated for the IL solutions at 25% volume fraction, corresponding approximately to a concentration of 38%wt.

The second photografting on Oxyplus[®] was therefore carried out with a 35%wt acetonitrile solution (composition 40-65). No more severe stretching was observed this time even with two lamps on. Fiber with good CO₂/N₂ selectivity was successfully prepared at velocity of 10 m/min with lamp power at 65% (Table 3.9).

The ATR-FTIR spectroscopy analysis shows the appearance of new absorption

bands for the grafted fiber. (Fig.3.14) The absorption at 1577 cm^{-1} and 1541 cm^{-1} correspond to imidazolium ring in-plane stretching. Absorption bands below 1500 cm^{-1} are mainly assigned to the vibrations of bis (trifluoromethylsulfonyl) imide anion: 1350 cm^{-1} associated with SO_2 asymmetric stretching; 1230 cm^{-1} and 1198 cm^{-1} assigned respectively to the symmetric and asymmetric stretching of CF_3 . The other absorption band at 1059 cm^{-1} is probably SNS asymmetric stretching with contribution from a ring in-plane asymmetric stretching and a CC stretching. These characteristic bands show the coverage of the hollow fiber surface with the ionic liquids. The penetration depth (d_p) of the evanescent wave in the ATR-IR analysis can be estimated by Eq.3.7 and found to be $1.27\text{ }\mu\text{m}$. The PES virgin membrane absorption bands were observed for all modified membrane samples. This is to say that the polyIL layer obtained on Oxyplus[®] membrane is thinner than $1.27\text{ }\mu\text{m}$, coherent with the measured values (table 3.9).

$$d_p = \frac{\lambda}{2\pi n_1 \sqrt{\sin^2 \theta_i - (n_2/n_1)^2}} \quad (3.7)$$

with λ as the wave length , n_1 as refractive index of the diamond crystal sample support (2.4 [291]), n_2 as the refractive index of the sample. The refractive index of polyILs that we used is unknown. An average value of 1.5 was taken for calculations [292–294]. θ_i is the angle of incidence (45°).

Figure 3.15 shows SEM images of fiber cross-section and surface after grafting. The surfaces of all grafted fibers, independent of the solvent used, are all alike, indicating a homogenous dispersion of polyRTIL on the support membrane surface. Oxyplus[®] virgin fiber has already a thin dense top layer whose thickness was measured to be $152 \pm 32\text{ nm}$. The polyRTIL layer could not be distinguished from the top layer of the virgin support membrane from SEM observation. The thickness of the polyRTIL-RTIL layer was therefore deduced by subtracting the Oxyplus[®] top layer thickness from the total thickness of the dense layer (see Table 3.9).

The theoretical CO_2 permeance and CO_2/N_2 selectivity in Table 3.9 was calculated using the resistance-in-serie model (Equation 3.3, the CO_2 permeance and CO_2/N_2 selectivity of the virgin membrane are respectively 1150 gpu and 1.8). The calculated permeance and selectivity values are in good agreement with the experimental values at velocity 10 m/min and 17 m/min, but not at 8/min. When ethyl acetate was used as solvent, the IL solution has a shorter Hansen distance towards Oxyplus[®]. As a result, the Oxyplus[®] support membrane may suffer from slight melting at a low fiber velocity (since a low velocity means a longer residence time in the UV reactor and more heat absorbed from the lamp), which can altered the porosity and permeability of the support membrane. This is probably why a permeance lower and a selectivity slightly higher than theoretical prediction were observed under the condition $v = 8\text{ m/min}$. Compared to the composite membrane obtained at $v = 8\text{ m/s}$, the other two polyRTIL-Oxyplus composite fibers were of more interest for their higher CO_2 permeances and CO_2/N_2 selectivity.

The mechanical properties of those two fibers were also studied (see Table 3.10). The modification did not cause obvious mechanical degradation for the grafted fiber obtained at 10 m/min with acetonitrile as solvent. Whereas, stress and strain elongation

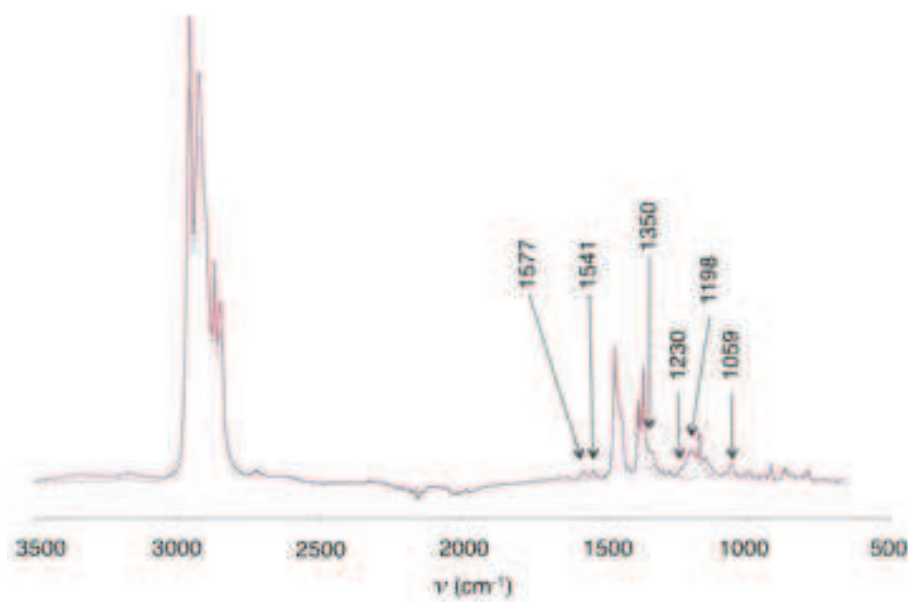


Figure 3.14: ATR-FTIR spectra of virgin Oxyplus® (dotted line) and grafted Oxyplus® with ACN as solvent at 10m/min (continuous line)

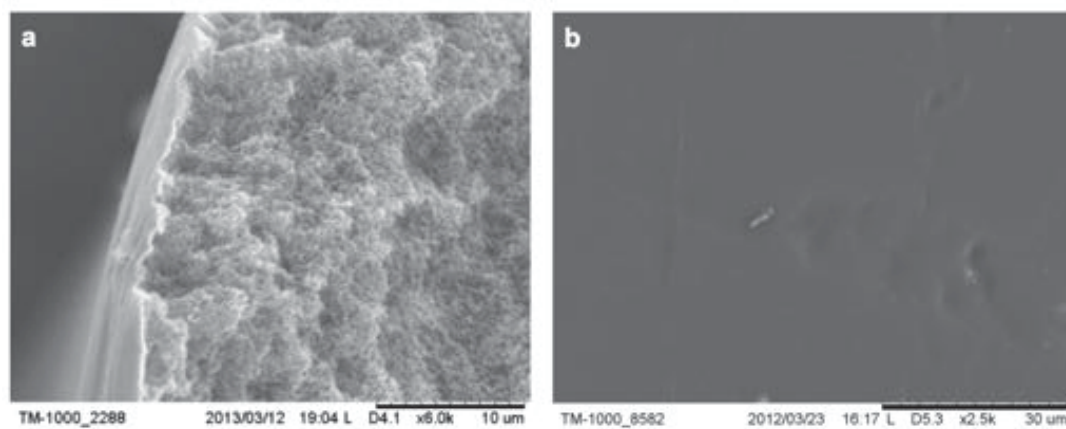


Figure 3.15: SEM images of the a) cross-section of IL grafted Oxyplus® obtained at 10 m/min with ACN as solvent and b) surface of polyRTIL grafted Oxyplus® fiber obtained at 17 m/min with ethyl acetate as solvent.

Table 3.9: Experimental conditions, permeability properties of the polyRTIL-Oxyplus composite fibers obtained and corresponding theoretical calculations

IL composition	40-65		
[c]	38%wt		35%wt
Solvent	ethyl acetate		acetonitrile
Fiber velocity	8 m/min	17 m/min	10 m/min
Lamp power	65%	85%	65%
Total dense layer thickness ^a	330±61 nm	494±68 nm	338±61 nm
polyRTIL layer average thickness	178 nm	308 nm	186 nm
Permeance of the polyRTIL layer	2640 gpu	1526 gpu	2527 gpu
Experimental $\text{Pe}(\text{CO}_2)$ ^b	549±15 gpu	613±14 gpu	724±15 gpu
Calculated $\text{Pe}(\text{CO}_2)$ ^{b,c}	796	653	792
Experimental $\alpha (\text{CO}_2/\text{N}_2)$ ^b	13	17	13
Calculated $\alpha (\text{CO}_2/\text{N}_2)$ ^{b,c}	12	17	13

^a Measured by SEM;

^b Values for the composite membrane;

^c Deduced by resistance-in-serie model.

at the elastic limit of the fiber obtained at 17 m/min decreased and the young modulus increased, indicating that the fiber obtained at 17 m/min became more rigid than the virgin Oxyplus[®]. Two facts may attribute to this change in rigidity: a thicker polyRTIL layer coated on the support membrane (compared to the fiber obtained at $v=10$ m/min); Changes possibly occurred to the support membrane during photo-grafting due to the short distance between IL-ethyl acetate solution and Oxyplus[®]. Meanwhile, the photografting did not result in the fragility of the fiber since the breaking stress and strain elongation at the break limit did not change much.

The most important polymers for dense gas-separation membranes and their CO_2 permeation properties are listed in Table 3.11 [295]. The majority of commercial membrane polymers possess CO_2/N_2 selectivity in the range of 20-30 and fairly low CO_2 permeance usually in the range of 60-100 GPU.

To compare the performance of polyRTIL-Oxyplus composite membrane with commercial membrane polymers, CO_2/N_2 selectivity vs CO_2 permeance graph was plotted (Fig.3.16). Two points that are theoretically achievable for polyRTIL-Oxyplus fiber were also included in the graph. One at selectivity of 20, the other 25. The permeances of commercial polymers are based on permeability value in reference [295] and on 100 nm selective layer thickness. The polyRTIL based composite membrane outperforms ethyl cellulose in terms of both permeance and selectivity. The CO_2/N_2 selectivity of the composite membrane (obtained at 17 m/min, polyRTIL thickness around 308 nm) is very close to that of polysulfone and brominated polycarbonate. While the CO_2 permeance of the polyRTIL-Oxyplus composite membrane is more than 10 times higher than the latters. Nevertheless, photo-grafting parameters still need to be optimized in order to achieve a CO_2/N_2 selectivity above 20 in the pursuit of a more efficient separation.

Table 3.10: Tensile test on polyRTIL-Oxyplus composite membrane obtained at different fiber velocities.

Membrane Solvent		Virgin Oxyplus [®]	$v = 10m/min$ acetonitrile	$v = 17m/min$ ethyl acetate
σ_e^a	MPa	8.16	7.46	2.94
σ_b^b	MPa	11.45	11.04	10.19
ϵ_e^c	%	5.81	5.58	0.955
ϵ_b^d	%	132.13	155.40	162.08
E^e	N/mm ²	128.72	120.76	255.51

^a σ_e =stress at the elastic limit

^b σ_b =breaking stress

^c ϵ_e =strain elongation at the elastic limit

^d ϵ_b =strain elongation at the break limit

^e E=Young modulus

Table 3.11: CO₂ and N₂ permeation properties of commercial membrane polymers [295]^a

Membrane	Pe (CO ₂) (GPU)	α (CO ₂ /N ₂)
Polyimide	110	34
Polysulfone	56	22
Cellulose acetate	63	29
Brominated polycarbonate	42	23
Generon polycarbonate ^b	70	35
Ethyl cellulose	265	8
Polyetherimide	13.2	28

^a Permeances based on permeability values given in indicated reference and on 0.1 μm membrane selective layer thickness.

^b Data from membrane manufacturer Generon

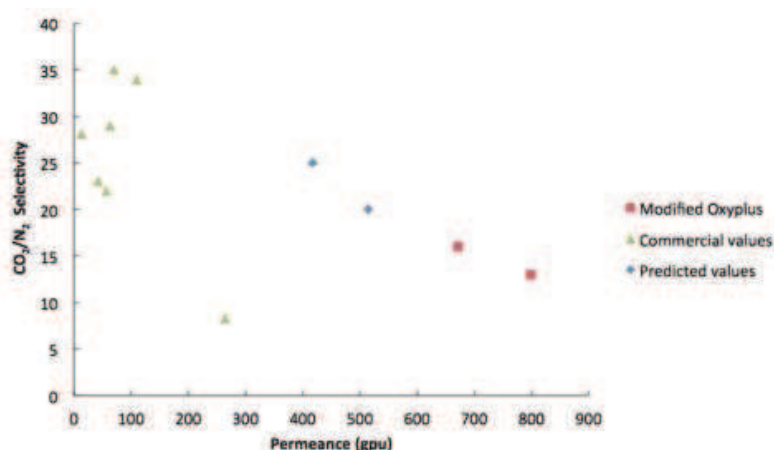


Figure 3.16: CO₂ capture capacities of commercial membrane polymers and polyRTIL-Oxyplus fibers.

Theoretical calculations show the possibility to obtain a selectivity of 25 with 390 gpu as permeance. This permeance value is still higher than those of the above-mentioned commercial membrane polymers with selectivity values being the same. While further improvement in selectivity is desirable for higher product CO₂ purity, the benefits of high selectivity would be difficult to realize without adequate CO₂ partial pressure driving force across the membrane. Researches show that the increase in permeability is more important than the increase in selectivity for the improvement of competitiveness of membranes in CO₂ capture from the flue gas [278,296]. Higher fluxes would reduce the membrane area required to process the large flue-gas volume, decreasing the membrane system cost. Although compared to the commercial hollow fiber PolarisTM (which has a CO₂ permeance of 1000 GPU and a CO₂/N₂ selectivity of 50), our fibers are not competitive enough, the strategy is the same: to minimize the detriments of defects by a multi-layer configuration. Further improvements of our fibers can be made by optimizing the choice of materials (support and upper-layers).

It is worth mentioning that CO₂ permeance measurements of the membranes were first carried out under a transmembrane pressure of 3 bar and then under 7 bar. PolyRTIL-Oxyplus composite membranes showed a slight (< 10%) decrease of permeance with pressure increase, implying that plasticization does not occur below a CO₂ pressure of 7 bar (the permeances given herein for Oxyplus based composite membranes are values measured at 7 bar). The permeation tests have also been carried out by switching back and forth between gases (CO₂ and N₂). Figure 3.17 shows a series of data nominated as ‘order of measurement – test gas’. A first permeance test was carried out with CO₂ at 3 bar (1-CO₂, Fig.3.17). Then the test gas was switched to N₂ (2-N₂, Fig.3.17) and again back to CO₂. When the test gas was switched from N₂ to CO₂, a lower CO₂ permeance was observed before it went back to the steady state (from 3-CO₂ to 6-CO₂, Fig.3.17). It took a while for CO₂ permeance to gradually increased back to the initial

value. This phenomenon may be attributed to the competitive sorption of N_2 or simply to a transition-state from less permeable N_2 to more permeable CO_2 (since no vacuum was exerted in between). No such transition was observed when CO_2 was switched back to N_2 (7- N_2 , Fig.3.17). However, to figure out the membrane performance under real conditions, permeance tests with gas mixtures are necessary.

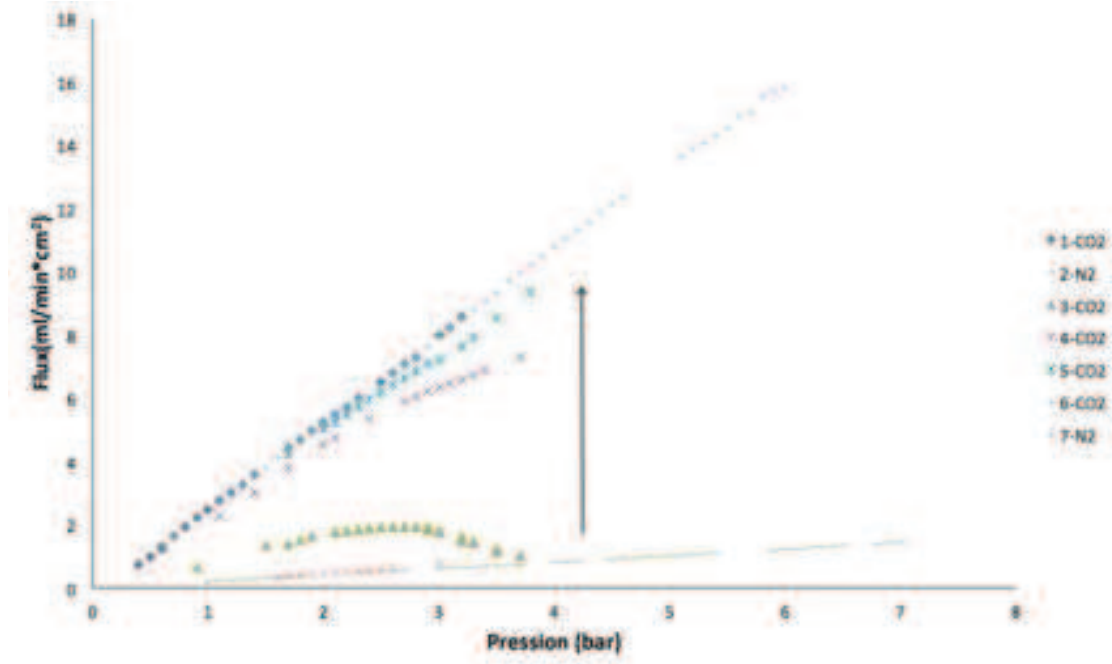


Figure 3.17: Permeance measurements on polyRTIL-Oxyplus composite membrane obtained at 8 m/min. (legends nominated as ‘order of measurement – test gas’)

The CO_2 permeance and CO_2/N_2 selectivity of Oxyplus[®] virgin fiber is respectively 1150 gpu and 1.8. According to the resistance-in-series model (Equation 3.3), when the support membrane is much more permeable than the polyRTIL layer, the mass transfer resistance of the support membrane ($1/L_{pB}$) is then negligible before that of the selective layer ($1/L_{pA}$). Thus, the permeability and selectivity of the composite membrane approximately equals that of the polyRTIL layer. This is the ideal situation. But when the polyRTIL layer becomes fairly thin (e much thinner than $10P_A/Pe_B$) and the term $1/L_{pB}$ is no more negligible, the permeation property of the composite membrane will become strongly dependent on the selective layer thickness and the support membrane permeance. In our case, the permeance of the polyRTIL was in the range of 1140-2640 gpu (Table 3.9, row ‘Permeance of the polyRTIL layer’), comparable to that of the Oxyplus[®] support membrane. To understand the influence of the selective layer thickness and the support membrane properties on the performance of the corresponding composite membrane, the CO_2/N_2 selectivity of the composite membrane was plotted as a function of its permeability by varying the thickness of the polyRTIL-RTIL layer (Fig.3.18). A large range of possibilities are achievable by varying the permeance of the

support membrane and the thickness of the selective layer. Materials and conditions can be tailored or selected according to the specific need.

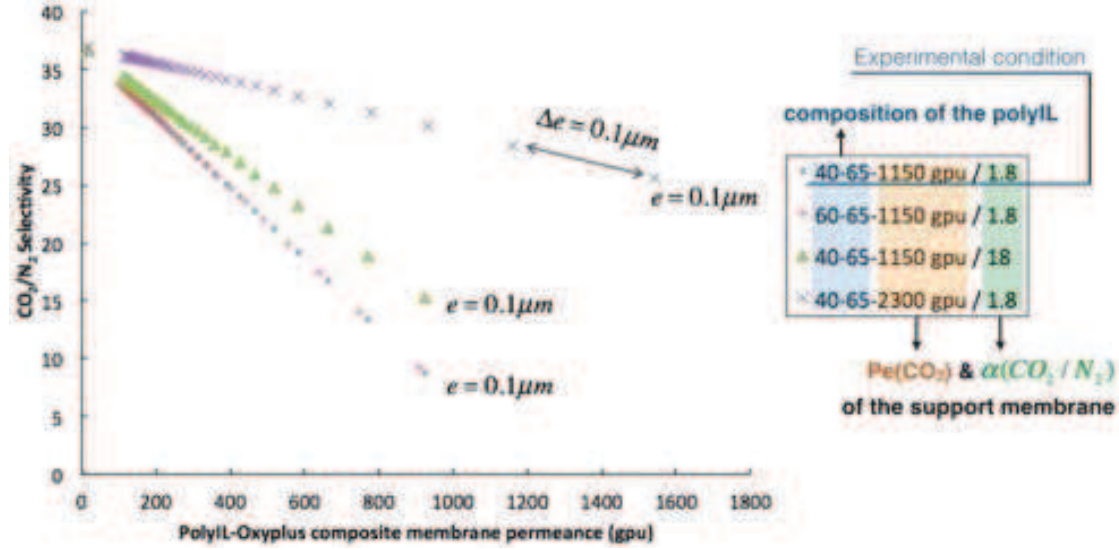


Figure 3.18: Theoretical calculations of expected composite membrane performance. The dots represent calculations carried out for different poly(IL) layer thicknesses, with an interval of $0.1 \mu\text{m}$, beginning from a thickness of $0.1 \mu\text{m}$. (data series ‘40-65-1150gpu/1.8’ correspond to experimental conditions. Other data series are hypothetical conditions, see Table 3.12)

The data series on Fig.3.18 were presented by dots. From right to left, the thickness of the poly (ionic liquid) layer increases from $0.1 \mu\text{m}$ by an interval of $0.1 \mu\text{m}$ between every two dots. The composite membrane performance was predicted for four conditions (one experimental condition and three hypothetical conditions, see Table 3.12): IL composition of 40-65 and 60-65 on virgin Oxyplus[®] fiber and for IL composition of 40-65 on two hypothetical support membranes: one with the same CO_2 permeance as virgin Oxyplus[®] (1150 gpu) but with 10 times the CO_2/N_2 selectivity (18), the other with the same selectivity but twice the CO_2 permeance (2300 gpu).

Table 3.12: Four conditions plotted in Fig.3.18.

	PolyRTIL composition	Support membrane	
		Pe (CO_2)/gpu	α (CO_2/N_2)
Experimental condition	40-65	1150	1.8
	60-65	1150	1.8
Hypothetical conditions	40-65	1150	18
	40-65	2300	1.8

The polyRTIL layer of composition 60-65 was 100 barrer less permeable than com-

position 40-65, resulting in a slightly higher CO₂/N₂ selectivity of the composite membrane. Compared to the composition of the polyIL layer, the permeation properties of the support membrane turn out to have more significant influence on the final properties of the composite membrane. And for the support membrane, a high CO₂ permeance is much more desirable than a high CO₂/N₂ selectivity: The composite membrane shows both higher permeability and selectivity using the support membrane with twice the permeance (2300 gpu) than using the support membrane with 10 times the selectivity (18). In fact, the more permeable the support membrane is, the less resistance it constitutes and the more the selectivity of the composite membrane approaches that of the selective layer. In that case, the support membrane really acts simply as a ‘physical support’ to retain mechanical strength without causing selectivity decrease.

To further improve the performance of the polyRTIL-Oxyplus composite membrane, two approaches are possible: to find a more permeable support membrane or to increase the thickness of the polyRTIL layer. Apparently, the first approach is a better choice as a higher permeance can be achieved. Teflon covered Oxyphan fiber has a CO₂ permeance almost twice as high as Oxyplus®. But more work should be done to realize a successful RTIL grafting on Teflon covered Oxyphan. IL solutions at higher concentrations were also tested in the pursuit of a thicker polyRTIL layer.

Effect of monomer solution concentration

Higher concentrations of IL monomer solution (40 %wt and 50%wt) were tested to see if higher CO₂/N₂ selectivities could be achieved. In Fig.3.19, the experimental points at four different concentrations (same IL solution composition: 40-65) were plotted in a CO₂/N₂ selectivity vs CO₂ permeance graph. The different data points at the same concentration in Fig.3.19 were obtained at varied fiber velocities. The highest CO₂/N₂ selectivities were obtained at concentration of 38%wt. If fully polymerized, a higher concentration leads to a thicker polyRTIL layer and accordingly a higher selectivity. The lowest CO₂/N₂ selectivities were observed at 50%wt. The decrease in selectivity with IL monomer concentration was owing to the low polymerization conversion at concentrations higher than 40%wt. The incomplete polymerization was a result of the relatively slow polymerization kinetics of ionic liquid **a** and **b**. Actually, at concentrations over 40%wt, fibers were found wet after the photo-grafting process. Non-polymerized ionic liquid monomers remained on the membrane outer surface in liquid state. Situation got no improvements when the ionic liquid composition changed to 60-65 at 45%wt (CO₂/N₂ selectivity of the composite membrane lower than 2).

Influence of fiber velocity

Figure 3.20 shows that in spite of the incomplete polymerization at high solution concentrations, the permeance dependence on fiber velocities remained fairly logical and reasonable: The liquid film thickness (hence graft layer thickness under complete polymerization) increases with fiber velocity in the visco-inertial regime (Eq.3.4-Eq.3.6). And permeance is related to inverse of the graft layer thickness. This dependence was more

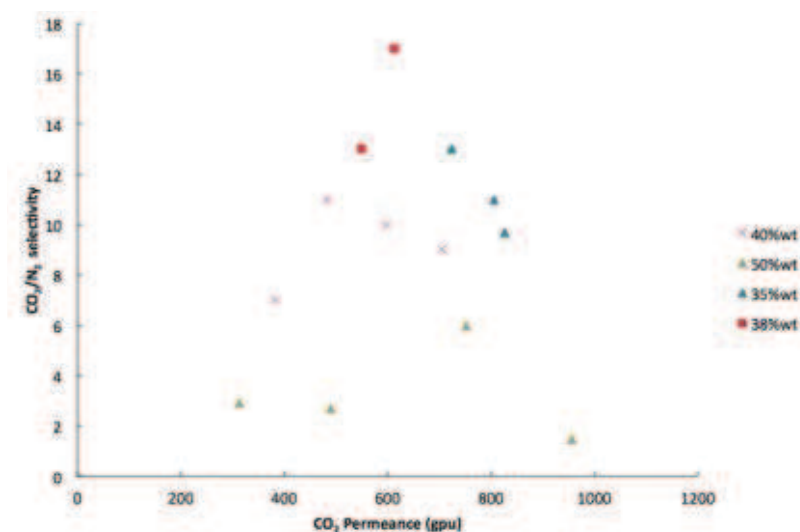


Figure 3.19: Permeation properties of polyRTIL-Oxyplus fibers obtained at different IL solution concentrations.

evident at higher concentrations. At 40%wt and 50%wt, CO₂ permeance decreased with increasing fiber velocity. The faster decrease of membrane permeance with velocity increase at 50% than at 40% can be attributed to the higher monomer solution viscosity (see Eq.3.4-3.6). The incomplete polymerization at 50%wt explained the higher permeance value observed than those observed at lower concentrations. For 35%wt – 40%wt, the influence of fiber velocity was much less evident. The dependence of selective layer thickness on fiber velocity tended to be influenced more by lamp power.

3.3.5 IL monomer type

Since the polymerization kinetics of IL monomers can have influences on the final polyRTIL layer thickness, and thus its gas separation performance. More possibilities can be conferred to the membrane if ionic liquid monomer structure is properly adjusted. Ionic liquid **d**, **e** were synthesized (Fig.3.21) (used later on for catalytic membrane preparation, see Chapter V). The vinyl group of the ionic liquids previously used were changed to styrene groups, whose polymerization kinetics was much faster. One preliminary permeation test was carried out on a flat sheet membrane by photopolymerization of a **d** and **e** mixture with a cross-linker/non-crosslinker molar ratio of 1/20. Table 3.13 shows that the obtained membrane has a good CO₂/N₂ permeability selectivity but low CO₂ permeability. Logically, by introducing a free IL into the polyRTIL matrix can largely increase the CO₂ permeability with almost no change in CO₂/N₂ permeability selectivity. To check this possibility, a preliminary photo-grafting on Oxyplus[®] was run using **d**, **e** and [MMPIM][NTf₂] (1,2-dimethyl-3-propylimidazolium bis(trifluoromethylsulfonyl)imide) as free IL. The ionic liquid solution was prepared at

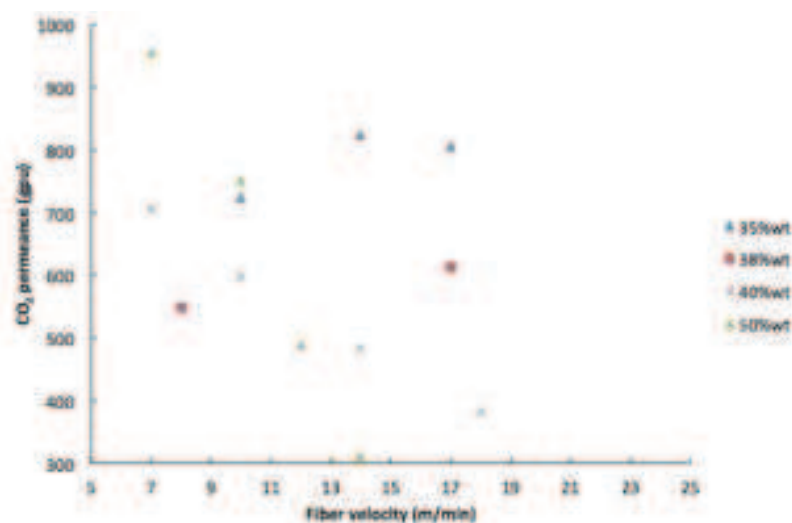


Figure 3.20: Permeance of polyRTIL-Oxyplus fibers obtained at different fiber velocities.

38%wt in acetonitrile with a composition of 40-65. Oxyplus[®] turn out not to be perfectly compatible with the above IL solution. In other words, their inter-distance in Hansen space is not far enough. The fiber broke at low velocity (8 m/min) during the photo-grafting. Nevertheless, grafted fibers were obtained at velocities above 11 m/min, slightly stretched.

Table 3.13: Permeation properties of a plat-sheet membrane made from **d** and **e**.

$P(\text{CO}_2)^a$	$\alpha(\text{CO}_2/\text{N}_2)$	$\alpha(\text{CO}_2/\text{H}_2)$
13	33	2

^a Permeability in barrer.

The permeation test started with CO_2 at 4-5 bar and N_2 was tested right after. During the permeation test, a 25% CO_2 permeability increase was observed at 4 bar before the permeability finally stabilized and data were collected after the stabilization. This phenomenon indicated that plasticization of the composite membrane occurred, induced by CO_2 . The membranes under plasticized condition were thus not selective towards CO_2 ($P(\text{CO}_2)/P(\text{N}_2) \approx 1.1\text{-}1.4$). CO_2 permeability was in the range of 100 to 200 gpu. The reversibility of the membrane was not studied. Katy Simons et al. reported the plasticization of polyRTIL membranes based on similar IL monomers (Fig. 3.22). They found that the plasticization of the polyRTIL membranes studied was more severe for longer C1 side chains [92]. The long side chain of RTIL **d** and **e** makes the plasticization

comprehensible. Nevertheless, no obvious plastification was observed with RTILs **a** and **b** under 7 bar although the C1 side chains were the same for **d** and **e**. As styrene group is more bulky than the vinyl group, it may result in a less tight ionic interactions for IL **d** and **e** compared to **a** and **b**. Hence, **d** and **e** are more sensitive to volume dilation-induced plasticization phenomena. The methyl group at C2 position may also have played a role.

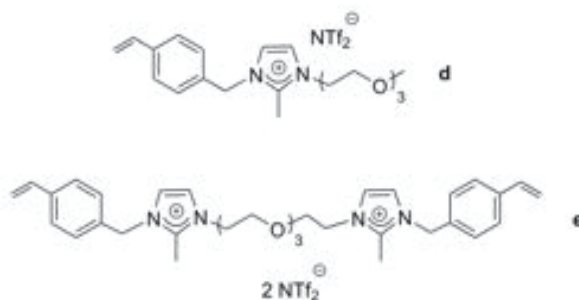


Figure 3.21: Structure of ionic liquid **d** and **e**.

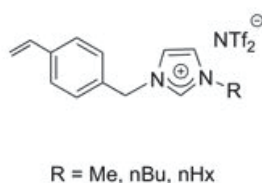


Figure 3.22: Structure of RTIL monomers studied in [92].

Although hollow fibers made from **d** and **e** plasticize under CO_2 feed pressure, it can still have other prospect applications other than gas separation, catalytic membrane, for example.

3.4 Conclusions

PolyRTIL-RTIL gel membranes are largely appreciated for their better pressure stability than SILMs and much higher permeability compared to polyRTILs while CO_2/N_2 permeability selectivities were almost the same. Coating polyRTIL-RTIL gel onto a high permeable support membrane can make it more interesting by a further increase in permeance and for a larger scale application. However, it is difficult to realize such a coating, especially on hollow fibers, using frequently applied coating techniques. In this work, possibilities of coating a polyRTIL-RTIL gel layer on a hollow fiber support have been explored using continuous UV-induced photo-grafting process, which gives a

homogenous modifying layer on the support fiber surface. However, parameters need to be carefully chosen to obtain a composite membrane with satisfying properties:

1. The solvent should not swell the support membrane and it should have a high boiling point to prevent overheating. A good wettability of the support membrane surface is also indispensable. Judgements of the compatibility between the monomer solution and the support membrane can be made based on Hansen solubility parameters. The interaction distance between the solution and the support membrane should be larger than the interaction distance of the support membrane. The influence of temperature rise in the UV lamps on HSPs should be taken into consideration.

2. The solution concentration, lamp power and fiber velocities are inter-related parameters that need to be considered comprehensively. In the viscoinertial regime, the entrained liquid film thickness increases with fiber velocity (at constant concentration). This increase is faster at high monomer solution concentrations. Precautions need to be taken on lamp powers under high fiber velocities and high monomer solution concentrations to provide enough UV energy for full polymerization conversion. Full polymerization can not always be achieved (especially for monomers with low polymerization kinetics) because the lamp powers are limited by the deflection temperature of the support membrane under the experimental conditions. Quantitative judgement on the whether UV energy is sufficient can probably be given by $P_{UV}/(C \cdot e \cdot v)$, with P_{UV} as UV lamp power, C the monomer solution concentration, e the liquid film thickness and v the fiber velocity. When polymerization is complete, increase in monomer solution concentration can increase the selective layer thickness and hence the selectivity of the composite fiber.

3. According to the resistance-in-series model, high permeance of the support membranes is desirable since its small mass transfer resistance gives both high composite membrane permeance and high selectivity (approaching that of the selective layer). The ideal selective layer thickness depends on the specific need and the support membrane permeance. In our case, we consider the optimum selective layer thickness to be approximately $e = 3P_A/Pe_B$. Thinner selective layer leads to decrease in (composite membrane) selectivity while thicker selective layer induces decrease in permeance.

In the experiment, four hollow fibers were tested as support membrane. MicroPES[®] was found incompatible with the RTIL solution. Oxyphan[®] was not adapted for severe penetration of RTIL solution into the pores, resulting in a significant drop in permeability.

Photo-grafting polyRTIL onto Oxyplus[®] was a success. Two polyRTIL-Oxyplus composite membranes were obtained, one with CO₂ permeance of 613 gpu and CO₂/N₂ permeability selectivity of 17, the other with CO₂ permeance of 724 gpu and CO₂/N₂ permeability selectivity of 13. The permeation properties of those polyRTIL-Oxyplus membrane are well predicted by resistance-in-series model. They are much more permeable than commercial membrane polymers. A higher membrane permeability requires less pressure difference across the membrane, saving energy cost on compression. In the case of post combustion, high permeability is especially important since CO₂ partial pressure is low in flue gas for its low concentration (around 3%-15%). Tensile test shows

that photo-grafting did not make the membrane fragile.

No plasticization was observed on the polyRTIL-Oxyplus membrane up to 7 bar. However, when the RTIL monomers were changed from vinylimidazolium to styrene-imidazolium, CO₂ induced plasticization occurred, probably due to looser ionic interactions. The styrene group substituted RTILs may not be good for gas separation application, but can be applied in catalytic membranes.

The best way to further improve the CO₂ capture performance of polyRTIL based composite hollow fibers is to find a highly permeable support membrane. When the resistance of the support is negligible before the polyRTIL selective layer, the permeability selectivity of the composite membrane will be the same as the polyRTIL-RTIL gel layer, while permeance will be high as long as the selective layer is thin. First trial in seeking a more permeable support using Teflon covered Oxyphan fiber (twice more permeable than Oxyplus[®]) did not succeed due to the membrane surface roughness and poor wetting of the membrane surface by the RTIL solution. Change of solvent and other parameters may still be possible to have Teflon covered Oxyphan as support.

Chapter 4

Study of the catalytic behavior of palladium nanoparticles dispersed in liquid phase

Résumé du Chapitre

Les nanoparticules de palladium (de NPPd) représentent un catalyseur polyvalent ayant une large gamme d'applications telles que la formation de la liaison C-C et de la liaison carbone-hétéroatome, l'hydrogénation et des réactions de carbonylation. Dans ce chapitre, les NPPd ont été préparées dans du liquide ionique à température ambiante qui permet de stabiliser les NPPd. Le liquide ionique utilisé est le [MMPIM][NTf₂] (1,2-diméthyl-3-propylimidazolium bis-(trifluorométhylsulfonyl)imide). En tant que système catalytique hétérogène, les NPPd dispersées dans le liquide ionique peuvent être séparées et réutilisées facilement avec peu de perte d'activité. L'objectif est de comparer la performance catalytique des NPPd dispersées dans du liquide ionique à celle des NPPd supportées par la membrane à base de polyLI (voir Chapitre 5).

Les suspensions colloïdales de NPPd sont préparées par méthodologie 'bottom-up' (soit sous pression dihydrogène, soit sous conditions thermiques) avec l'acétate de palladium comme précurseur. Parmi les 5 systèmes préparés, le système 4 (préparé sous condition thermique à 100°C en présence de PVP) a montré une meilleure dispersion de NPPd dans [MMPIM][NTf₂]. Ce système est actif pour les réactions d'hydrogénation, couplage croisé de Heck-Mizoroki et de Suzuki-Miyaura et également le procédé séquentiel de couplage croisé de Suzuki-Miyaura/hydrogénation. Pourtant, il n'est pas actif pour le procédé séquentiel de couplage croisé de Heck-Mizoroki/hydrogénation. Système 4 a aussi montré une bonne réutilisabilité pour l'hydrogénation de trans-4-phényl-3-buten-2-one : peu de perte d'activité a été observée après 12 fois de réutilisation.

4.1 Introduction

Palladium nanoparticles (PdNPs) represent a versatile catalyst with a wide range of applications such as C-C bond and carbon-heteroatom bond formation, hydrogenation [297, 298] and carbonylation processes [299, 300]. In this chapter, PdNPs were prepared in room temperature ionic liquid (RTIL), taking advantage of the dispersion effect on MNPs of the medium [301]. The imidazolium-based RTIL used plays a role of both stabilizer and solvent for PdNPs. Ionic liquids are solvents exhibiting high polarity, estimated between acetonitrile and methanol, and consequently capable to dissolve organic compounds, metallic salts, enzymes [302]. The use of ILs often permits an efficient immobilization of the catalyst, overcoming the main drawbacks of homogeneous catalysis. i.e. organic product separation and catalyst recovery. The separation of organic products from the ionic liquid phase can be easily realized by extraction (biphasic systems). IL phase containing the metallic catalyst could be readily reused without significant loss of catalytic activity [303, 304] and consequently favor its recycling. In addition, the good thermal stability of the ILs makes them convenient solvents for high temperature reactions. In this work, the ionic liquid used was [MMPIM][NTf₂] (1,2-dimethyl-3-propylimidazolium bis-(trifluoromethylsulfonyl)imide), which has a decomposition temperature of ca. 460 °C [242]

The aim is to compare the catalytic performance of PdNPs dispersed in RTIL to that of PdNPs supported by a polyRTIL based polymer membrane (see Chapter 5). Attempts to prepare the palladium colloidal system in RTIL-polyRTIL mixture ended in a very viscous system that was hard to be applied in further catalytic tests. Hence palladium colloidal systems were prepared in RTIL in the presence of a polymer (PVP=polyvinylpyrrolidone) instead. The PdNPs in RTIL and the polyRTIL modified catalytic membrane may not be in exactly the same chemical environment. But at least a rough understanding of the catalytic activity difference between the PdNPs in RTIL and membrane supported PdNPs (or catalytic membrane) can be gained.

In this chapter, PdNPs were prepared by ‘bottom-up’ methodology [305] using palladium acetate as metallic precursor. Two approaches were carried out: (i) under dihydrogen reducing conditions and (ii) under thermal decomposition conditions (where the acetate anions act as reducing agent) [306]. Parameters (such as temperature, PVP amount, dihydrogen pressure) were optimized in order to obtain the most active catalytic system. The thus-obtained system was tested in hydrogenations, C-C cross-couplings and one-pot multi-step reactions.

4.2 Synthesis of colloidal PdNPs

Although RTIL stabilizes nanoparticles by electrostatic effect, sometimes RTIL alone may still not be sufficient to well stabilize metallic nanoparticles (MNPs). In that case, an additional co-stabilizer is required. Poly(vinylpyrrolidone) (PVP) is one of the most frequently used polymers to stabilize MNPs since it is soluble in a lot of polar

solvents. L. D. Pachón et al. found that part of the PVP adsorbs on the NP surface as a protective shell, while the other part dissolves freely in the suspension, creating a second protective shell [307] and avoiding the collision between particles (Fig.4.1).

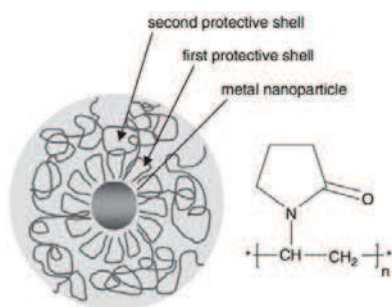
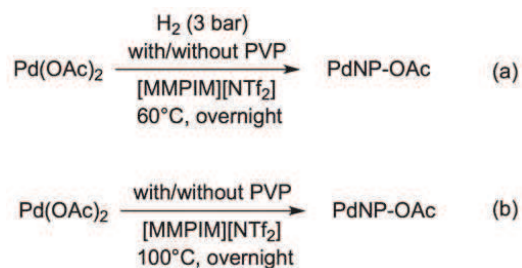


Figure 4.1: Conformation model of PVP-stabilization of metal nanoparticles [307].

Different conditions were applied for the preparation of PdNPs in [MMPIM][NTf₂] (Table 4.1). For the five resulting systems, palladium acetate was used as precursor in the presence or absence of dihydrogen and PVP (Scheme 4.1). System 1 and 3 were prepared with only RTIL as stabilizer for PdNPs while PVP (10,000 g/mol) was added at a molar ratio Pd/PVP repeating unit of 1/20 as a co-stabilizer for system 2, 4 and 5. During the synthesis, palladium turned from orange (color of palladium acetate) to black, indicating the formation of Pd⁰. System 2, 3, 4 turned out to be black colloids while black precipitates were observed in system 1 and 5 (Fig.4.2). In fact, the appearance of a black colloid points to a homogenous dispersion of PdNPs and the formation of precipitates indicates relatively big particles or formation of aggregates. TEM images of the five systems prepared are given in Fig.4.3. Judging from the difference between system 1 and 2, system 3 and 4, PdNPs were better dispersed with the presence of the additional polymer PVP in [MMPIM][NTf₂]. Aggregates were observed when H₂ pressure was present (system 1, 2 and 5 in contrast to system 3 and 4). Therefore, the effect of H₂ under thermal conditions could be detrimental for the formation of homogeneously dispersed PdNPs. Although the PdNPs' mean diameters of system 3 and 4 are almost the same (Table 4.1), the PdNPs of system 4 are more homogeneous in size. For catalytic purposes, the above systems were studied to understand the effect of PVP, which can also over-protect PdNPs and therefore reduce the accessibility of the reagents to the metallic surface.

Table 4.1: Colloidal PdNP systems prepared under different conditions in [MMPIM][NTf₂]

System	H ₂ pressure	Temperature(°C)	Presence of PVP	Nanoparticle mean diameter (nm)
1	3 bar	60	no	-
2	3 bar	60	yes	-
3	No H ₂	100	no	4.3 ± 4.1 (1277 particles counted)
4	No H ₂	100	yes	4.2 ± 1.6 (1389 particles counted)
5	3 bar	100	yes	-



Scheme 4.1: Synthesis of PdNPs in [MMPIM][NTf₂]: a) under H₂ pressure and b) via thermal decomposition in the presence or absence of PVP.

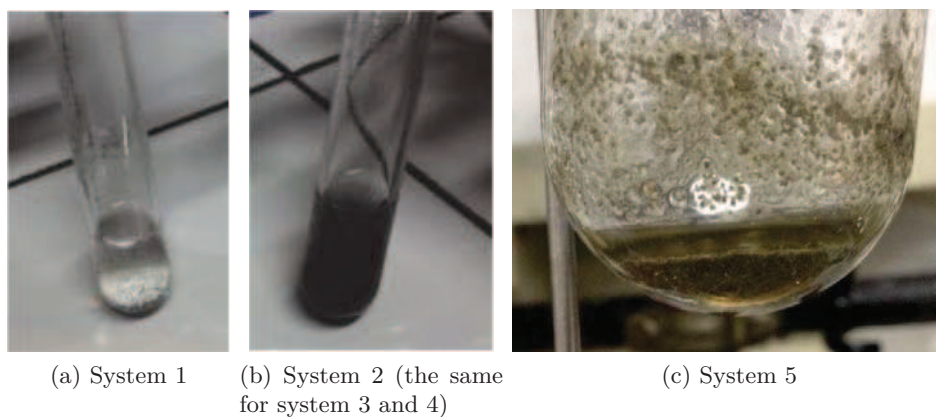
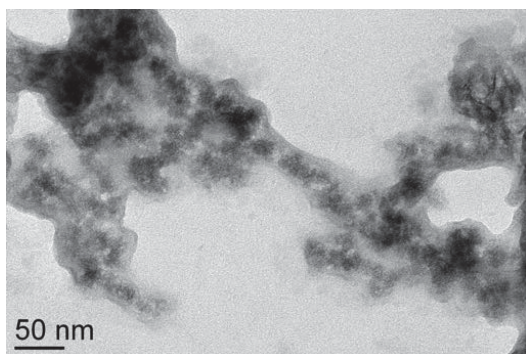
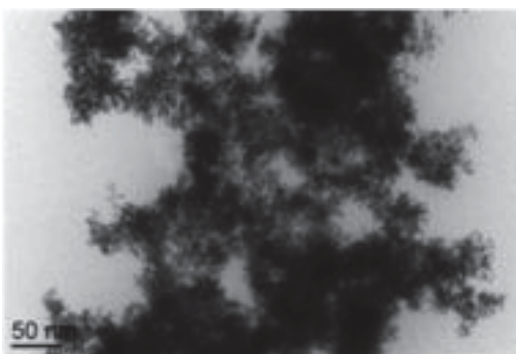


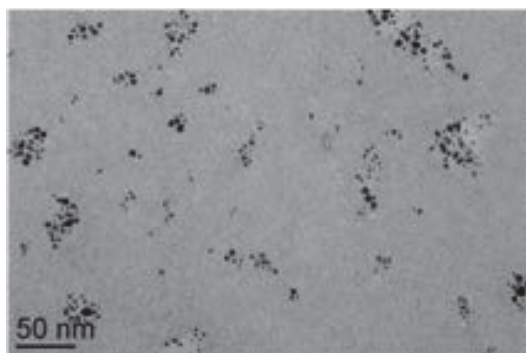
Figure 4.2: Appearance of PdNPs synthesized in [MMPIM][NTf₂].



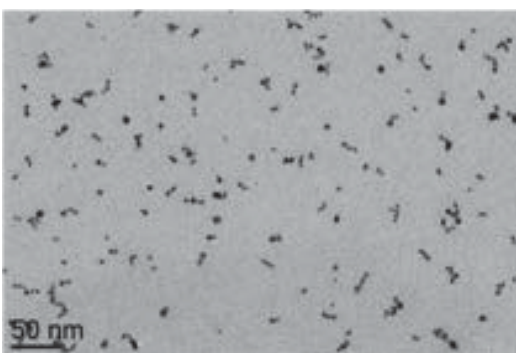
(a) System 1



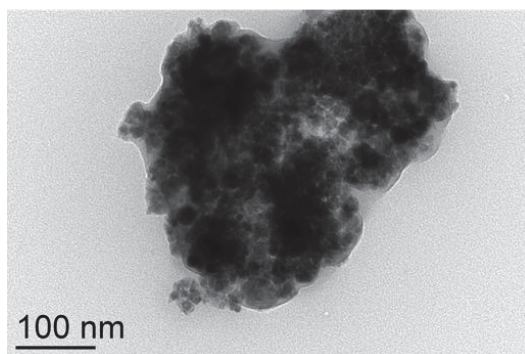
(b) System 2



(c) System 3



(d) System 4



(e) System 5

Figure 4.3: TEM images of PdNPs synthesized in $[\text{MMPIM}][\text{NTf}_2]$

4.3 Catalytic study in [MMPIM][NTf₂] under batch conditions

4.3.1 Pd-catalyzed hydrogenation reactions

Hydrogenation is the addition of H₂ to a multiple bond (C=C, C≡C, C=O, C=N, C≡N, N=O, N=N, N≡N, etc) to reduce it to a lower bond order, which is usually an exothermic process [308]. It has wide industrial applications, especially in petrochemicals and fine chemistry fields. Palladium is an efficient catalyst for hydrogenation of different functional groups; for example, it can be used for the selective reduction of C≡C triple bonds and C=C double bonds [309–312].

One of the accepted mechanisms for the heterogeneous hydrogenation of unsaturated compounds is the Horiuti-Polanyi mechanism [313,314]. Hydrogenation of alkenes proceeds through several steps (Fig.4.4). With the presence of a metal catalyst, the H-H bond cleaves, and each hydrogen attaches to the metal catalyst surface, forming metal-hydride bonds. The alkene is adsorbed on the catalyst surface as well, where H atoms on the surface transfers to the alkene, forming two new C-H σ bonds. Then the product (alkane) desorbs from the catalyst surface. Because of the physical arrangement of the alkene and the hydrides on a flat metal catalyst surface, the two hydrogen atoms must add to the same face of the double bond, displaying a *syn* addition. Furthermore, if one face is more hindered than the other, the addition can be stereoselective, favoring the less hindered side.

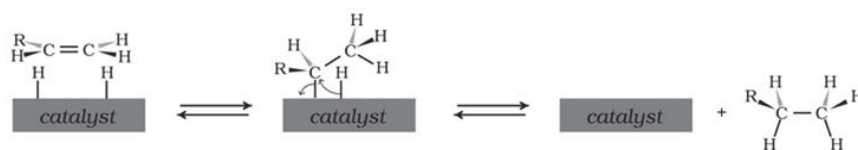


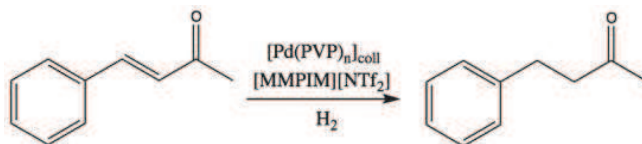
Figure 4.4: Text-book catalytic mechanism for the hydrogenation of alkenes.

The group of J. Dupont applied performed PdNPs (d_{mean} = 4.9 nm) in [C₁C₄Im][BF₄] (C₁=Me, C₄=n-butyl) in the hydrogenation of 1,3-butadiene. The high selectivity (97%) towards 1-butene demonstrated a pronounced surface-like reactivity rather than single site catalytic behavior [315]. The same group has recently proved that bigger PdNPs (d_{mean} = 7.3 nm), stabilized by [C₁RIm][NTf₂] (R = 1-butyronitrile), can induce different selectivity in the hydrogenation of alkynes depending on the catalytic conditions [301].

Hydrogenation of *trans*-4-phenyl-3-buten-2-one

Pd catalytic systems 3 and 4 were applied to the benchmark hydrogenation reaction of *trans*-4-phenyl-3-buten-2-one (Scheme 4.2), showing high activity (Table 4.2). 4-Phenylbutan-2-one was exclusively formed as product, which represents a model skeleton

of fragrances. System 4 maintained high activity under mild conditions (1 bar H₂, 1 mol% Pd, entry 3 and 4, Table 4.2) and also at low catalyst load (0.1 mol%, entry 5, Table 4.2). Despite the similarity in NP mean diameter, system 3 was less active than system 4 (25% vs 61% conversion after 0.5h, entry 6 vs 3, Table 4.2).



Scheme 4.2: Pd-catalyzed hydrogenation of *trans*-4-phenyl-3-buten-2-one

Table 4.2: Catalytic results on the hydrogenation of *trans*-4-phenyl-3-buten-2-one under different conditions^a.

Entry	System	Pd/substrate (%mol)	P(H ₂) (bar)	Temperature (°C)	Reaction time (hour)	Conversion (%) ^b
1	4	1	3	80	1	100
2	4	1	3	60	1	100
3	4	1	1	60	0.5	61
					1	100
4	4	1	1	35	1	60
					2	100
5	4	0.1	3	60	1	27
					3	66
					5	100
6	3	1	1	60	0.5	25

^a Starting from 1 mmol of substrate;

^b Determined by GC-MS and ¹H NMR using decane and mesitylene respectively as internal standard.

A recycle test of catalytic system 4 was then run for the benchmark hydrogenation reaction with a Pd/substrate ratio of 1%mol at 60 °C under 1 bar hydrogen pressure (for 1h each run, conditions corresponding to entry 3, Table 4.2). The catalytic system was reused 12 times virtually without catalytic activity loss. As shown in Fig.4.5, the conversion rate kept above 90% through the 12 runs (product was extracted by cyclohexane after each run). Although NP agglomerations were observed after 5 recycle runs (Fig.4.6-b), high conversions were retained. The influence brought about by the formation of agglomerations was not observed under the hydrogenation recycle conditions. The palladium NP organization after the recycle run became similar to System 2 (synthesized under H₂ pressure). The H₂ turned out to have an impact on aggregation

of PdNPs in [MMPIM][NTf₂]. Maybe the presence of hydrides at the NP surface made difficult the approach of PVP to the surface.

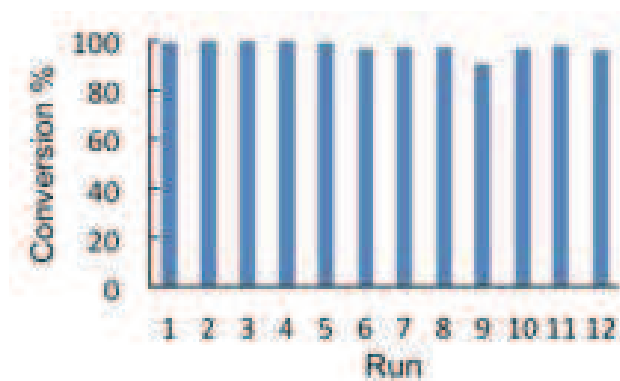


Figure 4.5: Recycling of System 4 for the hydrogenation of *trans*-4-phenyl-3-buten-2-one (60°C, 1 bar H₂, 1 h for each run, 1 mol% Pd, 1 mmol substrate).

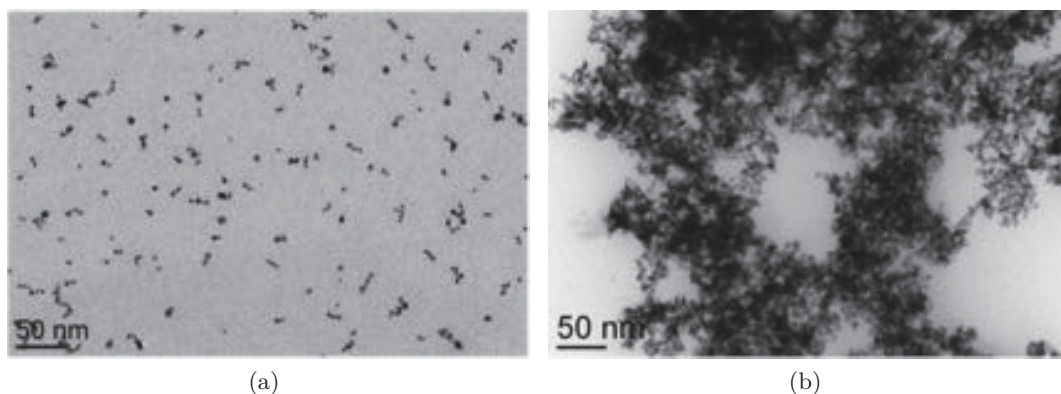


Figure 4.6: TEM images of System 4: (a) before catalysis; (b) after 5 recycling runs

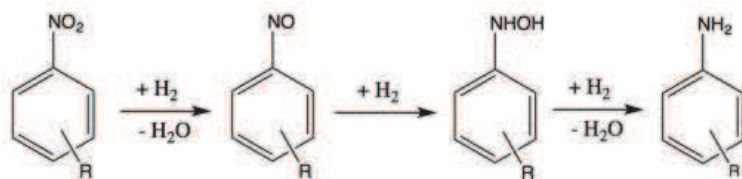
Hydrogenation of 4-nitrophenol

Aromatic and heterocyclic amines are fundamental building blocks in industrial-scale organic synthesis, as they are frequently used as intermediates for the production of dyes, pharmaceuticals and polymers [316–318]. Classical methods for the preparation of amines involve the reduction of the corresponding nitro groups. As an example, aniline and its derivatives are commonly produced through selective hydrogenation of substituted nitrobenzene [319].

The reduction of nitro compounds to amines follows a three-step mechanism in the presence of palladium (Scheme 4.3): the nitro group is first reduced to nitroso group, followed by the reductive addition of two hydrogen atoms to form the hydroxylamine.

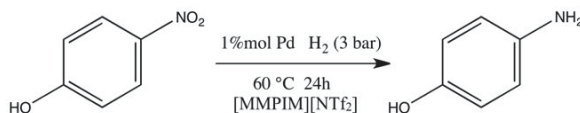
Then water is eliminated and the amine is formed [320,321].

System 4 was active on the hydrogenation of 4-nitrophenol, giving selectively



Scheme 4.3: Text-book catalytic mechanism for hydrogenation of aromatic nitro compounds.

4-aminophenol as the only product (Scheme 4.4).

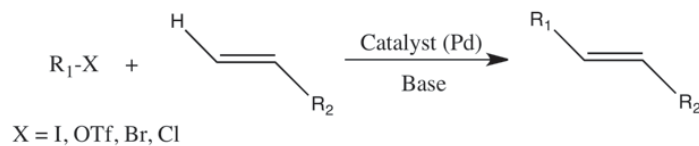


Scheme 4.4: Pd-catalyzed hydrogenation of 4-nitrophenol.

4.3.2 Pd-catalyzed C-C bond formation

Heck-Mizoroki cross-coupling

Published independently by Mizoroki in 1971 [322] and by Heck in 1972 [323], the Heck-Mizoroki cross-coupling is one of the most studied palladium-catalyzed reactions. It refers in the most cases to the Pd-catalyzed coupling between a halide compound and an alkene to form a substituted alkene in the presence of a base (Scheme 4.5). Heck-Mizoroki cross-couplings find industrial applications in fine chemistry. For example, one key step in the synthesis of the medicine Montelukast (trade name Singulair, commercialized by Merck) involves a Heck coupling [324,325].



Scheme 4.5: A general scheme for Pd-catalyzed Heck-Mizoroki cross-couplings

The general mechanism of Heck-Mizoroki reaction is shown in Figure 4.7. After the catalyst activation step, where the precursor is usually reduced from Pd(II) to Pd(0), the Pd(0) catalyst undergoes an oxidative addition of the aryl halide, forming a Pd(II) intermediate. This Pd(II) complex then binds to the olefin, inserting it into the aryl-Pd bond, creating a new carbon-carbon bond. β -Hydride elimination leads to the expected

product, generating a hydrido-palladium species $[L_2PdHX]$. The base then extracts “HX” from the intermediate, regenerating the $L_2Pd(0)$ species [326,327].

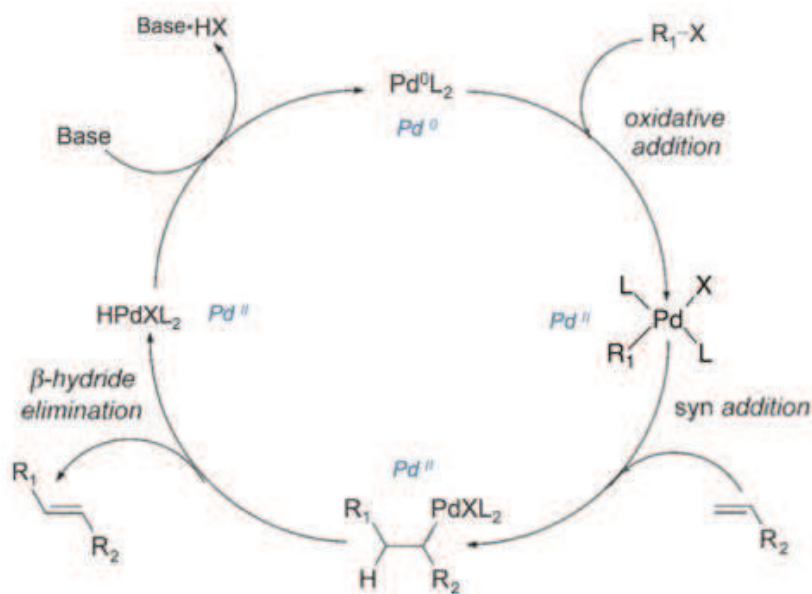


Figure 4.7: Text-book mechanism of palladium catalyzed Heck-Mizoroki cross-coupling. L represents the ligand linked to palladium molecular species.

Dupont and co-workers suggested that during the Heck reaction, Pd-NPs in the IL $[C_1C_4Im][PF_6]$ simply serve as reservoir of molecular active Pd species and that reaction pathway starts with oxidative addition of the aryl halide onto the metal surface. The oxidized Pd atoms on the metallic surface are immediately desorbed from the metal surface, giving active molecular Pd species. The molecular Pd species may either remain in the catalytic cycle up, or agglomerate into PdNPs or bulk metal depending on the reaction conditions [328] (Fig 4.8). This is coherent with previous reports by Reetz for ligand-free Heck reactions in common organic solvents [329,330].

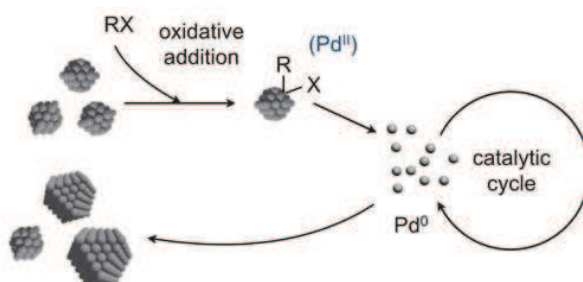
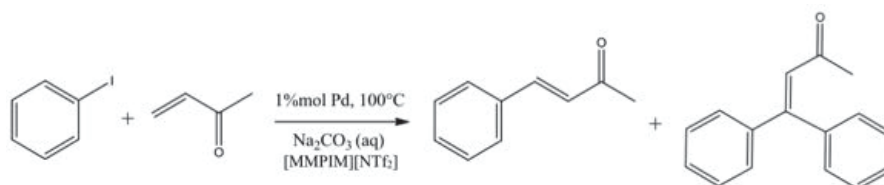


Figure 4.8: Leaching of Pd molecular species in Heck-Mizoroki cross-coupling.

System 1, 2 and 4 were tested on the model Heck-Mizoroki cross-coupling between iodobenzene and butenone (Scheme 4.6). Results are listed in Table 4.3. System 2 and 4 were active (entries 3-8, Table 4.3). The reaction mixture turned from black (before the reaction) to orange (after the reaction), indicating the generation of Pd molecular species. System 1 was practically inactive (entries 1-2, Table 4.3). For system 2 and 4, *trans*-4-phenyl-3-buten-2-one was exclusively obtained as product up to 37h of reaction (entries 3-7, Table 4.3). However at longer reaction time (>85h), a further cross-coupling product between *trans*-4-phenyl-3-buten-2-one and iodobenzene was observed for system 4, leading to an equimolar mixture of *trans*-4-phenyl-3-buten-2-one and 4,4-diphenyl-3-buten-2-one (entry 8, Table 4.3). System 4, the most dispersed system with the least aggregates, gave the highest conversion (entry 3-4 vs 6-7, Table 4.3).



Scheme 4.6: Heck-Mizoroki cross-coupling catalyzed by system 1, 2 and 4.

Table 4.3: System 1,2 and 4 applied in Heck-Mizoroki reaction (see Scheme 4.6)^a.

Entry	System	Reaction time (h)	Conversion ^b (%)	Selectivity ^{b,c} (%)
1	1	5	1.6	100
2		22	6.2	100
3	2	20.5	27.5	100
4		37	47.4	100
5	4	1	17.3	100
6		20.5	62.2	100
7		37	77.5	100
8		85	85.6	50

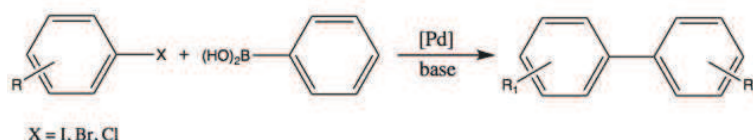
^a Pd/substrate=1/100, T=100 °C.

^b Determined by GC-MS with decane as internal standard.

^c Selectivity towards *trans*-4-phenyl-3-buten-2-one.

Suzuki-Miyaura cross-coupling

Suzuki-Miyaura reaction represents in general the C-C coupling between an aryl- or vinyl-boronic acid (or boron-esters) and an aryl- or vinyl-halide (or triflate) catalyzed by a Pd^0 based catalyst. In 1981, Suzuki proposed for the first time this reaction (Scheme 4.7) [331]. Suzuki-Miyaura reaction is widely used to synthesize biphenyls, dendrimers, and has been extended to the synthesis of unusual amino acids and peptides [332].



Scheme 4.7: Palladium catalyzed Suzuki-Miyaura cross-coupling.

The mechanism of this reaction is generally accepted to consist of three main steps (Figure 4.9): Oxidative addition of the substrate on palladium(0) species, followed by the transmetalation step where the functional group from the boronic acid transfers to the palladium(II) center. And eventually the reductive elimination to give the coupling product and regenerate the catalytically active palladium(0) species [333]. The nature of the active catalytic species in palladium-catalyzed Suzuki-Miyaura cross-coupling reaction starting from MNPs has been much debated over the years. In 2010, Ellis et al. used XAS, surface sensitive XPS and detailed kinetic profiling to quantitatively track the local structure of mono dispersed PdNP stabilized by PVP during the Suzuki-Miyaura coupling reaction of 4-iodoanisole with phenylboronic acid. By following the local coordination environment in an *operando* mode (real-time measurement under working conditions), they provided strong and direct evidence that PdNPs is a surface-driven catalysis in this reaction and that the reactivity is indeed heterogeneous in origin [334]. This is in agreement with the work of Gómez et al, who conclude that NP formation was required to lead to a catalytic active system in Suzuki reaction (through the study of Suzuki reaction of different functionalized ligands derived from norborn-5-ene-2,3-dicarboxylic anhydride in $[\text{C1C4Im}][\text{PF}_6]$, by using palladium acetate as catalytic precursor) [335].

System 1 and 2 were tested on the Suzuki-Miyaura coupling between bromobenzene and phenyl boronic acid (Scheme 4.8). The two systems shared similar low activities for Suzuki-Miyaura coupling (conversion lower than 25% after a reaction time of 24h; biphenyl as the only product). In this coupling reaction, it can not be judged if homo-coupling product (coupling between two molecules of boronic acid or bromobenzene) was formed. System 2 was then applied on the Suzuki coupling between 1-bromo-4-(trifluoromethyl)benzene and phenylboronic acid in order to achieve higher conversion rate (the trifluoride group can increase the reaction rate) (Scheme 4.9). Electron-withdrawing groups (such as CF_3) favors the oxidative addition, the commonly accepted rate determining step of the catalytic cycle, in consequence favoring the reaction rate. The hydrodebromation under alkaline conditions was observed. The resulting byproduct is trifluoromethylbenzene (molar ratio of cross-coupling product product = 2/1).

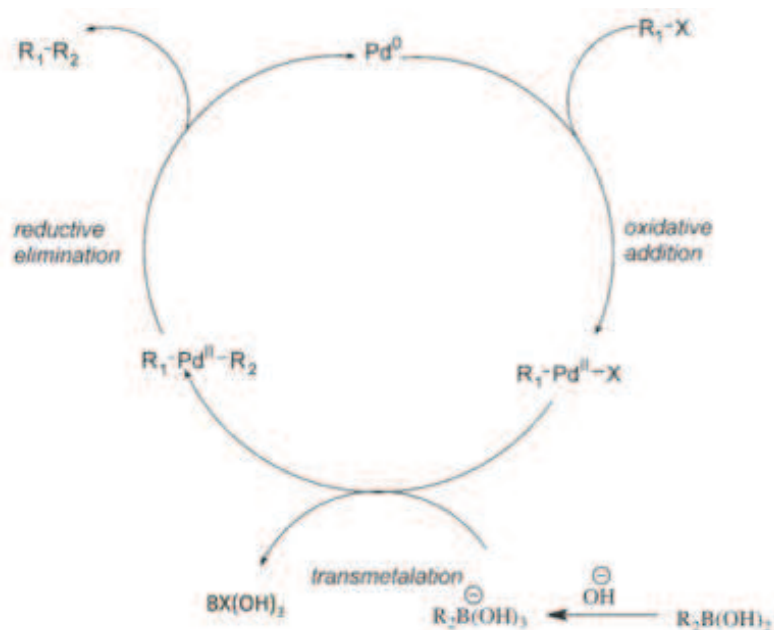
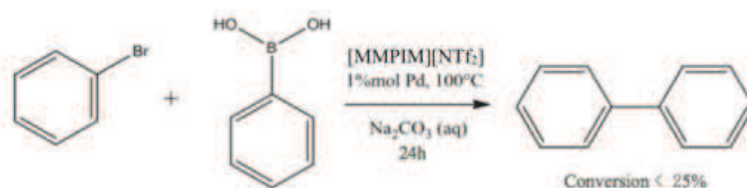


Figure 4.9: Text-book mechanism of palladium catalyzed Suzuki-Miyaura cross-coupling.

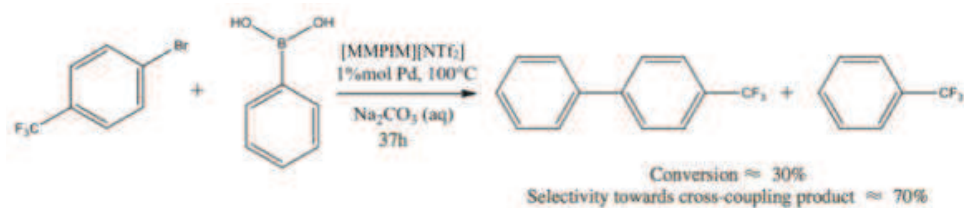
System 4 was then tested on the Suzuki cross-coupling between 1-iodo-4-nitrobenzene



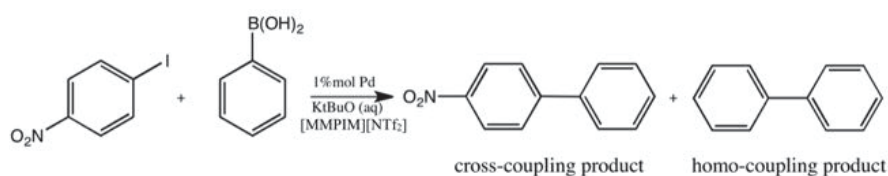
Scheme 4.8: Suzuki coupling between bromobenzene and phenylboronic acid

and phenyl boronic acid (Scheme 4.10). Results are summarized in Table 4.4. The reaction mixture remained black throughout the whole reaction. Total conversion was achieved within 1 h at 120 °C (entry 5, Table 4.4). However, the homo-coupling byproduct originating from phenylboronic acid could not be completely avoided whatever the temperature was (cross-coupling product/biphenyl \approx 9/1). TEM analyses before and after the catalytic reaction did not show significant changes except the formation of a few larger particles after the reaction ($d \approx$ 10-20 nm) (Fig. 4.10). The larger particles should result from Ostwald ripening.

The isolated organic products were analyzed by ICP-OES. No palladium was detected. The palladium concentration in the post-reaction solution was under the detection limit. No recycling test was done due to the limited product extraction efficiency (recovered mass \approx 60%-70%).



Scheme 4.9: Suzuki coupling between 1-bromo-4-(trifluoromethyl)benzene and phenylboronic acid



Scheme 4.10: Suzuki coupling between 1-iodo-4-nitrobenzene and phenyl boronic acid.

Table 4.4: Catalytic performances of system 4 on Pd-catalyzed Suzuki-Miyaura reaction^a.

Entry	Temperature (°C)	Reaction time (h)	Conversion ^b (%)	Selectivity ^{b,c} (%)
1	60	1	67	92
2		4	96	93
3		6	99	92
4	80	5	100	87
5	120	1	100	92

^a Reaction conditions: molar ratio: 1-iodo-4-nitrobenzene/phenyl boronic acid/KtBuO/Pd = 1/1.2/2.5/0.01; in [MMPIM][NTf₂] (1 mL).

^b Determined by GC and ¹H NMR using decane and mesitylene as internal standard respectively.

^c Selectivity towards the cross-coupling product.

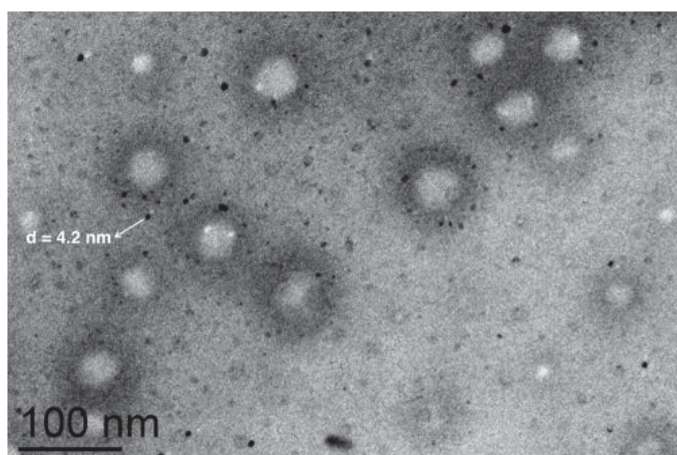
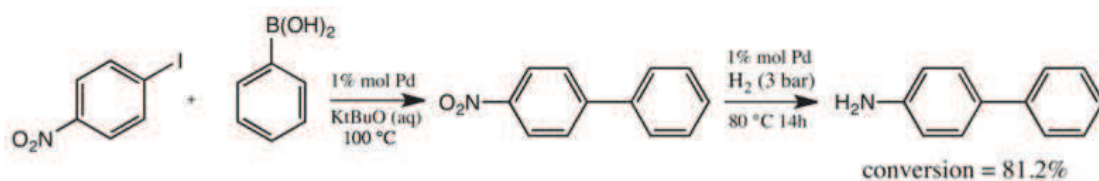


Figure 4.10: TEM image of System 4 after Suzuki-Miyaura cross-coupling (Scheme 4.10, entry 5, Table 4.4).

4.3.3 Pd-catalyzed cross-coupling/hydrogenation sequential process

The use of a single catalyst for multi-step syntheses is much appreciated because the lengthy separation and purification of intermediates can be avoided. Hence the dual catalytic behavior exhibited by metallic nanoparticles, acting as homogeneous (reservoir of molecular species) and heterogeneous (surface-like reactivity) catalysts, shows enormous potential in complex transformations for economic reasons [276, 336–338]

System 4 was applied to both Heck/hydrogenation and Suzuki/hydrogenation sequential reactions. The Suzuki/hydrogenation sequential reaction from 4-iodo-nitrobenzene and phenylboronic acid followed by hydrogenation catalyzed by system 4 gave the corresponding biphenyl aniline in a total conversion of 81% (Scheme 4.11), while sequential Heck-Mizoroki cross-coupling/hydrogenation process between iodobenzene and butenone followed by hydrogenation was not successful under 3 bar dihydrogen pressure at 80 °C, indicating that PdNPs were not reformed after the molecular leaching during the Heck coupling (see section 4.3.2) and consequently, the hydrogenation reaction could not proceed.



Scheme 4.11: Pd-catalyzed Suzuki/hydrogenation sequential reaction.

4.4 Catalytic study in glycerol — Exploration of other solvents with physicochemical properties close to RTILs

We studied the possibility to replace imidazolium-based RTILs by other eco-friendly solvents to see if the same synthesis methodologies can lead to similar PdNPs catalytic systems. Glycerol was chosen due to their physicochemical properties and their green character.

PdNPs dispersed in glycerol were synthesized under 3 bar H_2 pressure at 60 °C overnight and with the presence of respectively two types of PVP: $M=10,000$ g/mol and $M=29,000$ g/mol. Two molar ratios of Pd/PVP repeating unit (1/20 and 1/40) were applied. The TEM images of the four resulting catalytic systems show no obvious difference among them (Fig.4.11).

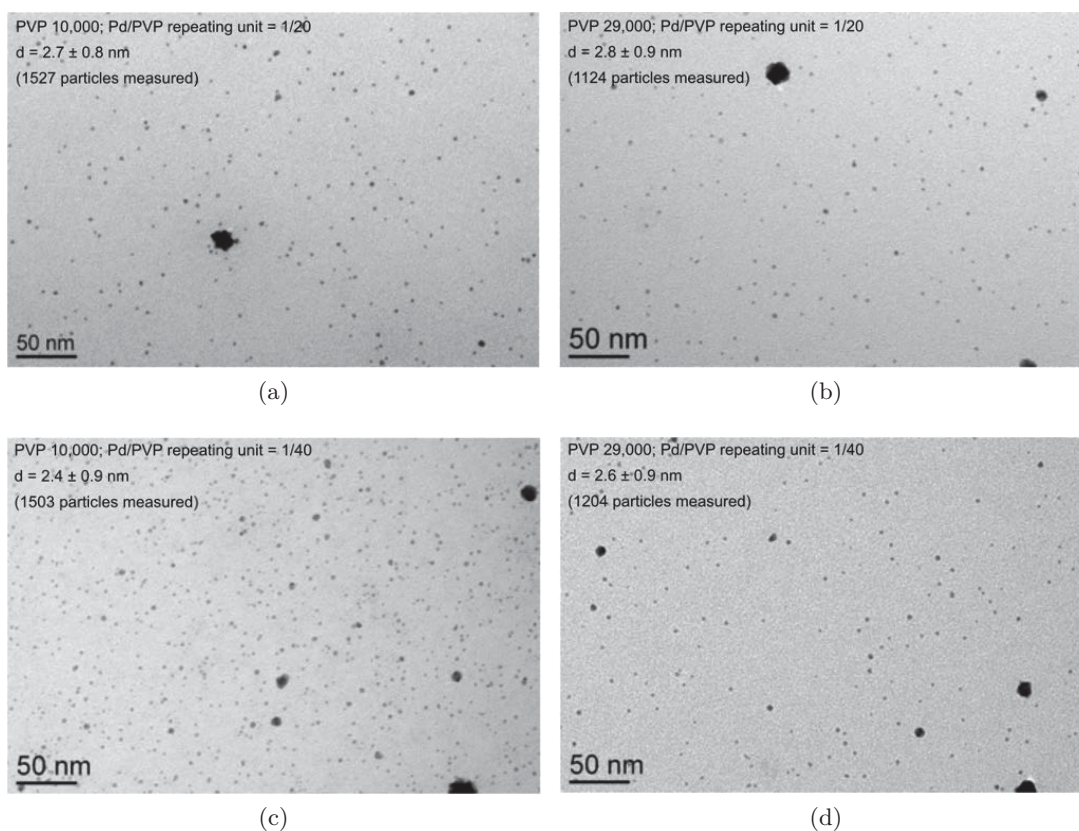


Figure 4.11: TEM images of PdNPs synthesized in glycerol

The influence of the PVP chain and Pd/PVP ratio on PdNP catalytic activity for hydrogenation of *trans*-4-phenyl-3-buten-2-one was then studied (Scheme 4.2). Catalytic results are presented in Table 4.5. For all the systems, the only product obtained corresponds to the hydrogenation of the exocyclic C=C bond.

Table 4.5: Catalytic results of glycerol-PVP colloidal PdNP systems on the hydrogenation of *trans*-4-phenyl-3-buten-2-one. (3 h at 80 °C)

Entry	PVP molecular weight	Pd/PVP repeating unit	Pd/substrate (%mol)	P(H ₂) (bar)	Conversion (%) ^a
1	10,000	1/20	0.1	3	100
2	29,000	1/20	0.1	3	100
3	10,000	1/40	0.1	3	97
4	29,000	1/40	0.1	3	92
5	10,000	1/20	0.1	1	91
6	29,000	1/20	0.1	1	46
7	10,000	1/40	0.1	1	98
8	10,000	1/20	0.01	1	19

^a Determined by GC-MS with decane as internal standard. No by-products observed

No significant differences were observed associated to the Pd/PVP repeating unit ratio (entries 1 and 3, 2 and 4, 5 and 7, Table 4.5). Under 3 bar of H₂ pressure, the nature of the polymer did not show an obvious consequence on the catalytic performance (entries 1–4, Table 4.5). However, at lower H₂ pressure (1 bar), PdNPs stabilized by PVP 29,000 were less active than those stabilized by PVP 10,000, for a Pd/ PVP repeating unit ratio of 1/20 (entries 5 and 6, Table 4.5). This is due to the encapsulation of PdNPs in long polymer chains that can induce a decrease in the metallic surface accessibility and in consequence a loss of the catalytic activity. It is noteworthy that the catalytic system based on PVP 10,000 with a molar ratio Pd/PVP repeating unit of 1/20 was still active at 0.01 mol% of palladium under 1 bar of H₂ (entry 8, Table 4.5).

4.5 Conclusions

To sum up, colloidal systems of palladium metallic nanoparticles were synthesized from palladium acetate (as precursor) in [MMPIM][NTf₂] via two methods: under hydrogen pressure and under thermal conditions. The thermal decomposition of palladium acetate generated a more homogeneously dispersed system than systems synthesized under hydrogen pressure. The presence of PVP helped to well stabilize palladium nanoparticles without hindering the access of reactants to the NP surface.

Among the 5 catalytic systems prepared, system 4 (prepared via thermal decomposition at 100 °C in the presence of PVP) shows the most homogeneous dispersion of PdNPs in [MMPIM][NTf₂]. System 4 was active for hydrogenation reactions, Heck-Mizoroki and Suzuki-Miyaura cross-couplings, and also for Suzuki cross-coupling/hydrogenation sequential process, but inactive for Heck cross-coupling/hydrogenation sequential process. This PdNP colloidal system also showed very good re-usability in hydrogenation of *trans*-4-phenyl-3-buten-2-one: almost no activity loss was observed after 12 times re-use.

The PdNPs prepared in the [MMPIM][NTf₂] show good and versatile reactivity, pro-

viding a guidance on types of reactions to be tested using the the catalytic membrane based on poly(ionic liquid) (Chapter 5), in order to compare the catalytic behavior of the colloidal system and that of the catalytic polymeric membrane.

Chapter 5

Catalytic polymeric membrane containing palladium nanoparticles

Résumé du Chapitre

Une membrane polymère catalytique a été préparée par la modification d'une membrane plane commerciale (MicroPES® membrana) en polyethersulfone servant de support au greffage de liquides ioniques de type imidazolium synthétisés au laboratoire. L'irradiation par UV peut générer des radicaux sur la chaîne de PES, permettant la formation de la liaison covalente entre le support et le gel de polyLI. La génération in situ de NPPd dans la membrane a été réalisée par la synthèse inter-matricielle. La membrane catalytique ainsi obtenue contient NPPd de 2 nm de diamètre moyen, bien dispersées dans la couche de polyLI. Les NPPd dans la membrane sont très concentrées (de l'ordre de 10^{14} NPs par mm^3). Leur répartition dans l'épaisseur de la membrane est hétérogène. Le relargage des NP n'a été observée ni au cours de filtrations ni au cours de la réaction catalytique avec une absence de Pd dans le perméat.

La membrane catalytique a montré une performance catalytique remarquable pour le couplage croisé de Suzuki-Miyaura entre le 1-iodo-4-nitrobenzène et l'acide phénylboronique. La membrane est tellement active qu'une conversion complète est obtenue par filtration des réactifs au travers de la membrane, sans formation de sous-produits, dans un temps de séjour de moins de 10 secondes à 60°C. Le produit souhaité est obtenu en continu dans le perméat.

Comparée à la suspension colloïdale de NPPd en batch (Chapitre 4), la membrane catalytique est environ 2000 fois plus rapide. Dans les deux cas, le couplage croisé de Suzuki-Miyaura est limité par la cinétique. L'accélération de la réaction réalisée par la membrane est probablement due à la haute concentration de palladium au sein de la membrane.

5.1 Introduction

Catalytic membranes have found applications in the field of fine chemistry, petrochemical industry, water treatment, etc. [339–342]. Unlike a batch reactor whose conversion rate slows down with time, a catalytic membrane gives constant conversion over time as it can be considered as a plug-flow reactor. Another advantage of a catalytic membrane is that no separation of the catalyst from the reaction medium is necessary to reuse the catalyst (if no leaching takes place).

Most catalytic membranes to the date are based on inorganic materials, with applications for steam reforming of methane, alkane dehydrogenation, oxidative coupling of methane, etc. [343–347]. Polymeric membranes used in membrane reactors, however, can have some advantages over the expensive inorganic membranes, namely lower production costs, crack-free thin membranes, and large scale production [344]. Polymeric membranes should be used under mild conditions ($<150\text{ }^{\circ}\text{C}$), and thus require a highly active catalyst to ensure good reactivity. Metallic nanoparticles (MNPs) have shown very interesting catalytic activity thanks to their high surface/volume ratio [348]. In general, their activity increases when they get smaller because of higher surface/volume ratio and higher fraction of the low-coordinated vertex and edge atoms. The high surface energy of MNPs makes them thermodynamically unstable. The presence of appropriate stabilizers is necessary to prevent their aggregation, which usually results in loss of activity. This is the reason why poly(ionic liquid)s (polyILs) were introduced into the membrane: to stabilize the MNPs by electrosteric effect.

H. Hagiwara et al. reported the immobilization of palladium acetate in an ionic liquid in silica pores [349]. Since no chemical bonding exists between the ionic liquid and silica, reaction can be carried out only in a hydrocarbon solvent in order to avoid removal of the ionic liquid layer from the silica. Nevertheless, palladium leaching from the silica support was still observed [349]. In our case, polyIL was chemically grafted to MicroPES[®]-2F support membrane to stabilize palladium nanoparticles (PdNPs) by electrosteric effect so that leaching of both nanoparticles and ionic liquid could be effectively prevented. The well-defined PdNPs immobilized inside the membrane provided catalytically active sites for the organic transformations envisaged [350].

It is generally believed that in a flow-through catalytic membrane contactor, the mass-transfer resistance towards the catalyst can be eliminated by forcing reactants to flow through membrane pores [351]. The intensive contact between the reactant mixture and the catalyst may lead to a higher apparent conversion rate [343]. In this chapter, we seek for the answers to the following questions based on experimental observations and theoretical calculations:

1. How fast can it be (The catalytic membrane can accelerate the apparent reaction rate to what extent)?
2. How it happens (What on earth is responsible for the acceleration)?
3. How far can it go (The catalytic membrane is efficient in what kind of reactions and inefficient for what kind of reactions)?

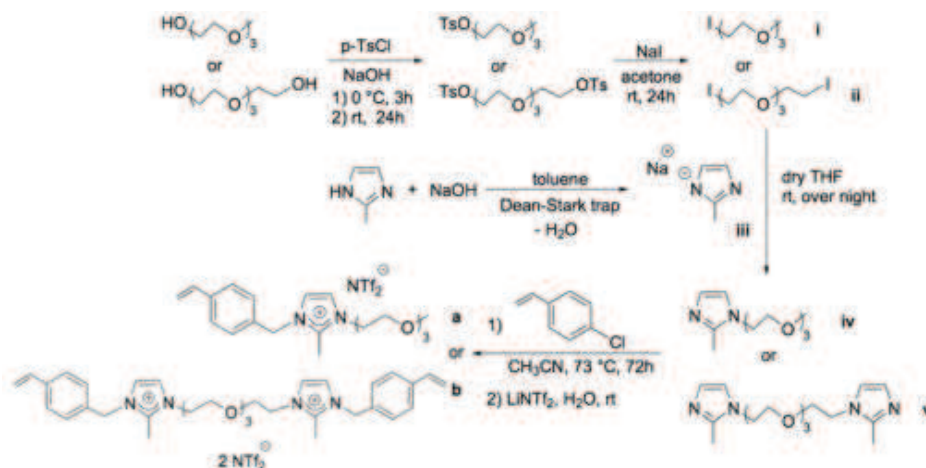
Part of the results in this chapter is published on Journal of Membrane Science [352].

5.2 Preparation and characterization of the catalytic membrane

5.2.1 Choice and synthesis of imidazolium-based ionic liquids

The ionic liquids **a** and **b**, serving as stabilizers for palladium nanoparticles, were synthesized following the methodology shown in Scheme 5.1. The cross-linker **b** is used to prevent the dissolution of the polyIL by the organic solvent during the catalytic reaction. A cross-linked polymer network, compared to a branched polymer, is probably also better for preventing palladium from leaching out of the membrane and polluting the product. The length and molecular weight of the cross-linking monomer were appropriately adapted to favor the formation of a homogeneous network [353–356]. The presence of the methyl group at C2 position on the imidazolium ring avoids the formation of molecular palladium N-heterocyclic carbene complexes under basic conditions [357], which could eventually promote palladium leaching from the membrane and surface poisoning.

As shown in Scheme 5.1, we prepared first the iodo-ethers **i** and **ii** following a two-step classical methodology where the corresponding alcohols were protected by reaction with p-tosyl chloride, giving the corresponding tosylate derivatives; a further nucleophilic substitution using sodium iodide led to **i** and **ii**. These iodo-ethers reacted with the sodium imidazole salt (prepared by deprotonation of imidazole with NaOH) to give the neutral mono- and bis(imidazole)s **iv** and **v**, which were quaternized by treatment with 4-vinylbenzyl chloride. The anion exchange reaction using LiNTf₂ led to the desired imidazolium derivatives **a** and **b**.



Scheme 5.1: Synthesis of imidazolium-based RTIL **a** and **b**.

5.2.2 Preparation of the catalytic membrane

The preparation of the catalytic membrane involves two main steps : (i) functionalization of the MicroPES®-2F (PES=polyethersulfone) with polyIL by UV-induced polymerization; (ii) loading the membrane with MNPs (Fig.5.1).

In a first step, the IL was photochemically grafted to a PES support membrane. In the second step, the membrane was loaded with palladium via intermatrix synthesis [358]. The IL-grafted membrane was soaked in a solution of $K_2[PdCl_4]$, where the IL anions (NTf_2^-) were exchanged by $[PdCl_4]^{2-}$. The membrane turned from white color to brown after the ion exchange. Consecutively, a $NaBH_4$ solution was filtered through the membrane, which immediately turned from brown to black due to the reduction of Pd(II) to Pd(0) (Fig.5.2). The solvent used for the intermatrix synthesis is a water/methanol (1/1 volume ratio) mixture.

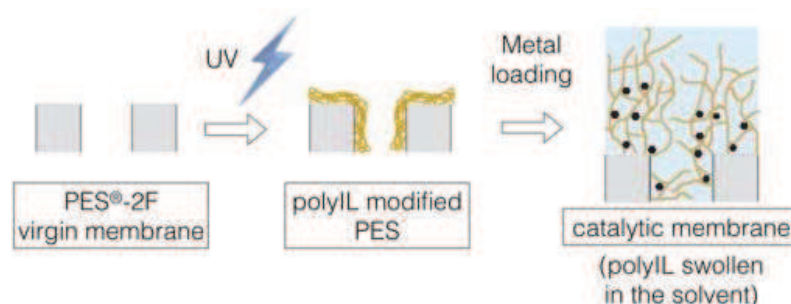


Figure 5.1: Preparation of the catalytic membrane (◆ = MNP; scale not respected).

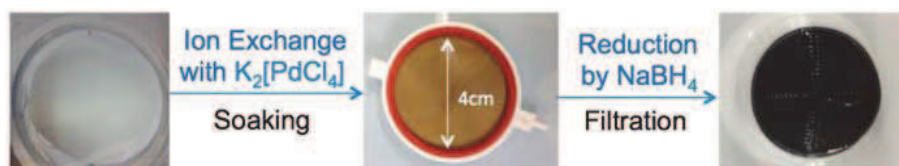


Figure 5.2: Palladium loading via intermatrix synthesis

5.2.3 Characterization of the catalytic membrane

Grafting degree

PES is a photosensitive material which generates radicals under UV irradiation [359]. Consequently, covalent bonds can be formed between the MicroPES® support membrane and the polyIL during the photografting. The membranes were weighed before and after the photografting step to determine the amount of ionic liquid grafted onto the PES membrane. The membrane was thoroughly rinsed with ethanol after photografting. The membrane mass after grafting was measured after ethanol evaporation

(when no more weight change could be observed). The grafting degree was calculated by Eq. 5.1

$$\text{Grafting degree} = \frac{m_g - m_i}{m_i} \times 100\% \quad (5.1)$$

where m_g is the membrane weight after photo-grafting and m_i is the membrane weight before photo-grafting.

The average degree of grafting was found to be 32.0% with standard deviation of 2.2%. The average mass of polyIL grafted onto the membrane was $1.2 \text{ mg}\cdot\text{cm}^{-2}$.

Ethanol permeability

Reactions were carried out on the catalytic membrane in ethanol. Therefore, ethanol permeability was measured instead of water permeability. The average ethanol (96% vol) permeability of the catalytic membrane at 25°C was $15 \pm 2 \text{ mL}\cdot\text{min}^{-1}\cdot\text{cm}^{-2}\cdot\text{bar}^{-1}$ ($9.00 \pm 1.20 \times 10^3 \text{ L}\cdot\text{h}^{-1}\cdot\text{m}^{-3}\cdot\text{bar}^{-1}$), which is comparable to the PES virgin membrane permeability ($17.9 \text{ mL}\cdot\text{min}^{-1}\cdot\text{cm}^{-2}\cdot\text{bar}^{-1}$, or $1.07 \times 10^4 \text{ L}\cdot\text{h}^{-1}\cdot\text{m}^{-3}\cdot\text{bar}^{-1}$). No significant drop in the permeability (or pore size reduction) of the membrane was triggered by the grafting.

Membrane surface change induced by photo-grafting

SEM, ATR-IR analyses and contact angle measurement were performed on the IL-grafted membrane. All results showed that the membrane surface was modified by the polyIL.

SEM analysis

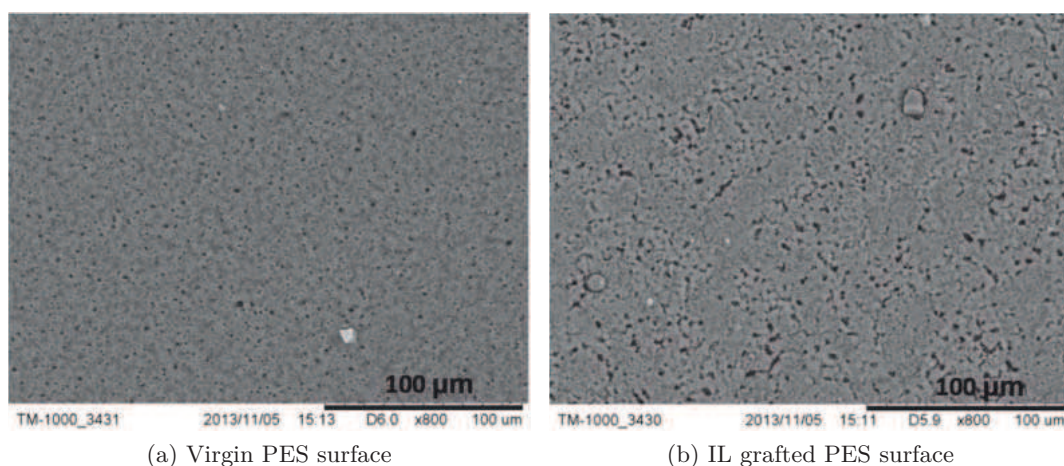
SEM images corroborated the chemical modification of the membrane after the photo-grafting treatment by an obvious morphology change (Fig. 5.3).

ATR-IR analysis

Change of the chemical composition on the membrane surface was confirmed by ATR-IR analysis. Fig.5.4 shows the appearance of new absorption bands for the grafted membrane. The absorption bands below 1500 cm^{-1} are mainly assigned to the vibrations of bis(trifluoromethylsulfonyl)imide anion: 1352 cm^{-1} is associated to the SO_2 asymmetric stretching; 1196 cm^{-1} is assigned to the CF_3 asymmetric stretching. The absorption band at 1058 cm^{-1} can be attributed to the SNS asymmetric stretching with contribution from a ring in-plane asymmetric stretching and a CC stretching [360]. These characteristic bands evidence the coverage of the membrane surface with the ionic liquids involved.

Contact angle and swelling effect

Contact angles of water and ethanol (96% vol.) were measured on the membrane surface before and after the UV treatment (Table 5.1). The polyIL layer turned the membrane surface from hydrophilic to hydrophobic, as evidenced by the increase of water contact angle. The contact angle of ethanol on the modified membrane surface was



(a) Virgin PES surface

(b) IL grafted PES surface

Figure 5.3: SEM images of the membrane surface (a) before and (b) after the photo-grafting.

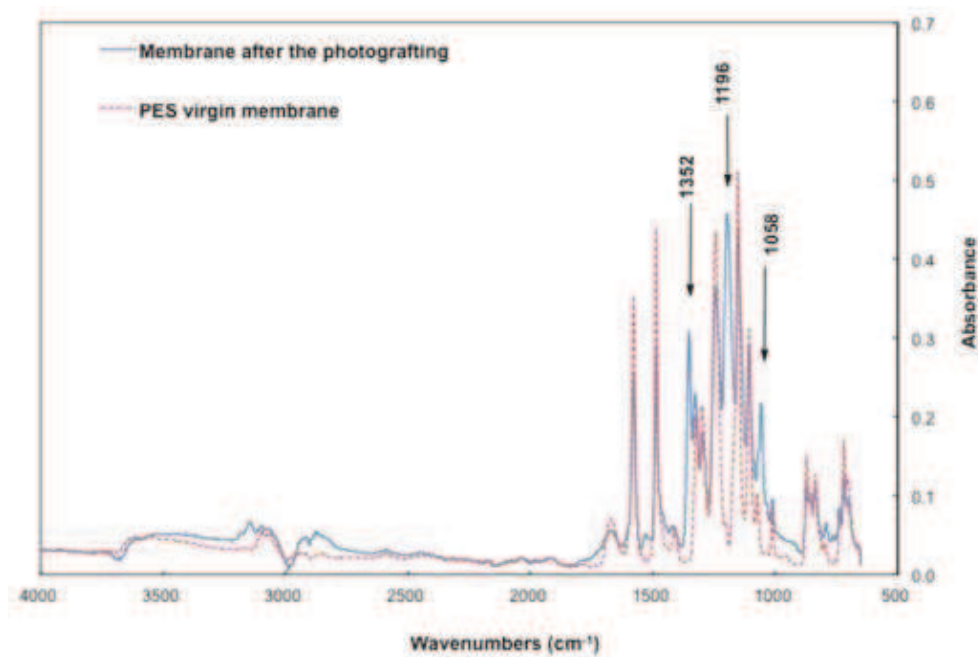


Figure 5.4: ATR-IR spectra of pristine PES membrane (dotted red line) and the photo-grafted membrane (solid blue line).

non-measurable: a local volume increase of the membrane was observed immediately after the ethanol drop was deposited. This phenomenon did not occur in the case of virgin membrane. The rapid volume increase signifies a severe swelling of the polyIL by ethanol, which is comprehensible since the ionic liquid polymer chains are easily solvated in ethanol.

Table 5.1: Contact angle of water and ethanol (96% vol.) on the surface of virgin PES membrane and polyIL modified membrane.

	water	ethanol
Virgin PES	$35.6^\circ \pm 2.0^\circ$	$19.4^\circ \pm 1.7^\circ$
PolyIL modified PES	$81.5^\circ \pm 9.3^\circ$	$\approx 0^\circ^*$

* Obvious swelling observed (sudden increase of volume once in contact with ethanol)

As explained in Chapter 1 (section 1.5.4), the size of MNPs formed inside the polymer matrix is limited by the nanoporosity of the swollen polymer [234, 235]. In the inter-matrix synthesis, the polyIL was probably partially swelled by the solvent (water/methanol 1/1 vol. mixture), hence PdNP size was effectively limited by the non fully expanded nano porosity. While catalytic reactions were carried out in ethanol (section 5.3), polymer chains can be swollen to a larger extent, leaving space for reactant molecules to diffuse through the polymer chains and reach the NP surface. If the reactant molecule size is smaller than the polymer correlation length (defined as the average distance from a monomer on one chain to the nearest monomer on another chain) in the swollen state, the diffusion coefficient of the molecule is mainly determined by the solvent viscosity [237].

Palladium loading and distribution inside the membrane

The average palladium loading of the catalytic membrane (4 cm of diameter) was $(7.5 \pm 0.4) \times 10^{-3}$ mmol, or $(0.60 \pm 0.03) \times 10^{-3}$ mmol·cm⁻² (normalized to the membrane surface area) or 0.52×10^{-3} mmol·mg⁻¹ (normalized to mass of polyIL). By comparing the quantity of the NTf₂ anion coming from the IL grafted onto the membrane and the final palladium loading, we can infer that ca. 60% of the NTf₂ anion was exchanged by [PdCl₄]²⁻.

Ethanol was filtered through the catalytic membrane to study the possible palladium leaching from the membrane. By ICP-OES analyses, no leaching was observed (in the permeate, the palladium concentration was below the detection limit of the technique, i.e. 3 and 15 ppb respectively for the detecting wavelength of 340.3 nm and 361.0 nm).

The PES flat sheet membrane is an anisotropic membrane, with the smallest pore sizes localized approximately 30-40 μ m from the IL-grafted membrane surface. The IL-grafted membrane surface was the side of the membrane facing the UV light during the

photo-grafting. Consequently, most of the ionic liquid was grafted to the part of the membrane facing the light near the surface. EDX SEM analysis provided us information about the palladium concentration along the membrane thickness. As shown in Fig.5.5, most palladium was essentially distributed from the IL-grafted surface to the densest part of the membrane.

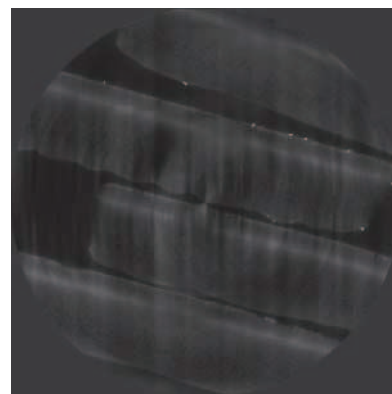
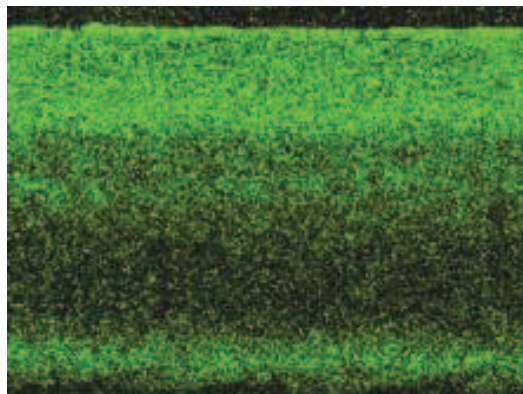
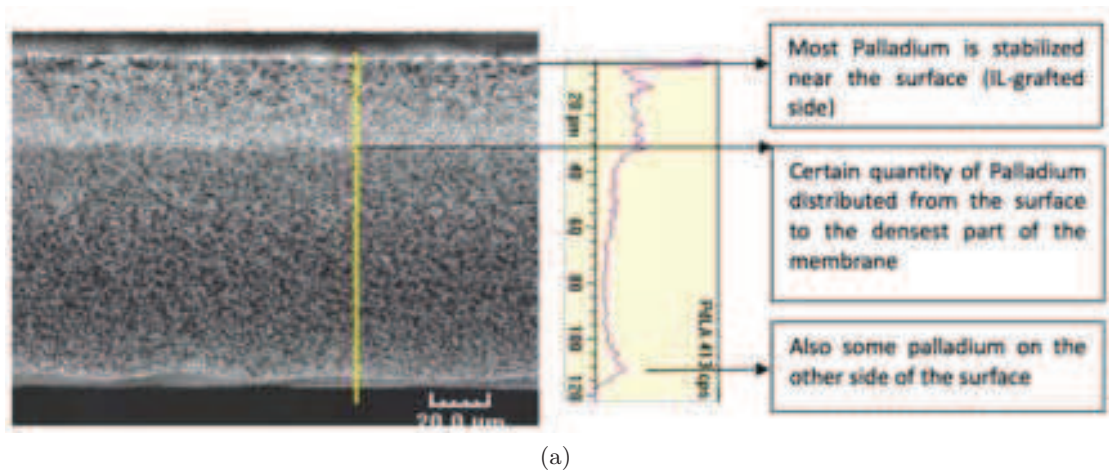


Figure 5.5: (a) Palladium distribution along the membrane thickness (SEM-EDX analysis); (b) palladium cartography (SEM-EDX analysis); (c) X-ray tomography (sample containing 4 membrane cross-sections)

TEM of the catalytic membrane's cross-section with zooming on the IL-modified side (Fig.5.6) and the electronic tomography analysis (Fig.5.7) showed that most palladium NPs were stabilized by the poly(ionic liquid) rather than by the PES support membrane. PdNPs (mean diameter: 2 ± 1 nm; see Fig.5.11) inside the membrane were very close to each other (inter-NP distance in the same order as the NP size). The large number of PdNPs per unit volume (ca. $4 \times 10^{14} \text{ mm}^{-3}$, value deduced from the palladium concentrated zone, i.e. reactive zone of the membrane, the blue circle zone in Fig.5.6-d

is an example) provides more active catalytic sites, which can proportionally increase the apparent reaction rate [361]. The small inter-particle distance helps to intensify the contact between reactants and catalyst by reducing the diffusion length but could also induce concentration gradient inside the PolyIL containing PdNPs.

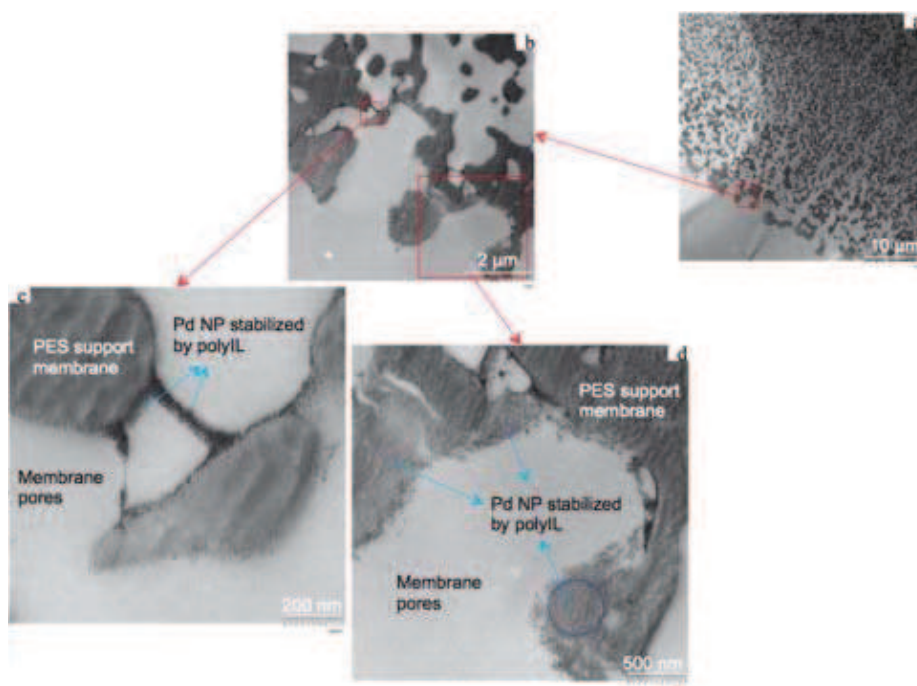


Figure 5.6: TEM images of the membrane cross-section with zooming on the surface.

Our group previously published a work on catalytic hollow fiber membranes obtained using acrylic acid as modifying agent instead of ionic liquid [139]. The PdNP mean diameter was found to be 5 ± 2 nm in the case of poly(acrylic acid) (polyAA). The difference in palladium size may result from the deviation of the swelling extent in the metal loading step. In fact, the graft layer material determines the partition coefficient between the liquid phase and the swollen-gel phase, and consequently the type of reactions adapted to that kind of graft material. As an example, the polyAA modified membrane was designed for water treatment (affinity towards water and water soluble compounds) and the polyIL modified membrane would rather be adapted for reactions in organic solvents (polyIL chains easily solvated by organic solvents).

Comparison to non-grafted PES membrane loaded with palladium

A PES virgin membrane was loaded with palladium in the same manner as described above (section 5.2.2). The membrane color was slightly tinged with pale grey after the metal loading. The palladium loading of the PES virgin membrane was 3.4×10^{-5}

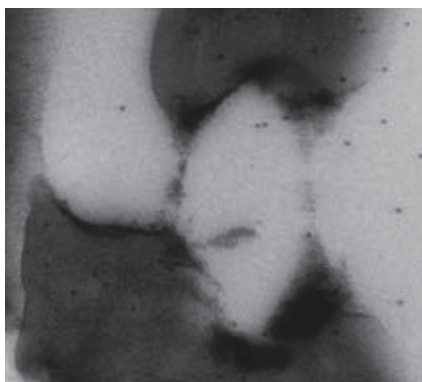


Figure 5.7: Visualization of the distribution of PdNPs stabilized by polyIL by electronic tomography (The spheric nanoparticles in the figure are gold nanoparticles added during the sample preparation for the distinction of depth inside the sample. PdNPs appear much smaller in the figure).

$\text{mmol}\cdot\text{cm}^{-2}$, 17 times less than that of IL modified membrane. Unlike the IL functionalized membrane, PdNPs present in the PES virgin membrane were mostly aggregated, as shown in Fig.5.8. The presence of PdNPs inside the non-modified PES membrane was probably due to the adsorption of the palladium salt on the membrane surface or to the encapsulation of the $\text{K}_2[\text{PdCl}_4]$ solution inside the membrane pores by capillary forces.

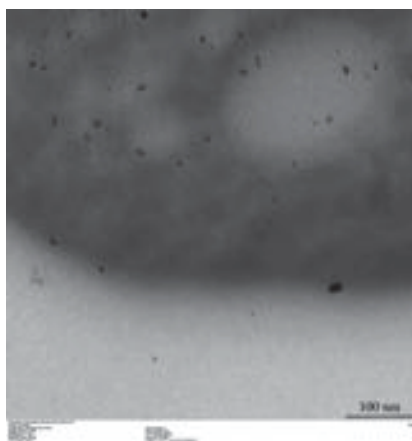
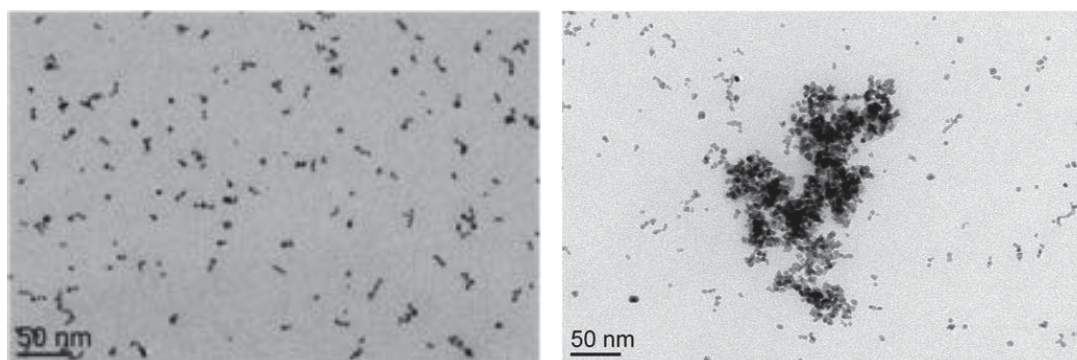


Figure 5.8: Non-modified PES membrane loaded with palladium.

5.3 Comparison of catalytic activity between the catalytic membrane and the colloidal PdNPs in batch reactor on Suzuki-Miyaura cross-coupling reaction

5.3.1 Catalytic performance of the colloidal PdNPs in the batch reactor

Colloidal palladium System 4 (see Chapter 4) was used as a reference for colloidal palladium activities in a batch reactor, to compare to the activity of the catalytic membrane. Here we recall the TEM image of system 4 (Fig.5.9-a) and its reactivity on Suzuki-Miyaura cross-coupling between 1-iodo-4-nitrobenzene and phenyl boronic acid at 60°C (Scheme 5.2, Table 5.2) to ease the reading. The mean diameter of the PdNPs was 4 ± 2 nm, about twice the size of those immobilized in the membrane. In addition, despite the presence of the co-stabilizer (PVP), agglomerates could not be completely avoided (Fig.5.9-b). Light scattering measurements evidenced the presence of particles larger than 100 nm. Increase in particle size or formation of aggregates can induce a decrease in reactivity (due to the smaller proportion of low-coordinate vertex, edge and surface atoms). Compared to the catalytic membrane, around 200 times fewer PdNPs per unit volume are present in the colloidal system. The mean inter-particle distance calculated from the Pd concentration and the particle diameter is in the range of 50-100 nm, larger than that observed in the catalytic membrane.

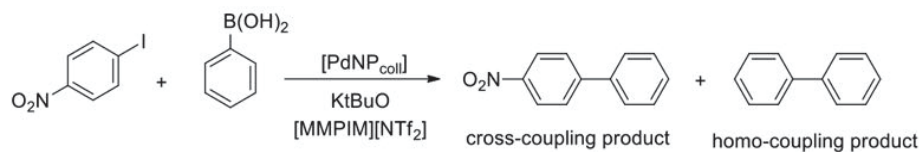


(a) PdNP size: 4 ± 2 nm (1389 particles measured)

(b) Presence of aggregates

Figure 5.9: TEM images of the PdNPs in the colloidal system

As can be seen in Table 5.2, it took 6h for the reaction to be complete using the colloidal palladium in the batch reactor. And around 10% of homo-coupling byproduct was observed. By plotting $\ln(C/C_0)$ as a function of time, a linear correlation was found (C_0 is the initial reactant concentration). Therefore, the apparent kinetics of the reaction in the batch reactor turned out to be a first order reaction with an apparent reaction rate constant determined as $k_{app,batch} = 2.2 \times 10^{-4} s^{-1}$, or $0.21 s^{-1} \cdot g^{-1}$ when



Scheme 5.2: The Suzuki-Miyaura cross-coupling reaction under batch conditions catalyzed by colloidal PdNPs.

Table 5.2: Pd-catalyzed Suzuki-Miyaura cross-coupling reaction at 60°C using the preformed colloidal system^a.

[C] ^b (mol·L ⁻¹)	Pd/substrate molar ratio	Reaction time (h)	Conversion ^c (%)	Selectivity ^{c,d} (%)
1	1/100	1	67	92
		4	96	93
		6	99	92

^a Reaction conditions: molar ratio: 1-iodo-4-nitrobenzene/phenylboronic acid/tBuOK/Pd = 1/1.2/2.5/0.01, in [MMPIM][NTf₂] (1 mL);

^b Concentration of 1-iodo-4-nitrobenzene;

^c Determined by GC and ¹H NMR using mesitylene as internal standard;

^d Selectivity towards the cross-coupling product.

normalized to mass of palladium and $6 \times 10^{-4} \text{ s}^{-1} \cdot \text{m}^{-2}$ when normalized to total catalyst surface area (PdNPs were considered as full-shell nanoparticles [362] (see Chapter 1, section 1.5); aggregates were not taken into consideration for surface area calculations).

Concerning the mass transfer resistance

Stokes number is a dimensionless value defined as the ratio of the characteristic time of a particle to a characteristic time of the flow (Eq.5.2). When $\text{Stk} \ll 1$, particles follow streamlines closely.

$$\text{Stk} = \frac{\rho d^2 N}{18\mu} \quad (5.2)$$

with ρ and d as respectively the density ($12.0 \times 10^3 \text{ kg} \cdot \text{m}^{-3}$) and diameter ($4 \times 10^{-9} \text{ m}$) of PdNPs, N as agitator speed ($8.3 \text{ tr} \cdot \text{s}^{-1}$) and μ as dynamic viscosity of [MMPIM][NTf₂] ($\approx 20 \times 10^{-3} \text{ kg} \cdot \text{m}^{-1} \cdot \text{s}^{-1}$ [363, 364]). The Stokes number of the colloidal system was calculated to be 5×10^{-12} , indicating that the PdNPs follow the streamline so closely that the relative velocity between PdNPs and the liquid phase is nearly zero. The convection is inefficient and actually negligible. The mass transfer is therefore effectuated uniquely by diffusion. The mass transport coefficient (k_d^b in the batch reactor) and the diffusion coefficient (D) can be correlated by the Sherwood number Sh (Eq.5.3), which can be

calculated by Eq.5.4 [365, 366].

$$\frac{k_d^b \cdot d}{D} = Sh \quad (5.3)$$

$$Sh = 2 + \frac{d}{\sqrt{\pi Dt}} \approx 2 \quad (5.4)$$

At $t > 1 \times 10^{-3} s$, $d/\sqrt{\pi Dt} < 0.02$, hence $Sh \approx 2$. The diffusion coefficient of the solute molecules at $60^\circ C$ can be calculated by Stokes-Einstein equation (Eq.5.5) and was found to be $1.22 \times 10^{-11} m^2 \cdot s^{-1}$ for the colloidal system.

$$D = \frac{k_B T}{6\pi\mu r} \quad (5.5)$$

where k_B is Boltzmann's constant, T is the absolute temperature and r is the solute molecule radius (in the order of 1 nm).

The mass transfer coefficient was calculated to be:

$$k_d^b = 5.8 \times 10^{-3} m \cdot s^{-1} \quad (5.6)$$

The boundary layer thickness around the particle is hence $\delta_p = D/k_d^b = 2 \text{ nm}$. The specific surface area a (total surface area of the NPs divided by the reaction mixture volume, $m^2 \cdot m^{-3}$) of the colloidal system was estimated to be in the range of $5.3 \times 10^3 m^2 \cdot m^{-3}$ to $3.6 \times 10^5 m^2 \cdot m^{-3}$ (NP mean diameter varying from 4 nm to 100 nm, taken into consideration the presence of aggregates). The mass transfer flux ($a \cdot k_d^b, s^{-1}$) was thus found much (5 to 7 orders of magnitude) higher than the apparent reaction rate constant. Therefore, the activity of the colloidal system was in reaction-limited regime. Mathematic expression of the intrinsic reaction rate constant on the catalyst surface (Eq.5.14) can be deduced based on the fact that there is no material accumulation on the catalyst surface (Eq.5.7-5.9, Fig.5.10, no internal diffusion inside the dense metallic nanoparticles):

$$\text{Reaction rate} = \text{Diffusion flux} \quad (5.7)$$

$$V \cdot a \cdot k_{batch} \cdot C_p = V \cdot a \cdot k_d^b \cdot (C_b - C_p) \quad (5.8)$$

$$C_b = (k_{batch}/k_d^b + 1) \cdot C_p \quad (5.9)$$

The real kinetic is therefore:

$$-\frac{dC_b}{dt} = a \cdot k_{batch} \cdot C_p \quad (5.10)$$

$$-\frac{dC_b}{dt} = \frac{ak}{k_{batch}/k_d^b + 1} C_b \quad (5.11)$$

$$C_b = C_{b0} \cdot \exp\left(-\frac{akt}{k_{batch}/k_d^b + 1}\right) = C_{b0} \cdot \exp(-k_{app} \cdot t) \quad (5.12)$$

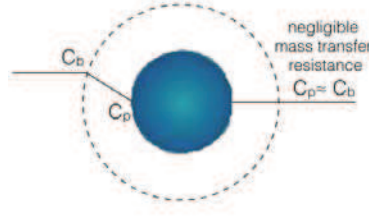


Figure 5.10: Visualization of the boundary layer around a NP (C_b = bulk reactant concentration; C_p = reactant concentration on the catalyst surface).

Herein, V is the reaction mixture volume; C_b is the reactant bulk concentration in the batch reactor; C_{b0} is the initial bulk concentration; C_p is the reactant concentration on the catalyst surface; k_{batch} and k_{app} are respectively the intrinsic and apparent reaction rate constant in the batch reactor.

Hence

$$k_{batch} = \frac{k_{app}}{a - k_{app}/k_d^b} \quad (5.13)$$

Since $k_{app}/k_d^b = 0.04 \ll a$, the intrinsic kinetic $a \cdot k_{batch}$ is approximately the same as the apparent kinetics (Eq.5.14).

$$a \cdot k_{batch} \approx k_{app} = 2.2 \times 10^{-4} \text{ s}^{-1} \quad (5.14)$$

The intrinsic reaction rate constant on the catalyst surface for the batch reactor k_{batch} is estimated to be in the range of $6.0 \times 10^{-10} - 4.1 \times 10^{-8} \text{ m} \cdot \text{s}^{-1}$ (exact value of specific surface area a can not be determined; only a range can be given, see above), which means that the concentration on the NP surface is the same as the bulk concentration ($C_p \approx C_b$, Eq.5.9, with $k_{batch}/k_d^b \ll 1$, Fig.5.10).

5.3.2 Performance of the catalytic membrane

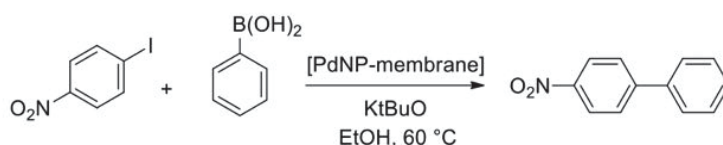
For a catalytic membrane, the reaction time can be expressed as the residence time of the solution inside the membrane (Eq. 5.15):

$$\tau = \frac{L}{F} \cdot \epsilon \cdot S = \epsilon \cdot \frac{L}{J} \quad (5.15)$$

with L as the membrane thickness ($110 \times 10^{-4} \text{ cm}$), F the permeate flow rate ($\text{mL} \cdot \text{s}^{-1}$), S the membrane surface area (12.6 cm^2) and J the flux density ($\text{ml} \cdot \text{s}^{-1} \cdot \text{cm}^{-2}$). The membrane surface porosity ϵ is unknown and is therefore taken to 1 for the following residence time calculations. Consequently, the reaction times given below do not take into account of the membrane porosity which is probably in the range of 0.7 to 0.8 for this kind of membrane. The real reaction is thus smaller than the values given below by a factor of 0.7 to 0.8.

The Suzuki-Miyaura cross-coupling reaction described above was carried out on the

catalytic membrane under flow-through conditions in ethanol at 60°C (Scheme 5.3). Full conversions were achieved by one single filtration with a residence time of ca.9 seconds (Table 5.3). No homo-coupling byproducts were observed. Given the selectivity observed in the batch reactor, the formation of biphenyl should be much slower than the cross-coupling product. In the case of the catalytic membrane, the residence time of reagents in the membrane was so short that the formation of the homo-coupling byproduct was prevented. Accordingly, the high reactivity of the catalytic membrane favors the chemoselectivity of the process. Interests on catalytic membranes have recently aroused, but the reaction times of those membranes for Suzuki coupling reactions are in the order of hours and catalyst leaching is produced [367,368].



Scheme 5.3: Pd-catalyzed Suzuki-Miyaura cross-coupling under flow-through conditions.

Table 5.3: Suzuki-Miyaura cross-coupling reaction catalyzed by the catalytic membrane at different conditions^a.

[C] ^b mol·L ⁻¹	Flow rate ml·min ⁻¹	Filtration volume mL	Pd/substrate molar ratio	τ s	Conversion ^c %	Selectivity ^c %
0.016	1.38	62	1/132	5.8	83.4	100
	0.88			9.1	100	100
0.032	0.88	31		9.1	100	100

^a Reaction conditions: molar ratio 1-iodo-4-nitrobenzene/phenyl boronic acid/tBuOK/Pd = 1/1.2/2.5/0.0076;

^b Concentration of 1-iodo-4-nitrobenzene.;

^c Determined by GC and ¹H NMR using mesitylene as internal standard.

The catalytic membrane was re-used 8 times without activity loss (no more runs were done), showing the robustness of the membrane. TEM analysis after catalytic membrane reusing did not evidence significant changes in the shape and size of the PdNPs (Fig. 5.11). In fact, a slight increase of the NP diameter occurs but, taking into account the standard deviation, the NP diameter remains practically constant. Neither palladium nor IL was detected in the product, which proved the membrane stability under catalytic conditions and filtration flows.

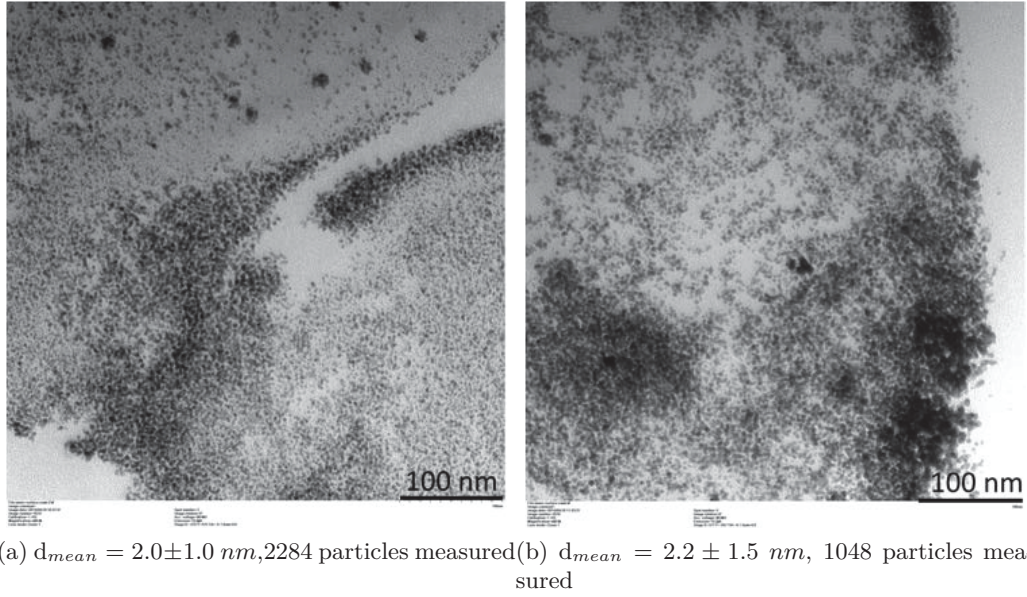


Figure 5.11: TEM images of the catalytic membrane: a) before and b) after the 9th catalytic run, showing the corresponding PdNP mean diameter

Calculations on mass transfer resistance and rationalization of the high catalytic activity

The mass transfer coefficient around the catalyst supported on the membrane k_d^m can be estimated by Eq.5.16 and found to be $0.41 \text{ m} \cdot \text{s}^{-1}$, much larger than that in batch reactor k_d^b ($5.8 \times 10^{-3} \text{ m} \cdot \text{s}^{-1}$) (Calculation deduced from $Sh = 2$, which is also valid for the catalytic membrane [369] gives the same k_d^m value). The intrinsic reaction rate constant should be approximately the same for PdNPs in the batch reactor and inside the membrane (maybe lightly higher in the membrane as NPs in the membranes are smaller). The mass transfer resistance imposed by the boundary layer around the catalyst is therefore also negligible in the case of the catalytic membrane.

$$k_d^m = D/e = 0.41 \text{ m} \cdot \text{s}^{-1} \quad (5.16)$$

In Equation 5.16, D is considered to be the reactant diffusion coefficient in ethanol at 60°C , $4.1 \times 10^{-10} \text{ m}^2 \cdot \text{s}^{-1}$, since obvious swelling of the polyIL occurs in ethanol (Diffusion coefficient mainly determined by the solvent viscosity when the molecule size is smaller than polymer correlation length ξ [237], see Chapter 1. section 1.5.4); and e the boundary layer thickness, considered to be half inter-particle distance ($e \approx 1 \text{ nm}$). Even if D is 100 times smaller, the mass transfer resistance imposed by the boundary layer around the catalyst is still not a limiting factor. The conventional belief on forced flow through membrane reactor is that the intensified contact between the catalyst and the reactants is responsible for the reaction acceleration as local mass transfer resistance can be effectively eliminated. However, improvement on mass transfer would not

have obvious contributions to the apparent reaction rate for kinetic-limited reactions, the Suzuki-Miyaura cross-coupling between 1-iodo-4-nitrobenzene and phenyl boronic acid is an example. The remarkable decrease in reaction time in the membrane (from 6h to 9s for complete conversion) points to the fact that the apparent reaction rate get multiplied. A simple calculation can help to understand how the apparent reaction rate was accelerated. The volume of the membrane used in the experiments is 0.14 cm³. Hence the liquid volume retained in the membrane is around 0.1 cm³, taking into account the porosity. For a reaction solution concentration of 0.016 mol/L, the reactant quantity inside the membrane volume is 1.6×10⁻⁶mol. The concentration profile in the membrane pores follows a plug flow pattern (see Chapter 6). When the reaction solution is filtered through the membrane (where the catalyst get into contact with the reagents and catalyzes the reaction), the Pd/substrate molar ratio in the local environment of the membrane is 4.7, 470 times higher than that in the batch reactor (1/100). The real Pd/substrate molar ratio can be even higher due to the heterogeneous catalyst distribution inside the membrane. As demonstrated above, there exist reactive zones inside the membrane where the catalyst is highly concentrated. It should be mentioned that molar ratio calculated here differs from that given in Table 5.3. The latter concerns the total reactant quantity treated by the membrane. To be more precise in describing the relative amount of reactant and catalyst, the ratio of catalyst surface to substrate amount should be compared (to reflect number of active sites) instead of Pd/substrate molar ratio (see further in Table 5.4, entry 4). The high local Pd/substrate ratio can only be achieved in the flow through configuration: every single volume of reaction solution is forced into the local high catalyst concentration environment. If the same membrane is submerged in a batch reactor, the catalytic performance will be no more outstanding [139]. It is also noteworthy that despite the high Pd/substrate ratio, the total palladium amount in the membrane is fairly low.

Modelling of the catalytic membrane

Isothermal plug flow is achieved in the membrane pores under the experimental conditions (see Chapter 6). Hence a monodimensional first order pseudo-homogeneous reaction with constant intrinsic reaction rate is assumed in a first approach to model the catalytic membrane. The differential mass balance for the catalytic membrane at steady state taking into consideration the convective flow, diffusion and reaction can be then expressed by Eq.5.17. The external mass transfer resistance through the boundary layer around the catalyst is neglected (concentration on the catalyst surface equals to the bulk concentration).

$$D \frac{d^2 C}{dz^2} - v \frac{dC}{dz} - a k_{mem} C = 0 \quad (5.17)$$

with D as diffusion coefficient ($4.1 \times 10^{-10} \text{ m}^2 \cdot \text{s}^{-1}$); v as convective velocity; C as concentration of the reactant, 1-iodo-4-nitrobenzene; a as specific surface area of the catalyst (total catalyst surface area divided by the membrane volume, $\text{m}^2 \cdot \text{m}^{-3}$); k_{mem} as the

surface intrinsic reaction rate constant; z as space coordinate. Equation 5.17 can be transformed to:

$$\frac{d^2c}{dZ^2} - Pe_M \cdot \frac{dc}{dZ} - \phi^2 c = 0 \quad (5.18)$$

where $c (= C/C_e)$ and $Z (= z/L)$ are respectively the dimensionless concentration and coordinate (C_e is the reactant concentration on the feed side surface of the membrane). Pe_M is the Péclet number for mass transfer inside the membrane ($Pe_M = vL/D$), ϕ is the Thiele modulus $\phi = \sqrt{\frac{ak_{mem}}{D}}L$. The boundary conditions for this differential equation are (Fig.5.12):

$$Z = 0 : \quad c = 1 \quad (5.19)$$

$$Z = 1 : \quad \frac{dc}{dZ} = 0 \quad (5.20)$$

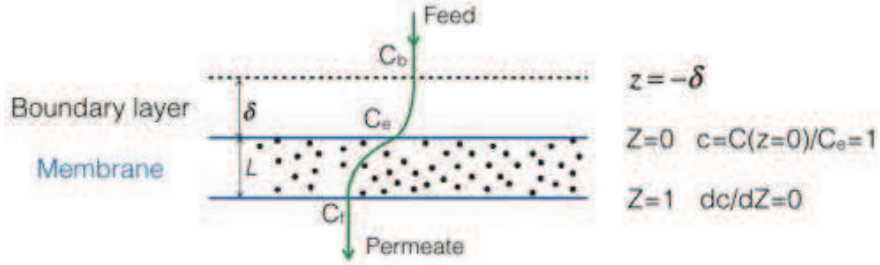


Figure 5.12: Schematic representation of the modeled catalytic membrane (black dots representing MNPs; scale not respected).

The solution of Eq. 5.17 is therefore:

$$c = \frac{e^{\frac{Pe_M - \sqrt{\Delta}}{2}Z}}{1 - \frac{Pe_M - \sqrt{\Delta}}{Pe_M + \sqrt{\Delta}}e^{-\sqrt{\Delta}}} + \frac{e^{\frac{Pe_M + \sqrt{\Delta}}{2}Z}}{1 - \frac{Pe_M + \sqrt{\Delta}}{Pe_M - \sqrt{\Delta}}e^{\sqrt{\Delta}}} \quad (5.21)$$

where

$$\Delta = Pe_M^2 + 4\phi^2 \quad (5.22)$$

When there exists a boundary layer of a thickness δ over the feed side of the membrane, a concentration gradient in the boundary layer is produced and C_e does not equal to the reactant concentration in the bulk solution C_b (Fig.5.12). The conversion X can be expressed as:

$$X = 1 - \frac{C_f}{C_b} = 1 - \frac{C_e}{C_b} \cdot \frac{C_f}{C_e} = 1 - \frac{C_e}{C_b} \cdot c|_{Z=1} \quad (5.23)$$

The differential mass balance in the boundary layer at steady state can be given by:

$$D \frac{d^2C}{dz^2} - v \frac{dC}{dz} = 0 \quad (5.24)$$

with boundary conditions:

$$C|_{z=-\delta} = C_b \quad (5.25)$$

$$C|_{z=0} = C_e \quad (5.26)$$

The mass transfer flux j can be obtained by means of Eq. 5.27, taking into account both the diffusive and the convective flows as follows:

$$j = -D \frac{dC}{dz} + vC \quad (5.27)$$

The relation between C_e and C_b can be thus deduced from Eq.5.24-5.27 as:

$$C_e = \frac{j|_{z=0}}{v} \cdot (1 - e^{Pe_{BL}}) + C_b \cdot e^{Pe_{BL}} \quad (5.28)$$

with Pe_{BL} as the Péclet number of the boundary layer: $Pe_{BL} = v\delta/D$. The boundary layer thickness can be estimated by Eq.5.29 [370] and found to be 190 μm in our case:

$$\delta = \sqrt{\frac{\mu}{\rho\omega}} = 190\mu\text{m} \quad (5.29)$$

with ω as the agitation velocity (22 $\text{rad}\cdot\text{s}^{-1}$).

We denote Sh as $Sh = j|_{z=0} \cdot Pe_M / (v \cdot C_e)$. Then from Eq.5.22 and Eq.5.27, the expression of Sh can be deduced as:

$$Sh = Pe_M - \frac{\frac{Pe_M - \sqrt{\Delta}}{2}}{1 - \frac{Pe_M - \sqrt{\Delta}}{Pe_M + \sqrt{\Delta}} e^{-\sqrt{\Delta}}} - \frac{\frac{Pe_M + \sqrt{\Delta}}{2}}{1 - \frac{Pe_M + \sqrt{\Delta}}{Pe_M - \sqrt{\Delta}} e^{\sqrt{\Delta}}} \quad (5.30)$$

By combining Eq.5.28 with Eq.5.30, the ratio of C_e/C_b can be given as follows:

$$\frac{C_e}{C_b} = \frac{e^{Pe_{BL}}}{1 - \frac{Sh}{Pe_M} \cdot (1 - e^{Pe_{BL}})} = \frac{e^{Pe_{BL}}}{1 - \left(1 - \frac{Pe_M - \sqrt{\Delta}}{2A \cdot Pe_M} - \frac{Pe_M + \sqrt{\Delta}}{2B \cdot Pe_M}\right) \cdot (1 - e^{Pe_{BL}})} \quad (5.31)$$

where

$$A = 1 - \frac{Pe_M - \sqrt{\Delta}}{Pe_M + \sqrt{\Delta}} \cdot e^{-\sqrt{\Delta}} \quad (5.32)$$

$$B = 1 - \frac{Pe_M + \sqrt{\Delta}}{Pe_M - \sqrt{\Delta}} \cdot e^{\sqrt{\Delta}} \quad (5.33)$$

The concentration profile inside the boundary layer can be obtained based on Eq.5.24-5.26 as follows:

$$C_{BL} = \frac{e^{Pe_{BL} \cdot Y/2}}{\sinh(Pe_{BL}/2)} \left[\sinh\left(Pe_{BL} \cdot \frac{1-Y}{2}\right) \cdot C_b + e^{-Pe_{BL}/2} \cdot \sinh\left(Pe_{BL} \cdot \frac{Y}{2}\right) \cdot C_e \right] \quad (5.34)$$

with $Y = (z + \delta)/\delta$.

Model fitting and insight into how the catalytic membrane works

The Suzuki-Miyaura cross-coupling reaction was tested at different flow rates at 60 °C at 1-iodo-4-nitrobenzene concentration of $0.016 \text{ mol}\cdot\text{L}^{-1}$. Conversion increased with residence time as shown in Fig. 5.13. The dimensionless productivity (interpreted as the product of Péclet number and conversion) was also plotted as a function of Péclet number (which reflects the flow rate). An increase of productivity with the flow rate was observed (Fig.5.14).

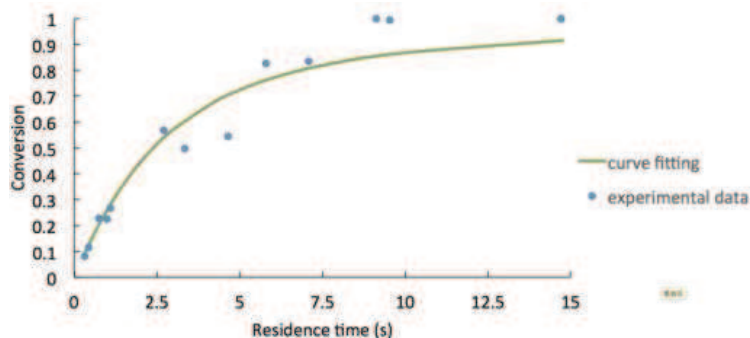


Figure 5.13: Conversion as a function of residence time, $T = 60^\circ\text{C}$, $[1\text{-iodo-4-nitrobenzene}] = 0.016 \text{ mol}\cdot\text{L}^{-1}$, Permeate flux density: $27\text{-}1277 \text{ L}\cdot\text{h}^{-1}\cdot\text{m}^{-2}$.

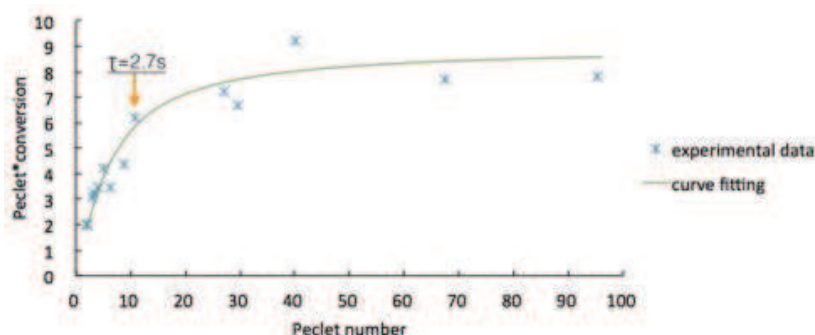


Figure 5.14: Dimensionless productivity as a function of Péclet number in the membrane

These two plots were fitted into the above described model and the resulting Thiele modulus $\phi = \sqrt{\frac{ak}{D}}$ is 3, showing that the reaction is still limited by diffusion. However, according to the reasoning in section 5.3.2, the diffusion in membrane pores and through the boundary layer of the catalyst is much faster than the reaction on the catalyst surface. The limiting mass transfer term leading to $\phi = 3$ is in fact imposed by the boundary layer at the feed side of the membrane (Fig.5.12 and Fig.5.15, discussed in the following paragraphs). By taking the diffusion coefficient of ethanol at 60°C , the apparent reaction

rate constant is deduced to be:

$$k_{app} = ak_{mem} = 3.05 \times 10^{-1} s^{-1} \quad (5.35)$$

When normalized to the palladium mass, the apparent reaction rate constant is then $382 s^{-1} \cdot g^{-1}$ and $0.47 s^{-1} \cdot m^{-2}$. Compared with the batch conditions (where $k_{app,batch} = 0.21 s^{-1} \cdot g^{-1}$), the catalytic membrane triggered an acceleration of the reaction by three orders of magnitude. The specific catalyst surface in the membrane is calculated as $a = 4.66 \times 10^6 m^2 \cdot m^{-3}$, and hence the intrinsic reaction rate constant on the catalyst supported on the membrane is $k_{mem} = 6.5 \times 10^{-8} m \cdot s^{-1}$, which is in the same order of magnitude as corresponding value k_{batch} in the batch reactor.

In Fig.5.13, deviations of model prediction and experimental data are more evident at longer residence times ($\tau > 9s$ or small flow rates). This deviation can be partly attributed to the heterogeneous distribution of the PdNPs inside the membrane along the membrane thickness (exhibiting a concentration gradient of PdNPs, see Fig.5.5). There also exists the possibility that the reactant partition coefficient is favored inside the membrane compared to the liquid phase, causing a ‘pumping’ effect as if the membrane sucks the reactant from the liquid phase.

Fig.5.15 shows the concentration profiles in the boundary layer at the feed side and inside the membrane, predicted by the model with $\phi = 3$ at different residence times (flow rates). The thick boundary layer significantly reduces the diffusion flux from the bulk solution to the membrane surface and becomes a limiting step. At high flow rates ($Pe_M \geq 19$), the convection is largely dominant over diffusion. The reactant is effectively brought to the membrane surface by convection so that $C_e \approx C_b$, while for Péclet numbers smaller than 19, the concentration at the membrane feed surface C_e differentiates from the bulk solution concentration C_b , exerting negative influence on the productivity. The transition Péclet value ($Pe_M = 19$) where $(C_b - C_e)$ becomes noticeable corresponds to the flux ($146 L \cdot h^{-1} \cdot m^{-2}$) from which the productivity begins to approach the maximum plateau (Fig.5.14). At high flux, the concentration profile in the boundary layer can be washed out by convection and become almost flat. The productivity is accordingly enhanced, but the short residence time is insufficient to achieve full conversion. As shown in Fig.5.14, the productivity increases with the flux until the convection become largely dominant, a maximum plateau is thus reached. At the maximum plateau, the reaction on the membrane become kinetically limited.

Table 5.4 summarizes the differences between the colloidal system (with PdNPs dispersed in [MMPIM][NTf₂]) in batch reactor and the catalytic membrane. Palladium works with higher efficiency in the catalytic membrane (entry 8): apparent reaction constant is almost 2000 times larger in the catalytic membrane with the same amount of palladium. It is because that palladium nanoparticles are well-dispersed and distributed so close to each other inside the membrane (with small inter-particle distances, entry 2), leading to extremely high particle number or catalyst active site per unit volume of the reactor (entry 3). One direct result is the large increase in local active sites/substrate ratio when the liquid is forced through the membrane pores (entry 4). The apparent

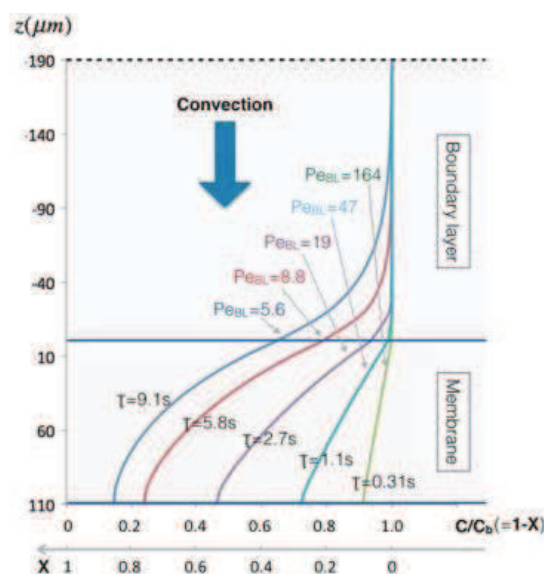


Figure 5.15: Concentration profiles along the coordinate at various flow rates (predicted by the model). X =conversion

reaction rate constant k_{app} (entry 7) is the product of the specific catalyst surface a (entry 10) and the intrinsic reaction rate on the catalyst surface k (entry 11). The large catalyst number per unit volume (entry 3) leads to a high specific surface (entry 10), which is mainly responsible for the reaction acceleration in the membrane. The difference on the intrinsic k (entry 11) between the two systems depends on particle size and distribution (entry 1), or more specifically, on the number of atoms on the NP surface. The ratio of number of atoms on the NP surface (catalytic membrane/batch reactor) is estimated to be 1.4, and the ratio of number of vertex and edge atoms is calculated to be 2.9, close to the ratio of intrinsic reaction constant k (entry 11). The influence of k on apparent kinetics (a factor of 1-3) should be much less remarkable than that exerted by the specific surface area a .

In brief, the Suzuki-Miyaura cross-coupling between 1-iodo-4-nitrobenzene and phenyl boronic acid is not limited by mass transfer under batch conditions. The substantial reaction acceleration by the catalytic membrane in the flow through configuration is attributed to the concentrating effect of the membrane (i.e. packing large number of particles into a tiny volume). The convective flow in our case serves to eliminate the concentration gradient in the boundary layer at the membrane feed side surface and to bring reactants from the bulk solution into the reactive membrane, while for mass transfer limited reactions, the catalytic membrane can eliminate the local mass transfer resistance (imposed by the boundary layer around the catalyst) to a large extent by convective flow.

Table 5.4: Comparison between the batch reactor and the catalytic membrane: PdNP size and distribution and performance on Suzuki-Miyaura cross-coupling

		Batch reactor	Flow through catalytic membrane	Factor of difference ^a
1	NP size (nm)	4 ± 2	2 ± 1	$1/2$
2	Inter-particle distance (nm)	50-100	≈ 2	$1/50 - 1/25$
3	Pd concentration (mm^{-3}) ^b	$1.7 \times 10^8 - 2.8 \times 10^{12c}$	$1.4 \times 10^{14} - 4.0 \times 10^{14d}$	143^e
4	S/substrate ratio ($m^2 \cdot mol^{-1}$) ^f	5 - 364	4.2×10^{5g}	>1144
5	Reaction time for full conversion	6h	$<10s$	$1/2160$
6	Selectivity (%) ^h	92	100	
7	k_{app} (s^{-1})	2.2×10^{-4}	3.05×10^{-1}	1390
8	k_{app}/m_{Pd} ($s^{-1} \cdot g^{-1}$) ⁱ	0.21	382	1870
9	k_{app}/S ($s^{-1} \cdot m^{-2}$) ^f	$6.0 \times 10^{-4} - 4.1 \times 10^{-2}$	4.7×10^{-1}	$11 - 783$
10	a ($m^2 \cdot m^{-3}$) ^j	$5.3 \times 10^3 - 3.6 \times 10^5$	4.66×10^6	13-879
11	k ($m \cdot s^{-1}$) ^k	$6.0 \times 10^{-10} - 4.1 \times 10^{-8g}$	6.5×10^{-8}	≥ 1.6

^a (catalytic membrane)/(batch reactor) value ratio ;

^b Number of palladium particles per unit volume;

^c Values calculated taken into consideration the presence of aggregates (d=4-100 nm);

^d Value for reactive zones where palladium is highly concentrated (4.0×10^{14}) and an average value obtained by (amount of Pd)/(membrane volume) (1.4×10^{14});

^e $4.0 \times 10^{14} / (2.8 \times 10^{12})$ (difference factor between the reactive zone of the membrane and the Pd concentration in the batch reactor calculated with d=4 nm);

^f S=total catalyst surface area;

^g Local ratio inside the membrane environment, porosity= 0.7;

^h Selectivity towards the cross-coupling product;

ⁱ Apparent reaction rate constant normalized to palladium mass;

^j Specific surface: catalyst surface area divided by the reactor volume;

^k Intrinsic reaction rate constant on the catalyst surface;

5.4 Catalytic performance of the catalytic membrane on other reactions

Besides Suzuki-Miyaura cross-coupling reaction, the membrane was also tested on hydrogenation reaction, Heck cross-coupling and Sonogashira C-C coupling/cyclization tandem reaction. All reactions were carried out in ethanol.

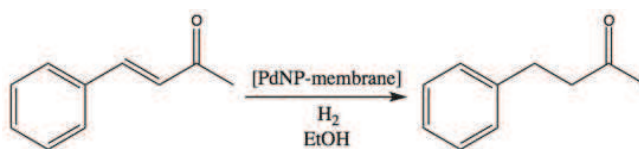
5.4.1 Hydrogenation

The hydrogenation reaction of *trans*-4-phenyl-3-buten-2-one previously carried out on the colloidal system in batch reaction in [MMPIM][NTf₂] (Scheme 5.4) was also tested on the catalytic membrane under three conditions (see Fig.5.16). The catalytic performance of the colloidal system on the same reaction (with Pd/substrate=1/100 mol%) is taken as a reference for comparison (Table 5.5, see Chapter 4, section 4.3.1).

Table 5.5: Catalytic performance of the colloidal system (PdNPs dispersed in [MMPIM][NTf₂]) on hydrogenation of *trans*-4-phenyl-3-buten-2-one.

P(H ₂) (bar)	Temperature (°C)	Reaction time (h)	Conversion ^a (%)
1	60	0.5	61
		1	100
	35	1	60
		2	100

^a Determined by GC-MS and ¹H NMR using decane and mesitylene as internal standard respectively



Scheme 5.4: Pd-catalyzed hydrogenation of *trans*-4-phenyl-3-buten-2-one.

In the flow through configuration, the reaction solution was bubbled with dihydrogen before filtered through the membrane (Fig.5.16-a). In the bubbling mode (Fig.5.16-b) and inside the autoclave (Fig.5.16-c), no filtration was involved. The membrane was submerged in the solution under bubbling (Fig.5.16-b) or under H₂ pressure (Fig.5.16-c). The reaction conditions and conversions are given in Table 5.6. It turned out that the performance of the catalytic membrane was worse than the colloidal system when no filtration was involved (i.e. in bubbling and autoclave mode). This is coherent with the

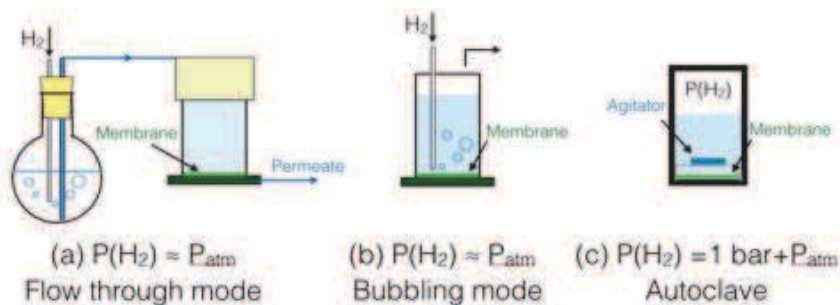


Figure 5.16: Schematic representation of three different modes of using the catalytic membrane.

Table 5.6: Reaction conditions for hydrogenation of *trans*-4-phenyl-3-buten-2-one using the catalytic membrane.

	Flow through ^a	Bubbling	Autoclave
T (°C)	35	35	65
P(H ₂) (bar)	Bubbling under atmospheric pressure		1
Reaction time	2.6 s	30 min	1 h
Conversion (%) ^b	100	<10	27%
V _{EtOH} (ml)	50	20	5

^a Quantity of reactant is 0.2 mmol.

^b Determined by GC-MS and ¹H NMR using decane and mesitylene as internal standard.

previous reasoning on the mechanism of reaction acceleration by the catalytic membrane: when no forced flow through is involved, the high local catalyst concentration inside the membrane will not be able to play its role in multiplying the apparent reaction rate constant. In the flow through configuration, complete conversion was achieved within 2.6s of residence time. The striking contrast of the catalytic performance between the flow through configuration and submerged configurations highlights the indispensability of forced flow in reaching remarkable reaction acceleration.

It should be mentioned that liquid phase hydrogenation reaction carried out in the flow through membrane reactor is limited by hydrogen solubility in the solvent (ethanol). In the course of experiments, we observed obvious drop in conversion when the substrate (*trans*-4-phenyl-3-buten-2-one) quantity rose from 0.2 mmol to 1 mmol. Using the catalytic membrane as an interfacial contactor may be a better choice to conquer the solubility limit. But as no convective flow is involved, the catalytic efficiency of the membrane contactor is still an open question to be explored.

5.4.2 More challenging reactions

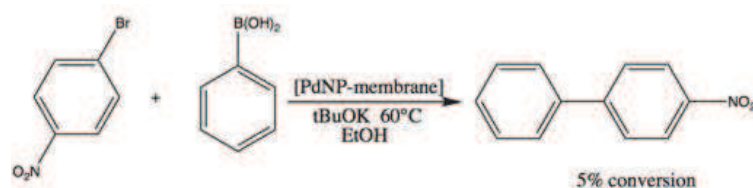
We then use the membrane to catalyze slower reactions (reactions with higher activation energy) to explore its potential and limits, and to seek possible improvements. All those reactions were carried out in ethanol at 60°C in the flow through mode. The above mentioned colloidal PdNPs dispersed in [MMPIM][NTF₂] were not tested on those reactions. Hence a colloidal palladium system stabilized in glycerol (previously used by M. Gómez et al) was taken as reference [276,371,372].

Suzuki-Miyaura cross-coupling

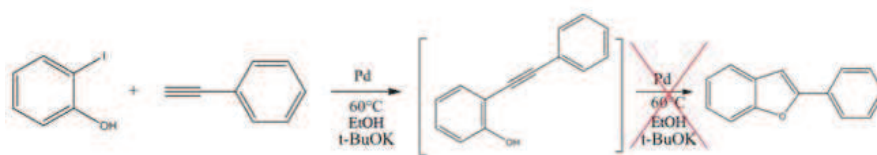
Suzuki-Miyaura cross-coupling is slower for bromo-substituted nitrobenzene than iodo-substituted ones. For the cross-coupling between 1-bromo-4-nitrobenzene and phenyl boronic acid (Scheme 5.5, molar ratio: 1-bromo-4-nitrobenzene/ phenylboronic acid/tBuOK =1/1.2/2.5), 5% conversion was achieved through one single filtration ($\tau = 9.1s$). In contrast, full conversion could be achieved in 2 hours at 100°C using the colloidal palladium in glycerol in batch reactor (with Pd/substrate molar ratio= 1/100). The conversion rate given by the catalytic membrane (5% conversion in 9 s) is fair, but the low conversion makes the catalytic membrane practically uninteresting for this reaction: 45 membranes need to be connected in series, or a recycling loop should be used in order to achieve a conversion of 90%.

Sonogashira tandem reaction

When the catalytic membrane was used for the Sonogashira C-C coupling/cyclization tandem reaction (Scheme 5.6), the reaction stopped at the first step (after Sonogashira C-C coupling) and no cyclization product was obtained. The protocol for Sonogashira C-C coupling/cyclization tandem reaction using colloidal palladium in glycerol is 2.5 mol% of Pd, at 100°C for 12 hours. Assuming the same acceleration factor in terms of reaction time as calculated above (Table 5.4), 2 to 5 catalytic membranes connected in series should be able to give complete conversion at 100°C.



Scheme 5.5: Pd-catalyzed Suzuki-Miyaura cross-coupling between 1-bromo-4-nitrobenzene and phenyl boronic acid.

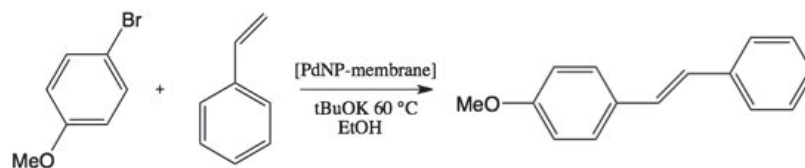


Scheme 5.6: Pd-catalyzed Sonogashira C-C coupling cyclization tandem reaction.

As a matter of fact, the non-satisfactory performance of the catalytic membrane for those two reactions (and also for other slow reactions) is owing to the low reaction temperature (60°C), which in our case is limited by the boiling point of the solvent. If we could find another appropriate solvent to replace ethanol, the catalytic membrane would display better versatility.

Heck cross-coupling

For the Heck cross-coupling between 4-methoxybromobenzene and styrene using tBuOK as base (scheme.5.7) carried out on the catalytic membrane, no product was observed. The reaction condition of the colloidal system for the Heck cross-coupling (2h under 100°C) is the same as the Suzuki cross-coupling between 1-bromo-4-nitrobenzene and phenylboronic acid (scheme 5.5, nearly complete conversion). It means that the Heck reaction and the Suzuki cross-coupling for 1-bromo-4-nitrobenzene should share approximately the same activation energy. We should accordingly have observed small amount of product just as in the case of the Suzuki cross coupling for 1-bromo-4-nitrobenzene. The reason accounts for the inactivity of the catalytic membrane for the Heck cross-coupling should be the ‘non leaching’ behavior of the PdNPs supported on the membrane. The real active catalyst for Heck cross-coupling is the molecular metal species [328,373]. The immobilization of the PdNPs by the polyIL inside the membrane have probably prevented leaching, directly resulting in the loss of catalytic activity of the membrane for Heck cross-coupling. This is coherent with the good Pd stability observed during the experiments: palladium leaching was never detected. This also implies that the Suzuki-Miyaura reaction using the catalytic membrane is heterogeneous in origin (surface-like).



Scheme 5.7: Pd-catalyzed Heck coupling reaction.

5.5 Conclusions

A catalytic polymeric membrane was prepared by modifying the PES support with lab-synthesized imidazolium-based polymerizable ionic liquids. UV irradiation generates free radicals on PES chains which permits the covalent bonding between the PES support and the polyIL gel. Metal loading of the membrane was realized by inter-matrix synthesis. The resulting catalytic polymeric membrane was loaded with PdNPs with a mean diameter of 2 nm, which are dispersed/stabilized in the polyIL. The palladium nanoparticles inside the membrane are highly concentrated (in the order of 10^{14} NPs per mm^3) and heterogeneously distributed along the membrane thickness. No leaching of palladium or polyIL from the membrane was observed, neither during filtrations nor in the course of the catalytic reaction.

The graft layer material determines the liquid phase reactions targeted (e.g. water phase reactions for hydrophilic polymers [139] and organic phase reactions for hydrophobic polymers, as in our case). An efficient use of the catalytic membrane requires as premises the swelling of the graft layer by the solvent and a favored reactant partition coefficient towards the graft material, so that the reaction mixture can have free access into the polymer chains and reach the catalyst surface. The choice of the graft material also affects the degree of metal loading, NP size and accordingly the apparent reaction rate constant [374].

The catalytic membrane showed remarkable catalytic performance on Suzuki-Miyaura cross-coupling between 1-iodo-4-nitrobenzene and phenyl boronic acid. The membrane was so active that at $T=60^\circ\text{C}$ with a residence time of less than 10 seconds, the conversion was complete, without formation of byproducts. The desired Pd-free product was directly and continuously obtained in the permeate once the reaction started. No separation of the catalyst from the product was required. The high efficiency of the catalytic membrane favored a better chemoselectivity towards the kinetically favored product, achieving full conversion under mild conditions. Concerning the questions posed in the beginning:

How fast can it be and how it happens?

The performance of the catalytic membrane for Suzuki-Miyaura cross-coupling in flow through configuration was compared to that of the colloidal palladium in batch reactor. In either case, it concerns the reaction-limited regime. The catalytic membrane greatly accelerated the reaction (ca. 2000 times both in terms of reaction time for total conversion and in terms of apparent reaction rate normalized to palladium mass),

benefiting mainly from the large catalyst specific surface area and partially from the difference in proportion of surface, vertex and edge atoms. The latter influences the intrinsic reaction rate constant, which generates the apparent reaction rate constant when multiplied by the catalyst specific surface area. When the reactant solution is filtered through the membrane, the reactant molecules enter an environment where they are surrounded by numerous PdNPs. The local ratio of catalyst surface area to substrate amount inside the membrane is more than 1144 times higher than in the batch reactor. Therefore, the large catalyst specific surface area inside the membrane is the principal reason accounting for the reaction acceleration by the catalytic membrane in the case of kinetic-limited reactions. The membrane must be used in a flow-through contactor configuration in order that the advantage of high catalyst concentration can be embodied in terms of catalytic performance.

In Suzuki-Miyaura cross-coupling reaction, when liquid flux increases, the conversion decreases but productivity rises. The enhancement in productivity is induced by the convective flow which brings the reagents into the (NP highly concentrated) membrane and eliminates the concentration gradient in the boundary layer at the feed side of the membrane. When reactions are diffusion-controlled, the role of convective flow will become more important: The boundary layer in the membrane pores and around the catalyst surface can be effectively eliminated by the convective flow. The apparent reaction rate constant can thus be improved through mass transfer acceleration.

In conclusion, the catalytic membrane can accelerate reactions both in terms of mass transfer and apparent reaction rate constant. Which one has a major impact on the overall performance depends on the nature of the reaction carried out (i.e. activation energy and mass transfer resistance). The high permeability of the catalytic membrane ($9000 \text{ L} \cdot \text{h}^{-1} \cdot \text{m}^{-3} \cdot \text{bar}^{-1}$) means that it is capable to give high productivity.

How far can it go?

For gas-liquid two phase reactions carried out on the catalytic membrane in the flow through configuration, the gas solubility in the liquid phase set up a limitation on the reaction conversion and thus has to be taken into consideration. The use of the catalytic membrane as an interfacial contactor might an option to go over the solubility limit (need further validation).

For reactions with high activation energy, the conversion achieved through one filtration can drop to a large extent, due to the slow kinetics. But the apparent reaction rate is still faster in the catalytic membrane than in the batch reactor. To obtain a high conversion using the catalytic membrane for reactions with high activation energy, there are several possibilities including:

1. Membranes connected in series or use of loops to prolong the residence time.
2. Increasing the metal loading without inducing increase in particle size, so that the acceleration factor would increase proportionally with the metal loading.
3. Applying higher temperatures. All reactions were carried out on the catalytic membrane below or equal to 60°C , due to the limit imposed by ethanol boiling point. Ethanol was chosen as solvent because of its compatibility with the PES support membrane and its polyIL-swelling property. The number of choices on the solvent is mainly

limited by the support membrane (PES dissolves easily in a lot of organic solvents). To enlarge the application of the catalytic membrane, we should look for other possible alcohol solvents with higher boiling point or other support materials that are solvent-resistant. It will be ideal if the support membrane is photo-sensitive, permitting the formation of covalent bonds between the support and the modifying agents and a high grafting degree accordingly. The covalent bond ensures the composite membrane's stability. While a higher grafting degree gives rise to higher metal loading (beneficial for catalysis) since the metal was loaded to the membrane by ion exchange with the graft polymer. If the PES support membrane is replaced by a solvent-resistant support membrane, the reaction temperature can be raised according to the solvent boiling point or the polymer retraction temperature.

Chapter 6

Extrapolation of the catalytic membrane for exothermic reactions and industrial-scale applications

Résumé du Chapitre

L'objectif de ce chapitre est d'extrapoler l'utilisation potentielle de la membrane catalytique élaborée dans Chapitre 5 à des réactions exothermiques et son application à l'échelle industrielle. Les prédictions sont faites pour des réactions en phase liquide à travers des calculs basés sur les paramètres dépendant de la géométrie de la membrane. Avec des dimensions caractéristiques submicroniques, la membrane catalytique est pratiquement un microréacteur. Il partage donc les propriétés favorables telles qu'un transfert de chaleur efficace, une distribution de temps de séjour étroite et l'amélioration du transfert de masse en raison du mélange diffusif rapide.

Selon le modèle de Taylor pour les écoulements pistons, le fluide dans les pores de la membrane dont la taille est de 0,2 micron a un profil de concentration plat dans le sens radial sous conditions expérimentales. Cela conduit à une distribution de temps de séjour étroite, favorisant la sélectivité de la réaction. En plus, l'écoulement piston permet de réduire la modélisation de la membrane catalytique à une seule dimension (l'épaisseur de la membrane).

La possibilité d'utiliser la membrane catalytique plate pour des réactions exothermiques a été explorée selon le modèle développé par Westermann. Les calculs sont faits avec l'éthanol technique (96% vol.) comme solvant. Nous constatons que l'écoulement piston et la condition isotherme se réalisent simultanément à l'intérieur de la membrane catalytique dans nos conditions expérimentales.

La dernière partie est consacrée à l'extrapolation de la capacité de production des membranes catalytiques sous forme de fibres creuses en supposant que l'activité de la membrane plate est bien reproduite. En fonction de la compacité du module, la capacité de production du réacteur membranaire peut atteindre plus de $25000 \text{ tonne} \cdot \text{year}^{-1} \cdot \text{m}^{-3}$ (pour la concentration en réactif de $1,6 \times 10^{-2} \text{ mol} \cdot \text{L}^{-1}$), 1250 fois plus élevée qu'un réacteur en batch. Si la désactivation du catalyseur n'est pas prise en compte, moins de 10 mol de palladium est suffisant pour un réacteur membranaire dont volume est de 107 L.

En bref, la membrane catalytique surpasse donc les réacteurs discontinus classiques en batch dans plusieurs aspects : capacité de production plus élevée, coût de catalyseur plus faible et également une mise en oeuvre plus facile (pas de séparation du catalyseur nécessaire). La capacité de production du réacteur membranaire est du même ordre de grandeur ou plus que les microréacteurs. Une étude sur la durée de vie du catalyseur serait intéressante pour permettre une estimation plus précise de la quantité de palladium nécessaire et le coût correspondant le catalyseur. Les avantages des réacteurs membranaires par rapport aux microréacteurs devraient comprendre la facilité de préparation et de mise à l'échelle ainsi que le faible coût des membranes polymères.

Mathematical symbols used in this chapter are listed here below:

Symbol	Unit	Meaning
A	m^2	cross-section area of one pore
A_{wp}	m^2	wall area allocated to each pore
A_{pore}	m^2	total pore area of the membrane cross-section
A_{wall}	m^2	total wall area of the membrane cross-section
A_{mem}	m^2	membrane surface area
B_0		Bodenstein number
$[c]$	$\text{mol}\cdot\text{L}^{-1}$	solution concentration
c_p	$\text{J}\cdot\text{mol}^{-1}\cdot\text{K}^{-1}$	molar heat capacity
d	m	pore diameter
D	$\text{m}^2\cdot\text{s}^{-1}$	diffusion coefficient
D_{ext}	m	hollow fiber outer diameter
D_M	m	module diameter
\mathbf{D}	$\text{m}^2\cdot\text{s}^{-1}$	Taylor dispersion coefficient
F_0		Fourrier number
h	$\text{W}\cdot\text{m}^{-2}\cdot\text{K}^{-1}$	heat transfer coefficient
J	$\text{L}\cdot\text{m}^{-2}\cdot\text{h}^{-1}$	flux density
k	$\text{W}\cdot\text{m}^{-1}\cdot\text{K}^{-1}$	thermal conductivity
l	m	module length
L_p	$\text{L}\cdot\text{h}^{-1}\cdot\text{m}^{-2}\cdot\text{bar}^{-1}$	liquid permeability
L	m	pore length
M	$\text{g}\cdot\text{mol}^{-1}$	molecular weight
N		number of fibers in one module
\dot{n}	$\text{mol}\cdot\text{s}^{-1}$	molar flow rate passing in one pore
\dot{n}_{tot}	$\text{mol}\cdot\text{s}^{-1}$	total molar flow rate
n		number of hollow fiber modules
ΔP	mbar	transmembrane pressure
\dot{Q}	W	heat transfer rate
Q	$\text{m}^3\cdot\text{s}^{-1}$ or $\text{L}\cdot\text{h}^{-1}$	volumetric flow rate
S_{fiber}	m^2	total membrane surface area
SSA	m^{-1}	specific surface area of the membrane module
T	K	temperature
\bar{v}	$\text{m}\cdot\text{s}^{-1}$	average flow velocity
V	m^3	hollow fiber module volume
X		conversion
z	m	axial coordinate
Z		dimensionless axial coordinate $Z = z/L$
δ	m	boundary layer thickness
ϵ		membrane porosity
β		geometry parameter (=48 for circular pore)
τ_{mix}	s	characteristic mixing time

τ	s	mean residence time
χ		initial reactant mole fraction
Θ		normalized temperature
ρ	$\text{kg}\cdot\text{m}^{-3}$	fluid density
ϕ		module packing density
Bi		Biot number
Nu		Nusselt number
Pe_h		heat transfer Péclet number
Pe_M		mass transfer Péclet number inside the membrane
St		Stanton number $St = Nu/Pe_h$

6.1 Introduction

With sub-micron characteristic dimensions, the catalytic membrane is practically a microreactor. It shares therefore the favorable properties such as high heat transfer rates, narrow residence time distribution and improved mass transfer due to fast diffusive mixing, etc. The objective of this chapter is to explore the potential use of the catalytic membrane elaborated in Chapter 5 for exothermic reactions and its applications on an industrial scale. Predictions were made for reactions in liquid phase through calculations of several determinative parameters based on the geometry of the membrane.

6.2 Fluid dynamics and concentration profile inside membrane pores

In micro reactors, the fluid is virtually always laminar flow pattern. It is also true for our catalytic membrane whose nominal pore size is $0.2 \mu\text{m}$ since the Reynolds number is in the range of 10^{-6} to 10^{-4} for ethanol flow rates under the experimental conditions. The laminar flow pattern can end in a parabolic flow profile and the wide residence time distribution can hence adversely affect yield and selectivity. However efficient radial mixing can mitigate concentration differences, washing out the parabolic shape so that plug flow behavior starts to take. Given the diameter of the membrane pores, the radial mixing is realized uniquely by diffusion. The characteristic mixing time τ_{mix} is the time to diffuse halfway across the pore, expressed as Equation 6.1 according to Fick's law, where d is the pore diameter and D is the diffusion coefficient.

$$\tau_{mix} = \frac{d^2}{4D} \quad (6.1)$$

Reconciling a parabolic flow velocity profile with plug flow behavior (flat concentration profile) is only possible if radial diffusion across the pore is much faster than convective mass transfer in the axial direction. In the early 1950s, Taylor and Aris developed a general framework to estimate when to apply the plug flow model with dispersion [375, 376]. The necessary condition is given by Equation 6.2 in the case of porous membrane.

$$\frac{L}{\bar{v}} > 0.04 \frac{d^2}{D} \quad (6.2)$$

Here we introduce the Fourier number, which is the ratio of the mean residence time τ to the characteristic mixing time (Eq.6.3, mean residence time equals the membrane thickness divided by the average flow velocity $\tau = \frac{L}{\bar{v}}$). Eq.6.2 then can be expressed in terms of Fourier number as Equation 6.4.

$$F_0 = \frac{\text{residence time}}{\text{characteristic mixing time}} = \frac{4D\tau}{d^2} \quad (6.3)$$

$$F_0 > 0.16 \quad (6.4)$$

Dispersion is a spreading phenomenon under combined action of velocity variation over the cross-section and molecular diffusion, causing deviations from ideal plug flow. Estimation of deviation from plug flow can be made through the ratio of convection to dispersion (the Bodenstein number B_0 , Eq. 6.5) [351,377].

$$B_0 = \frac{\text{movement by bulk flow}}{\text{movement by axial dispersion}} = \frac{\bar{v}L}{\mathbf{D}} \quad (6.5)$$

\mathbf{D} in Equation 6.5 is the Taylor dispersion coefficient, incorporating the effect of both diffusion D and convection [375,377] (Eq.6.6). As convection dominates the mass transfer (Chapter 5), the diffusion term can be neglected. This approximation actually stands for most small-scale flow systems except for extremely small flow rates.

$$\mathbf{D} = D + \frac{\bar{v}^2 d^2}{4\beta D} \approx \frac{\bar{v}^2 d^2}{4\beta D} \quad (6.6)$$

The parameter β depends on the geometry. Considering a membrane pore as a circular tube, β equals to 48 here. Combining Eq. 6.5 and Eq. 6.6, the Bodenstein can be expressed in terms of the Fourier number (Eq. 6.7).

$$B_0 = \frac{4\beta D\tau}{d^2} = F_0\beta \quad (6.7)$$

The value of the diffusion coefficient D of the reactant 1-iodo-4-nitrobenzene in ethanol at 60° C $D = 4.1 \times 10^{-10} \text{ m}^2 \cdot \text{s}^{-1}$ was taken to plot Fig.6.1.

Systems with $B_0 < 100$ ($F_0 < 2.1$) display large deviations from plug flow; systems with $B_0 > 100$ ($F_0 > 2.1$) show small deviations from plug flow (< 5%) [377]. And with $B_0 > 1000$ ($F_0 > 21$), the system can be considered as behaving in a plug flow manner [351]. Different flow behavior regions were presented in Fig.6.1 by plotting pore diameter as a function of residence time at critical Fourier numbers (0.16, 2.1, 21). Since the residence time under our experimental conditions was in the range of 0.3 s to 15 s (Chapter V), the residence time axis was set from 0 to 16 s. The maximum pore sizes to ensure a small deviation from plug flow behavior are respectively 15 μm at $\tau = 0.3$ s and 112 μm at $\tau = 16$ s. To achieve a plug flow, we should work in the region where $F_0 > 21$, area marked in green, magnified in the upper left corner on a logarithmic scale. In the magnified graph, experimental points are represented by a horizontal line ($d = 0.2\mu\text{m}$). Corresponding F_0 values vary in the range of 1×10^4 ($B_0 = 6 \times 10^5$ at $\tau = 0.3\text{s}$) to 6×10^5 ($B_0 = 3 \times 10^7$ at $\tau = 15\text{s}$), largely above 21, showing that the fluid flows through membrane pores in almost ideal plug flow pattern during the reaction. As a matter of fact, pore diameter of 4.9 μm is sufficient to attain plug flow behavior for residence time longer than 0.3 s. This is to say that with a diffusion coefficient in the order of $10^{-10} \text{ m}^2\text{s}^{-1}$, almost all micro filtration membranes can meet the requirement for plug flow behavior. When no separation of small molecules is required for the reaction system, micro filtration membranes have advantages over other types of membranes (e.g. UF,NF) for their high permeability, offering higher productivity. Figure 6.2 shows the maximum pore diameter to achieve plug flow with different values of diffusion coefficient

(from $0.2 \mu m$ for $D = 1 \times 10^{-12} m^2 \cdot s^{-1}$ to $7.6 \mu m$ for $D = 1 \times 10^{-9} m^2 \cdot s^{-1}$). As for the concentration profile inside the polyRTIL layer of our catalytic membrane, even if the diffusion coefficient is 100 times smaller than in ethanol (dropping into the order of magnitude of $10^{-12} m^2 \cdot s^{-1}$), concentration within the polyRTIL gel still follows the plug flow pattern. (In reality, the diffusion coefficient in the polyRTIL gel and in the pores should be close to each other owing to the high swelling of the polyRTIL by the solvent [237]). The plug flow behavior of the fluid inside the membrane pores validates the simplification of the system from three-dimension to single dimension in the modeling of the membrane reactor.

Due to the presence of tortuosity, the geometry of membrane pores deviates from

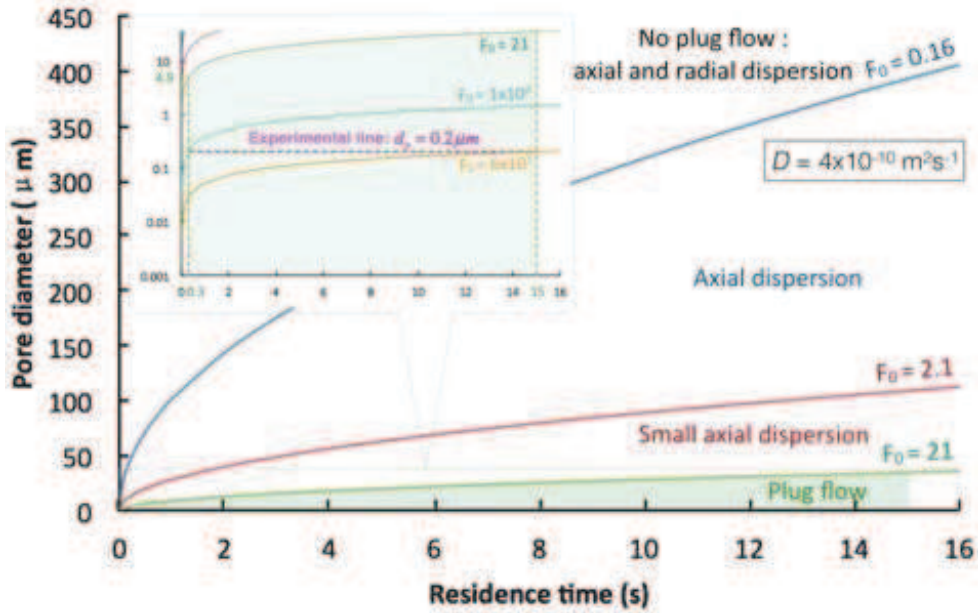


Figure 6.1: Membrane pore diameter - residence time diagram showing dispersion effects under varied Fourier number.

cylinders considered here. The tortuosity generates a transverse component of flow [378] which significantly improves mixing. Therefore, the influence of tortuosity on radial mixing is beneficial. The membrane behaves kind of like a micromixer.

6.3 The catalytic membrane for exothermic reactions

Microreactors, one of the main process intensification technologies, have high heat and mass transport rates owing to small characteristic dimensions ($< 1 mm$). Almost isothermal conditions can be achieved in the micro reactor while fast exothermic reactions are carried out. For quasi-instantaneous exothermic reactions, dimensions smaller than $100 \mu m$ are required to prevent hot spot formation. Our catalytic membrane has characteristic dimensions even smaller than microreactors, hence prospective for efficient

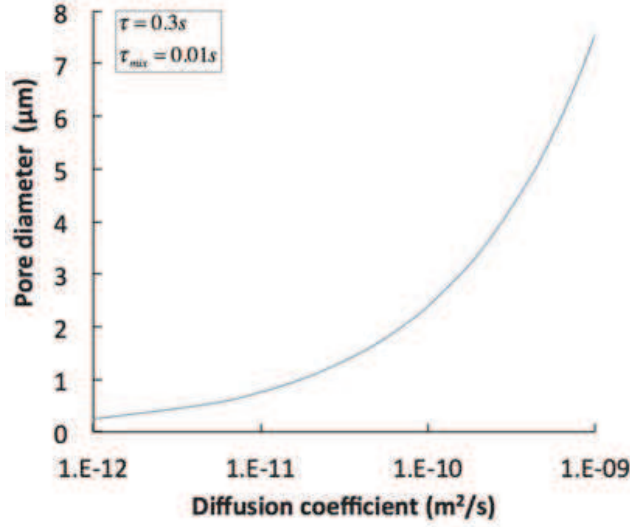


Figure 6.2: Maximum pore diameter to attain plug flow behavior for residence time longer than 0.3 s ($F_0=21$).

heat transfer.

6.3.1 Reactor model

Thomas Westermann et al. modeled the heat transfer in flow-through catalytic ceramic membrane reactors and experimentally validate the model [379]. The membrane reactor was a flat-sheet membrane considered to be in contact with exclusively the fluid on the feed side and with a porous metal support on the permeate side. By assuming all membrane pores are identical and cylindrical, the model system was reduced to a single pore and the surrounding pore wall, with symmetry in radial direction. Their second assumption is quasi-homogeneous reaction with small radial concentration gradients inside the pore. Fluid properties were assumed to be constant along the reactor. MicroPES[®] 2F, the support membrane of our catalytic membrane, has a low pore size distribution and low tortuosity [380]. Fluid inside the pores shows plug flow behavior, as demonstrated above. Therefore, Westermann's model can be applied on our catalytic membrane to predict the axial temperature profile along the membrane reactor.

To determine the axial temperature profiles of both the fluid and the membrane pore wall, differential energy balances at steady state were applied respectively on the fluid and on the pore wall, coupled by the heat exchange term between them.

Energy balance on the fluid:

Consider a volume element $dV = A \cdot dz$ with A as the cross-section area of the pore ($A = \frac{1}{4}\pi d^2$) for an exothermic reaction whose reaction enthalpy is $-\Delta H_R$ (Fig.6.3). The steady state differential energy balance is expressed in Eq. (6.8), which takes into account the heat convection \dot{Q}_{conv} into and out of the control volume, heat conduction

\dot{Q}_{cond} in and against flow direction, heat exchange between the fluid and pore wall \dot{Q}_{ex} and heat generation by chemical reaction \dot{Q}_{react} .

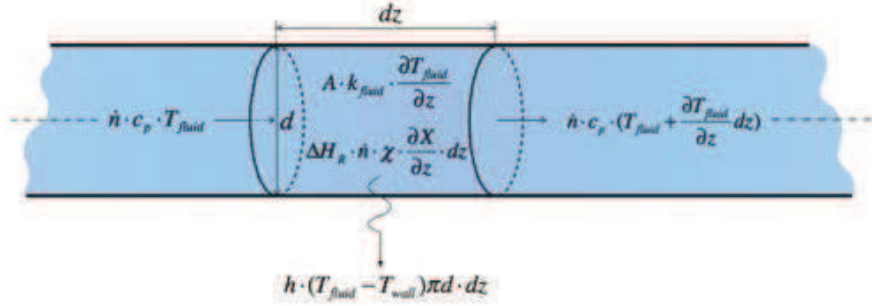


Figure 6.3: Differential energy balance for a small pore section dz .

$$-\dot{Q}_{conv} - \dot{Q}_{cond} - \dot{Q}_{ex} + \dot{Q}_{react} = 0 \quad (6.8)$$

with

$$\dot{Q}_{conv} = \dot{n} \cdot c_p \cdot \frac{\partial T_{fluid}}{\partial z} \cdot dz \quad (6.9)$$

$$\dot{Q}_{cond} = \nabla \cdot (-A \cdot k_{fluid} \cdot \frac{\partial T_{fluid}}{\partial z}) \quad (6.10)$$

$$\dot{Q}_{ex} = h \cdot (T_{fluid} - T_{wall}) \cdot \pi d \cdot dz \quad (6.11)$$

$$\dot{Q}_{react} = -\Delta H_R \cdot \dot{n} \cdot \chi \cdot \frac{\partial X}{\partial z} \cdot dz \quad (6.12)$$

where \dot{n} is the total (reactant plus solvent) molar flow rate ($mol \cdot s^{-1}$) in one pore, c_p is the molar heat capacity ($J \cdot mol^{-1} \cdot K^{-1}$) of the fluid, k_{fluid} is the fluid thermal conductivity ($W \cdot m^{-1} \cdot K^{-1}$), T_{fluid} and T_{wall} are respectively the fluid and wall temperature (K), χ as the initial reactant mole fraction, h is the heat transfer coefficient ($W \cdot m^{-2} \cdot K^{-1}$), X is the reaction conversion.

By introducing the dimensionless length $Z = z/L$ (L the membrane thickness), temperature $\Theta = T/T_{feed}$ (T_{feed} the feed temperature of the fluid) and the following dimensionless parameters (Eq. 6.13,6.14,6.15), equation 6.8 can be transformed into Eq. 6.16.

$$Nu = \frac{h \cdot \pi d L^2}{A \cdot k_{fluid}} \quad (6.13)$$

$$Pe_h = \frac{\dot{n} \cdot c_p \cdot L}{A \cdot k_{fluid}} \quad (6.14)$$

$$\Delta\Theta_{ad} = \frac{\Delta T_{ad}}{T_{feed}} = -\frac{\Delta H_R \cdot \chi}{c_p \cdot T_{feed}} \quad (6.15)$$

$$\frac{d^2\Theta_{fluid}}{dZ^2} = Pe_h \cdot \frac{d\Theta_{fluid}}{dZ} + Nu \cdot (\Theta_{fluid} - \Theta_{wall}) - Pe_h \cdot \Delta\Theta_{ad} \cdot \frac{dX}{dZ} \quad (6.16)$$

The Nusselt number Nu describes the ratio between heat exchange (between the fluid and the pore wall) and heat conduction in the fluid. The heat transfer Péclet number Pe_h characterizes the ratio between heat convection and heat conduction in the fluid. $\Delta\Theta_{ad}$ is the dimensionless adiabatic temperature difference normalized to T_{feed} .

Energy balance on the pore wall:

The membrane surface area A_{mem} can be divided into two parts: total pore area A_{pore} and total wall area A_{wall} . A proportionality between them exists as a function of membrane porosity ϵ . We assume the same local proportionality between pore area to wall area as the overall proportionality: the same proportionality retains for the cross-sectional area of a single pore A and the wall area allocated equally to each pore A_{wp} (Eq. 6.17, Fig.6.4):

$$\frac{A_{pore}}{A_{wall}} = \frac{\epsilon \cdot A_{mem}}{(1 - \epsilon) \cdot A_{mem}} = \frac{A}{A_{wp}} \quad (6.17)$$

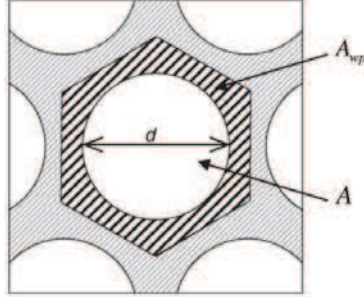


Figure 6.4: Axial membrane cross-section with pore area A and allocated wall area A_{wp} [379].

Although the catalyst distribution inside our catalytic membrane is not homogeneous along the membrane thickness, it is almost homogenous on the plane parallel to the membrane surface (Fig.5.5, Chapter 5). Identical heat transfer characteristics in each pore can be assumed. And thus no radial heat transfer occurs between pore walls. Heat transfer in radial direction towards the module can also be neglected given the limited membrane thickness. To simplify the model, the thermal conductivity of the polyIL layer and MicroPES[®] are considered the same. Consequently, the steady state differential energy balance for a volume element of the pore wall $dV_{wall} = A_{wp} \cdot dz$ includes the heat conduction in and against flow direction in the wall and heat exchange between the fluid and pore wall:

$$-\dot{Q}_{cond} + \dot{Q}_{ex} = 0 \quad (6.18)$$

with

$$\dot{Q}_{cond} = -A_{wp} \cdot k_{wall} \cdot \frac{\partial T_{fluid}}{\partial z} = -\frac{1-\epsilon}{\epsilon} \cdot A \cdot k_{wall} \cdot \frac{\partial T_{fluid}}{\partial z} \quad (6.19)$$

$$\dot{Q}_{ex} = h \cdot (T_{fluid} - T_{wall}) \cdot \pi d \cdot dz \quad (6.20)$$

By introducing the dimensionless Biot number (Eq. 6.21), which characterizes the ratio between heat exchange and conduction in the pore wall. The pore wall energy balance became Eq. 6.22:

$$Bi = \frac{\epsilon}{1-\epsilon} \frac{h \cdot \pi d L^2}{A \cdot k_{wall}} \quad (6.21)$$

$$\frac{d^2 \Theta_{wall}}{dZ^2} = -Bi \cdot (\Theta_{fluid} - \Theta_{wall}) \quad (6.22)$$

Boundary conditions:

The boundary conditions applied at the pore entrance for both fluid and wall were the well-known boundary conditions proposed by Danckwerts [381]:

$$\Theta_{fluid}(Z=0) = 1 + \frac{1}{Pe_h} \cdot \left. \frac{d\Theta_{fluid}}{dZ} \right|_{Z=0} \quad (6.23)$$

$$\Theta_{wall}(Z=0) = 1 + \frac{1}{Bi_0} \cdot \left. \frac{d\Theta_{wall}}{dZ} \right|_{Z=0} \quad (6.24)$$

The above boundary conditions at $Z=0$ allow for a temperature step between feed temperature T_{feed} and fluid and wall temperatures at $Z=0$. Here an additional Biot number at the pore entrance Bi_0 appears in the pore wall energy balance (Eq.6.25) which describes the ratio of the heat exchange between the fluid and the membrane front surface to the heat conduction inside the wall. Since the heat exchange characteristics are different inside the pores and on the membrane front surface, Bi_0 differs from the Biot number defined in Eq.6.21 by both the characteristic length and the heat transfer coefficient h_0 .

$$Bi_0 = \frac{h_0 \cdot L}{k_{wall}} \quad (6.25)$$

As for the boundary conditions at the pore outlet, two models were applied. In the case of model 1 (Eq.6.26,6.27), temperature steps similar to those at the entrance area are also allowed at the outlet. This assumption is close to reality when the catalytic membrane is cooled from the outlet side. The Biot number at the pore outlet Bi_1 is defined in the same way as Bi_0 . It should be noted that the dimensionless permeate temperature is unknown if the model is predictive (Fig.6.5-a).

$$\Theta_{fluid}(Z=1) = \Theta_{permeate} - \frac{1}{Pe_h} \cdot \left. \frac{d\Theta_{fluid}}{dZ} \right|_{Z=1} \quad (6.26)$$

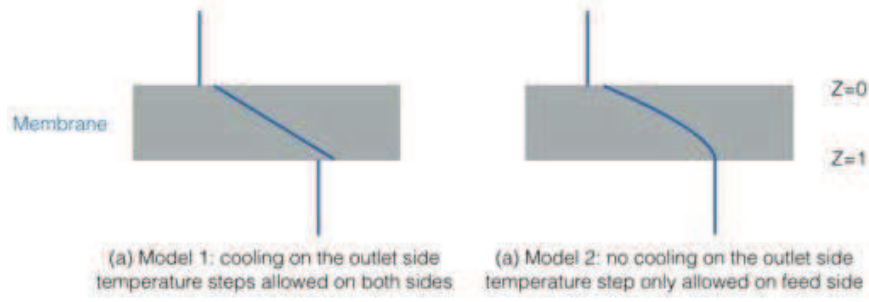


Figure 6.5: Schematic presentation of two boundary layer conditions.

$$\Theta_{wall}(Z = 1) = \Theta_{permeate} - \frac{1}{Bi_1} \cdot \frac{d\Theta_{wall}}{dZ} \Big|_{Z=1} \quad (6.27)$$

Model 2 considers the case when the fluid and wall temperature at the pore outlet are close to the permeate temperature. Heat conduction at $Z = 1$ as well as heat transfer from the pore wall to the reactor module can correspondingly be neglected. In this case, the temperature gradients at $Z = 1$ turn to zero, yielding the classical Danckwerts boundary conditions at the outlet (Eq.6.28,6.29). This assumption is a severe simplification, especially if the catalytic membrane is actively cooled (Fig.6.5-a). This should be the boundary layer condition better adapted to our catalytic membrane since there is neither reaction nor cooling taking place outside the membrane.

$$\frac{d\Theta_{fluid}}{dZ} \Big|_{Z=1} = 0 \quad (6.28)$$

$$\frac{d\Theta_{wall}}{dZ} \Big|_{Z=1} = 0 \quad (6.29)$$

The two models differ in the temperature gradients allowed at the outlet. Nevertheless, they lead to identical temperature profiles, as reported by Thomas Westermann [379]. Model 2 does not require knowledge of the permeate temperature, neither of the additional parameter Bi_1 , and thus is more convenient to apply. In model 2, four dimensionless quantities Nu , Pe_h , Bi and Bi_0 are included, which are functions of material properties and operating parameters.

6.3.2 Heat transfer coefficient and Nusselt number

The heat transfer coefficient h can be calculated by means of Nusselt correlations $\overline{Nu}_d = h \cdot d/k_{fluid}$. Assuming constant wall temperature, the mean Nusselt number can be considered as $\overline{Nu}_d = 3.66$ for laminar flow at low Reynolds number in a circular channel [382]. The heat transfer coefficient h can hence be calculated by Eq.6.30. The thermal properties of ethanol (solvent) in liquid state at 60 °C were taken for all the

calculations below [383] assuming that the solution concentration is low enough to neglect the influence of solutes on the thermal properties.

$$h = 3.66 \cdot \frac{k_{fluid}}{d} = 3.66 \cdot \frac{0.171 \text{ W} \cdot \text{m}^{-1} \cdot \text{K}^{-1}}{0.2 \times 10^{-6} \text{ m}} = 3 \times 10^6 \text{ W} \cdot \text{m}^{-2} \cdot \text{K}^{-1} \quad (6.30)$$

Since the heat transfer coefficient h is inversely proportional to the pore diameter d , heat transfer in microchannels is much better than in channels of conventional size. With a length to diameter ratio of $L/d = 550$ (value for our catalytic membrane), the Nusselt number Nu for the pore channel defined in Eq.6.13 (different from the mean Nusselt number \overline{Nu}_d) results in :

$$Nu = \frac{h \cdot \pi d L^2}{A \cdot k_{fluid}} = \frac{3.66 \cdot \frac{k_{fluid}}{d} \cdot \pi d L^2}{A \cdot k_{fluid}} = 3.66 \cdot 4 \cdot \left(\frac{L}{d}\right)^2 = 4 \times 10^6 \quad (6.31)$$

It has to be noted that for small scale channels, correct Nusselt numbers are generally smaller than those calculated applying normal size relations. And the deviation increases with smaller channels owing to increased role of surface roughness [384]. But even if the macroscopic relation cannot be applied and this number has to be reduced by several orders of magnitude, any temperature difference between liquid and wall inside the membrane pore would immediately disappear and radial isothermal condition would be achieved.

6.3.3 Flow rate and heat transfer Péclet number

The Péclet number is proportional to the convective heat transfer and thus to the flow rate in the pores. It can be calculated either from the flow rate through a single pore divided by the cross-sectional area of the pore or from the total flow rate divided by the open membrane area, producing equal values (Eq.6.32, with \dot{n}_{tot} as total flow rate). The experimental flow rates applied in Suzuki-Miyaura cross-coupling ($1.6 \times 10^{-4} \text{ mol} \cdot \text{s}^{-1} - 7.5 \times 10^{-3} \text{ mol} \cdot \text{s}^{-1}$) were taken for the calculation. With $c_p = 128 \text{ J} \cdot \text{mol}^{-1} \cdot \text{K}^{-1}$ (for ethanol at 60 °C) and a porosity of 0.7, the resulting Péclet number range is

$$Pe_h = \frac{\dot{n} \cdot c_p \cdot L}{A \cdot k_{fluid}} = \frac{\dot{n}_{tot} \cdot c_p \cdot L}{\epsilon \cdot A_{mem} \cdot k_{fluid}} = 1.5 \times 10^{-2} \text{ to } 7.0 \times 10^{-1} \quad (6.32)$$

These values indicate intensified heat conduction compared to heat convection in the fluid, which does not allow a pronounced temperature profile of the fluid along the membrane thickness.

6.3.4 Temperature profile and Stanton number

The ratio of Nusselt and Péclet number is commonly referred to as Stanton number St , characterizing the ratio between heat exchange in the pore and heat convection. T.

Westermann et al. concluded that for values of $St \geq 1000$, the resulting fluid and wall temperature of the system are always in complete agreement and the reactor temperature is constant [379]. Temperature immediately jumps from the lower feed side fluid temperature T_{feed} to the constant reactor temperature at $Z = 0$, $T_{wall}(Z = 0)$. And the permeate leaves the membrane keeping the same temperature.

The Stanton number of the system under assumed conditions (60 °C with ethanol as solvent) was found to be much larger than 1000 (Eq.6.33). In fact, a Nusselt number above 700 at the given Péclet numbers is already sufficient to achieve isothermal behavior ($St > 1000$). With the Nusselt number determined in the order of 10^6 (Eq.6.31), the Péclet number can be increased accordingly by orders of magnitude in the potential benefit of higher productivity. Whereas, an increase in flow rate by several orders of magnitude will very likely lead to fairly low conversion at the exit of the membrane reactor, making the high flow rates meaningless. The maximum feasible flow rate is therefore limited by reaction kinetics rather than by the isothermal conditions here imposed. In other words, isothermal operation can be realized under any practical operating conditions due to the small characteristic reactor dimensions. (The maximum feasible flow rate depends on the reaction kinetics. Here for our catalytic membrane applied on the Suzuki-Miyaura cross-coupling between 1-iodo-4-nitrobenzene and phenyl boronic acid, the value is considered as $1280 \text{ L} \cdot \text{h}^{-1} \cdot \text{m}^{-2}$, above which conversion becomes less than 10%)

$$St = \frac{Nu}{Pe_h} = 6 \times 10^6 \text{ to } 3 \times 10^8 \gg 1000 \quad (6.33)$$

If the total flow rate \dot{n}_{tot} in Eq.6.32 is expressed in volume instead of moles, then it can be replaced by:

$$\dot{n}_{tot} = \frac{1000 \cdot Q \cdot \rho}{M} \quad (6.34)$$

where Q the total volumetric flow rate ($\text{m}^3 \cdot \text{s}^{-1}$); ρ the fluid density ($\text{kg} \cdot \text{m}^{-3}$) and M the molar mass ($\text{g} \cdot \text{mol}^{-1}$).

Together with the correlation between volumetric flow rate and flow mean velocity (Eq.6.35), the Péclet number can be expressed as Eq.6.36 and the Stanton number St thus becomes a function of F_0 (Eq.6.37) (F_0 is defined Eq.6.3). With ethanol as solvent (at 60°C), $F_0 = 2.1$ gives $St = 1.5 \times 10^3$ and $F_0 = 21$ leads to $St = 1.5 \times 10^4$. As the real Nusselt number in micro scale can be smaller than predicted by Eq.6.31, it cannot be concluded for sure that $F_0 > 2.1$ is sufficient to ensure $St \geq 1000$ (Fig.6.1). But at $F_0 > 21$, plug flow with flat concentration profile (Fig.6.6-b) and an isothermal temperature profile along the membrane thickness (Fig.6.6-a) can be achieved almost simultaneously. Hence for reactions carried out in ethanol, same requirements are imposed on the membrane configuration (pore size and membrane thickness) and experimental conditions (flow rates) for efficient radial mass and heat transfer, reflected by the Fourier number F_0 ($F_0 > 21$).

$$\frac{Q}{\epsilon \cdot A_{mem}} = \bar{v} = \frac{L}{\tau} \quad (6.35)$$

$$Pe_h = \frac{L^2}{\tau} \cdot \frac{1000 \cdot \rho \cdot c_p}{M \cdot k_{fluid}} \quad (6.36)$$

$$St = \frac{Nu}{Pe_h} = 3.66 \cdot 4 \cdot \left(\frac{L}{d}\right)^2 \cdot \frac{\tau}{L^2} \cdot \frac{M \cdot k_{fluid}}{1000 \cdot \rho \cdot c_p} = 3.66 \cdot 10^{-3} \cdot \frac{M \cdot k_{fluid}}{\rho \cdot c_p \cdot D} \cdot F_0 \quad (6.37)$$

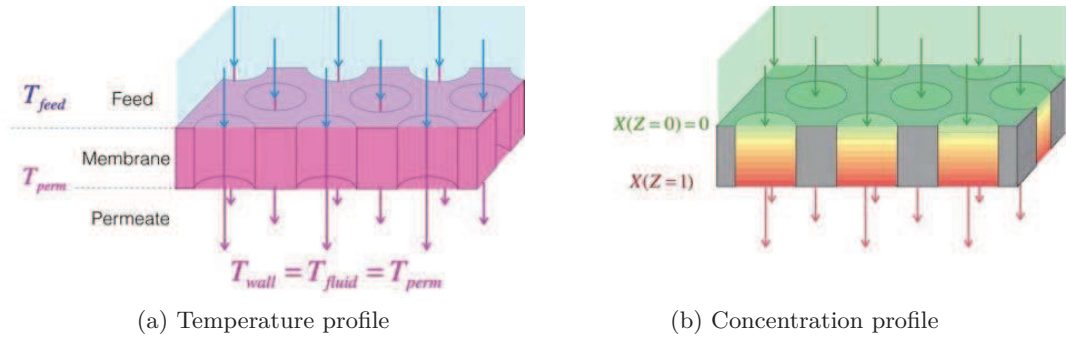


Figure 6.6: Membrane temperature profile (for exothermic reactions) and concentration profile at $F_0 > 21$ (color differences signify respectively temperature (a) and concentration gradient (b), scales not respected in the figure.)

6.3.5 Reactor temperature and external Stanton number

When $St > 1000$, an isothermal integral energy balance can be applied on the system (Eq.6.38). Introducing another dimensionless quantity, the external Stanton number St_0 , which unites the four dimensionless numbers in the differential energy balances (Eq.6.39), the integral energy balance results as Eq.6.40.

$$\dot{n}_{tot} c_p \Delta T_{ad} X(Z=1) - \dot{n}_{tot} c_p (T_{perm} - T_{feed}) - h_0 (1 - \epsilon) A_{mem} (T_{wall}(Z=0) - T_{feed}) = 0 \quad (6.38)$$

$$St_0 = \frac{Nu}{Pe_h} \frac{Bi_0}{Bi} = \frac{h_0 \cdot (1 - \epsilon) A_{mem}}{\dot{n}_{tot} \cdot c_p} \quad (6.39)$$

$$\Delta \Theta_{ad} \cdot X(Z=1) + 1 - \Theta_{perm} - St_0 \cdot (\Theta_{wall}(Z=0) - 1) = 0 \quad (6.40)$$

Under the isothermal condition ($St \geq 1000$), the inlet wall temperature $\Theta_{wall}(Z=0)$ and the permeate temperature Θ_{perm} are equal and can be replaced by the membrane

reactor temperature Θ_r , which is thus a function of the heat generation term $\Delta\Theta_{ad} \cdot X(Z = 1)$ and St_0 :

$$\Theta_r = 1 + \frac{\Delta\Theta_{ad} \cdot X(Z = 1)}{1 + St_0} \quad (6.41)$$

Therefore, in the case where $St \geq 1000$, the heat transfer inside the membrane pores turns out to be irrelevant for the resulting membrane temperature, which is exclusively determined by the external Stanton number St_0 and the conversion at the exit of the membrane reactor. The heat transfer coefficient at the membrane front face h_0 in the St_0 accounts for the membrane material property.

The heat removal ratio, defined as the ratio between heat removed from the reactor and heat generated in the reactor can also be specified in terms of St_0 :

$$\text{Heat removal ratio} = 1 - \frac{T_{perm} - T_{feed}}{\Delta T_{ad} \cdot X} = \frac{St_0}{1 + St_0} \quad (6.42)$$

This part of the heat is removed from the membrane, and then transferred to a metal porous support on the permeate side and further to the external surface of the module. The remaining part of the reaction heat contributes to the temperature step at the reactor inlet, i.e. is transported convectively.

6.3.6 Case study

The reaction enthalpy for Suzuki-Miyaura cross-coupling has not been reported. No heat release of this reaction was observed in the experiment either. Hence herein, hydrogenation of alkenes was taken as model reactions for case study. With a reaction enthalpy of $-30 \text{ kcal} \cdot \text{mol}^{-1}$ ($-126 \text{ kJ} \cdot \text{mol}^{-1}$), hydrogenations are usually classified as moderately to highly exothermic [385]. Experimental conditions in Chapter 5, (i.e. ethanol as solvent, feed temperature of 60°C) were taken for calculations. In order to predict the situation under harsher conditions, a solution concentration 10 times higher than previously used for Suzuki-Miyaura cross-coupling was applied for the calculation. Assumed reaction conditions are listed in Table 6.2.

Table 6.2: Assumed conditions for exothermic reaction carried out on the catalytic membrane.

Reaction enthalpy ^a	Solvent	Initial concentration	T_{feed}	$X(Z = 1)$
$-30 \text{ kcal} \cdot \text{mol}^{-1}$	ethanol	$0.3 \text{ mol} \cdot \text{L}^{-1}$	60°C	1

^a The reaction enthalpy for hydrogenation of alkenes is usually about $-28 \sim -30 \text{ kcal} \cdot \text{mol}^{-1}$ [386].

The adiabatic temperature rise of the hydrogenation reaction is calculated to be 17.6 K at full conversion (Eq.6.43). Consequently, temperature will rise from 60°C up

to approximately 78°C , the boiling point of ethanol.

$$\Delta T_{ad} = \frac{\chi(-\Delta H_R)}{c_p} = 17.6K \quad (6.43)$$

When the reaction is carried out on the catalytic membrane, isothermal regime can always be achieved. The maximum experimental flow rate leading to 100% conversion, $43.4 \text{ L} \cdot \text{m}^{-2} \cdot \text{h}^{-1}$ (Chapter 5) is used to calculate the external Stanton number. We took $100 \text{ W} \cdot \text{m}^{-2} \cdot \text{K}^{-1}$ as the heat transfer coefficient at the front surface of the membrane knowing that for forced convection of liquids, the heat transfer coefficient drops in the range of $100 \sim 10,000 \text{ W} \cdot \text{m}^{-2} \cdot \text{K}^{-1}$ [387]. The resulting external Stanton number St_0 , membrane and permeate temperature, heat removal ratio from the reactor are given in Table 6.3: with a membrane (and permeate temperature) of 68°C , 54% of the heat generated by the reaction is evacuated from the catalytic membrane. This part of the heat can then be transferred to the surrounding reactor module via a metal porous support which is in contact with the permeate side of the membrane. The remaining 46% of the heat is contributed to the temperature jump of the reaction solution from $T_{feed} = 60^\circ\text{C}$ to $T_{perm} = 68^\circ\text{C}$. Westermann et al. discovered from experiments that St_0 remained constant for varying flow rates. For an increasing flow rate \dot{n}_{tot} , the heat transfer coefficient h_0 on the feed side increases proportionally. The external Stanton number St_0 is therefore characteristic for the membrane reactor. Thus the heat removal ratio is also a constant.

Table 6.3: Calculated heat transfer values under the assumed condition.

St_0	Membrane temperature (equals T_{perm})	heat removal ratio from the membrane
1.16	68°C	54%

Through the above calculations, it can be concluded that it is feasible to run exothermic reactions on the catalytic membrane, although it is made of polymers. All like microreactors, the membrane possesses a substantially high heat transfer coefficient owing to the small characteristic dimension. An isothermal temperature profile can be systematically achieved in the membrane. However, in contrast to microreactors, heat removal from the membrane is limited. Thus isothermal conditions with equal feed and permeate temperature can hardly be realized for strongly exothermic reactions (e.g. combustions, $-1000 \text{ kJ} \cdot \text{mol}^{-1}$ [385]).

Discussion on limitations

Although isothermal operations can always be achieved for the catalytic membrane, there are limitations on the membrane and permeate temperature, imposed by solvent boiling point and membrane glass transition temperature. Combining Eq.6.41 with Eq.6.15 results in a general correlation between the feed-permeate fluid temperature dif-

ference and an enthalpy term (reactant molar fraction times reaction enthalpy) (Eq.6.44).

$$\chi \cdot (-\Delta H_R) = (T_r - T_{feed}) \cdot (1 + St_0) \cdot c_p \quad (6.44)$$

For liquid phase reactions with low to moderate reactant concentrations, the reactant molar fraction approximately equals to the reactant/solvent molar ratio, thus Eq.6.44 can be expressed in terms of volumetric concentration $[c]$ (Eq.6.45). The term $[c] \cdot (-\Delta H_R)$ can be interpreted as volumetric enthalpy density ($J \cdot L^{-1}$).

$$[c] \cdot (-\Delta H_R) = (T_r - T_{feed}) \cdot (1 + St_0) \cdot c_p \cdot \frac{\rho}{M} \quad (6.45)$$

with $[c]$ in $mol \cdot L^{-1}$, ΔH_R in $J \cdot mol^{-1}$, ρ and M respectively as the density ($kg \cdot m^{-3}$ or $g \cdot L^{-1}$) and molar mass ($g \cdot mol^{-1}$) of the solvent.

Taking ethanol as an example, the maximum volumetric enthalpy density respecting the boiling point limit is plotted in Fig.6.7 as a function of feed temperature (T_{feed} should be chosen depending on the activation energy of the reaction). At a feed temperature of $60^\circ C$, the $[c] \cdot (-\Delta H_R)$ limit is found to be $20 Kcal \cdot L^{-1}$ ($84 KJ \cdot L^{-1}$). At $[c] = 0.3 mol \cdot L^{-1}$, the reaction enthalpy should not exceed $66 Kcal$ ($276 KJ$). For exothermic reactions with higher enthalpy, the solution need to be diluted proportionally. For example, the solution should be diluted to $0.03 mol \cdot L^{-1}$ for a reaction enthalpy of $-664 Kcal$ ($2780 KJ$). Another possible strategy is to lower the T_{feed} once the reaction is activated at the temperature required.

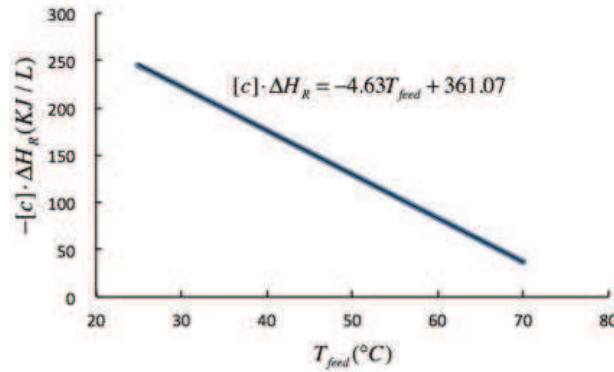


Figure 6.7: Volumetric enthalpy density limit imposed by ethanol boiling point at various feed temperatures.

In the case of gas phase reactions or when the solvent boiling point is higher than the membrane glass transition temperature, then the reaction enthalpy becomes limited by the membrane glass transition temperature and deflection temperature (pressure dependent). For PES, $T_g = 224^\circ C$ [388]. While it is suggested that temperatures should be remained below $204^\circ C$ for long-term use [389]. It should be noted that the

reactor model is also valid for gas phase reactions and the reaction enthalpy limit can be calculated by Eq.6.44.

When hollow fibers are concerned, no support is directly in contact with the fibers since they are auto-supported. In consequence, special designs on module configuration will be needed to effectively evacuate the heat from the membrane towards the outer environment.

6.4 Potential for industrial-scale production

The aim of this subsection is to predict the approximate productivity of the catalytic membrane on an industrial scale and the corresponding reactor size. Compared to flat-sheet membranes, hollow fibers offer a more compact process due to a higher surface/volume ratio. As a matter of fact, catalytic hollow fibers can be prepared using the photografting setup described in Chapter 2. Calculations are therefore based on hollow fibers assuming that the same catalytic performance as the flat-sheet membrane is retained. The hollow fibers would work in an outside-in filtration mode since polyIL layer would be grafted on the outer membrane surface.

6.4.1 Reactor configurations and corresponding working points

As demonstrated in the modeling of the catalytic membrane (Chapter 5, section 5.3.2), the reaction conversion is independent of the solution concentration below a certain limit where all catalyst active sites get saturated. For a given Thiele module, there exists a maximum productivity, expressed in terms of the product of the dimensionless mass transfer Péclet number and the conversion: $Pe_M \cdot X$. The dimensionless productivity and conversion as a function of Peclet number is plotted in Figure 6.8.

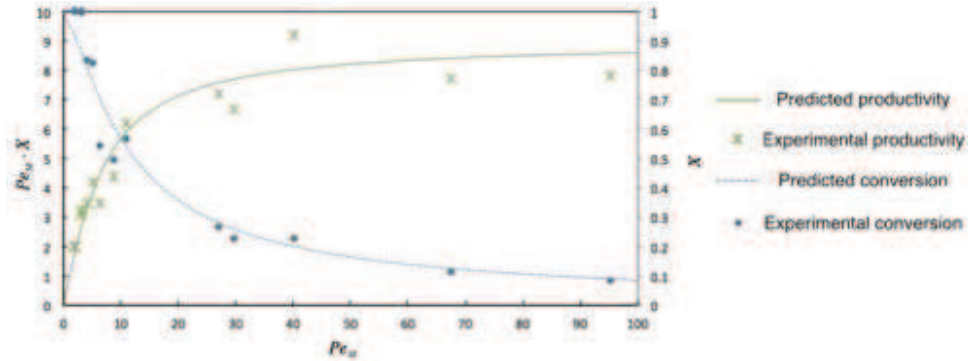


Figure 6.8: Dimensionless productivity and conversion as a function of Péclet number.

Concerning the working conditions, there are three choices:

Choice 1: Working at low flow rate, conversion $X_1 \approx 1$, low productivity: n_1

modules should be connected in parallel to increase the total flux Q_{T1} ($L \cdot h^{-1}$) given as (Fig.6.9-a):

$$Q_{T1} = n_1 \cdot J_1 \cdot SSA \cdot V \quad (6.46)$$

with J_1 as the flux density ($L \cdot m^{-2} \cdot h^{-1}$) under the parallel condition; SSA as the specific surface area of the membrane modules (ratio of total membrane surface area to module reactor volume, m^{-1}), V as the volume of one single module (m^3).

The total conversion $X_T = X_1 = 1$. The trans-membrane pressure is $\Delta P = J_1/L_p$. The experimental point corresponding to this parallel working condition is given in Table 6.4.

Table 6.4: Working point for reactors-in-parallel configuration.

Flux (J_1)	Péclet	Conversion (X_1)	$Pe_M \cdot X$
43 $L \cdot m^{-2} \cdot h^{-1}$	3.2	100%	3.2

* Values based on experimental data

Choice 2: Working at high flow rate and hence maximum productivity ($Pe_M \cdot X$)_{Max}, low conversion. This configuration will need a continuous loop system or large numbers of membrane modules connected in series to increase the conversion. The working condition at the maximum productivity is the same as choice 3.

Choice 3: Working at an intermediate flow rate ($J_2 > J_1$), conversion and productivity (an intermediate between choice 1 and 3). In this case, n_2 modules need to be connected in series (Fig.6.9-b) to increase the total conversion $X_T = 1 - (1 - X_2)^n$. The total flux can be given as:

$$Q_{T2} = J_2 \cdot SSA \cdot V \quad (6.47)$$

with the trans-membrane pressure as $\Delta P = n_2 \cdot J_2/L_p$. The corresponding data point that we chose for the following calculations are given in Table 6.5, with the productivity at 78% of the maximum value (approximately where the conversion and productivity curves cross in Fig.6.8).

Table 6.5: Working point for reactors-in-series configuration*.

Flux (J_2)	Péclet	Conversion (X_2)	$Pe_M \cdot X$
146 $L \cdot m^{-2} \cdot h^{-1}$	10.9	57%	6.2

* Values based on experimental data

In the following study, the number of membrane modules in both parallel and in-series configuration is considered to be 4 ($n_1 = n_2 = 4$, because 4 module reactors are needed for the in-series configuration to achieve a conversion of 97%). As the catalytic

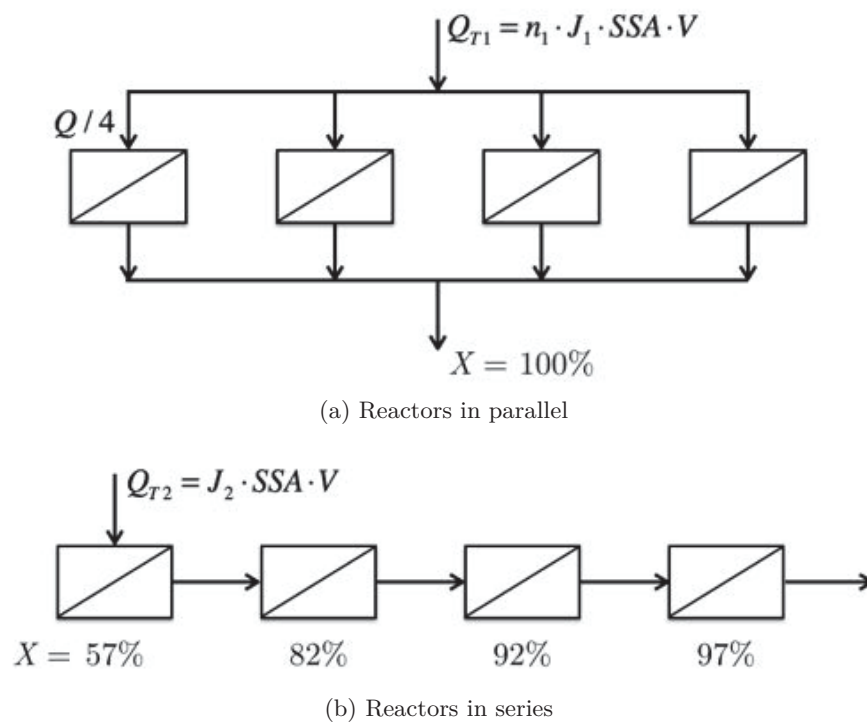


Figure 6.9: Two reactor configurations proposed.

membrane is highly permeable, the demand on pumping energy is low for either configuration (ΔP in the range of 15 – 150 *mbar*).

The specific surface area SSA (m^{-1}) of the module depends on not only the module packing density ϕ but also the fiber external diameter D_{ext} (Eq.6.48).

$$SSA = \frac{S_{fiber}}{V_{module}} = \frac{N \cdot \pi D_{ext} \cdot l}{\frac{1}{4}\pi D_M^2 \cdot l} = \frac{4\phi}{D_{ext}} \quad (6.48)$$

with l as module length (m), S_{fiber} signifying the total membrane surface area within one module (m^2), V_{module} representing the module volume (m^3), D_{ext} and D_M as respectively the fiber outer diameter and module diameter (m), and N is the number of fibers packed inside the module, calculated by $N = \phi \cdot (D_M/D_{ext})^2$.

Herein, we take a module with one of the typical sizes of water purification hollow fiber modules whose dimensions are given in Table.6.6 for calculation. The total reactor volume with 4 modules included is 107 *L*. The three packing densities considered are values in common use, with 65% as the highest practically achievable packing density.

Table 6.6: Assumed hollow fiber module dimensions

Diameter (cm)	Length (cm)	Volume (<i>L</i>)	Packing density ^a (%)
16.8	121	27	40
			55
			65

^a Defined as the ratio of total cross-sectional area of fibers to that of the module [390].

Compared to the reactor-in-series configuration, the parallel configuration can treat 18% more flow per unit time ($\Delta Q_T = 0.7 \cdot SSA$ ($L \cdot h^{-1}$)) and also offer a higher conversion. Hence the parallel configuration should be more interesting. The following productivity calculations are based this configuration.

6.4.2 Considerations on boundary layer and filtration mode

Working at constant flux (i.e. constant flow rate per unit membrane surface area) in hollow fiber modules can ensure a constant required Péclet. Thus the extrapolation of the catalytic membrane from flat sheets to hollow fibers is unlikely to induce noticeable changes in catalytic performance as long as the boundary layer is not significantly thicker in hollow fiber modules than in flat-sheet membranes. As already explained in Chapter 5. section 5.3.2, the increase of boundary layer thickness makes the reaction more limited by mass transfer, decreasing the productivity at given flow rates.

A correlation can be made between the boundary layer thickness and the inter-fiber distance: the boundary layer thickness does not exceed the half inter-fiber distance. And the latter can be calculated based on the module packing density and fiber diameter. In hollow fiber modules, regular fiber stacking is always desirable to avoid preferential paths. Assuming a hexagonal optimal stacking of fibers (see Fig.6.10-a), the basic mesh is a rhombus with the four neighboring fiber center as vertices, as shown in Fig.6.10-b. By noting the inter-fiber distance equally allocated to each fiber as δ , the packing density can be expressed as Eq.6.49 [391]. Thus δ , can be calculated by Eq.6.50. This relationship is plotted in Figure 6.11 by varying the fiber outer diameter from 250 μm to 1500 μm . (The membrane wall thickness is assumed to be 100 μm , identical to the flat-sheet catalytic membrane.) High packing densities and small fiber diameters leads to small inter-fiber distances, and thus probably thinner boundary layer as well. This is coherent with the experimental results published by Costello et. al. showing that the mass transfer coefficient increases with the module packing density at constant flow rate per unit surface area [392].

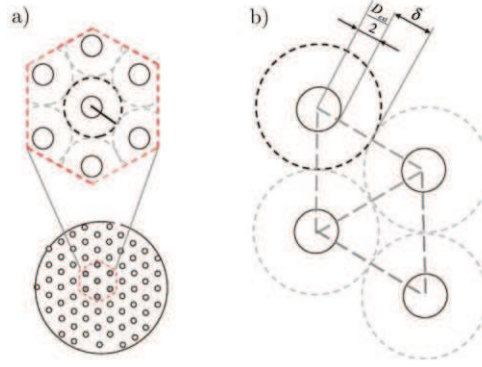


Figure 6.10: a) Schematic representation of module packing in hexagonal stacking and (b) basic rhombus mesh [391] .

$$\phi = \frac{\frac{1}{4}\pi D_{ext}^2}{2\sqrt{3}(D_{ext}/2 + \delta)^2} = \frac{\pi D_{ext}^2}{8\sqrt{3}(D_{ext}/2 + \delta)^2} \quad (6.49)$$

$$\delta = \frac{D_{ext}}{2} \cdot \left(\frac{1}{\sqrt{3}} \cdot \sqrt{\frac{\pi}{2\phi}} - 1 \right) \quad (6.50)$$

Our catalytic membrane is non-permselective. The reaction solution is also clear, without particles. Therefore, fouling is not a major problem to consider for the system. When the half inter-fiber distance is below 190 μm (the boundary layer thickness estimated in the case of flat sheet membrane), it would be more straightforward to adopt the dead-end filtration mode in hollow fiber modules since normal flow filtrations were applied on the flat sheet catalytic membranes during the experiments. This is the case for packing densities above 60% in all assumed range of fiber diameter. While cross-flow

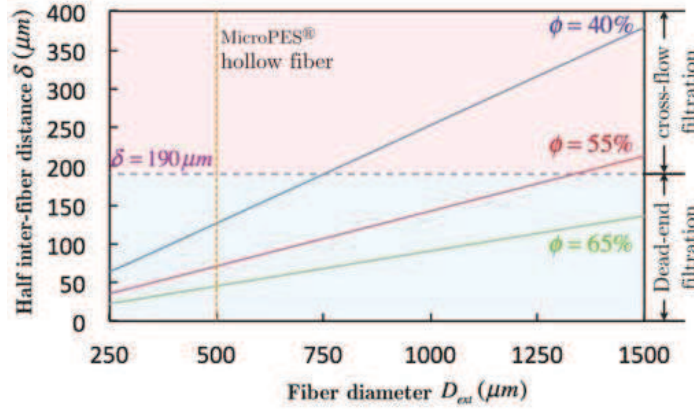


Figure 6.11: Half inter-fiber distance as a function of packing density ϕ and fiber diameter, with corresponding suggested filtration mode.

filtration should be adopted at packing density of 55% for fiber diameters above 1.35 mm and at $\phi = 40\%$ for fiber diameters above 750 μm (as indicated in Fig.6.11) so that the boundary layer thickness can be effectively limited by the high shell side circulation velocity. When it comes to low permeate flow rate and low shell side circulation velocity, a module with low packing density (40%) and fiber diameter $D_{ext} > 800 \mu\text{m}$ may require some minor process modifications to eliminate the detrimental effects of thick boundary layer and the consequent performance deviation from the flat sheet membrane. If MicroPES® hollow fibers were used ($D_{ext} = 500 \mu\text{m}$), the half inter-fiber distance δ is smaller than the boundary layer thickness estimated in the case of flat sheet membrane whatever the packing density is (Fig.6.11).

In brief, the assumption that the catalytic performance of the flat-sheet catalytic membrane can be retained for hollow fibers working under constant flux is a reasonable one. For packing densities below 55%, the hollow fiber module can work in dead-end filtration mode with little deviation from the performance of flat-sheet membrane since both the Péclet number and the boundary layer thickness are kept (almost) the same. At lower packing densities, the boundary layer thickness increases rapidly with fiber diameter. But working in cross-flow mode under appropriate shell side circulation velocity, the boundary layer thickness can be effectively reduced.

6.4.3 Production capacity of the membrane reactor and estimation on the cost of palladium

Different from the dimensionless productivity, the productivity in $\text{mol} \cdot \text{h}^{-1}$ is a function of the reaction solution concentration $[c]$, calculated as Eq.6.51. Combined with Eq.6.46 and Eq.6.48, the production capacity of the membrane reactors (productivity normalized to reactor volume, in $\text{mol} \cdot \text{h}^{-1} \cdot \text{m}^{-3}$) can be deduced as Eq.6.52.

$$Productivity = Q \cdot [c] \cdot X \quad (6.51)$$

$$\begin{aligned} \frac{Productivity}{V} &= J \cdot SSA \cdot [c] \cdot X \\ &= J \cdot \frac{4\phi}{D_{ext}} \cdot [c] \cdot X \end{aligned} \quad (6.52)$$

The production capacity was calculated for two experimental reaction solution concentrations: $0.016 \text{ mol} \cdot \text{L}^{-1}$ and $0.032 \text{ mol} \cdot \text{L}^{-1}$, and plotted as a function of fiber outer diameter at the three packing densities (Fig.6.12). The corresponding specific surface area of the hollow fiber modules is also given (on the ordinate on the right) in the figure. A module with high packing density and small fiber diameter has high specific surface area, and consequently a greater productivity per reactor volume. As shown in Fig.6.12, within the fiber diameter range considered, the production capacity at $[c]=0.032 \text{ mol} \cdot \text{L}^{-1}$ varies from the maximum $25205 \text{ ton} \cdot \text{year}^{-1} \cdot \text{m}^{-3}$ ($D_{ext} = 250 \mu\text{m}$, $\phi = 0.65$) to the minimum $2585 \text{ ton} \cdot \text{year}^{-1} \cdot \text{m}^{-3}$ ($D_{ext} = 1500 \mu\text{m}$, $\phi = 0.40$), a difference of one order of magnitude. As for MicroPES[®] fibers, the corresponding productivity capacity at packing densities of 40%, 55% and 65% is respectively 7755, 10663 and 12602 $\text{ton} \cdot \text{year}^{-1} \cdot \text{m}^{-3}$ (832, 1144 and 1352 $\text{ton} \cdot \text{year}^{-1}$ for $[c]=0.032 \text{ mol} \cdot \text{L}^{-1}$). According to LONZA [393], the production capacity of microreactors in commercial manufacturing of azide chemicals is around $12000 \text{ ton} \cdot \text{year}^{-1} \cdot \text{m}^{-3}$. Catalytic membranes, with their small characteristic dimensions, can be considered as a counterpart of microreactors. From the above calculations, the productivity capacity of catalytic membranes is in the same order of magnitude as microreactors, or even higher.

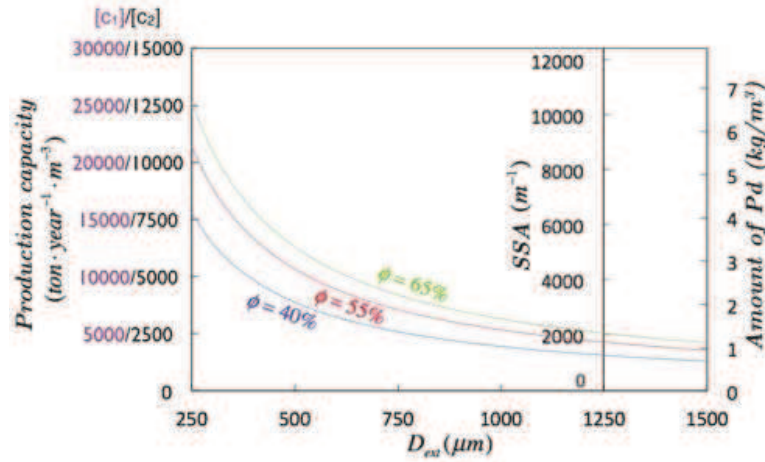


Figure 6.12: Production capacity, specific surface area and palladium quantity (ordinates from left to right) as a function of fiber outer diameter at different packing densities. The production capacity ordinate is calculated at two reaction concentrations ($[c_1]=0.032 \text{ mol} \cdot \text{L}^{-1}$, $[c_2]=0.016 \text{ mol} \cdot \text{L}^{-1}$), given in the ordinate as values at $[c_1]/\text{values at } [c_2]$. The three ordinates are proportional to each other. Three ordinate values can be read for one abscissa value.

Palladium quantity necessary for the assumed industrial scale membrane reactors is also estimated based on the experimentally measured metal loading per membrane surface area ($(0.60 \pm 0.03) \times 10^{-3} \text{ mmol} \cdot \text{cm}^{-2}$). The palladium quantity contained in the membrane reactor (also indicated in Fig.6.12) is hence proportional to the total membrane surface. It is highly interesting that less than 10 mol of palladium is already enough for the reactor volume of 107 L (without considering the possible catalyst deactivation). Taking the average palladium price for the last 6 months, 21 €/g, the cost on palladium is then inferior to 17900 €. To make a conservative estimation, we assume that palladium nanoparticles lose catalytic activity and have to be replaced after 1 week (168 h) continuous use. (The assumed the catalyst life is shorter than the usual range for catalysts in fixed beds, which usually varies from around 200 h to above 10000 h [394].) The resulting total annual palladium quantity will not exceed 44 kg. The corresponding cost on palladium catalyst is then inferior to 930,000 €/y. If deactivated palladium can be recycled, then the total capital investment on the catalyst is approximately this value, or below, if palladium lasts longer than the 1 week life span assumption.

Comparison to batch reactor:

Now consider a batch reactor of the same volume as the catalytic membrane module reactors (107 L) filled at 70%. Assuming that reaction is complete within 2 h (the experimental reaction time is 6 h), the corresponding annual production capacities and required palladium amount at several different initial reaction solution concentrations are given in Table 6.7. The quantity of palladium is deduced based on a catalyst/product ratio of 1/100 (ratio applied in experiments).

At the same concentrations assumed for the catalytic membrane ($1.6 \times 10^{-2} \text{ mol} \cdot \text{L}^{-1}$ and $3.2 \times 10^{-2} \text{ mol} \cdot \text{L}^{-1}$, entry 1-2), the production capacity of the batch reactor is 10 and 20 $\text{ton} \cdot \text{year}^{-1} \cdot \text{m}^{-3}$ (1.1 to 2.2 $\text{ton} \cdot \text{year}^{-1}$, with $V = 107 \text{ L}$), two to three orders of magnitude less than the catalytic membrane reactor. At $[c] = 0.125 \text{ mol} \cdot \text{L}^{-1}$, which leads to a productivity of 76 $\text{ton} \cdot \text{year}^{-1} \cdot \text{m}^{-3}$ (entry 3, 8.2 $\text{ton} \cdot \text{year}^{-1}$), the palladium quantity needed in the batch reactor already reaches the same amount as in the catalytic membrane reactor under a high catalyst deactivation rate (44 kg, deactivation time=168 h). The production capacity of the batch reactor at $[c] = 1.0 \text{ mol} \cdot \text{L}^{-1}$ (entry 4) is still 2-4 times less than the minimum production capacity of the membrane reactor ($\phi = 40\%$, $D_{ext} = 1500 \mu\text{m}$, Fig.6.12). And the production capacity of the batch reactor at an initial concentration of 10 $\text{mol} \cdot \text{L}^{-1}$ (entry 5) corresponds to the production capacity of the membrane reactor running under $[c] = 3.2 \times 10^{-2} \text{ mol} \cdot \text{L}^{-1}$ with $\phi = 40\%$, $D_{ext} = 634 \mu\text{m}$ or $\phi = 65\%$, $D_{ext} = 1030 \mu\text{m}$. As given in entry 4 and 5, the palladium amount required in the latter two cases, is greatly larger than in the case of catalytic membrane

In general, catalytic membrane reactors offer much higher production capacity than conventional batch reactors, thanks to a high process compactness of the membrane reactor. Different from batch reactors, reactions in the catalytic membrane reactors are carried out in continue. The productivity is irrelevant for the amount of catalyst

Table 6.7: Production capacity and palladium quantity needed at various initial concentrations in batch reactor.

Entry	<i>Concentration</i> $mol \cdot L^{-1}$	Production capacity $ton \cdot year^{-1} \cdot m^{-3}$	Amount of palladium $kg \cdot year^{-1} \cdot m^{-3}$
1	1.6×10^{-2}	10	52
2	3.2×10^{-2}	20	102
3	1.25×10^{-1}	76	411
4	1.0	611	3271
5	10	6108	32710

required, which depends uniquely on the total membrane surface area and the deactivation kinetics. The above advantages make membrane reactors a very interesting process that has a good potential for industrial scale applications.

6.5 Conclusions

In this chapter, the radial concentration profile inside membrane pores is studied in the first place based on Taylor's plug flow model [375]. It is found that for most micro filtration membranes, radial diffusion of fluid with a diffusion coefficient larger than $1.0 \times 10^{-10} m^2 \cdot s^{-1}$ occurs in the pores instantly so that pseudo-ideal plug flow behavior can be achieved. The judgement of when ideal plug flow behavior is achieved can be made based on the value of the Fourier number: $F_0 > 21$. Plug flow behavior leads to small dispersion of residence time, favoring the improvements on reaction selectivity.

In the catalytic membrane, reactions occur on the pore wall where reactants and the catalyst gets into contact. A concentration gradient will consequently appear from the center of the pore to the wall, and in the case of exothermic reactions, a temperature gradient will be created as well. But thanks to the small characteristic dimensions of the pores, the radial concentration and temperature gradients induced by the reaction can be immediately eliminated, showing a plug flow behavior. In consequence, the membrane reactor can be simplified to one dimension (along the axial direction).

The possibility to use the catalytic flat sheet membrane for exothermic reactions was explored according to the model developed by Westermann [379]. Calculations were made with ethanol as solvent. The small characteristic dimension of the membrane reactor ($0.2\mu m$) generates high intrinsic heat transfer coefficient between the fluid and pore wall and hence a large Nusselt number, indicating intensified heat exchange compared to heat conduction in the fluid, and in consequence small temperature difference between fluid and the membrane. The Péclet number is smaller than 1, showing an intensified heat conduction compared to heat convection, or a small temperature gradient along the axial direction. As a matter of fact, the membrane reactor reaches the isothermal temperature condition when the Stanton number (ratio between Nu and Pe_h) $St \geq 1000$. This coincides with the condition $F_0 > 2.1$. Therefore, plug flow behavior and isothermal

operation are simultaneously achieved inside the catalytic membrane.

Under the isothermal condition, the problem can be solved by a simple integral energy balance, from which the membrane temperature, and heat ratio removed from the membrane can be deduced. The fluid temperature jumps from the initial value to the membrane temperature once entering the membrane pores, and remains constant all along the membrane thickness. A case study is carried out concerning hydrogenation reactions on the catalytic membrane with a feeding temperature of 60 °C. At least 54% of the reaction heat is removed from the membrane and transferred to the surrounding environment. The resulting reactor temperature is 10 °C lower than the temperature that would have been reached under the adiabatic condition. The maximum reaction enthalpy feasible on the membrane is imposed by the solvent boiling point and glass transition temperature of the membrane material.

In the last part, considerations on the potential application of the catalytic membrane in the form of hollow fibers on an industrial scale are elaborated. The hollow fibers will work in an outside-in filtration mode. For modules packed with thin fibers at high packing densities, the boundary layer thickness is comparable to that found for the flat sheet catalytic membrane. And in this case the catalytic activity of the flat sheet membrane can be retained in hollow fibers working in dead-end filtration mode. Two reactor configurations (in parallel and in series, working at different flow rates) grouping four hollow fiber modules are proposed. The parallel configuration offers a higher productivity and conversion, thus is primarily considered for further extrapolation of production capacity. The production capacity of the membrane reactor can reach as high as more than $25000 \text{ ton} \cdot \text{year}^{-1} \cdot \text{m}^{-3}$ ($2682 \text{ ton} \cdot \text{year}^{-1}$, for a reaction solution concentration of $3.2 \times 10^{-2} \text{ mol} \cdot \text{L}^{-1}$), 1250 times higher than that of a batch reactor working under the same initial concentration. If the catalyst deactivation is not taken into account, less than 10 mol palladium is already sufficient for a membrane reactor volume of 107 L. Even with a fairly conservative estimation assuming fast catalyst deactivation in the membranes, the membrane reactors still demand less catalyst than a batch reactor of the same size working at a reaction solution concentration above $0.125 \text{ mol} \cdot \text{L}^{-1}$. The catalytic membrane therefore outperforms the conventional batch reactor in several aspects, larger production capacity, lower catalyst cost and also operation convenience (no need for catalyst separation). A study on the catalyst life would be interesting to permit a more accurate estimation of the amount of palladium needed and the cost on catalyst.

With small characteristic dimensions, catalytic membranes share the advantages of their counterpart, microreactors, such as efficient mass transfer, adaptability for exothermic reactions and process compactness. The productivity capacity of the membrane reactor is in the same level as, or outreaches microreactors. The advantages of membrane reactors over microreactors should lie in the ease of preparation and scale up, and low cost in the case of polymeric membranes. Although not studied here, the comparison between those two processes can also be interesting.

Conclusions and perspectives

Membranes have gained an important place in chemical technology in a broad range of applications mainly for its high compactness (productivity/module volume ratio) and low energy demand. Membrane based processes are hence in the logic of process intensification and sustainable development. Among membrane materials, inorganic membranes are generally used for highly acidic or basic environments for their inertness [395]. While polymer membranes have more versatile applications under mild conditions (from microfiltration to desalination and gas separation). Compared to inorganic membranes, polymer membranes are much lighter and also much cheaper. In this thesis, the functionalization of polymer membranes were effectuated in order to confer them with advanced properties towards more applications and possibilities.

We realized the modification of polymeric membranes with polymerizable room temperature ionic liquids by UV-induced polymerization. Two applications were targeted: CO₂ capture and catalytic membranes.

Despite the numerous researches on polyRTIL-RTIL gel for CO₂ capture, the preparation of a composite hollow fiber with a selective layer of polyRTIL-RTIL gel has never been reported, probably owing to the technical difficulty (conventional coating and extrusion methods are not adapted). In this work, we proved the feasibility of coating a polyRTIL-RTIL layer on a hollow fiber support using photo-grafting method. The main benefits of this composite membrane is the improvement on CO₂ permeance (compared to commercial membrane polymers) and possibility for other domains of applications (e.g. antistatic agents and electrolytes in lithium ion batteries).

Guidances on parameter choices (concerning material choice and experimental settings) are given in Chapter 3 based on experimental runs. PolyRTIL-Oxyplus composite membranes were obtained with CO₂ permeance in the range of ca. 610-730 gpu and CO₂/N₂ selectivity in the range of 13-17. The thickness of the selective polyRTIL-RTIL layer varies from c.a. 200 nm to 300 nm. No plasticization phenomenon was observed (in pure gas permeation tests) on the polyRTIL-Oxyplus composite membrane.

Catalytic membrane was prepared through photo grafting polyRTILs onto a PES flat sheet membrane, followed by palladium nanoparticle incorporation via intermatrix synthesis. PdNPs of 2±1 nm stabilized by polyRTILs were dispersed inside the membrane homogeneously on the plane parallel to the membrane surface but heterogeneously along the membrane thickness.

The catalytic membrane is similar to, and thus can be considered as a micro-reactor for its small characteristic dimensions ($\approx 0.2\mu\text{m}$). Theoretical calculations show that a plug flow behavior is always expected in the catalytic membrane pores. And the membrane is adapted for exothermic reactions: isothermal conditions can be achieved.

It is indispensable to adopt the flow-through configuration when using the catalytic membrane to achieve a high catalytic activity. The convective flow brings the reagents into the catalyst highly concentrated membrane local environment where the reaction takes place. The convection also helps to eliminate the mass transfer limit.

The Suzuki-Miyaura cross-coupling with 1-iodo-4-nitrobenzene as substrate is complete within 10 seconds using the catalytic membrane without formation of by-products. This reaction was in the reaction-limited regime either in the batch reactor or in the

catalytic membrane. Mathematical modeling of the catalytic membrane shows that there is a thick boundary layer on the feed side of the membrane and that the reactant concentration gradient inside this boundary layer can be eliminated at high flux (by convection). This explains the productivity increase with the flux increase. The much higher efficiency of the catalytic membrane (compared to the PdNPs dispersed in RTIL under batch condition) is principally attributed to the high local catalyst concentration (large number of NPs) inside the membrane and to the small NP size. When extrapolated to hollow fibers, this polymeric catalytic membrane can provide a productivity as high as $25000 \text{ ton} \cdot \text{year}^{-1} \cdot \text{m}^{-3}$ for 4-nitrophenyl, showing possibility for applications on an industrial scale.

Improvements on the current research and advices for future work are given below:

Concerning polyRTIL based composite hollow fibers for CO₂ capture:

1. Mixture gas tests are desirable to study the membrane performance under varied pressure and feed gas compositions in order to understand the performance of the composite membrane under real conditions. The most adapted working range of the polyRTIL-Oxyplus composite membrane can also be distinguished.
2. High permeance of the support membrane has significant benefits on both the composite membrane permeability and selectivity. Seeking a highly permeable support membrane with a smooth surface (commercial or lab-prepared) should be the major direction of improvement. An ideal support membrane should have a permeance of at least 3 times that of the selective layer. If we consider a $0.3 \mu\text{m}$ thick selective polyRTIL layer, then the permeance of the support membrane required is 4700 gpu.
3. Adjustment of the ionic liquid monomer structure can offer more space of imagination: polyRTIL with better CO₂ capture properties is conceivable. Their polymerization kinetics can also be turned faster (diffusion of the monomer solution into the membrane pores can be effectively inhibited). Other types of tailored ionic liquids can also give rise to domains of applications other than CO₂ capture.

Concerning the catalytic membrane

1. The diffusion of reactive species, metal atoms and nanoparticles inside the polymer gel structures has direct influence on the mass transfer of reagents (from the bulk solution to the catalyst surface) in the course of reactions, on the stability or leaching behavior of the MNPs supported on the membrane, and on the size of the MNPs formed. It is therefore a very interesting subject for further research. A thorough understanding on that may also give guidance on the optimization of some parameters, for example, the amount and chain length of the modifying cross-linker.
2. Study on the catalytic membrane performance under higher reactant concentrations and for long-term use is necessary to exploit the maximum treating capacity of the catalytic membrane (maximum feasible reactant concentration & deactivation time). The knowledge of the catalyst life span can give a more precise estimation on the catalyst cost and the potential of the catalytic membrane towards industrial applications.
3. A support membrane with better solvent resistance and high melting point is prefe-

rable so that more reactions (reactions with slower kinetics that requires higher temperature) can be carried out on the catalytic membrane, broadening the catalytic membrane's applications. The possibility and ease to form covalent bonding between the support membrane and the modifying agents should be considered during the choice of the support material: a higher grafting degree allows the membrane to immobilize more nanoparticles, which directly leads to the high catalytic activity of the membrane.

4. Change of the grafting material can alter their swelling behavior and partition coefficient of reactants inside the grafting layer. Since the swelling of the polymer gel is a premise of the reaction, we can therefore tailor the grafting polymer according to the target reactions.

5. Catalytic membranes with metals other than palladium can also be prepared with the same methodology. This can add to the versatility of the catalytic membrane. Rhodium, gold, iron, ruthenium and copper are all good candidates.

6. Preparation of the corresponding catalytic hollow fibers can valid the scale-up, constituting a further step towards the industrial applications for the catalytic membrane.

In short, the functionalization of the polymer membrane with polyRTILs using photo-grafting method proves to be highly prospective for both CO₂ capture and catalytic application. And more possibilities are out there for us to explore!

Bibliography

- [1] Baker R.W. *Membrane Technology and Applications, 3rd Edition*. John Wiley & Sons, Ltd, 2012.
- [2] Pabby A.K., Rizvi S.S.H., and Requena A.M.S. *Handbook of Membrane Separations: Chemical, Pharmaceutical, Food, and Biotechnological Applications*. CRC Press, 2008.
- [3] Merten U. *Desalination by reverse osmosis*. M.I.T. Press, 1966.
- [4] Drioli E., Stankiewicz A.I., and Macedonio F. Membrane engineering in process intensification—an overview. *J. Membrane Sci.*, 380(1–2):1–8, 2011.
- [5] II A.L.M., Carlisle T.K., LaFrate A.L., Voss B.A., Bara J.E., Hudiono Y.C., Wiesener B.R., Gin D.L., and Noble R.D. Design of functionalized room-temperature ionic liquid-based materials for CO₂ separations and selective blocking of hazardous chemical vapors. *Sep. Sci. Technol.*, 47(2):169–177, 2012.
- [6] Bara J.E., Hatakeyama E.S., Gin D.L., and Noble R.D. Improving CO₂ permeability in polymerized room-temperature ionic liquid gas separation membranes through the formation of a solid composite with a room-temperature ionic liquid. *Polym. Adv. Technol.*, 19(10):1415–1420, 2008.
- [7] Li P., Paul D.R., and Chung T.S. High performance membranes based on ionic liquid polymers for CO₂ separation from the flue gas. *Green Chem.*, 14(4):1052–1063, 2012.
- [8] Paul D.R. Poly(RTIL)-RTIL composite membrane for CO₂ separation from the flue gas. 2012.
- [9] Carlisle T.K., Nicodemus G.D., Gin D.L., and Noble R.D. CO₂/light gas separation performance of cross-linked poly(vinylimidazolium) gel membranes as a function of ionic liquid loading and cross-linker content. *J. Membrane Sci.*, 397–398:24–37, 2012.
- [10] Scott K. *Handbook of Industrial Membranes*. Elsevier B.V., 2nd edition edition, 1998.

- [11] Kohl A.L. and Nielsen R.B. Chapter 15 - membrane permeation processes. In A.L. Kohl and R.B. Nielsen, editors, *Gas Purification (Fifth Edition)*, pages 1238–1295. Gulf Professional Publishing, Houston, 1997.
- [12] Woodside G. and Kocurek D. *Environmental, Safety, and Health Engineering*. John Wiley & Sons, 1997.
- [13] Aptel P., Cuny J., Jozefowicz J., Morel G., and Neel J. Liquid transport through membranes prepared by grafting of polar monomers onto poly(tetrafluoroethylene) films. i. some fractionations of liquid mixtures by pervaporation. *J. Appl. Polym. Sci.*, 16(5):1061–1076, 1972.
- [14] Gas separation with membranes. In Klaus-Viktor Peinemann and N. Suzana Pereira, editors, *Membrane Technology*, pages 39–67. Wiley-VCH Verlag GmbH, 2001.
- [15] Marcano J.G.S. and Tsotsis T.T. *Catalytic Membranes and Membrane Reactors*. Wiley-VCH, 2002.
- [16] Robeson L.M. Correlation of separation factor versus permeability for polymeric membranes. *J. Membrane Sci.*, 62(2):165–185, 1991.
- [17] Baker R.W. Future directions of membrane gas separation technology. *Ind. Eng. Chem. Res.*, 41(6):1393–1411, 2002.
- [18] Crespo J.G. and Bøddeker K.W. *Membrane Processes in Separation and Purification*. Springer Science & Business Media, 1994.
- [19] Mulder M. *Basic Principles of Membrane Technology*. Springer Netherlands, Dordrecht, 1996.
- [20] Abedini R. and Nezhadmoghadam A. Application of membrane in gas separation processes: its suitability and mechanisms. *Pet. Coal*, 52(2):69–80, 2010.
- [21] Lonsdale H.K., Merten U., and Riley R.L. Transport properties of cellulose acetate osmotic membranes. *J. Appl. Polym. Sci.*, 9(4):1341–1362, 1965.
- [22] Stern S.A., Mi Y., Yamamoto H., and Clair A.K.S. Structure/permeability relationships of polyimide membranes. applications to the separation of gas mixtures. *J. Polym. Sci. B Polym. Phys.*, 27(9):1887–1909, 1989.
- [23] Lee W.M. Selection of barrier materials from molecular structure. *Polym Eng Sci*, 20(1):65–69, 1980.
- [24] Ganesh K., Nagarajan R., and Duda J.L. Rate of gas transport in glassy polymers: a free volume based predictive model. *Ind. Eng. Chem. Res.*, 31(3):746–755, 1992.

- [25] Mark H.F., Bikales N., Overberger C.G., Menges G., and Kroschwitz J.I., editors. *Encyclopedia of Polymer Science and Engineering: Volume 5, Dielectric Heating to Embedding*. Wiley-Interscience, New York, volume 5 edition edition, 1986.
- [26] Frisch H.L. Diffusion of gases and liquids in glassy and semi-crystalline polymers. In L.A. Kleintjens and P.J. Lemstra, editors, *Integration of Fundamental Polymer Science and Technology*, pages 259–264. Springer Netherlands, 1986.
- [27] DiBenedetto A.T. Molecular properties of amorphous high polymers. i. a cell theory for amorphous high polymers. *J. Polym. Sci. A Gen. Pap.*, 1(11):3459–3476, 1963.
- [28] Brandt W.W. Model calculation of the temperature dependence of small molecule diffusion in high polymers. *J. Phys. Chem.*, 63(7):1080–1085, 1959.
- [29] Barbari T.A. Dual-mode free volume model for diffusion of gas molecules in glassy polymers. *J. Polym. Sci. B Polym. Phys.*, 35(11):1737–1746, 1997.
- [30] Journois D. *Continuous Hemofiltration in the Intensive Care Unit*. CRC Press, 1997.
- [31] what-when-how, in depth tutorial and information, topic nanofiltration separations.
- [32] Loeb S. and Sourirajan S. Sea water demineralization by means of an osmotic membrane. In *Saline Water Conversion II*, volume 38 of *Advances in Chemistry*, pages 117–132. American Chemical Society, 1963.
- [33] Khulbe K.C., Feng C.Y., and Matsuura T. *Synthetic Polymeric Membranes: Characterization by Atomic Force Microscopy*. Springer Science & Business Media, 2007.
- [34] Comstock M.J. *Synthetic Membranes: volume I. Desalination*, volume 153. ACS, 1981.
- [35] Khulbe K.C., Feng C., and Matsuura T. The art of surface modification of synthetic polymeric membranes. *J. Appl. Polym. Sci.*, 115(2):855–895, 2010.
- [36] Luo M.L., Zhao J.Q., Tang W., and Pu C.S. Hydrophilic modification of poly(ether sulfone) ultrafiltration membrane surface by self-assembly of TiO₂ nanoparticles. *Appl. Surf. Sci.*, 249(1–4):76–84, 2005.
- [37] Kim K.J., Park S.H., So W.W., Ahn D.J., and Moon S.J. CO₂ separation performances of composite membranes of 6fda-based polyimides with a polar group. *J. Membrane Sci.*, 211(1):41–49, 2003.
- [38] Hamad F., Khulbe K.C., and Matsuura T. Comparison of gas separation performance and morphology of homogeneous and composite PPO membranes. *J. Membrane Sci.*, 256(1–2):29–37, 2005.

- [39] Cadotte J.E. Interfacially synthesized reverse osmosis membranes, US patent, US4277344, 1981.
- [40] Cadotte J.E. Reverse osmosis membrane, US patent, US4039440, 1977.
- [41] Schrenk W.J. and Alfrey Jr. T. Chapter 15 - coextruded multilayer polymer films and sheets. In D.R.P. NEWMAN, editor, *Polymer Blends*, pages 129–165. Academic Press, 1978.
- [42] Crawford M. Extrusion providers push technology’s limits. *Your Online Source Med. Device Prod. Inf. - Med. Prod. Outsourcing*, 2013.
- [43] Henne W., Dunweg G., Schmitz W., Pohle R., and Lawitzki F. Dialyzing membrane with adsorbent layer, US patent, US4267047, 1979.
- [44] Masao S., Tetsuo S., and yoshiyuki H. Production of semipermeable membrane composed of polysulfone hollow fiber, Japanese patent, JPS63218213, 1988.
- [45] Suzuki H., Tanaka K., Kita H., Okamoto K., Hoshino H., Yoshinaga T., and Kusuki Y. Preparation of composite hollow fiber membranes of poly(ethylene oxide)-containing polyimide and their CO₂/N₂ separation properties. *J. Membrane Sci.*, 146(1):31–37, 1998.
- [46] Kusuki Y., Yoshinaga T., and Shimazaki H. Separators for reverse osmosis, ultrafiltration, dehydration, heat and chemical resistance, strength, gas permeability, US patent, US5141642, 1989.
- [47] Ekiner O.M., Hayes R.A., and Manos P. Porous polymeric substrate and polyamide separating layer, US patent, US5085676, 1990.
- [48] Gröning P., Collaud-Coen M., Küttel O.M., and Schlapbach L. Influence of gas pressure on the plasma reaction on polyethersulphone. *Appl. Surf. Sci.*, 103(1):79–89, 1996.
- [49] Sarmadi M. Advantages and disadvantages of plasma treatment of textile materials, in 21st International Symposium on Plasma Chemistry. 2013.
- [50] Teng M.Y., Lee K.R., Liaw D.J., Lin Y.S., and Lai J.Y. Plasma deposition of acrylamide onto novel aromatic polyamide membrane for pervaporation. *Eur. Polym. J.*, 36(4):663–672, 2000.
- [51] Roualdes S., Van der Lee A., Berjoan R., Sanchez J., and Durand J. Gas separation properties of organosilicon plasma polymerized membranes. *AIChE J.*, 45(7):1566–1575, 1999.
- [52] Yamagishi H., Crivello J.V., and Belfort G. Development of a novel photochemical technique for modifying poly (arylsulfone) ultrafiltration membranes. *J. Membrane Sci.*, 105(3):237–247, 1995.

- [53] Taniguchi M., Pieracci J., Samsonoff W.A., and Belfort G. UV-assisted graft polymerization of synthetic membranes: mechanistic studies. *Chem. Mater.*, 15(20):3805–3812, 2003.
- [54] Bernstein R., Antón E., and Ulbricht M. UV-photo graft functionalization of polyethersulfone membrane with strong polyelectrolyte hydrogel and its application for nanofiltration. *ACS Appl. Mater. Interfaces*, 4(7):3438–3446, 2012.
- [55] Farmer G.T. *Modern Climate Change Science: An Overview of Today’s Climate Change Science*. Springer, 2014.
- [56] IPCC special report carbon dioxide capture and storage summary for policymakers. Technical report, Intergovernmental Panel on Climate Change Working Group, 2011.
- [57] Ocean acidification due to increasing atmospheric carbon dioxide. Technical report, The Royal Society, 2005.
- [58] Intergovernmental Panel on Climate Change Working Group. *Carbon Dioxide Capture and Storage: Special Report of the Intergovernmental Panel on Climate Change*. Cambridge University Press, 2005.
- [59] Capturing carbon dioxide. Technical report, CO2CRC, 2012.
- [60] Luis P., Van Gerven T., and Van der Bruggen B. Recent developments in membrane-based technologies for CO₂ capture. *Prog. Energy Combust. Sci.*, 38(3):419–448, 2012.
- [61] Faiz R., El-Naas M.H., and Al-Marzouqi M. Significance of gas velocity change during the transport of CO₂ through hollow fiber membrane contactors. *Chem. Eng. J.*, 168(2):593–603, 2011.
- [62] Feng C., Wang R., Zhang H., and Shi L. Diverse morphologies of PVDF hollow fiber membranes and their performance analysis as gas/liquid contactors. *J. Appl. Polym. Sci.*, 119(3):1259–1267, 2011.
- [63] Zhang W., Li J., Chen G., You W., Jiang Y., and Sun W. Experimental study of mass transfer in membrane absorption process using membranes with different porosities. *Ind. Eng. Chem. Res.*, 49(14):6641–6648, 2010.
- [64] Mansourizadeh A., Ismail A.F., and Matsuura T. Effect of operating conditions on the physical and chemical CO₂ absorption through the PVDF hollow fiber membrane contactor. *J. Membrane Sci.*, 353(1–2):192–200, 2010.
- [65] Ismail A.F. and Mansourizadeh A. A comparative study on the structure and performance of porous polyvinylidene fluoride and polysulfone hollow fiber membranes for CO₂ absorption. *J. Membrane Sci.*, 365(1–2):319–328, 2010.

- [66] Khaisri S., deMontigny D., Tontiwachwuthikul P., and Jiraratananon R. Comparing membrane resistance and absorption performance of three different membranes in a gas absorption membrane contactor. *Sep Purif Technol*, 65(3):290–297, 2009.
- [67] Luis P., Van der Bruggen B., and Van Gerven T. Non-dispersive absorption for CO₂ capture: from the laboratory to industry. *J. Chem. Technol. Biotechnol.*, 86(6):769–775, 2011.
- [68] Chabanon E., Roizard D., and Favre E. Membrane contactors for postcombustion carbon dioxide capture: A comparative study of wetting resistance on long time scales. *Ind. Eng. Chem. Res.*, 50(13):8237–8244, 2011.
- [69] Nguyen P.T., Lasseuguette E., Medina-Gonzalez Y., Remigy J.C., Roizard D., and Favre E. A dense membrane contactor for intensified CO₂ gas/liquid absorption in post-combustion capture. *J. Membrane Sci.*, 377(1–2):261–272, 2011.
- [70] Dal-Cin M.M., Kumar A., and Layton L. Revisiting the experimental and theoretical upper bounds of light pure gas selectivity–permeability for polymeric membranes. *J. Membrane Sci.*, 323(2):299–308, 2008.
- [71] Robeson L.M. The upper bound revisited. *J. Membrane Sci.*, 320(1–2):390–400, 2008.
- [72] Freeman B.D. Basis of permeability/selectivity tradeoff relations in polymeric gas separation membranes. *Macromolecules*, 32(2):375–380, 1999.
- [73] Reijerkerk S.R., Nijmeijer K., Ribeiro Jr. C.P., Freeman B.D., and Wessling M. On the effects of plasticization in CO₂/light gas separation using polymeric solubility selective membranes. *J. Membrane Sci.*, 367(1–2):33–44, 2011.
- [74] Bernardo P., Drioli E., and Golemme G. Membrane gas separation: A review/state of the art. *Ind. Eng. Chem. Res.*, 48(10):4638–4663, 2009.
- [75] Yang H., Xu Z., Fan M., Gupta R., Slimane R.B., Bland A.E., and Wright I. Progress in carbon dioxide separation and capture: A review. *J. Environ. Sci.*, 20(1):14–27, 2008.
- [76] Ho M.T., Allinson G.W., and Wiley D.E. Reducing the cost of CO₂ capture from flue gases using membrane technology. *Ind. Eng. Chem. Res.*, 47(5):1562–1568, 2008.
- [77] Heydari Gorji A. and Kaghazchi T. CO₂/h₂ separation by facilitated transport membranes immobilized with aqueous single and mixed amine solutions: Experimental and modeling study. *J. Membrane Sci.*, 325(1):40–49, 2008.
- [78] Francisco G.J., Chakma A., and Feng X. Separation of carbon dioxide from nitrogen using diethanolamine-impregnated poly(vinyl alcohol) membranes. *Sep Purif Technol*, 71(2):205–213, 2010.

- [79] Hernández-Fernández F.J., de los Ríos A.P., Tomás-Alonso F., Palacios J.M., and Villora G. Preparation of supported ionic liquid membranes: Influence of the ionic liquid immobilization method on their operational stability. *J. Membrane Sci.*, 341(1–2):172–177, 2009.
- [80] Fortunato R., Afonso C.A.M., Benavente J., Rodriguez-Castellón E., and Crespo J.G. Stability of supported ionic liquid membranes as studied by x-ray photoelectron spectroscopy. *J. Membrane Sci.*, 256(1–2):216–223, 2005.
- [81] Noble R.D. and Gin D.L. Perspective on ionic liquids and ionic liquid membranes. *J. Membrane Sci.*, 369(1–2):1–4, 2011.
- [82] Myers C., Pennline H., Luebke D., Ilconich J., Dixon J.K., Maginn E.J., and Brennecke J.F. High temperature separation of carbon dioxide/hydrogen mixtures using facilitated supported ionic liquid membranes. *J. Membrane Sci.*, 322(1):28–31, 2008.
- [83] Petropoulos J.H. Plasticization effects on the gas permeability and permselectivity of polymer membranes. *J. Membrane Sci.*, 75(1–2):47–59, 1992.
- [84] Paul D.R. and Yampol'skii Y.P. *Polymeric Gas Separation Membranes*. CRC Press, 1993.
- [85] Omole I.C. *Crosslinked Polyimide Hollow Fiber Membranes for Aggressive Natural Gas Feed Streams*. ProQuest, 2008.
- [86] Bos A., Pünt I.G.M., Wessling M., and Strathmann H. CO₂-induced plasticization phenomena in glassy polymers. *J. Membrane Sci.*, 155(1):67–78, 1999.
- [87] Chiou J.S., Barlow J.W., and Paul D.R. Plasticization of glassy polymers by CO₂. *J. Appl. Polym. Sci.*, 30(6):2633–2642, 1985.
- [88] Wessling M., Schoeman S., Van der Boomgaard T., and Smolders C. Plasticization of gas separation membranes. *Gas Sep. Purif.*, 5:222–228, 1991.
- [89] Sanders E.S. Penetrant-induced plasticization and gas permeation in glassy polymers. *J. Membrane Sci.*, 37(1):63–80, 1988.
- [90] Koros W.J., Chern R.T., Stannett V., and Hopfenberg H.B. A model for permeation of mixed gases and vapors in glassy polymers. *J. Polym. Sci. Polym. Phys. Ed.*, 19(10):1513–1530, 1981.
- [91] Karadas F., Köz B., Jacquemin J., Deniz E., Rooney D., Thompson J., Yavuz C.T., Khraisheh M., Aparicio S., and Atihan M. High pressure CO₂ absorption studies on imidazolium-based ionic liquids: Experimental and simulation approaches. *Fluid Phase Equilib.*, 351:74–86, 2013.

- [92] Simons K., Nijmeijer K., Bara J.E., Noble R.D., and Wessling M. How do polymerized room-temperature ionic liquid membranes plasticize during high pressure CO₂ permeation? *J. Membrane Sci.*, 360(1–2):202–209, 2010.
- [93] Hert D.G., Anderson J.L., Aki S.N.V.K., and Brennecke J.F. Enhancement of oxygen and methane solubility in 1-hexyl-3-methylimidazolium bis(trifluoromethylsulfonyl) imide using carbon dioxide. *Chem. Commun.*, 20:2603–2605, 2005.
- [94] Forrest J.A. and Dalnoki-Veress K. The glass transition in thin polymer films. *Adv. Colloid Interface Sci.*, 94(1–3):167–195, 2001.
- [95] Jones R.L., Kumar S.K., Ho D.L., Briber R.M., and Russell T.P. Chain conformation in ultrathin polymer films. *Nature*, 400(6740):146–149, 1999.
- [96] Jordan S.M., Henson M.A., and Koros W.J. The effects of carbon dioxide conditioning on the permeation behavior of hollow fiber asymmetric membranes. *J. Membrane Sci.*, 54(1–2):103–118, 1990.
- [97] Shishatskii A.M., Yampol’skii Y.P., and Peinemann K.V. Effects of film thickness on density and gas permeation parameters of glassy polymers. *J. Membrane Sci.*, 112(2):275–285, 1996.
- [98] Dorkenoo K.D. and Pfromm P.H. Accelerated physical aging of thin poly[1-(trimethylsilyl)-1-propyne] films. *Macromolecules*, 33(10):3747–3751, 2000.
- [99] Pfromm P.H., Pinnau I., and Koros W.J. Gas transport through integral-asymmetric membranes: A comparison to isotropic film transport properties. *J. Appl. Polym. Sci.*, 48(12):2161–2171, 1993.
- [100] Wessling M., Lidon Lopez M., and Strathmann H. Accelerated plasticization of thin-film composite membranes used in gas separation. *Sep. Purif. Technol.*, 24(1–2):223–233, 2001.
- [101] Kapantaidakis G.C., Koops G.H., Wessling M., Kaldis S.P., and Sakellaropoulos G.P. CO₂ plasticization of polyethersulfone/polyimide gas-separation membranes. *AIChE J.*, 49(7):1702–1711, 2003.
- [102] Barsema J.N., Kapantaidakis G.C., van der Vegt N.F.A., Koops G.H., and Wessling M. Preparation and characterization of highly selective dense and hollow fiber asymmetric membranes based on BTDA-TDI/MDI co-polyimide. *J. Membrane Sci.*, 216(1–2):195–205, 2003.
- [103] Vu D.Q., Koros W.J., and Miller S.J. Effect of condensable impurities in CO₂/CH₄ gas feeds on carbon molecular sieve hollow-fiber membranes. *Ind. Eng. Chem. Res.*, 42(5):1064–1075, 2003.

- [104] Yoshino M., Nakamura S., Kita H., Okamoto K.i., Tanihara N., and Kusuki Y. Olefin/paraffin separation performance of asymmetric hollow fiber membrane of 6FDA/BPDA–DDBT copolyimide. *J. Membrane Sci.*, 212(1–2):13–27, 2003.
- [105] Visser T., Koops G.H., and Wessling M. On the subtle balance between competitive sorption and plasticization effects in asymmetric hollow fiber gas separation membranes. *J. Membrane Sci.*, 252(1–2):265–277, 2005.
- [106] Wang R., Liu S.L., Lin T.T., and Chung T.S. Characterization of hollow fiber membranes in a permeator using binary gas mixtures. *Chem. Eng. Sci.*, 57(6):967–976, 2002.
- [107] Ramshaw C. HIGEE distillation - an example of process intensification. *Chem. Engr. (London)*, 389:13–14, 1983.
- [108] Heggs P.J. Experimental techniques and correlations for heat exchanger surfaces: packed beds. *Chem. Engr. (London)*, 394:13, 1983.
- [109] Ramshaw C. Process intensification: a game for n players. *Chem. Engr. (London)*, 416:30–33, 1985.
- [110] Stankiewicz A. and Moulijn J.A. *Re-Engineering the Chemical Processing Plant: Process Intensification*. CRC Press, 2003.
- [111] Stankiewicz A.I. and Moulijn J.A. Process intensification: transforming chemical engineering. *Chem. Eng. Prog.*, 96(1):22–34, 2000.
- [112] Ehrfeld W., Hessel V., and Löwe H. *Microreactors: New Technology for Modern Chemistry*. Wiley, 2000.
- [113] Wörz O., Jäckel K.P., Richter T., and Wolf A. Microreactors, a new efficient tool for optimum reactor design. *Chem. Eng. Sci.*, 56(3):1029–1033, 2001.
- [114] Gokhale S.V., Tayal V.K., Jayaraman V.K., and Kulkarni B.D. Microchannel reactors: Applications and use in process development. *Int. J. Chem. Reat. Eng.*, 3(1):1–51, 2005.
- [115] Bayer T., Matlosz M., and Jenck J. IMPULSE – ein neuartiger ansatz für die prozessentwicklung. *Chem. Ing. Tech.*, 76(5):528–533, 2004.
- [116] Jähnisch K., Hessel V., Löwe H., and Baerns M. Chemistry in microstructured reactors. *Angew. Chem. Int. Ed.*, 43(4):406–446, 2004.
- [117] Koros W.J., Ma Y.H., and Shimidzu T. Terminology for membranes and membrane processes (IUPAC recommendations 1996). *Pure Appl. Chem*, 68(7), 1996.
- [118] Saracco G. and Specchia V. Catalytic inorganic-membrane reactors: Present experience and future opportunities. *Catal. Rev.*, 36(2):305–384, 1994.

- [119] Julbe A., Farrusseng D., and Guizard C. Porous ceramic membranes for catalytic reactors—overview and new ideas. *J. Membrane Sci.*, 181(1):3–20, 2001.
- [120] Dixon A.G. Recent research in catalytic inorganic membrane reactors. *Int. J. Chem React Eng.*, 1(1):1–35, 2003.
- [121] Pashkova A., Dittmeyer R., Kaltenborn N., and Richter H. Experimental study of porous tubular catalytic membranes for direct synthesis of hydrogen peroxide. *Chem. Eng. J.*, 165(3):924–933, 2010.
- [122] Shi L., Goldbach A., Zeng G., and Xu H. H₂O₂ synthesis over PdAu membranes. *Catal. Today*, 156(3–4):118–123, 2010.
- [123] Pashkova A., Svajda K., and Dittmeyer R. Direct synthesis of hydrogen peroxide in a catalytic membrane contactor. *Chem. Eng. J.*, 139(1):165–171, 2008.
- [124] S. Abate G.C. Preparation, performances and reaction mechanism for the synthesis of H₂O₂ from H₂ and O₂ based on palladium membranes. *Catal. Today*, 104:323–328, 2005.
- [125] Sanchez Marcano J.G. and Tsotsis T.T. Catalytic membrane separation process: Oxidation reactions. In *Catalytic Membranes and Membrane Reactors*, pages 31–61. Wiley-VCH Verlag GmbH & Co. KGaA, 2002.
- [126] Zaspalis V.T., Van Praag W., Keizer K., Van Ommen J.G., Ross J.R.H., and Burggraaf A.J. Reactions of methanol over catalytically active alumina membranes. *Appl. Catal.*, 74(2):205–222, 1991.
- [127] Zalamea S., Pina M.P., Villellas A., Menéndez M., and Santamaría J. Combustion of volatile organic compounds over mixed-regime catalytic membranes. *React Kinet Catal Lett*, 67(1):13–19, 1999.
- [128] Pina M.P., Menéndez M., and Santamaría J. The knudsen-diffusion catalytic membrane reactor: An efficient contactor for the combustion of volatile organic compounds. *Appl. Catal., B*, 11(1):L19–L27, 1996.
- [129] Saracco G. and Specchia V. Catalytic ceramic filters for flue gas cleaning. 2. catalytic performance and modeling thereof. *Ind. Eng. Chem. Res.*, 34(4):1480–1487, 1995.
- [130] Liu Q., Rogut J., Chen B., Falconer J.L., and Noble R.D. Improved methanol yield from methane oxidation in a non-isothermal reactor. *Fuel*, 75(15):1748–1754, 1996.
- [131] Kobayashi M., Togawa J., Kanno T., Horiuchi J.i., and Tada K. Dramatic innovation of propene epoxidation efficiency derived from a forced flow membrane reactor. *J. Chem. Technol. Biotechnol.*, 78(2-3):303–307, 2003.

- [132] Gröschel L., Haidar R., Beyer A., Cölfen H., Frank B., and Schomäcker R. Hydrogenation of propyne in palladium-containing polyacrylic acid membranes and its characterization. *Ind. Eng. Chem. Res.*, 44(24):9064–9070, 2005.
- [133] Vincent M.J. and Gonzalez R.D. Selective hydrogenation of acetylene through a short contact time reactor. *AIChE J.*, 48(6):1257–1267, 2002.
- [134] Lambert C.K. and Gonzalez R.D. Activity and selectivity of a Pd/ γ -Al₂O₃ catalytic membrane in the partial hydrogenation reactions of acetylene and 1,3-butadiene. *Catal. Lett.*, 57(1-2):1–7, 1999.
- [135] Lange C., Storck S., Tesche B., and Maier W.F. Selective hydrogenation reactions with a microporous membrane catalyst, prepared by sol–gel dip coating. *J. Catal.*, 175(2):280–293, 1998.
- [136] Lüdtke K., Peinemann K.V., Kasche V., and Behling R.D. Nitrate removal of drinking water by means of catalytically active membranes. *J. Membrane Sci.*, 151(1):3–11, 1998.
- [137] Ilinich O.M., Gribov E.N., and Simonov P.A. Water denitrification over catalytic membranes: hydrogen spillover and catalytic activity of macroporous membranes loaded with Pd and Cu. *Catal. Today*, 82(1–4):49–56, 2003.
- [138] Ilinitch O.M., Cuperus F.P., Nosova L.V., and Gribov E.N. Catalytic membrane in reduction of aqueous nitrates: operational principles and catalytic performance. *Catal. Today*, 56(1–3):137–145, 2000.
- [139] Emin C., Remigy J.C., and Lahitte J.F. Influence of UV grafting conditions and gel formation on the loading and stabilization of palladium nanoparticles in photografted polyethersulfone membrane for catalytic reactions. *J. Membrane Sci.*, 455:55–63, 2014.
- [140] Schmid G. *Nanoparticles: From Theory to Application*. John Wiley & Sons, 2011.
- [141] Zhang H., Schmid G., and Hartmann U. Reduced metallic properties of ligand-stabilized small metal clusters. *Nano Lett.*, 3(3):305–307, 2003.
- [142] Aiken III J.D. and Finke R.G. A review of modern transition-metal nanoclusters: their synthesis, characterization, and applications in catalysis. *J. Mol. Catal. A: Chem.*, 145(1–2):1–44, 1999.
- [143] van Leeuwen D.A., van Ruitenbeek J.M., Schmid G., and de Jongh L.J. Size-dependent magnetisation of pd clusters and colloids. *Physics Letters A*, 170(4):325–333, 1992.
- [144] Schmid G. Large clusters and colloids. metals in the embryonic state. *Chem. Rev.*, 92(8):1709–1727, 1992.

- [145] Zhang H.F., Stender M., Zhang R., Wang C., Li J., and Wang L.S. Toward the solution synthesis of the tetrahedral Au₂₀ cluster. *J. Phys. Chem. B*, 108(33):12259–12263, 2004.
- [146] Li J., Li X., Zhai H.J., and Wang L.S. Au₂₀: A tetrahedral cluster. *Science*, 299(5608):864–867, 2003.
- [147] Xia Y., Xiong Y., Lim B., and Skrabalak S.E. Shape-controlled synthesis of metal nanocrystals: simple chemistry meets complex physics? *Angew. Chem. Int. Ed. Engl.*, 48(1):60–103, 2009.
- [148] Durand J., Teuma E., and Gómez M. An overview of palladium nanocatalysts: surface and molecular reactivity. *Eur. J. Inorg. Chem.*, 2008(23):3577–3586, 2008.
- [149] Liddle J.A. and Gallatin G.M. Lithography, metrology and nanomanufacturing. *Nanoscale*, 3(7):2679–2688, 2011.
- [150] Yaman M., Khudiyev T., Ozgur E., Kanik M., Aktas O., Ozgur E.O., Deniz H., Korkut E., and Bayindir M. Arrays of indefinitely long uniform nanowires and nanotubes. *Nat Mater*, 10(7):494–501, 2011.
- [151] Krämer S., Fuierer R.R., and Gorman C.B. Scanning probe lithography using self-assembled monolayers. *Chem. Rev.*, 103(11):4367–4418, 2003.
- [152] Rogers J.A. *Unconventional Nanopatterning Techniques and Applications*. Wiley, New Jersey, 2009.
- [153] Ando Y., Miyake K., Mizuno A., Korenaga A., Nakano M., and Mano H. Fabrication of nanostripe surface structure by multilayer film deposition combined with micropatterning. *Nanotechnology*, 21(9):095304, 2010.
- [154] Mailly D. Nanofabrication techniques. *Eur. Phys. J. Spec. Top.*, 172(1):333–342, 2009.
- [155] Gates B.D., Xu Q., Stewart M., Ryan D., Willson C.G., and Whitesides G.M. New approaches to nanofabrication: molding, printing, and other techniques. *Chem. Rev.*, 105(4):1171–1196, 2005.
- [156] Gaffet E., Tachikart M., El Kedim O., and Rahouadj R. Nanostructural materials formation by mechanical alloying: Morphologic analysis based on transmission and scanning electron microscopic observations. *Mater. Charact.*, 36(4–5):185–190, 1996.
- [157] Volume 3. In H.S. Nalwa, editor, *Handbook of Surfaces and Interfaces of Materials*. Academic Press, Burlington, 2001.
- [158] Ariga K., Lee M.V., Mori T., Yu X.Y., and Hill J.P. Two-dimensional nanoarchitectonics based on self-assembly. *Adv. Colloid Interface Sci*, 154(1–2):20–29, 2010.

- [159] Sakakibara K., Hill J.P., and Ariga K. Thin-film-based nanoarchitectures for soft matter: controlled assemblies into two-dimensional worlds. *Small*, 7(10):1288–1308, 2011.
- [160] Ariga K., Hill J.P., Lee M.V., Vinu A., Charvet R., and Acharya S. Challenges and breakthroughs in recent research on self-assembly. *Sci. Technol. Adv. Mater.*, 9(1):014109, 2008.
- [161] Corain B., Schmid G., and Toshima N. *Metal Nanoclusters in Catalysis and Materials Science: The Issue of Size Control: The Issue of Size Control*. Elsevier, 2011.
- [162] Ott L.S. and Finke R.G. Transition-metal nanocluster stabilization for catalysis: A critical review of ranking methods and putative stabilizers. *Coord. Chem. Rev.*, 251(9–10):1075–1100, 2007.
- [163] Fedlheim D.L. and Foss C.A. *Metal Nanoparticles: Synthesis, Characterization, and Applications*. CRC Press, New York, 1st edition edition, 2001.
- [164] Roucoux A., Schulz J., and Patin H. Reduced transition metal colloids: a novel family of reusable catalysts? *Chem. Rev.*, 102(10):3757–3778, 2002.
- [165] Crooks R.M., Zhao M., Sun L., Chechik V., and Yeung L.K. Dendrimer-encapsulated metal nanoparticles: synthesis, characterization, and applications to catalysis. *Acc. Chem. Res.*, 34(3):181–190, 2001.
- [166] Scott R.W.J., Wilson O.M., and Crooks R.M. Synthesis, characterization, and applications of dendrimer-encapsulated nanoparticles. *J Phys Chem B*, 109(2):692–704, 2005.
- [167] Narayanan R. and El-Sayed M.A. Effect of nanocatalysis in colloidal solution on the tetrahedral and cubic nanoparticle SHAPE: electron-transfer reaction catalyzed by platinum nanoparticles. *J. Phys. Chem. B*, 108(18):5726–5733, 2004.
- [168] Li, Petroski J., and El-Sayed M.A. Activation energy of the reaction between hexacyanoferrate(III) and thiosulfate ions catalyzed by platinum nanoparticles. *J. Phys. Chem. B*, 104:10956–10959, 2000.
- [169] Henglein A. Preparation and optical absorption spectra of $\text{Au}_{\text{core}}\text{Pt}_{\text{shell}}$ and $\text{Pt}_{\text{core}}\text{Au}_{\text{shell}}$ colloidal nanoparticles in aqueous solution. *J. Phys. Chem. B*, 104(10):2201–2203, 2000.
- [170] Ohde H., Wai C.M., Kim H., Kim J., and Ohde M. Hydrogenation of olefins in supercritical CO_2 catalyzed by palladium nanoparticles in a water-in- CO_2 microemulsion. *J. Am. Chem. Soc.*, 124(17):4540–4541, 2002.
- [171] Fu X., Wang Y., Wu N., Gui L., and Tang Y. Shape-selective preparation and properties of oxalate-stabilized Pt colloid. *Langmuir*, 18(12):4619–4624, 2002.

- [172] Toshima N. and Wang Y. Novel preparation, characterization and catalytic properties of polymer-protected Cu/Pd bimetallic colloid. *J. Phys. Chem. Lett.*, 22(9):1611–1614, 1993.
- [173] Esumi K., Sato N., Torigoe K., and Meguro K. Size control of gold particles using surfactants. *J. Colloid Interface Sci.*, 149(1):295–298, 1992.
- [174] Esumi K., Sadakane O., Torigoe K., and Meguro K. Preparation of platinum particles by thermal decomposition of platinum complex in organic solvent. *Colloids Surf.*, 62(3):255–257, 1992.
- [175] Esumi K., Suzuki M., Tano T., Torigoe K., and Meguro K. Dispersion of uniformly sized palladium particles in organic solvents. *Colloids Surf.*, 55:9–14, 1991.
- [176] Esumi K., Tano T., Torigoe K., and Meguro K. Preparation and characterization of bimetallic palladium-copper colloids by thermal decomposition of their acetate compounds in organic solvents. *Chem. Mater.*, 2(5):564–567, 1990.
- [177] Esumi K., Tano T., and Meguro K. Preparation of organo palladium particles from thermal decomposition of its organic complex in organic solvents. *Langmuir*, 5(1):268–270, 1989.
- [178] Tano T., Esumi K., and Meguro K. Preparation of organopalladium sols by thermal decomposition of palladium acetate. *J. Colloid Interface Sci.*, 133(2):530–533, 1989.
- [179] Smith T.W. Preparation of colloidal iron dispersions by the polymer-catalyzed decomposition of iron carbonyl and iron organocarbonyl compounds, US patent, US4252671, 1979.
- [180] Smith T.W. Preparation of colloidal cobalt dispersions by the polymer-catalyzed decomposition of cobalt carbonyl and cobalt organocarbonyl compounds, US patent, US4252673, 1979.
- [181] Smith T.W. Preparation of colloidal dispersions of ruthenium, rhodium, osmium and iridium by the polymer-catalyzed decomposition of carbonyl cluster compounds thereof, US patent, US4252678, 1979.
- [182] Henglein A., Holzwarth A., and Mulvaney P. Fermi level equilibration between colloidal lead and silver particles in aqueous solution. *J. Phys. Chem.*, 96(22):8700–8702, 1992.
- [183] Ershov B.G., Janata E., and Henglein A. Study of the formation of the dispersed phase in aqueous solutions of Cu(II). *Int J Radiat Appl Instrum C Radiat Phys Chem*, 39(1):123–126, 1992.
- [184] Ershov B.G., Janata E., Michaelis M., and Henglein A. Reduction of aqueous copper(2+) by carbon dioxide(1-): first steps and the formation of colloidal copper. *J. Phys. Chem.*, 95(22):8996–8999, 1991.

- [185] Marignier J.L., Belloni J., Delcourt M.O., and Chevalier J.P. Microaggregates of non-noble metals and bimetallic alloys prepared by radiation-induced reduction. *Nature*, 317(6035):344–345, 1985.
- [186] Delcourt M.O., Belloni J., Marignier J.L., Mory C., and Colliex C. Metal microaggregates prepared by radiolytic reduction in liquids. *Radiat. Phys. Chem. (1977)*, 23(4):485–487, 1984.
- [187] Delcourt M., Keghouche N., and Belloni J. Radiation reduced platinum sols - characterization and catalytic efficiency. *Nouv. J. Chim.*, 7(2):131–136, 1983.
- [188] Mills G. and Henglein A. Radiation chemical formation of colloidal iridium and mechanism of catalysed hydrogen formation by radicals. *Radiat. Phys. Chem. (1977)*, 26(4):385–390, 1985.
- [189] Belloni J., Delcourt M.O., and Leclerc C. Radiation induced preparation of metal catalysts: iridium aggregates. *Nouv. J. Chim.*, 6:507, 1982.
- [190] Mosseri S., Henglein A., and Janata E. Reduction of dicyanoaurate(i) in aqueous solution: formation of nonmetallic clusters and colloidal gold. *J. Phys. Chem.*, 93(18):6791–6795, 1989.
- [191] Henglein A. and Lilie J. Radiation electrochemistry of the colloidal cadmium microelectrode. catalysis of hydrogen formation by organic free radicals. *J. Phys. Chem.*, 85(9):1246–1251, 1981.
- [192] Henglein A. The reactivity of silver atoms in aqueous solutions (a γ -radiolysis study). *Ber. Bunsenges. Phys. Chem.*, 81(6):556–561, 1977.
- [193] Henglein A., Mulvaney P., Holzwarth A., Sosebee T.E., and Fojtik A. Electrochemistry of colloidal silver particles in aqueous solution: Deposition of lead and indium and accompanying optical effects. *Ber. Bunsenges. Phys. Chem.*, 96(6):754–759, 1992.
- [194] Ershov B.G. and Henglein A. Optical spectrum and some chemical properties of colloidal thallium in aqueous solution. *J. Phys. Chem.*, 97(13):3434–3436, 1993.
- [195] Butler J. and Henglein A. Elementary reactions of the reduction of tl^+ in aqueous solution. *Radiation Physics and Chemistry (1977)*, 15(5):603–612, 1980.
- [196] Henglein A. and Tausch-Treml R. Optical absorption and catalytic activity of subcolloidal and colloidal silver in aqueous solution: A pulse radiolysis study. *J. Colloid Interface Sci.*, 80(1):84–93, 1981.
- [197] Henglein A., Gutierrez M., Janata E., and Ershov B.G. Absorption spectrum and chemical reactions of colloidal cadmium in aqueous solution. *J. Phys. Chem.*, 96(11):4598–4602, 1992.

- [198] Salkar R.A., Jeevanandam P., Aruna S.T., Koltypin Y., and Gedanken A. The sonochemical preparation of amorphous silver nanoparticles. *J. Mater. Chem.*, 9(6):1333–1335, 1999.
- [199] Koltypin Y., Fernandez A., Rojas T.C., Campora J., Palma P., Prozorov R., and Gedanken A. Encapsulation of nickel nanoparticles in carbon obtained by the sonochemical decomposition of $\text{Ni}(\text{C}_8\text{H}_{12})_2$. *Chem. Mater.*, 11(5):1331–1335, 1999.
- [200] Dhas N.A. and Gedanken A. Sonochemical preparation and properties of nanostructured palladium metallic clusters. *J. Mater. Chem.*, 8(2):445–450, 1998.
- [201] Suslick K.S. and Price G.J. Applications of ultrasound to materials chemistry. *Annu. Rev. Mater. Sci.*, 29(1):295–326, 1999.
- [202] Chaudret B. Organometallic approach to nanoparticles synthesis and self-organization. *C. R. Physique*, 6(1):117–131, 2005.
- [203] López-Vinasco A.M., Favier I., Pradel C., Huerta L., Guerrero-Ríos I., Teuma E., Gómez M., and Martin E. Unexpected bond activations promoted by palladium nanoparticles. *Dalton Trans.*, 43(24):9038–9044, 2014.
- [204] Favier I., Gómez M., Muller G., Axet M.R., Castellón S., Claver C., Jansat S., Chaudret B., and Philippot K. Palladium catalytic species containing chiral phosphites: Towards a discrimination between molecular and colloidal catalysts. *Adv. Synth. Catal.*, 349(16):2459–2469, 2007.
- [205] Sanhes D., Raluy E., Rétory S., Saffon N., Teuma E., and Gómez M. Unexpected activation of carbon-bromide bond promoted by palladium nanoparticles in suzuki C-C couplings. *Dalton Trans.*, 39(40):9719–9726, 2010.
- [206] Turkevich J., Stevenson P.C., and Hillier J. A study of the nucleation and growth processes in the synthesis of colloidal gold. *Discuss. Faraday Soc.*, 11(0):55–75, 1951.
- [207] Turkevich J. and Kim G. Palladium: preparation and catalytic properties of particles of uniform size. *Science*, 169(3948):873–879, 1970.
- [208] Turkevich J. Colloidal gold. Part I. *Gold Bull.*, 18(3):86–91, 1985.
- [209] Murray C.B., Kagan C.R., and Bawendi M.G. Synthesis and characterization of monodisperse nanocrystals and close-packed nanocrystal assemblies. *Annu. Rev. Mater. Sci.*, 30(1):545–610, 2000.
- [210] Peng X., Wickham J., and Alivisatos A.P. Kinetics of II-VI and III-V colloidal semiconductor nanocrystal growth: “focusing” of size distributions. *J. Am. Chem. Soc.*, 120(21):5343–5344, 1998.
- [211] LaMer V.K. and Dinegar R.H. Theory, production and mechanism of formation of monodispersed hydrosols. *J. Am. Chem. Soc.*, 72(11):4847–4854, 1950.

- [212] Sugimoto T. *Monodispersed Particles*. Elsevier, Amsterdam, New York, 2001.
- [213] Watzky M.A. and Finke R.G. Transition metal nanocluster formation kinetic and mechanistic studies. a new mechanism when hydrogen is the reductant: slow, continuous nucleation and fast autocatalytic surface growth. *J. Am. Chem. Soc.*, 119(43):10382–10400, 1997.
- [214] Masuda Y., editor. *Nanocrystal*. InTech, 2011.
- [215] El Nakat J.H., Dance I.G., Fisher K.J., and Willett G.D. Gas phase copper chalcogenide cluster ions, formed by laser-ablation. *Inorg. Chem.*, 30(15):2957–2958, 1991.
- [216] Vernal R. Nucleation control in size and dispersity in metallic nanoparticles: The prominent role of particle aggregation. Thesis, Washington University in St Louis, St Louis, 2010.
- [217] Joachim P. Spatz, Thomas Herzog, Stefan Mössmer, Paul Ziemann, and Martin Möller. Inorganic nanostructures on surfaces using micellar diblock copolymer templates. In *Micro- and Nanopatterning Polymers*, volume 706 of *ACS Symposium Series*. American Chemical Society, 1998.
- [218] Möller M., Spatz J.P., Roescher A., Mößmer S., Selvan S.T., and Klok H.A. Mineralization of gold in block copolymer micelles. *Macromol. Symp.*, 117(1):207–218, 1997.
- [219] Spatz J.P., Mößmer S., Möller M., Herzog T., Plettl A., and Ziemann P. Functional nanostructures by organized macromolecular-metallic hybrid systems. *J. Lumin.*, 76–77:168–173, 1998.
- [220] Favier I., Massou S., Teuma E., Philippot K., Chaudret B., and Gómez M. A new and specific mode of stabilization of metallic nanoparticles. *Chem. Commun.*, (28):3296–3298, 2008.
- [221] Jansat S., Picurelli D., Pelzer K., Philippot K., Gómez M., Muller G., Lecante P., and Chaudret B. Synthesis, characterization and catalytic reactivity of ruthenium nanoparticles stabilized by chiral n-donor ligands. *New J. Chem.*, 30(1):115–122, 2006.
- [222] Piner R.D., Zhu J., Xu F., Hong S., and Mirkin C.A. "dip-pen" nanolithography. *Science*, 283(5402):661–663, 1999.
- [223] Spatz J.P., Mössmer S., Hartmann C., Möller M., Herzog T., Krieger M., Boyen H.G., Ziemann P., and Kabius B. Ordered deposition of inorganic clusters from micellar block copolymer films. *Langmuir*, 16(2):407–415, 2000.
- [224] Spatz J.P., Eibeck P., Mößmer S., Möller M., Herzog T., and Ziemann P. Ultrathin diblock copolymer/titanium laminates—a tool for nanolithography. *Adv. Mater.*, 10(11):849–852, 1998.

- [225] Dupont J. From molten salts to ionic liquids: A “nano” journey. *Acc. Chem. Res.*, 44(11):1223–1231, 2011.
- [226] Scholten J.D., Leal B.C., and Dupont J. Transition metal nanoparticle catalysis in ionic liquids. *ACS Catal.*, 2(1):184–200, 2012.
- [227] Tadros T. Steric stabilization. In T. Tadros, editor, *Encyclopedia of Colloid and Interface Science*, pages 1048–1049. Springer Berlin Heidelberg, 2013.
- [228] Schmid G., Pfeil R., Boese R., Bandermann F., Meyer S., Calis G.H.M., and van der Velden J.W.A. $\text{Au}_{55}[\text{P}(\text{C}_6\text{H}_5)_3]_{12}\text{Cl}_6$ — ein goldcluster ungewöhnlicher gröÙe. *Chem. Ber.*, 114(11):3634–3642, 1981.
- [229] Vargaftik M.N., Zagorodnikov V.P., Stolyarov I.P., Moiseev I.I., Likholobov V.A., Kochubey D.I., Chuvilin A.L., Zaikovskiy V.I., Zamaraev K.I., and Timofeeva G.I. A novel giant palladium cluster. *J. Chem. Soc., Chem. Commun.*, (14):937–939, 1985.
- [230] van der Velden J.W.A., Vollenbroek F.A., Bour J.J., Beurskens P.T., Smits J.M.M., and Bosnian W.P. Gold clusters containing bidentate phosphine ligands. preparation and x-ray structure investigation of $[\text{Au}_5(\text{dppmH})_3(\text{dppm})](\text{NO}_3)_2$ and $[\text{Au}_{13}(\text{dppmH})_6](\text{NO}_3)_n$. *Recl. Trav. Chim. Pays-Bas*, 100(4):148–152, 1981.
- [231] Briant C.E., Theobald B.R.C., White J.W., Bell L.K., Mingos D.M.P., and Welch A.J. Synthesis and x-ray structural characterization of the centred icosahedral gold cluster compound $[\text{Au}_{13}(\text{PMe}_2\text{Ph})_{10}\text{Cl}_2](\text{PF}_6)_3$; the realization of a theoretical prediction. *J. Chem. Soc., Chem. Commun.*, (5):201–202, 1981.
- [232] Schmid G. and Corain B. Nanoparticulated gold: Syntheses, structures, electronics, and reactivities. *Eur. J. Inorg. Chem.*, 2003(17):3081–3098, 2003.
- [233] Favier I., Lavedan P., Massou S., Teuma E., Philippot K., Chaudret B., and Gómez M. Hydrogenation processes at the surface of ruthenium nanoparticles: A NMR study. *Top Catal.*, 56(13-14):1253–1261, 2013.
- [234] Corain B., Zecca M., Canton P., and Centomo P. Synthesis and catalytic activity of metal nanoclusters inside functional resins: an endeavour lasting 15 years. *Phil. Trans. R. Soc. A*, 368(1915):1495–1507, 2010.
- [235] Corain B., Centomo P., and Zecca M. Hybrid phase metal catalysis based on crosslinked functional polymers. *Chim. Ind. (Milan)*, 86:114–121, 2004.
- [236] Burato C., Centomo P., Pace G., Favaro M., Prati L., and Corain B. Generation of size-controlled palladium(0) and gold(0) nanoclusters inside the nanoporous domains of gel-type functional resins: Part II: Prospects for oxidation catalysis in the liquid phase. *J. Mol. Catal. A: Chem.*, 238(1–2):26–34, 2005.

- [237] Cai L.H., Panyukov S., and Rubinstein M. Mobility of nonsticky nanoparticles in polymer liquids. *Macromolecules*, 44(19):7853–7863, 2011.
- [238] Rubinstein M. and Colby R.H. *Polymer Physics*. Oxford University Press, Oxford ; New York, 1 edition edition, 2003.
- [239] Hallett J.P. and Welton T. Room-temperature ionic liquids: Solvents for synthesis and catalysis. 2. *Chem. Rev.*, 111(5):3508–3576, 2011.
- [240] Bhargava B.L., Balasubramanian S., and Klein M.L. Modelling room temperature ionic liquids. *Chem. Commun.*, (29):3339–3351, 2008.
- [241] Yan F., Xia S., Wang Q., and Ma P. Predicting the decomposition temperature of ionic liquids by the quantitative structure–property relationship method using a new topological index. *J. Chem. Eng. Data*, 57(3):805–810, 2012.
- [242] Maton C., Vos N.D., and Stevens C.V. Ionic liquid thermal stabilities: decomposition mechanisms and analysis tools. *Chem. Soc. Rev.*, 42(13):5963–5977, 2013.
- [243] Crosthwaite J.M., Aki S.N.V.K., Maginn E.J., and Brennecke J.F. Liquid phase behavior of imidazolium-based ionic liquids with alcohols. *J. Phys. Chem. B*, 108(16):5113–5119, 2004.
- [244] Giraud G., Gordon C.M., Dunkin I.R., and Wynne K. The effects of anion and cation substitution on the ultrafast solvent dynamics of ionic liquids: A time-resolved optical kerr-effect spectroscopic study. *J. Chem. Phys.*, 119(1):464–477, 2003.
- [245] Husson-Borg P., Majer V., and Costa Gomes M.F. Solubilities of oxygen and carbon dioxide in butyl methyl imidazolium tetrafluoroborate as a function of temperature and at pressures close to atmospheric pressure†. *J. Chem. Eng. Data*, 48(3):480–485, 2003.
- [246] Bara J.E., Carlisle T.K., Gabriel C.J., Camper D., Finotello A., Gin D.L., and Noble R.D. Guide to CO₂ separations in imidazolium-based room-temperature ionic liquids. *Ind. Eng. Chem. Res.*, 48(6):2739–2751, 2009.
- [247] Bara J.E., Camper D.E., Gin D.L., and Noble R.D. Room-temperature ionic liquids and composite materials: Platform technologies for CO₂ capture. *Acc. Chem. Res.*, 43(1):152–159, 2010.
- [248] Hasib-ur Rahman M., Sijaj M., and Larachi F. Ionic liquids for CO₂ capture—development and progress. *Chem. Eng. Process.*, 49(4):313–322, 2010.
- [249] Favier I., Madec D., and Gómez M. Metallic nanoparticles in ionic liquids – applications in catalysis. In P. Serp and K. Philippot, editors, *Nanomaterials in Catalysis*, pages 203–249. Wiley-VCH Verlag GmbH & Co. KGaA, 2013.

- [250] Durand J., Teuma E., and Gómez M. Ionic liquids as a medium for enantioselective catalysis. *C. R. Chimie.*, 10(3):152–177, 2007.
- [251] Dupont J., Fonseca G.S., Umpierre A.P., Fichtner P.F.P., and Teixeira S.R. Transition-metal nanoparticles in imidazolium ionic liquids: recycable catalysts for biphasic hydrogenation reactions. *J. Am. Chem. Soc.*, 124(16):4228–4229, 2002.
- [252] Dupont J. and Suarez P.A.Z. Physico-chemical processes in imidazolium ionic liquids. *Phys. Chem. Chem. Phys.*, 8(21):2441–2452, 2006.
- [253] Hardacre C., Holbrey J.D., McMath S.E.J., Bowron D.T., and Soper A.K. Structure of molten 1,3-dimethylimidazolium chloride using neutron diffraction. *J. Chem. Phys.*, 118(1):273–278, 2003.
- [254] DaSilveira Neto B.A., Santos L.S., Nachtigall F.M., Eberlin M.N., and Dupont J. On the species involved in the vaporization of imidazolium ionic liquids in a steam-distillation-like process. *Angew. Chem. Int. Edit.*, 45(43):7251–7254, 2006.
- [255] Gozzo F.C., Santos L.S., Augusti R., Consorti C.S., Dupont J., and Eberlin M.N. Gaseous supramolecules of imidazolium ionic liquids: “magic” numbers and intrinsic strengths of hydrogen bonds. *Chemistry*, 10(23):6187–6193, 2004.
- [256] Suarez P.A., Einloft S., Dullius J.E., de Souza R.F., and Dupont J. Synthesis and physical-chemical properties of ionic liquids based on 1-n-butyl-3-methylimidazolium cation. *J. chim. Phys. Phys.-Chim. Biol.*, 95(7):1626–1639, 1998.
- [257] Schrekker H.S., Gelesky M.A., Stracke M.P., Schrekker C.M.L., Machado G., Teixeira S.R., Rubim J.C., and Dupont J. Disclosure of the imidazolium cation coordination and stabilization mode in ionic liquid stabilized gold(0) nanoparticles. *J. Colloid Interface Sci.*, 316(1):189–195, 2007.
- [258] Pan C., Pelzer K., Philippot K., Chaudret B., Dassenoy F., Lecante P., and Casanove M.J. Ligand-stabilized ruthenium nanoparticles: synthesis, organization, and dynamics. *J. Am. Chem. Soc.*, 123(31):7584–7593, 2001.
- [259] Dupont J. and Scholten J.D. On the structural and surface properties of transition-metal nanoparticles in ionic liquids. *Chem. Soc. Rev.*, 39(5):1780–1804, 2010.
- [260] Ott L.S., Cline M.L., Deetlefs M., Seddon K.R., and Finke R.G. Nanoclusters in ionic liquids: evidence for n-heterocyclic carbene formation from imidazolium-based ionic liquids detected by (2)h NMR. *J. Am. Chem. Soc.*, 127(16):5758–5759, 2005.
- [261] Cavell K.J. and McGuinness D.S. Redox processes involving hydrocarbylmatal (n-heterocyclic carbene) complexes and associated imidazolium salts: ramifications for catalysis. *Coord. Chem. Rev.*, 248(7–8):671–681, 2004.

- [262] Magna L., Chauvin Y., Niccolai G.P., and Basset J.M. The importance of imidazolium substituents in the use of imidazolium-based room-temperature ionic liquids as solvents for palladium-catalyzed telomerization of butadiene with methanol. *Organometallics*, 22(22):4418–4425, 2003.
- [263] Dupont J. and Spencer J. On the noninnocent nature of 1,3-dialkylimidazolium ionic liquids. *Angew. Chem. Int. Ed.*, 43(40):5296–5297, 2004.
- [264] Bara J.E., Noble R.D., and Gin D.L. Effect of “free” cation substituent on gas separation performance of polymer-room-temperature ionic liquid composite membranes. *Ind. Eng. Chem. Res.*, 48(9):4607–4610, 2009.
- [265] Baltus R.E., Culbertson B.H., Dai S., Luo H., and DePaoli D.W. Low-pressure solubility of carbon dioxide in room-temperature ionic liquids measured with a quartz crystal microbalance. *J. Phys. Chem. B*, 108(2):721–727, 2004.
- [266] Shiflett M.B. and Yokozeki A. Solubilities and diffusivities of carbon dioxide in ionic liquids: [bmim][PF₆] and [bmim][BF₄]. *Ind. Eng. Chem. Res.*, 44(12):4453–4464, 2005.
- [267] Hou Y. and Baltus R.E. Experimental measurement of the solubility and diffusivity of CO₂ in room-temperature ionic liquids using a transient thin-liquid-film method. *Ind. Eng. Chem. Res.*, 46(24):8166–8175, 2007.
- [268] Cadena C., Anthony J.L., Shah J.K., Morrow T.I., Brennecke J.F., and Maginn E.J. Why is CO₂ so soluble in imidazolium-based ionic liquids? *J. Am. Chem. Soc.*, 126(16):5300–5308, 2004.
- [269] Aki S.N.V.K., Mellein B.R., Saurer E.M., and Brennecke J.F. High-pressure phase behavior of carbon dioxide with imidazolium-based ionic liquids. *J. Phys. Chem. B*, 108(52):20355–20365, 2004.
- [270] Tang J., Tang H., Sun W., Plancher H., Radosz M., and Shen Y. Poly(ionic liquid)s: a new material with enhanced and fast CO₂ absorption. *Chem. Commun.*, (26):3325–3327, 2005.
- [271] Tang J., Tang H., Sun W., Radosz M., and Shen Y. Low-pressure CO₂ sorption in ammonium-based poly(ionic liquid)s. *Polymer*, 46(26):12460–12467, 2005.
- [272] Bara J.E., Gin D.L., and Noble R.D. Effect of anion on gas separation performance of polymer-room-temperature ionic liquid composite membranes. *Ind. Eng. Chem. Res.*, 47(24):9919–9924, 2008.
- [273] Akbari A., Desclaux S., Rouch J.C., and Remigy J.C. Application of nanofiltration hollow fibre membranes, developed by photografting, to treatment of anionic dye solutions. *Journal of Membrane Sci.*, 297(1–2):243–252, 2007.

- [274] Goma-Bilongo T., Akbari A., Clifton M.J., and Remigy J.C. Numerical simulation of a UV photografting process for hollow-fiber membranes. *J. Membrane Sci.*, 278(1–2):308–317, 2006.
- [275] M. J. Assael S.K.P. Measurements of the viscosity of alcohols in the temperature range 290–340 K at pressures up to 30 MPa. *Int. J. Thermophys.*, 15(1):95–107, 1994.
- [276] Chahdoura F., Pradel C., and Gómez M. Palladium nanoparticles in glycerol: A versatile catalytic system for C-X bond formation and hydrogenation processes. *Adv. Synth. Catal.*, 355(18):3648–3660, 2013.
- [277] Energy efficiency indicators for public electricity production from fossil fuels. Technical report, International Energy Agency, 2008.
- [278] Favre E. Membrane processes and postcombustion carbon dioxide capture: Challenges and prospects. *Chem. Eng. J.*, 171(3):782–793, 2011.
- [279] CO₂ capture and storage projects. Technical report, European Commission, 2007.
- [280] Plechkova N.V. and Seddon K.R. Applications of ionic liquids in the chemical industry. *Chem. Soc. Rev.*, 37(1):123–150, 2007.
- [281] Ríos A.P.d.l., Hernández-Fernández F.J., Lozano L.J., and Godínez C. Supported ionic liquid membranes: Preparation, stability and applications. In A. Mohammad and D. Inamuddin, editors, *Green Solvents II*, pages 275–288. Springer Netherlands, 2012.
- [282] Bara J., Carlisle T.K., Hatakeyama E.S., Gin D.L., Noble R.D., Kerr R.L., and LaFratre A.L. Imidazolium-based room-temperature ionic liquids, polymers monomers and membranes incorporating same.
- [283] Missan H.P.S., Duncan A., and Noriega N. Novel lithium ionic liquid-based gel type electrolytes for lithium ion batteries. *IUP J. Phys.*, 3(1):43–54, 2010.
- [284] Yang M. and Hou J. Membranes in lithium ion batteries. *Membranes*, 2(3):367–383, 2012.
- [285] Applications: Free radical initiators (sigma-aldrich).
- [286] Lampman S. *Characterization and Failure Analysis of Plastics*. ASM International, 2003.
- [287] Weingärtner H. Understanding ionic liquids at the molecular level: facts, problems, and controversies. *Angew. Chem. Int. Ed. Engl.*, 47(4):654–670, 2008.
- [288] Hansen C.M. The three dimensional solubility parameter and solvent diffusion coefficient: Their importance in surface coating formulation. Ph.D. thesis, Danish Technical Press, Copenhagen, 1967.

- [289] Quéré D. Fluid coating on a fiber. *Annu. Rev. Fluid Mech.*, 31(1):347–384, 1999.
- [290] Remigy J.C., Nakache E., and Brechot P.D. Computer-aided method for the determination of hansen solubility parameters. application to the miscibility of refrigerating lubricant and new refrigerant. *Ind. Eng. Chem. Res.*, 38(11):4470–4476, 1999.
- [291] Hecht E. *Optics: International Edition, 4th ed.* Pearson Higher Education, 2003.
- [292] Verdía P., Hernaiz M., González E.J., Macedo E.A., Salgado J., and Tojo E. Effect of the number, position and length of alkyl chains on the physical properties of polysubstituted pyridinium ionic liquids. *J. Chem. Thermodyn.*, 69:19–26, 2014.
- [293] Kumar A., Singh T., Gardas R.L., and Coutinho J.A.P. Non-ideal behaviour of a room temperature ionic liquid in an alkoxyethanol or poly ethers at $T = (298.15 \text{ to } 318.15) \text{ K}$. *J. Chem. Thermodyn.*, 40(1):32–39, 2008.
- [294] Wu T.Y., Chen B.K., Hao L., Lin Y.C., Wang H.P., Kuo C.W., and Sun I.W. Physicochemical properties of glycine-based ionic liquid [QuatGly-OEt][EtOSO₃] (2-ethoxy-1-ethyl-1,1-dimethyl-2-oxoethanaminium ethyl sulfate) and its binary mixtures with poly(ethylene glycol) ($M_w = 200$) at various temperatures. *Int J Mol Sci*, 12(12):8750–8772, 2011.
- [295] Nunes S.P. and Peinemann K.V. Gas separation with membranes. In S.P. Nunes and K.V. Peinemann, editors, *Membrane Technology, 2nd ed.*, pages 39–67. Wiley-VCH Verlag GmbH, 2001.
- [296] Merkel T.C., Lin H., Wei X., and Baker R. Power plant post-combustion carbon dioxide capture: An opportunity for membranes. *J. Membrane Sci.*, 359(1–2):126–139, 2010.
- [297] Tsuji J. *Palladium Reagents and Catalysts*. John Wiley & Sons, Ltd, 2004.
- [298] Favier I., Madec D., Teuma E., and Gómez M. Palladium nanoparticles applied in organic synthesis as catalytic precursors. *Curr. Org. Chem.*, 15:3127–3174, 2011.
- [299] Barnard C.F.J. Palladium-catalyzed carbonylation—a reaction come of age. *Organometallics*, 27(21):5402–5422, 2008.
- [300] Gadge S.T. and Bhanage B.M. Recent developments in palladium catalysed carbonylation reactions. *RSC Adv.*, 4(20):10367–10389, 2014.
- [301] Venkatesan R., Precht M.H.G., Scholten J.D., Pezzi R.P., Machado G., and Dupont J. Palladium nanoparticle catalysts in ionic liquids: synthesis, characterisation and selective partial hydrogenation of alkynes to α -alkenes. *J. Mater. Chem.*, 21(9):3030–3036, 2011.
- [302] Aki S.N.V.K., Brennecke J.F., and Samanta A. How polar are room-temperature ionic liquids? *Chem. Commun.*, (5):413–414, 2001.

- [303] Wasserscheid P. and Welton T., editors. *Ionic Liquids in Synthesis*. Wiley-VCH Verlag GmbH & Co. KGaA, 2007.
- [304] Baudequin C., Baudoux J., Levillain J., Cahard D., Gaumont A.C., and Plaquevent J.C. Ionic liquids and chirality: opportunities and challenges. *Tetrahedron: Asymmetry*, 14(20):3081–3093, 2003.
- [305] Biswas A., Bayer I.S., Biris A.S., Wang T., Dervishi E., and Faupel F. Advances in top-down and bottom-up surface nanofabrication: Techniques, applications & future prospects. *Adv. Colloid Interface Sci.*, 170(1–2):2–27, 2012.
- [306] Gallagher P.K. and Gross M.E. The thermal decomposition of palladium acetate. *J. Therm. Anal.*, 31(6):1231–1241, 1986.
- [307] Pachón L.D. and Rothenberg G. Transition-metal nanoparticles: synthesis, stability and the leaching issue. *Appl. Organometal. Chem.*, 22(6):288–299, 2008.
- [308] Sherman J. The heats of hydrogenation of unsaturated hydrocarbons. *Oil Soap*, 16(2):28–28, 1939.
- [309] Lindlar H. and Dubuis R. Palladium catalyst for partial reduction of acetylenes. In *Organic Syntheses*. John Wiley & Sons, Inc., 2003.
- [310] Mosettig E. and Mozingo R. The rosenmund reduction of acid chlorides to aldehydes. In *Organic Reactions*. John Wiley & Sons, Inc., 2004.
- [311] Frolov V.M., Parenago O.P., Novikova A.V., and Kovaleva L.S. Highly active supported palladium catalysts for selective hydrogenation of conjugated dienes into olefins. *React Kinet Catal Lett*, 25(3–4):319–322, 1984.
- [312] Teschner D., Vass E., Zafeiratos S., Schnörch P., Kleimenov E., Hävecker M., Knop-Gericke A., and Schlögl R. Selective gas-phase hydrogenation of aliphatic triple and double bond using palladium based catalysts. In K. Godehusen, editor, *BESSY Annual Report 2005*, pages 257–259. Berliner Elektronenspeicherring-Gesellschaft für Synchrotronstrahlung m.b.H. (BESSY), Berlin, 2006.
- [313] Mattson B., Foster W., Greimann J., Hoette T., Le N., Mirich A., Wankum S., Cabri A., Reichenbacher C., and Schwanke E. Heterogeneous catalysis: The horiuti-polanyi mechanism and alkene hydrogenation. *J. Chem. Educ.*, 90(5):613–619, 2013.
- [314] Horiuti I. and Polanyi M. Exchange reactions of hydrogen on metallic catalysts. *Trans. Faraday Soc.*, 30(0):1164–1172, 1934.
- [315] Umpierre A., Machado G., Fecher G., Morais J., and Dupont J. Selective hydrogenation of 1,3-butadiene to 1-butene by Pd(0) nanoparticles embedded in imidazolium ionic liquids. *Adv. Synth. Catal.*, 347(10):1404–1412, 2005.

- [316] Ono N. *The Nitro Group in Organic Synthesis*. John Wiley & Sons, Inc., 2001.
- [317] Downing R.S., Kunkeler P.J., and van Bekkum H. Catalytic syntheses of aromatic amines. *Catal. Today*, 37(2):121–136, 1997.
- [318] Blaser H.U., Baiker A., and Prins R. *Heterogeneous Catalysis and Fine Chemicals IV*. Elsevier, 1997.
- [319] Weissermel K. and Arpe H.J. *Industrial Organic Chemistry, 3rd edition*. VCH, Weinheim, 1997.
- [320] Haber F. *Z. Elektrochem. Angew. Phys. Chem.*, 4:506–514, 1898.
- [321] Avelino Corma P.C. A different reaction pathway for the reduction of aromatic nitro compounds on gold catalysts. *Angew. Chem. Int. Ed. Engl.*, 46(38):7266–9, 2007.
- [322] Mizoroki T., Mori K., and Ozaki A. Arylation of olefin with aryl iodide catalyzed by palladium. *Bull. Chem. Soc. Jpn*, 44:581–581, 1971.
- [323] Heck R.F. and Nolley J.P. Palladium-catalyzed vinylic hydrogen substitution reactions with aryl, benzyl, and styryl halides. *J. Org. Chem.*, 37(14):2320–2322, 1972.
- [324] King A.O., Corley E.G., Anderson R.K., Larsen R.D., Verhoeven T.R., Reider P.J., Xiang Y.B., Belley M., and Leblanc Y. An efficient synthesis of LTD₄ antagonist 1-699,392. *J. Org. Chem.*, 58(14):3731–3735, 1993.
- [325] Larsen R.D., Corley E.G., King A.O., Carroll J.D., Davis P., Verhoeven T.R., Reider P.J., Labelle M., Gauthier J.Y., Xiang Y.B., and Zamboni R.J. Practical route to a new class of LTD₄ receptor antagonists. *J. Org. Chem.*, 61(10):3398–3405, 1996.
- [326] Dieck H.A. and Heck R.F. Organophosphinepalladium complexes as catalysts for vinylic hydrogen substitution reactions. *J. Am. Chem. Soc.*, 96(4):1133–1136, 1974.
- [327] Littke A.F. and Fu G.C. Palladium-catalyzed coupling reactions of aryl chlorides. *Angew. Chem. Int. Ed. Engl.*, 41(22):4176–4211, 2002.
- [328] Cassol C.C., Umpierre A.P., Machado G., Wolke S.I., and Dupont J. The role of Pd nanoparticles in ionic liquid in the Heck reaction. *J. Am. Chem. Soc.*, 127(10):3298–3299, 2005.
- [329] Reetz M.T. and Vries J.G.d. Ligand-free heck reactions using low Pd-loading. *Chem. Commun.*, (14):1559–1563, 2004.
- [330] Reetz M.T. and Westermann E. Phosphane-free palladium-catalyzed coupling reactions: The decisive role of Pd nanoparticles. *Angew. Chem. Int. Ed.*, 39(1):165–168, 2000.

- [331] Miyaura N., Yanagi T., and Suzuki A. The palladium-catalyzed cross-coupling reaction of phenylboronic acid with haloarenes in the presence of bases. *Synth. Commun.*, 11(7):513–519, 1981.
- [332] Kotha S., Lahiri K., and Kashinath D. Recent applications of the suzuki–miyaura cross-coupling reaction in organic synthesis. *Tetrahedron*, 58(48):9633–9695, 2002.
- [333] Smith G.B., Dezeny G.C., Hughes D.L., King A.O., and Verhoeven T.R. Mechanistic studies of the suzuki cross-coupling reaction. *J. Org. Chem.*, 59(26):8151–8156, 1994.
- [334] Ellis P., Fairlamb I., Hackett S., Wilson K., and Lee A. Evidence for the surface-catalyzed suzuki–miyaura reaction over palladium nanoparticles: An operando XAS study. *Angew. Chem. Int. Ed.*, 49(10):1820–1824, 2010.
- [335] Fernández F., Cordero B., Durand J., Muller G., Malbosc F., Kihn Y., Teuma E., and Gómez M. Palladium catalyzed suzuki C–C couplings in an ionic liquid: nanoparticles responsible for the catalytic activity. *Dalton Trans.*, (47):5572–5581, 2007.
- [336] Durand J., Teuma E., Malbosc F., Kihn Y., and Gómez M. Palladium nanoparticles immobilized in ionic liquid: An outstanding catalyst for the suzuki C–C coupling. *Catal. Commun.*, 9(2):273–275, 2008.
- [337] Susanna Jansat Dr J.D.D. A single catalyst for sequential reactions: Dual homogeneous and heterogeneous behavior of palladium nanoparticles in solution. *ChemCatChem*, 1(2):244 – 246, 2009.
- [338] Rodríguez-Pérez L., Pradel C., Serp P., Gómez M., and Teuma E. Supported ionic liquid phase containing palladium nanoparticles on functionalized multiwalled carbon nanotubes: Catalytic materials for sequential Heck coupling/hydrogenation process. *ChemCatChem*, 3(4):749–754, 2011.
- [339] Westermann T. and Melin T. Flow-through catalytic membrane reactors—principles and applications. *Chem. Eng. Process. Process Intensif.*, 48(1):17–28, 2009.
- [340] Pendergast M.M. and Hoek E.M.V. A review of water treatment membrane nanotechnologies. *Energy Environ. Sci.*, 4(6):1946–1971, 2011.
- [341] Armor J.N. Applications of catalytic inorganic membrane reactors to refinery products. *J. Membrane Sci.*, 147(2):217–233, 1998.
- [342] Heng S. Catalytic membrane reactor for water and wastewater treatment. Ph.D. thesis, Hong Kong University of Science and Technology, Hong Kong, 2006.
- [343] Julbe A., Farrusseng D., and Guizard C. Porous ceramic membranes for catalytic reactors — overview and new ideas. *J. Membrane Sci.*, 181(1):3–20, 2001.

- [344] Armor J.N. Membrane catalysis: Where is it now, what needs to be done? *Catal. Today*, 25(3–4):199–207, 1995.
- [345] Kapteijn F., Moulijn J.A., Weitzkamp J., and Dalmon J.A. Catalytic membrane reactors. In J.W. G. Ertl H. Knözinger, editor, *Handbook of Heterogeneous Catalysis*, page 1387. Weinheim, Germany, VCH, 1997.
- [346] Saracco G., Neomagus H., Versteeg G.F., and Van Swaaij W.P.M. High-temperature membrane reactors: potential and problems. *Chem. Eng. Sci.*, 54(13):1997–2017, 1999.
- [347] Paturzo L., Basile A., and Drioli E. High temperature membrane reactors and integrated membrane operations. *Rev. Chem. Eng.*, 18(6):511–552, 2002.
- [348] Astruc D. *Nanoparticles and Catalysis*. WILEY-VCH, 2008.
- [349] Hagiwara H., Sugawara Y., Isobe K., Hoshi T., and Suzuki T. Immobilization of Pd (OAc)₂ in ionic liquid on silica: application to sustainable mizoroki-heck reaction. *Org. Lett.*, 6(14):2325–2328, 2004.
- [350] Yamada Y.M.A., Watanabe T., Beppu T., Fukuyama N., Torii K., and Uozumi Y. Palladium membrane-installed microchannel devices for instantaneous suzuki-miyaura cross-coupling. *Chem. – Eur. J.*, 16(37):11311–11319, 2010.
- [351] Nagy E. Diffusive plus convective mass transport through catalytic membrane layer with dispersed nanometer-sized catalyst. *Int. J. Compos. Mater.*, 2(5):79–91, 2012.
- [352] GU Y., Favier I., Pradel C., Gin D.L., Lahitte J.F., Noble R.D., Gómez M., and Remigy J.C. High catalytic efficiency of palladium nanoparticles immobilized in a polymer membrane containing poly(ionic liquid) in suzuki-miyaura cross-coupling reaction. *J. Membrane Sci.*, 492:331–339, 2015.
- [353] Kannurpatti A.R., Anseth J.W., and Bowman C.N. A study of the evolution of mechanical properties and structural heterogeneity of polymer networks formed by photopolymerizations of multifunctional (meth) acrylates. *Polymer*, 39(12):2507–2513, 1998.
- [354] Ward J.H., Furman K., and Peppas N.A. Effect of monomer type and dangling end size on polymer network synthesis. *J. Appl. Polym. Sci.*, 89(13):3506–3519, 2003.
- [355] Lin-Gibson S., Jones R.L., Washburn N.R., and Horkay F. Structure-property relationships of photopolymerizable poly (ethylene glycol) dimethacrylate hydrogels. *Macromolecules*, 38(7):2897–2902, 2005.

- [356] Ortega A.M., Kasprzak S.E., Yakacki C.M., Diani J., Greenberg A.R., and Gall K. Structure–property relationships in photopolymerizable polymer networks: Effect of composition on the crosslinked structure and resulting thermomechanical properties of a (meth) acrylate-based system. *J. Appl. Polym. Sci.*, 110(3):1559–1572, 2008.
- [357] Glorius F. *N-Heterocyclic Carbenes in Transition Metal Catalysis*, volume 28 of *Top. Organomet. Chem.* Springer-Verlag,, Berlin/Heidelberg, 2007.
- [358] Muraviev D.N., Macanás J., Parrondo J., Muñoz M., Alonso A., Alegret S., Ortueta M., and Mijangos F. Cation-exchange membrane as nanoreactor: Intermatrix synthesis of platinum–copper core–shell nanoparticles. *React. Funct. Polym.*, 67(12):1612–1621, 2007.
- [359] A Rivaton J.G. Photodegradation of polyethersulfone and polysulfone. *Polym. Degrad. Stab.*, 66(3):385–403, 1999.
- [360] Kiefer J., Fries J., and Leipertz A. Experimental vibrational study of imidazolium-based ionic liquids: Raman and infrared spectra of 1-ethyl-3-methylimidazolium bis (trifluoromethylsulfonyl) imide and 1-ethyl-3-methylimidazolium ethylsulfate. *Appl. Spectrosc.*, 61(12):1306–1311, 2007.
- [361] Davis M.E. and Davis R.J. *Fundamentals of Chemical Reaction Engineering*. Courier Corporation, 2013.
- [362] Finke R.G. *Metal nanoparticles: synthesis, characterization and applications*. Marcel Dekker, New York, 2002.
- [363] Atilhan M., Jacquemin J., Rooney D., Khraisheh M., and Aparicio S. Viscous behavior of imidazolium-based ionic liquids. *Ind. Eng. Chem. Res.*, 52(47):16774–16785, 2013.
- [364] Jacquemin J., Husson P., Padua A.A.H., and Majer V. Density and viscosity of several pure and water-saturated ionic liquids. *Green Chem.*, 8(2):172–180, 2006.
- [365] Friedlander S.K. A note on transport to spheres in stokes flow. *AIChE J.*, 7(2):347–348, 1961.
- [366] Nagy E., Blickle T., and Ujhidy A. Spherical effect on mass transfer between fine solid particle and liquid accompanied by chemical reaction. *Chem. Eng. Sci.*, 44(1):198–201, 1989.
- [367] Seto H., Yoneda T., Morii T., Hoshino Y., Miura Y., and Murakami T. Membrane reactor immobilized with palladium-loaded polymer nanogel for continuous-flow Suzuki coupling reaction. *AIChE J.*, 61(2):582–589, 2014.

- [368] Faria V.W., Oliveira D.G.M., Kurz M.H.S., Gonçalves F.F., Scheeren C.W., and Rosa G.R. Palladium nanoparticles supported in a polymeric membrane: an efficient phosphine-free “green” catalyst for Suzuki–Miyaura reactions in water. *RSC Adv.*, 4(26):13446–13452, 2014.
- [369] Leybros J. and Frémeaux P. Extraction solide-liquide, aspects théoriques, *Technique de l’ingénieur*, j2780.
- [370] Becht N.O., Malik D.J., and Tarleton E.S. Evaluation and comparison of protein ultrafiltration test results: Dead-end stirred cell compared with a cross-flow system. *Sep Purif Technol*, 62(1):228–239, 2008.
- [371] Chahdoura F. Nanoparticules métalliques en milieu glycérol: un catalyseur unique pour des procédés multi-étapes. Ph.D. thesis, l’Université de Toulouse, 2014.
- [372] Chahdoura F., Mallet-Ladeira S., and Gómez M. Palladium nanoparticles in glycerol: a clear-cut catalyst for one-pot multi-step processes applied in the synthesis of heterocyclic compounds. *Org. Chem. Front.*, 2(4):312–318, 2015.
- [373] Vries J.G.d. A unifying mechanism for all high-temperature heck reactions. the role of palladium colloids and anionic species. *Dalton Trans.*, (3):421–429, 2006.
- [374] GU Y., Emin C., Remigy J.C., Favier I., Gómez M., Noble R.D., Macanás J., Domènech B., and Lahitte J.F. Hybrid catalytic membranes: tunable and versatile materials for fine chemistry applications (to be published). *Mater. Today. Proc.*, 2015.
- [375] Taylor G. Dispersion of soluble matter in solvent flowing slowly through a tube. *Proc. R. Soc. Lond. Math. Phys. Eng. Sci.*, 219(1137):186–203, 1953.
- [376] Aris R. On the dispersion of a solute in a fluid flowing through a tube. *Proc. R. Soc. London, Ser. A*, 235(1200):67–77, 1956.
- [377] Levenspiel O. *Chemical Reaction Engineering, 3rd Edition*. John Wiley & Sons, New York, 1999.
- [378] Stroock A.D., Dertinger S.K.W., Ajdari A., Mezic I., Stone H.A., and Whitesides G.M. Chaotic mixer for microchannels. *Science*, 295(5555):647–651, 2002.
- [379] Westermann T., Kretzschmar E., Pitsch F., and Melin T. Heat transfer and temperature profiles in flow-through catalytic membrane reactors. *Chem. Eng. J.*, 155(1–2):371–379, 2009.
- [380] Bakeri G., Ismail A.F., DashtArzhandi M.R., and Matsuura T. Porous PES and PEI hollow fiber membranes in a gas–liquid contacting process—a comparative study. *J. Membrane Sci.*, 475:57–64, 2015.
- [381] Danckwerts P.V. Continuous flow systems: Distribution of residence times. *Chem. Eng. Sci.*, 2(1):1–13, 1953.

- [382] Bergman T.L. and Incropera F.P. *Introduction to Heat Transfer*. John Wiley & Sons, 2011.
- [383] Thermal-fluids central.
- [384] Sabry M.N. Scale effects on fluid flow and heat transfer in microchannels. *IEEE Trans. Compon. Packag. Technol.*, 23(3):562–567, 2000.
- [385] Cybulski A., Sharma M.M., Sheldon R.A., and Moulijn J.A. *Fine Chemicals Manufacture: Technology and Engineering*. Gulf Professional Publishing, 2000.
- [386] Murthy C.P. *University Chemistry*. New Age International, 2008.
- [387] Bergman T.L., Incropera F.P., and Lavine A.S. *Fundamentals of Heat and Mass Transfer, 7th edition*. John Wiley & Sons, 2011.
- [388] McKeen L.W. *The Effect of Long Term Thermal Exposure on Plastics and Elastomers*. William Andrew, 2013.
- [389] Plastic and thermoplastic elastomer materials, minnesota rubber and QMR plastics. Technical report, Minnesota Rubber and QMR Plastics.
- [390] Zhang Y., Quek X.Y., Wu L., Guan Y., and Hensen E.J. Palladium nanoparticles entrapped in polymeric ionic liquid microgels as recyclable hydrogenation catalysts. *J. Mol. Catal. Chem.*, 379:53 – 58, 2013.
- [391] Günther J., Schmitz P., Albasi C., and Lafforgue C. A numerical approach to study the impact of packing density on fluid flow distribution in hollow fiber module. *Journal of Membrane Sci.*, 348(1–2):277–286, 2010.
- [392] Costello M.J., Fane A.G., Hogan P.A., and Schofield R.W. The effect of shell side hydrodynamics on the performance of axial flow hollow fibre modules. *Journal of Membrane Sci.*, 80(1):1–11, 1993.
- [393] Microreactor technology at lonza, 2009.
- [394] Guisnet M. and Pinard L. Catalyse hétérogène: désactivation et régénération des catalyseurs, *Technique de l’ingénieur*, j1265, 2014.
- [395] Hsieh H.P. *Inorganic Membranes for Separation and Reaction*. Elsevier, 1996.

Membranes polymères fonctionnalisées par des poly(liquide ionique)s et des nanoparticules de palladium: applications au captage de CO₂ et aux membranes catalytiques

Des membranes supports en polymère ont été photo-greffées par des poly(liquide ionique)s (polyLIs) à base d'imidazolium. Les polyLIs permettent de séparer le CO₂ d'autres gaz et de stabiliser des nanoparticules. Dans le cas du captage de CO₂, les expériences montrent qu'une couche fine homogène de gel réticulé en polyLI gonflé par du liquide ionique (LI) est obtenue sur la surface de fibres creuses. Les fibres ainsi obtenues ont montré des perméances au CO₂ plus élevées (600-700 GPU) que des membranes commerciales et des sélectivités de CO₂/N₂ comparables (13 et 17). Dans le cas de membranes catalytiques, des nanoparticules de palladium (NPPd) servant de catalyseur ont été immobilisées en forte concentration locale au sein d'une couche de polyLI greffée à la surface de membranes. La réactivité des membranes catalytiques a été testée en configuration de contacteur traversé sur différentes réactions (couplage croisé C-C, hydrogénation, etc). Une conversion totale est obtenue pour des temps de séjours de quelques secondes, sans aucun sous-produit formé. Comparée aux NPPd colloïdaux dans un réacteur en batch, la membrane catalytique accélère les réactions d'environ 2000 fois en terme de temps de réaction sans perte de NPPd; la sélectivité est aussi accrue. Le réacteur membranaire catalytique a été modélisé afin d'obtenir les profils de concentration et de température et une meilleure compréhension des performances obtenues. Les membranes catalytiques se révèlent isothermes et les constantes cinétiques sont calculées. Enfin, les capacités de production de ces membranes catalytiques à une échelle industrielle sont estimées à environ 3 t/(h· m³) pour le couplage de Suzuki.

Mots clés: Membrane polymère, photo-greffage, liquides ioniques, nanoparticules métalliques, séparation de gaz, membrane catalytique.

Polymeric membranes functionalized by poly(ionic liquid)s and palladium nanoparticles: application for CO₂ capture and catalytic membranes

Polymeric support membranes were modified via photo-grafting by poly(ionic liquid)s (polyILs), featuring in the capability to separate CO₂ from other gases and to stabilize metallic nanoparticles (MNPs). For CO₂ capture, a thin polyIL-IL gel layer was homogeneously coated on support hollow fibers. The composite fibers show high CO₂ permeance and reasonable CO₂/N₂ selectivity. For the catalytic membrane, palladium NPs were generated inside a grafted polyLI layer. Compared to colloidal palladium system in a batch reactor, the catalytic membrane, as a contactor membrane reactor, is more efficient in terms of reaction time (ca. 2000 times faster), selectivity and MNP retainability. Theoretical study on reactor modeling, concentration & temperature profiles, and production capacity was done for an overall understanding of the catalytic membrane.

Key words: Polymeric membrane, photo-grafting, ionic liquid, metallic nanoparticles, gas separation, catalytic membrane